UNIVERSITY OF NAPOLI FEDERICO II

Department of Civil, Building and Environmental Engineering

Ph. D. in Civil Systems Engineering

XXXVIII cycle

STATIC AND DYNAMIC EFFECTS OF DEEP EXCAVATIONS ON THE SURROUNDINGS: TWO CASE STUDIES IN NAPOLI

Ilaria Esposito

A thesis submitted for the degree of Doctor of Philosophy

Ph. D. Coordinator: Prof. Andrea Papola

Tutor: Prof. Gianpiero Russo

March 2026

Index

Chapter 1
Introduction

The development of public transport in city centers has led to an increase in infrastructure projects involving underground structures, such as tunnels and deep excavations. Their frequent construction in densely urbanized areas has drawn attention to the effects that they have on existing structures and infrastructure. In order to minimize these effects in terms of induced displacements, very rigid, hyperstatic, and multi-anchored structures are built to support deep excavations, in which the interaction with the ground (which in turn depends, among other factors, on the construction phases) is very important in the development and distribution of loads. These are complex structural systems, whose behavior is a function of multiple factors, including those depending on the construction site itself. This makes it difficult to generalize the study and design method, with the result that existing literature and, as a consequence, professional practice often refer to simplified (*e.g.*, spring methods) and cautious methods (such as the empirical and semi-empirical methods developed since the second half of the 20th century) that generally lead to an overestimation of loads and displacements and the consequent oversizing of support structures. The still incomplete understanding of the behavior of these structures in static conditions and the strong dependence of the results on the modeling of the contact between soil and structure, together with a preconception about their low vulnerability to seismic actions, meant that for many years the seismic performance of underground structures was neglected in research and, consequently, in regulations. The famous collapse of the Daikai station in Japan during the 1995 Kobe earthquake brought attention back to this issue, which in the last years has been addressed with experimental campaigns on scaled models and numerical simulations, thanks to the development of FEM or FDM modeling software. In analogy with the approach adopted in the static field – *i.e.*, studying the structure and its effects on the surrounding environment – a similar approach can also be adopted when seismic action occurs, in which the underground structure is not considered isolated but immersed in the surrounding environment and, as such, not only undergoes additional seismic loads but can itself be the cause of effects in the propagation of seismic motion and the modification of seismic risk associated with structures and facilities included in the surrounding environment. Among the reasons why this field of research is still largely unexplored are, on the one hand, the almost total absence of experimental data on full-scale structures, the strong dependence of results on site conditions, which makes them difficult to generalize, and, finally, the time-consuming nature of the calculations required to perform accurate numerical simulations that take into account the interaction between the soil and the structure and the non-linearity of the soil. This latter aspect leads to adopt many simplifying assumptions when modelling such problems, *e.g.*, assuming linear elastic or viscoelastic behavior of soil, treating the problem in planar conditions, disregarding the static excavation sequence, which is found, instead to have an impact also on results of seismic coupled analyses. Moreover, the contributions available in literature are mostly dedicated to the characterization of circular or squared tunnel behavior, while open, deep supported excavations, are almost completely disregarded. This is the context for the thesis presented here, with the aim of providing an additional contribution to the state of the art by filling some gaps found in the literature: two case studies of deep open-pit excavations carried out in the center of Napoli are used as a starting point. These are Chiaia and San Pasquale stations on Line 6 of the Napoli metro, whose effects on the surrounding environment have been investigated both statically (during construction, by conducting a very detailed back-analysis based on monitoring data) and seismically (hypothetical scenario of seismic loads) using three-dimensional modeling of the case studies on finite element software, in which the construction phases, the interaction between the support structures and the ground, and the non-linear behavior of the soil are accurately reproduced. In addition to this introductory chapter (*Chapter 1*), the thesis is structured as follows:

Chapter 2 presents the state of the art in underground works, with particular attention to large-scale excavation projects. After an introduction on construction technologies and Italian and European regulations, the chapter is divided into two parts: one concerning the statics of excavations and the methods, both recent and less recent, for calculating the stresses resulting from interaction with the ground, the induced displacements, and for assessing damage to buildings; the second part is dedicated to soil-structure interaction under seismic loads: this includes a section on structure-soil-structure interaction, with particular attention to the interaction of underground structures with the surrounding environment and therefore also with above-ground structures, and vice versa.

Chapter 3 is dedicated to the case study of Chiaia station. An introduction describing the case study and the monitoring results, is followed by a static back-analysis of the construction process, which investigates and highlights the role of various modeling details, including the assumptions necessary for a simplified but rational modeling of the buildings of greatest interest. Finally, the construction of the numerical model and the results of the coupled dynamic analyses are presented with particular reference to the effects induced on the buildings in terms of displacements and peak ground accelerations.

Chapter 4: San Pasquale station is the case study covered in this chapter, which follows the same structure of the previous one. Compared to the *Chapter 3*, however, greater attention is paid to the structural modeling of the buildings affected by the most significant subsidence and, thanks to the characteristics of the case study in question, it has been possible to parameterize the analyses carried out under seismic excitation to a greater extent, placing emphasis on the spatial distribution of the quantities of interest.

Chapter 5 reports on the simulation using FEM analysis, and subsequent comparison, of centrifuge experiments conducted to characterize the seismic behavior of a rectangular tunnel in dry sand. The chapter aims to characterize the capacity of the tools used in numerical analysis to reproduce experimental data.

Chapter 6: the results presented in the thesis are summarized in this concluding chapter which, in addition to referring to individual case studies, contains some general considerations validated in the thesis by comparison with the existing literature, mainly referred to tunnels, which is almost the only reference point, since open deep excavations are scarcely investigated.

Chapter 2
Literature review

2.1. Underground structures: technology and limit states

Sustained excavations are vertical underground structures and, as such, they cross different soil layers, sometimes reaching rocky formations (bedrock, in earthquake engineering). This kind of work is realized for the construction of parking spots, subway stations and new underground floors of existing buildings, often in the city centers, close to buildings and public facilities that can be affected by the displacement field induced by the excavation itself. It is a soil-structure interaction problem that controls the displacement field produced by the excavation activity on the nearby, as well as the stresses acting on the retaining system, and that in turn is controlled by many technological factors, in addition to soil properties. That's why a thorough analysis of the site geotechnical characteristics and an adequate design of retaining structures are required.

Geometry, type and installation of retaining system, sequence of works (bottom-up or top-down method), presence of water and type of drainage, execution, are factors influencing the observed behavior of the soil around the excavation area. Therefore, the soil-structure interaction topic in static conditions can be addressed analyzing the dual following aspects:

- the stresses acting on the retaining system;
- the displacement induced by the work on the surroundings.

The Italian building code – NTC 2018 (Ministero delle Infrastrutture, 2018) – states that, besides an adequate factor of safety against global stability and collapse mechanisms of walls or bottom of the excavations (hydraulic, geotechnical and structural ultimate limit states), good performances at the service limit states must be ensured as well, especially when the excavation is realized in urban areas: the induced displacements must be evaluated and their compatibility with the interacting buildings and facilities must be assessed before proceeding.

2.1.1. Retaining systems of deep excavations

According to Terzaghi (1943) excavations are defined deep when their depth is greater than their widths. In 1967, Terzaghi and Peck revised the definition, stating that deep excavations are those with a depth of at least 6 m: greater depths made no longer economical to construct the retaining system with sheet pile walls or soldier piles, and it became convenient to use concrete structures such as diaphragm or pile walls. Nowadays in dense urban environments the distinction between shallow and deep excavations is not so strict anymore and the use of reinforced concrete structures (bulkheads) with anchorage systems to minimize displacement as much as possible, is very common thanks, in part, to availability of bentonite slurry and certain technical advances, such as improved excavation techniques (Clayton *et al.*, 2014). Bulkheads are flexible retaining structures usually built in Reinforced Concrete (RC), whose resistance entirely depends on the depth of penetration when no anchorage system is provided. The elements constituting the bulkhead can have different shapes and length, depending on the adopted technology and on the requirements on site.

Pile walls. Based on the ratio between spacing *i* and diameter *d*, they can be distinguished in:

- $i<d$ secant piles
- $i=d$ tangent piles
- $i>d$ contiguous piles

as illustrated in Figure 1.

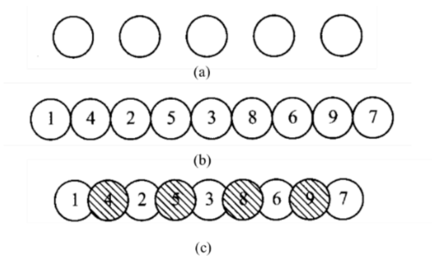

Figure 1. (a) Secant, (b) tangent, (c) contiguous piles (Ou, 2014).

As the number of piles per linear meter increases, the resistance of the pile wall increases as well, but since there is no connection among the pile reinforcements, the section of the pile wall doesn't have structural continuity. Secant piles can guarantee impermeability, but in this case, it is of primary importance to control the verticality. It can be done by building guide walls and following a suitable sequence of realization of piles so that the machine can work in symmetrical conditions: first piles with no reinforcement or with a reduced one are realized, then they are milled to host the secondary piles, reinforced (dashed circles in Figure 1). The technologies are the same used for foundation piles, therefore pile walls are suitable for maximum depth of about 50 m and maximum compression strength of 400 kg/cm^2. Moreover, the technologies allow for the control of verticality with a tolerance of about 1-2%.

Diaphragm walls. Used for the first time in Italy in 1950s, they are made by parallelepiped panels jointed to each other, whose length and width depend on the dimension of the excavation machine that, depending on the depth to be reached and the crossed soil properties, can be a clamshell bucket or a hydro-mill (usually adopted for great depths, up to 250 m, and compressive strength values above 100-200 kg/cm^2). The joints between adjacent panels are usually weakness points both for structural continuity and impermeability, but it is possible to extend the reinforcement to make the panels work together (*i.e.*, transmitting shear forces and bending moments) and use gum joints to obtain watertight structures. In Figure 2 different possible types of joints are represented.

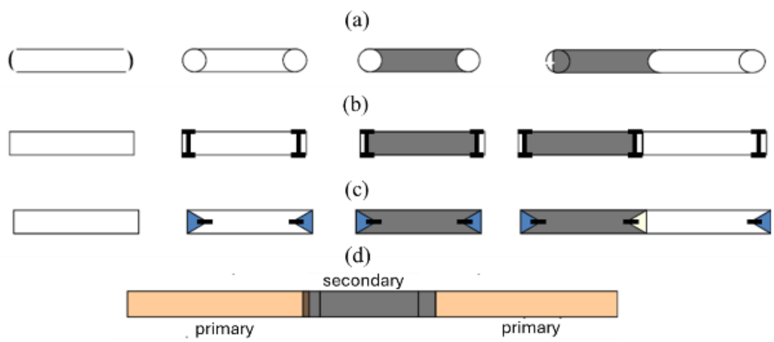

Figure 2. Types of joints between two adjacent diaphragm panels: a) pipes; b) soldier piles; c) end-stops (or water-stops when hydraulic isolation is guaranteed); d) milling of the primary panel during execution of the secondary one (even in this case the joint guarantees hydraulic isolation).

The two machines work differently: clamshell bucket advances only because of its own weight, therefore it cannot penetrate very consistent soil; it can be moved with cables, with a system of rods or with hydraulic pistons (Figure 3a and b; Figure 4). Hydro-mill (Figure 3c and Figure 4) is provided with gear wheels breaking up the soil, which is then dragged upward by the bentonite slurry, responsible for the stability of the excavation before concrete casting. The cutting wheels often are four, rotating two by two in opposite direction. Even in this case the excavation sequence is very important to control verticality, that with hydro-mill can reach tolerance of about 1‰ thanks to automatized systems.

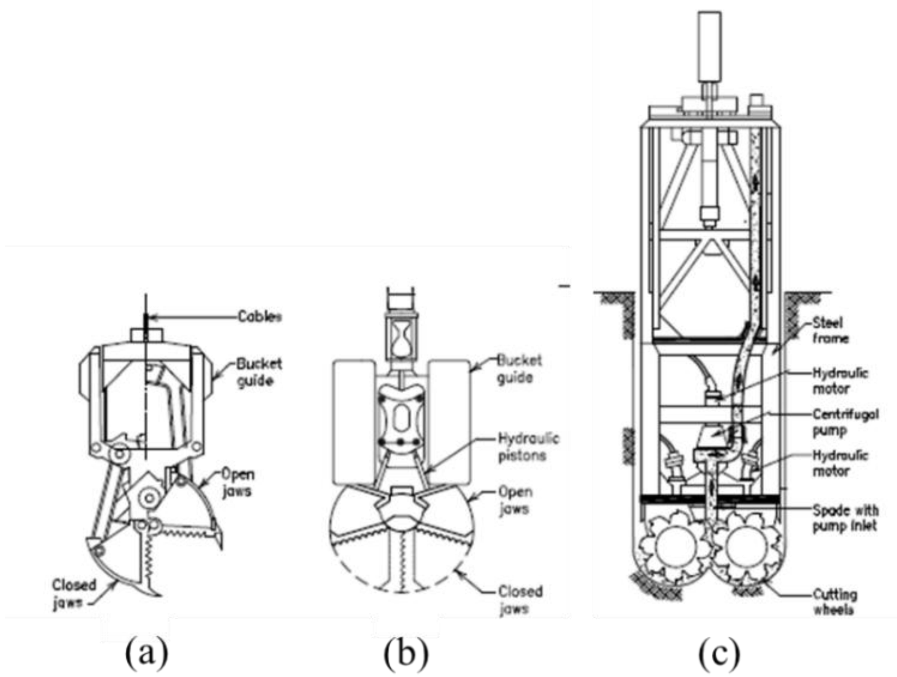

Figure 3. a) Clamshell bucket; b) hydraulic clamshell bucket; c) hydro-mill.

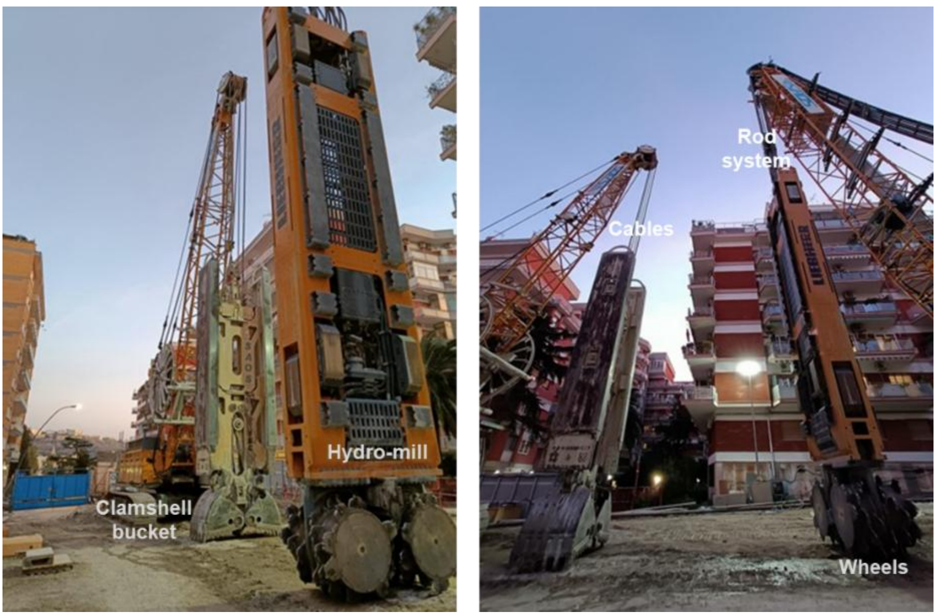

Figure 4. Clamshell bucket and hydro-mill on site (photo courtesy of Eng. Giuseppe Cipolletta).

2.1.2. Methods of excavation

Depending on several considerations that may be related to the geological characteristics of the site or the presence of water, economic reasons, availability of machinery, or consideration about available time, many different solutions can be adopted for the excavation.

Full open cut. This is a method suitable for shallow excavation. No retaining system is adopted (neither struts nor walls), instead a slope is given to the excavation sides to avoid the collapse. This is a cheap method for shallow excavations, suitable for cemented soil or rocks; as the depth increases, though, the amount of soil to remove to maintain the side slopes becomes huge and difficult to dispose of. As an alternative it is possible to proceed installing a cantilever retaining wall without anchors or struts: the stiffness of the cantilever wall is the only source of stability.

Braced or anchored excavations. When the retaining structure is built with the aim of containing displacements often anchor systems are added. They can be classified as follows:

- *struts*, that work in compression, can be realized with steel, wooden or RC beams (provisional structures) or with permanent structures like concrete slabs appropriately designed with eyelets to allow the movements of the excavating machine
- *tie rods* (or anchors), that work in traction. They are composed of two parts (Figure 5): a free length or free section, that is a steel strand free to move into the soil thanks to a plastic membrane placed around it – only solicited in traction – and a foundation, or fixed section, *i.e.*, a RC bulb subjected to tangential stresses which is responsible for the grip. Anchors can also be pre-stressed ensuring better grip and therefore reduced movement. They count solely on soil strength to offer resistance: the higher the soil strength, the higher the anchoring force. Sands and gravels can offer higher strength than clays, which even reduce their strength due to creep phenomena. Thus, the anchoring section should avoid being installed in clays. Moreover, anchors are not appropriate when the groundwater level is high: because of the high permeability of granular soils, it can be difficult to seal the bores.

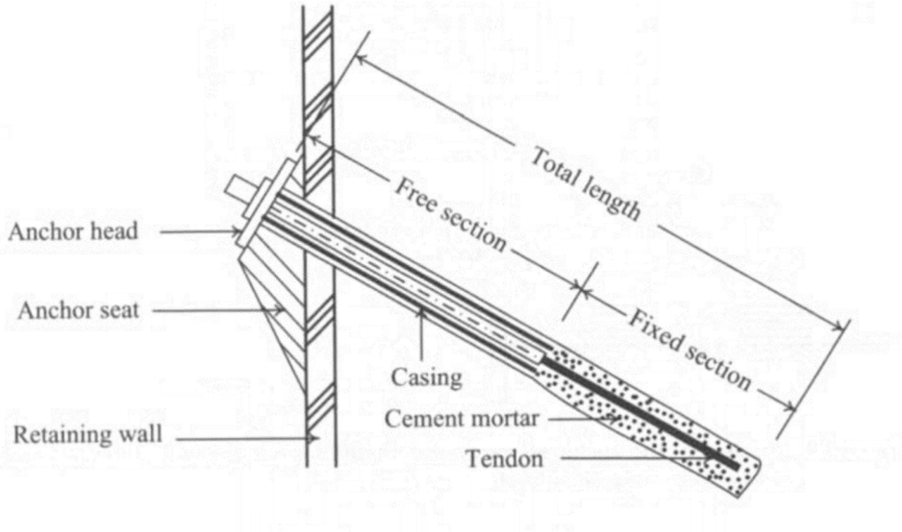

Figure 5. Grouted anchor general scheme (after Ou, 2006).

For both systems, struts and anchors, the sequence of work involves an initial excavation without support, for a reduced depth (~1.5 m), followed by the installation of the first level of anchors or the casting of the first slab, then the excavation can proceed. The choice of anchorage influences the construction sequence. In fact, open cut and anchored excavations belong to the bottom-up construction method which consists in first completing the excavation, installing the foundation at the base, and then building the internal structure working upwards. If the structure is anchored the anchor levels are cut step by step as one goes up.

The braced excavation can lead to both a bottom-up or a top-down construction sequence depending on the type of struts. If the struts are permanent structures (*i.e.*, slabs), the construction of the internal structures proceeds simultaneously to the excavation works.

2.1.3. Eurocodes and Italian national code for flexible retaining structures

A probabilistic approach is adopted by Italian national code (NTC 2018) and Eurocodes (for geotechnical systems, EC7 – EN 1997 – for static conditions, and EC8 – EN 1997 – for seismic conditions) for evaluating the hazard and verifying that the works satisfy the requirements in terms of strength and stability. The probabilistic approach admits a non-zero probability of failure P_F, and in the cited codes it takes the form of Limit States (LS). LS are divided into Service LS (SLS) and Ultimate LS (ULS), depending

on the performances expected by the structure or the system, under a given stress or displacement distribution. SLS are often addressed in the form of comparison of expected vs. admissible movements, *e.g*., NTC 2018 regarding SLS of retaining structure, prescribes that: "*[...] the movements of the retaining structure and the surrounding ground must be assessed to verify their compatibility with the functionality of the structure and with the safety and functionality of adjacent structures [...]. In the presence of structures that are particularly sensitive to the movements of the retaining structure, a specific analysis of the interaction between the structures and the ground must be developed, taking into account the sequence of construction phases*".
ULS, instead, must satisfy the following relationship between design loads (L_d) and design resistance (R_d):

$$R_d > L_d \qquad (1)$$

Which means that the resistances, appropriately reduced, must be greater than the loads, appropriately amplified. The verification procedure applies reduction and amplification through partial or total safety factors:

- PRFD (Partial Resistance Factor Design): partial safety factors are included in a non-linear way in the calculation of the design resistance. The values of these factors are such that, once applied to the correct quantities, they give a constant probability of failure. This approach can be written in the form:

  $$R_k\left\{\frac{X_k}{[\gamma_m]}\right\} > [\gamma_l]L_k \qquad (2)$$

  Where X_k is the characteristic value of the soil property and γ_m the partial safety factor to be applied to material properties.
- Total Resistance Factor Design (TRFD): in this approach a single safety factor is used to take into account all the uncertainties involved in the evaluation of soil resistance and it can be written in the form:

  $$\frac{R_k}{[\gamma_r]} > [\gamma_l]L_k \qquad (3)$$

In 2025 the final versions of the so-called second generation EC7 and EC8 have been released. The former version of EC7 contained three different Design Approaches (DA) for geotechnical verifications, which can be summarized in the information of Table 1.

Table 1. Design approaches contained in EC7 (EN 1997)

Application of SF	Design Approach 1		Design Approach 2	Design Approach 3
	C1	C2		
Loads	✓		✓	✓
Geotechnical parameters		✓		✓
Global resistance			✓	

Italian building code (NTC 2018) predates the latest release of the Eurocodes; therefore, it includes only the former version and, in NTC 2018, DA1 is the only design approach used for verification of flexible retaining structures (*i.e.*, those characterized by a significant deformability, that cannot be disregarded in design), in both its combinations, C1 and C2. It is worth noticing that combination C1 is usually heavier for structural sizing, whereas C2 penalizes geotechnical verifications. The ultimate limit states (whose mechanisms are illustrated in Figure 6) to verify flexible retaining structures in static conditions, according to prescriptions of NTC 2018 are the followings (Lancellotta *et al.*, 2020):

- EQU (equilibrium of the aboveground structure): the equilibrium of the structure is the first thing to assess: this permits the sizing of the minimum penetration length.
- STR (structural LS): assessment of compatibility of structural demand and capacity of structural elements, included foundations.
- GEO (geotechnical LS): it treats the ultimate resistance of the soil interacting with the structure, and the development of possible collapse mechanisms.
- HYDRO (heaving, siphoning).
- UPL (uplift): loss of equilibrium due to hydraulic under pressure at the bottom of excavation.

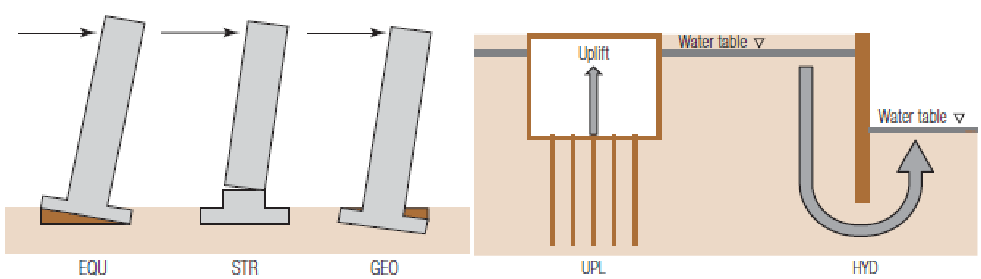

Figure 6. Limit states according to NTC 2018 (after Manual for the geotechnical design of structures to Eurocode 7).

The new release of EC7, instead, talks about:

- Material factor approach: partial safety factors are applied to the loads (or their effects) and to geotechnical parameters (material). This approach corresponds to C1 and C2 of DA1.
- Resistance factor approach: partial safety factors are applied to the loads (or their effects) and to global resistance of the system. This approach corresponds to DA2.

The new EC7 introduces the distinction between three Geotechnical Categories (GC) whose definition depends on two quantities: Consequence Class (CC) and Geotechnical Complexity Class (GCC). CC, first introduced in EN1990, indicates the consequences of an eventual failure of the system in terms of human lives, and from economic and environmental point of view. GCC, instead, takes into account the uncertainties and complexities related to the soil and to soil-structure interaction involved in the work. Moreover, CC influences the values of partial safety factors that are affected by the so-called consequence factors to be applied to loads, material properties and in the calculation of the return period T_R for seismic actions: according to EC8-5 the return period becomes a function of the consequence expected when a given limit state is attained. As the CC increases, the return period increases as well, and so does the design peak acceleration. As an alternative to T_R EC8-5 prescribes the adoption of an amplification coefficient for the design acceleration, again depending on CC.
For what concerns tie-back anchors verifications, NTC 2018 incorporates the approach proposed by EC7 which treats the problem referring only to ULS. The code states that the ULS of anchors refer to possible collapse mechanisms occurring because the maximum soil resistance or the resistance in structural elements is attained. In addition, a pull-out verification must be conducted. However, more in-depth discussion of the design process to be followed for checking tie rods is contained in the AGI (Associazione Geotecnica Italiana) guidelines. The guidelines indicate a two-step assessment procedure:

I. Global stability assessment: it is required to determine the minimum free length of the anchor (see Figure 5). This may involve uplift, or stability of excavation front.
II. Local check: the capacity of the anchor to sustain the design load must be verified. In this case three different scenarios must be considered:
    - Pull-out of the anchor foundation from soil
    - Failure of the reinforcement
    - Pull-out of reinforcement from the mortar used for foundation.

2.2. Soil-structure interaction under static loads

2.2.1. Lateral earth pressure: classical earth pressure theory

As mentioned in 2.1.3, it is necessary, for structural design, to establish the loads acting on the bulkhead. It must be done with a soil-structure interaction analysis, which can be conducted in different ways depending on the desired degree of approximation. In the simple case of cantilevered or single-constrained structures, the design is carried out at the ultimate limit state, assuming a rigid-plastic constitutive relationship for the soil, which means assuming that the soil-structure system attains the collapse for any value of displacement, of which only the direction will count in determining the distribution of horizontal stresses. Considering the rotational motion of a bulkhead supporting an embankment behind it, around its base, we can assume that, for any value of this rotation, there is active thrust on the downstream side and passive thrust on the upstream side. In this way, only the limit conditions are taken into account, while all the intermediate values of the thrust coefficients, which would otherwise be a function of the magnitude of the displacement, are neglected.

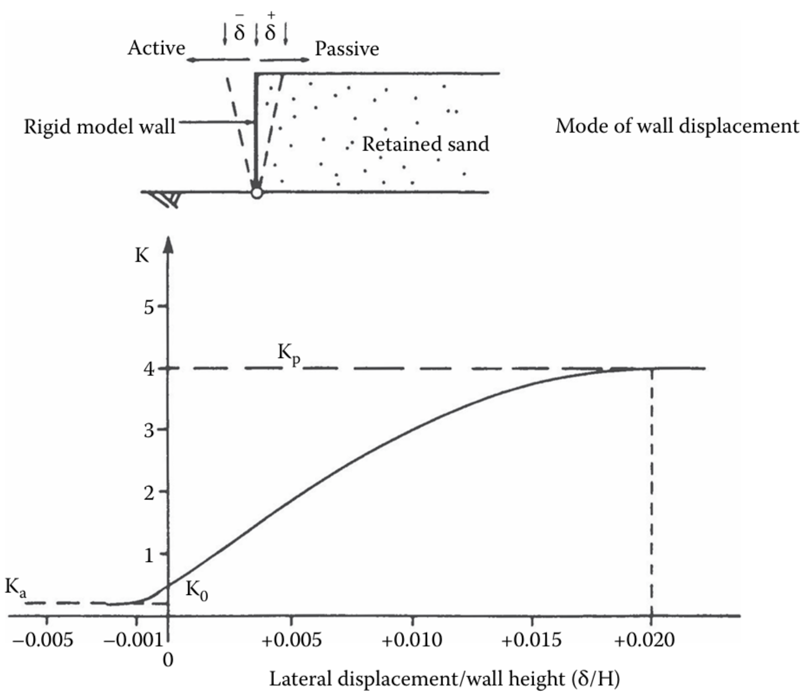

Figure 7. Qualitative evolution of k_p and k_a with the horizontal movement of the wall (after Clayton et al., 2014).

The diagram in Figure 7 (known as Terzaghi experiment) shows that between the two limit conditions mentioned above there is a substantial difference in the extent of displacement for which the collapse condition occurs. In fact, while the active thrust is fully mobilized for displacement values approximately equal to 0.1% of the total height of the bulkhead, the passive thrust is mobilized around values of 1%, *i.e.*, one order of magnitude higher. The reason for the difference is twofold:

- experimental data from load tests on soils lead to the conclusion that the stiffness during loading (associated with the passive thrust condition) is less than that observed during unloading and subsequent reloading (active thrust)
- the state at rest for normally consolidated soils is closer to the active state than to the passive state, therefore the stress variation necessary to reach the active thrust condition, $\Delta\sigma_a$, is much less than that required to completely mobilize the passive thrust, $\Delta\sigma_p$.

Once the hypotheses on the interaction between soil and structure have been defined, the thrust coefficients can be determined, which, depending on the approximations and hypotheses made, can be calculated in different ways:

1) Rankine's formulation (1857): assuming the wall being smooth (no tangential stresses acting at the interface) and infinitely rigid, and surface of the soil behind being horizontal, the horizontal and vertical stresses acting on the generic soil element below ground level are principal stresses. Under these conditions, the expressions for the active and passive thrust coefficients are obtained simply by assuming a constitutive relationship for the soil according to Mohr Coulomb criterion and then, from geometric constructions, on Mohr circles. This gives:

$$k_{a,p} = \frac{1 \mp sin\phi}{1 \pm sin\phi} = tan^2\left(\frac{\pi}{4} \pm \frac{\phi}{2}\right) \qquad (4)$$

With ϕ friction angle of the soil: k_a decreases with increasing of friction angle, while k_p increases. If the ground surface is inclined at a generic angle ε with respect to the horizontal direction, the Rankine coefficients for calculating horizontal stresses depend on ε and are expressed by the following relationships, valid for loose soils and cohesive soils, respectively:

$$loose\ soil: k_{a,p} = \frac{cos\varepsilon \mp \sqrt{sin^2\phi \mp sin^2\varepsilon}}{cos\varepsilon \pm \sqrt{sin^2\phi \mp sin^2\varepsilon}} \qquad (5)$$

$$cohesive\ soil: k_{a,p} = \frac{cos\varepsilon \mp \sqrt{sin^2\phi(c \cdot \frac{cot\phi}{\sigma_m} + 1)^2 \mp sin^2\varepsilon}}{cos\varepsilon \pm \sqrt{sin^2\phi(c \cdot \frac{cot\phi}{\sigma_m} + 1)^2 \mp sin^2\varepsilon}} \tag{6}$$

2) Limit equilibrium methods: if the smooth wall assumption no longer applies, the wall roughness, δ, is introduced. It is a quantity that has its upper limit in the value of the soil friction angle and determines the creation of tangential stresses at the soil-wall interface, with the consequent rotation of the main stress directions and the modification of the failure surfaces compared to the smooth wall case. The general procedure for these methods is as follows: once the wall kinematics has been hypothesized, it is assumed that the failure surface passing through the bottom of the bulkhead is flat or mixed-line depending on the method; along the failure surface, inclined at a certain angle α with respect to the horizontal, it is assumed that the shear strength is completely mobilized and the active thrust and passive thrust are calculated accordingly as the angle α varies. The passive thrust is the minimum among the maximum thrusts calculated as the angle varies, and vice versa for the passive thrust. The simplest method among these for calculating the effective thrust coefficients is Coulomb's method (1776), illustrated in Figure 8. This method disregards the analysis of local equilibrium conditions: the distribution of stresses on the wall face is unknown, and by closing the polygon of forces, the modulus of the active thrust P_A and the reaction R acting on the sliding surface are determined (see Figure 8). It is based on two important simplifying assumptions:

- the failure surface is assumed to be planar
- the problem of the equilibrium of the wedge of soil affected by the failure is solved by referring exclusively to the translational equilibrium, neglecting the rotational one.

This second assumption is fundamental to solve the problem. In fact, if both rotational and translational equilibrium are considered, we would have a problem with four unknowns and three equations, which would be unsolvable. However, by removing the rotational equilibrium equation, we also remove the two unknowns constituted by the points of application of the acting forces, leaving a system of two equations with two unknowns (magnitudes of the two forces), which is therefore solvable.

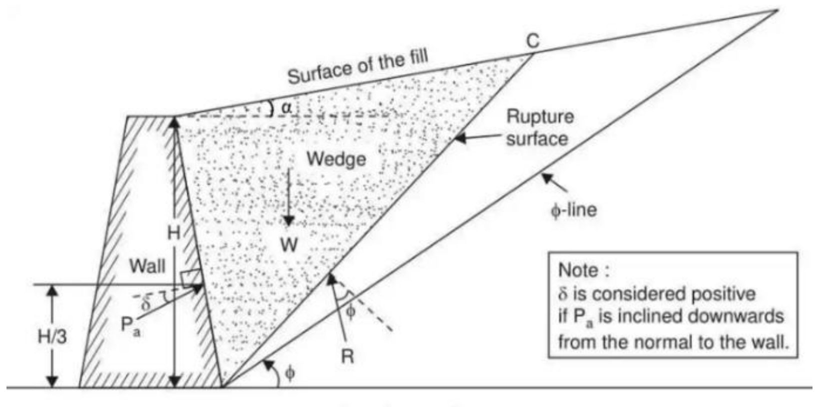

Figure 8. Soil wedge according to Coulomb's theory, in active thrust conditions.

Among limit equilibrium methods Caquot and Kerisel (1948) must be cited: they also applied the global limit equilibrium and presented tables of active earth pressure coefficients derived from a method which directly integrates the equilibrium equations along the combined planer and logarithmic spiral failure surface. They included the friction factor between the retaining wall and the soil and assumed a curved failure surface which is recognized to be very close to the actual failure surface. The active and passive coefficients were developed for cohesionless soils, but they can be used for evaluating long-term conditions in cohesive soils where complete dissipation of excess pore water pressure has occurred. The values of the passive resistance coefficient are lower than those that could be calculated using Coulomb's theory, while the active thrust coefficients are quite similar.

Although Coulomb's method is the simplest to use, it does not always give reliable results. The thrust coefficients calculated using this method vary greatly with the roughness angle δ, as can be seen in Figure 9.

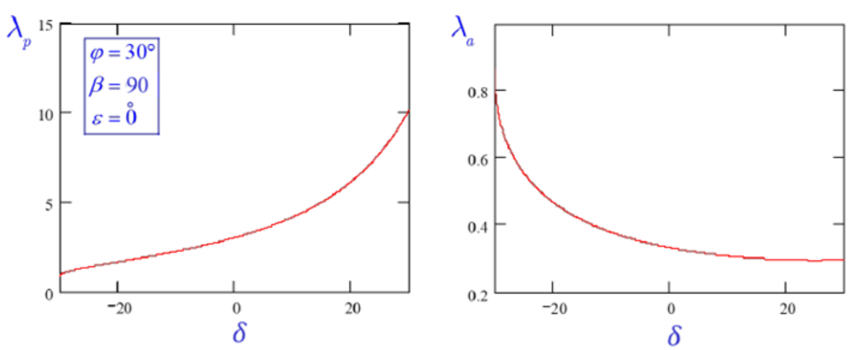

Figure 9. Evolution of active and passive thrust coefficients with roughness, according to Coulombs theory.

In particular, for positive kinematics ($\delta>0$), the variation in the active thrust coefficient with δ is negligible, but this is not the case for the passive thrust coefficient. For this reason, it is reasonable to assume zero roughness in the first case but not in the second, where it would be too cautious. Furthermore, it has been experimentally observed that for $\delta < \phi/3$, the results obtained using the Coulomb method are in line with the solutions of the more complex methods; for $\phi/3 \leq \delta \leq \phi/2$, the solutions are overestimated; for higher values, the solution diverges. To overcome the problem the solution proposed by Lancellotta (2002) can be used: based on the static theory of plasticity, it represents a conservative estimate of the exact solution.
In new release of EC7 the formulation for the thrust coefficient considers separately the contribution of weight, the eventual presence of an overload and cohesion: the addition of the three contributions determines the effective normal stress acting on the wall, in active or passive conditions.

2.2.2. Lateral earth pressure: stress paths

It is now of general knowledge that the behavior of the soil is dependent not only on the current state of stress but also on how it is approached, *i.e.*, the stress history (Ng, 1999). Considerations about the stress-strain behavior of soils become important when it comes to mechanisms not involving the ultimate resistance, which is the case of many site conditions, like excavation work where pre-failure condition governs the behavior of the whole system; in these cases, it is more adequate referring to non-linear elastic laws that consider the stress-strain behavior at small deformation levels.
Classical solutions of earth pressure problems (discussed in section 2.2 of this chapter) are only valid in limit conditions and do not provide pre-failure information. Thus, the lateral earth pressure is unknown for any state intermediate between active and passive state: this is why many studies investigated the problem of the distribution of lateral earth pressure assuming different movements of the retaining wall (Terzaghi, 1934; Clough and Duncan, 1971; Bang, 1985). Lambe in 1967 introduced the stress path method: starting from the case of a supported excavation and assuming plane strain conditions, he showed how soil elements placed in different locations of a transversal section underwent different stress paths: the stress path behind the wall consists of a reduction of the horizontal stress with a constant value of the vertical stress, while below the bottom of the excavation a reduction in the vertical stress is associated with a nearly constant value in the horizontal stress. Medeiros and Eisenstein (1983) conducted tests in triaxial passive compression (conventional triaxial test) and triaxial active extension on specimens of glacial sand, with the aim of reproducing the stress

path that they experience during the excavation (see Figure 10). The results show a strong dependance of the sand tangent moduli on the stress path imposed. A smaller strain to failure was observed for the extension test, indicating a much earlier mobilization of shear strength than in the conventional triaxial test.

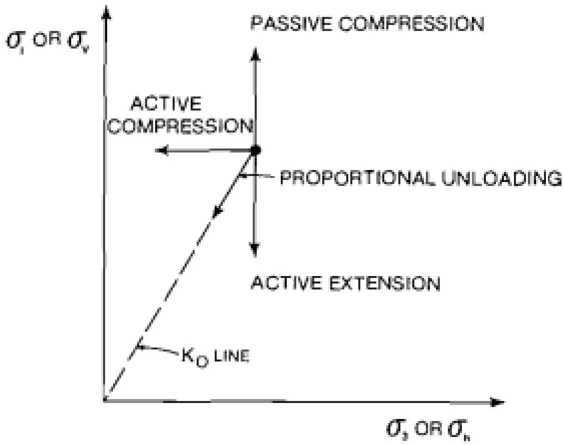

Figure 10. Stress paths experienced by soil elements behind the retaining wall (active extension) under the bottom of the excavation (active compression) (Medeiros and Eisenstein, 1983).

More recently Nikolinakou *et al.*, (2011) conducted a campaign of laboratory tests on Berlin sand specimens aimed at characterizing it at small strain level in order to calibrate a numerical model (MIT-S1) implemented in finite element software Plaxis to accurately estimate the displacements produced during excavation activity in Berlin sand for the subway. Once again, the soil stress history shows its importance since the results indicate a significant dependence on K_0 and e_0 value (*i.e.*, coefficient of earth pressure at rest and initial void ratio). Based on the same case study, in 2017, Nawir *et al.*, compared numerical analyses where the soil properties were estimated using a calibration based on conventional compressive triaxial stress paths, and others were the calibration was made using a set of conversion ratios to convert the general soil parameters (*i.e.*, axial compression stress path) to the soil parameters of the other stress paths. It was found that the stress path dependent approach produced better prediction of diaphragm-wall deformation.

The topic, with reference to clays, was addressed by Ng (1999) who conducted an extensive experimental study to characterize the behavior of soil specimens under different triaxial stress path tests aimed at reproducing the stress relief observed in situ during excavation work under the bottom of the excavation and behind the retaining structure.

In the last few decades more accurate studies about displacement-dependent behaviors of lateral earth pressure in proximity of retaining structures were conducted aided also by the development and diffusion of numerical tools. The lateral earth pressure is highly dependent on the displacement of retaining structures which, according to Fang *et al.* (1994) can happen in three main modes: translation (T), rotation about a point above the top (RTT) and rotation about the base (RBT) (Figure 11).

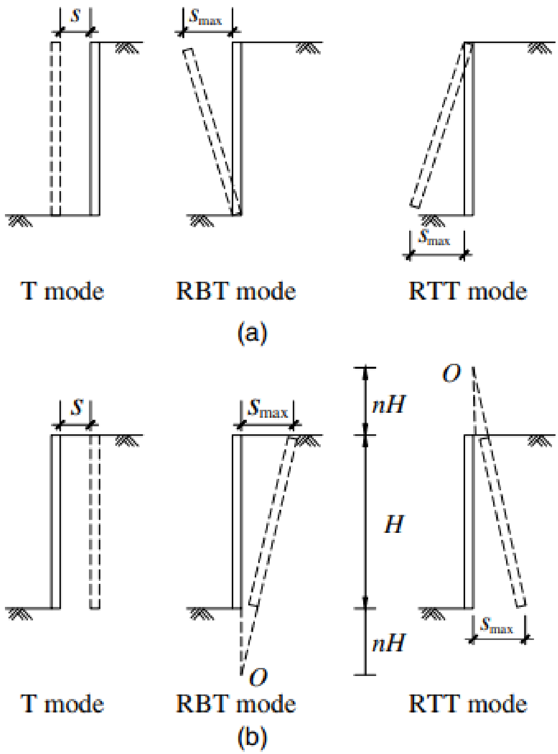

Figure 11. Modes of displacement of retaining structures (a. active mode; b. passive mode) (Ni et al., 2018)

The experimental data, reported by the Fang *et al*., (1994), of earth pressures at the intermediate passive state for soil specimens of air-dried Ottawa sand tested in all three displacement modes above described, were, together with other data, used by Mei *et al*., (2009) to validate an empirically calibrated equation describing the lateral earth pressure in intermediate condition between active and passive state, foreseeing an inflection point in correspondence with the point with null displacement, corresponding to the switch of the curve between intermediate active (upward concave) and intermediate passive (downward concave) state. Ni *et al*. (2018) improved the methods

of Bang (1985) and Mei *et al*. (2009) to calculate the displacement-dependent lateral earth pressure with more complicated deformation of retaining structures.
Another kind of theoretical method for estimation of lateral earth pressure is based on the Duncan Chang model (Duncan and Chang, 1970), which is one of the most widely used models to describe the non-linear elastic stress–strain relationship of soil before yielding. The stress–strain relationship of soil mass can be expressed as the following hyperbolic equation:

$$\sigma_1 - \sigma_3 = \frac{\varepsilon_1}{a + b\varepsilon_1} \qquad (7)$$

Where σ_1 and σ_3 are maximum and minimum principal stress respectively, ε_1 is the axial strain in principal direction 1, *a* and *b* are model parameters. Liang *et al*., (2023) correlate the hyperbolic law with the displacement-dependent lateral earth pressure behind the retaining structure, with special focus on the active state, for different displacement modes of the structure. The influence of different parameters on the stress-strain relationship was analyzed, and the initial tangential modulus E_i was found to increase with relative density and with K_i parameter (initial ratio σ_{3i} / σ_1).
However, most of the contributions available in literature about the description of lateral earth pressure in pre-failure conditions, are based on the assumption that the walls are not anchored and then it can be made a hypothesis on the displacement mode of the structure, and then of the soil.
A simple mathematical formulation to compute earth pressure on a wall with plate anchors in cohesionless soil is proposed by Hua and Shen (1987). They start from the work by Bang (1985) to compute the distribution of horizontal loads on a wall for a given stress state between at-rest and active. The hypothesized mechanism is a rigid body rotation of the wall around its base and a state parameter β (ranging from 0 to 1) is used as an indicator of the stress state between the initial active state and the full active state. The state parameter is involved in both the equations for the calculation of lateral earth pressure and the system of equations that can be written to derive the tension forces in tie-rods, assuming that each post of the wall system is a continuous rigid beam supported by (n + 2) elastic supports, at the tie rod levels (Figure 12).

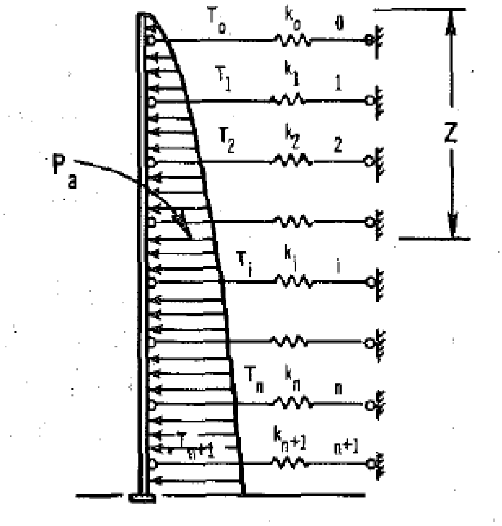

Figure 12. Tension forces in tie rods (after Hua and Shen, 1987)

The equilibrium is reached when the value of β is found such that the displacement of the wall at a given level is equal to that of the tie-rod at the same level. Based on results of previous works of the same authors, with respect to the full active state (Coulomb theory), in site the earth pressure is usually comprised between +5% and +30% of what expected with limit equilibrium methods. This percentage (which depends on the entity of the wall movement) is found to be particularly sensitive to the parameter m that is the ratio of the area of the anchor plates to the area of the panel wall: the higher m, the higher the earth pressure.
Apart from this study, usually when it comes to multi-strutted or multi-anchored retaining walls hypothesizing a mechanism is not straightforward anymore due to the stress concentration which occurs at the support levels along the depth of the wall (Chowdhury, 2019) and the attempt to foresee stress paths and lateral earth pressure on structures is delegated to semi-empirical methods, or numerical models able to describe the behavior of soils at very small levels of strain (for example Abbas *et al.*, 2025).
Empirical and semi-empirical methods can be applied in design for evaluating pressures in walls and anchorages in case of relatively small structures and if there is no high risk of damaging adjacent structures. Among them it is worth citing the following:

- The apparent earth envelopes by Terzaghi and Peck (1967): in the study, strut loads were measured at various sections during construction with the loads then distributed as a pressure on the back of the wall between two consecutive struts. The authors collected many experimental results deriving roughly approximated envelopes valid for sands (in drained conditions, effective stresses) and clays (total stresses), respectively. In case of sands the resulting diagram has a constant value equal to $0.65k_a\gamma H$ where k_a is the active pressure coefficient, γ is the unit weight of the soil, H is the total height of the excavation. With respect to the active earth pressure triangular diagram ($0.5k_a\gamma H$) Terzaghi and Peck provide an earth pressure higher of 30%, which is the upper bound of what Hua and Shen (1987) found with the equilibrium approach. In case of clays two different earth pressure diagrams must be considered based on the value of stability number N_s. For N_s <4 struts shouldn't be a necessity: in this case a trapezoidal interaction diagram (maximum value $0.2 - 0.4\gamma H$) is suggested, with a reduction of earth pressure before the bottom of the excavation, going to zero at the bottom which is due to the fact that the soil between the last strut and the bottom is constrained both by the strut and the soil below the bottom of excavation. For N_s >4 a trapezoidal-rectangular interaction diagram is suggested, with maximum horizontal pressure equal to $k_a\gamma H$. Based on the data published by Terzaghi and Peck, FHWA (Federal Highway Administration; Sabatini *et al.*, 1999) suggests earth pressure diagrams, valid for tieback anchored excavations also adding trend below the excavation bottom. Unlike internal braces, loads in tiebacks do not vary much during the excavation process, but remain close to the lock-off load (Finno *et al.*, 2002; Russo *et al.*, 2024). The tieback location directly affects the distribution of apparent pressure, and it is reflected in FHWA recommendations (Finno, 2010).

- The spring method, in which the bulkhead is schematized as a beam interacting with an elastic medium consisting of springs (the ground) characterized by a subgrade reaction that varies with the stress level, and, therefore, with depth. In fact, it is possible to take into account the increase in stiffness as the acting stresses increase and the phenomenon of hardening, which consists of an enlargement of the failure domain as the applied load increases.

- The hypothesized constraint method is based on the results of the Standard Penetration Test (SPT), which is used to establish the distance below the bottom of the excavation at which the soil reaction is concentrated, *i.e.*, the constraint that gives the method its name. The stiffer the soil, the shorter the distance is. Once the position of the soil reaction has been calculated, it is possible to proceed with "one stage loading" (the forces acting on the wall are evaluated directly referring to the final configuration), or "phased loading", it is a cumulative procedure where the forces are evaluated referring to each phase of excavation, in this case as the excavation depth increases the soil horizontal reaction moves downward. The latter is the most correct approach, as it allows for the accumulation of bending moment on the bulkhead during different excavation phases.

However, "*limits imposed on excavation-induced ground movements has made stiffness-based design of support systems more common, and a necessity when making deep excavations in urban areas*" (Finno, 2010).

2.2.3. Interaction between underground structures and surroundings

Induced displacements, monitoring system and observational approach

In addition to ultimate limit states, addressed in the previous sections, technical codes prescribe paying attention to service limit states, which are related to displacement induced by excavations in the surroundings, possibly affecting the existing structures and facilities at different levels. Nowadays there are many possibilities to address the problem, and the method chosen for the evaluation of such displacements, and the related level of approximation, is linked to the design phase one is approaching. First, a difference can be made between empirical, semi-empirical and numerical approaches. Empirical observations of real works started to be carried out during the second half of the 20th century, when excavations became frequent in urban environment, and they allowed for the individuation of the factors influencing the displacement field in the vicinity of soil removal. Among other factors, there are:

- Mechanical properties of soil: stiffness and strength both influence soil displacements. The well-known abacus of subsidence profiles normalized with respect to excavation height, proposed by Peck in 1969 (Figure 13), showed that the magnitude of vertical displacement δ_v and of horizontal displacement d behind the support structure (both dimensionless with respect to the excavation height) are comparable and they are smaller for excavations in soils with greater stiffness (granular soils and consistent clays).

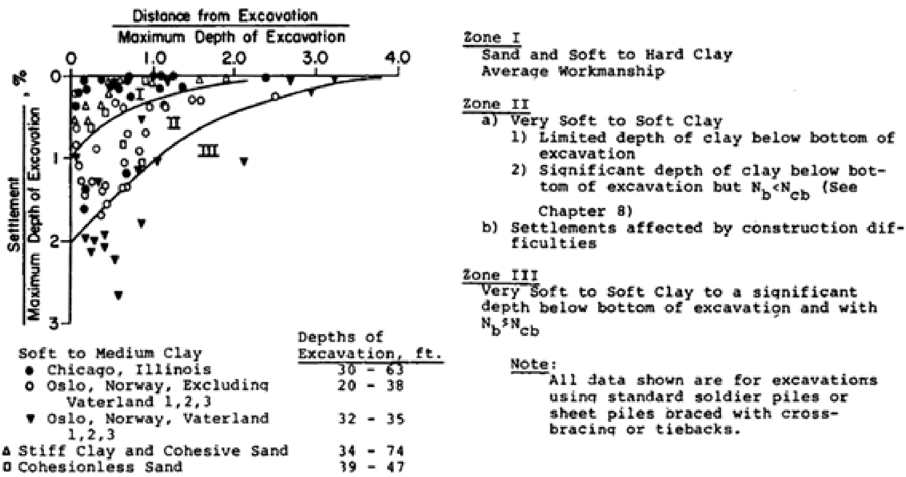

Figure 13. Peck's abacus. N_b is the stability number, N_{cb} is the critical stability number for basal heave.

The resistance characteristics also play an important role in determining displacements: soils are more susceptible to displacement if they are loose, and even more in presence of water. Furthermore, an empirical relationship between the risk of excavation bottom uplift (expressed in terms of stability number $N_b = \gamma H/c_u$) and the extent and rate of displacement of excavation retaining structures in clays, was determined in 1981 by Mana and Clough (Figure 14). The relationship was derived for excavations supported by metal sheet piles or pile walls, free or fixed at the foot, equipped with multiple levels of struts. It is worth noting that in some cases, the anisotropy and stress history of the deposits crossed by the excavation can also play an important role in determining the displacements. For example, for highly over-consolidated clays, characterized by a high coefficient of undisturbed pressure k_0, soil displacements can be considerable even at modest excavation depths (Potts and Fourie, 1984).

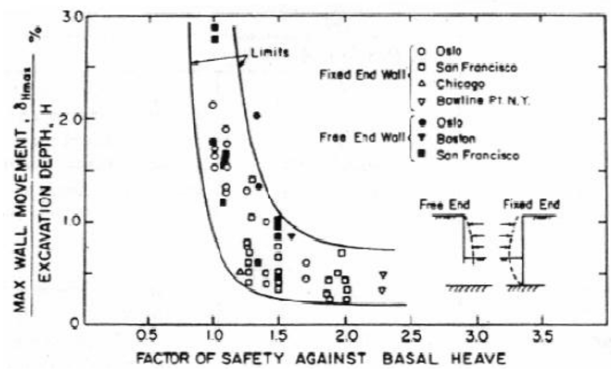

Figure 14. Empirical relationship between stability vs displacement of clay excavation support structures (after Mana and Clough 1981)

- Geometry of the excavation: if the excavation presents one the plan dimensions significantly greater than the other one, it can be assumed that plan deformation conditions occur near the centerline, and it is usually believed that the volume of soil that moves horizontally toward the excavation, per unit length of the bulkhead, coincides with the volume of soil that moves vertically at ground level, again per unit length of the bulkhead. On the contrary, near the edges, both horizontal and vertical displacements are reduced due to the tridimensional effects, known as “corner effect”, firstly introduced by Ou *et al*., (1996). If the dimensions of the excavation in plan are comparable, the behavior of the excavation will be markedly three-dimensional and should be studied as such. In this sense, in addition to complex numerical models (*e.g*., FEM), some semi-empirical derived functions have been proposed by different authors describing the subsidence trough along two orthogonal directions: some examples are Ou and Hsieh (2011) who focused on the forecast and description of subsidence trough in direction orthogonal to the bulkhead development direction, Roboski and Finno (2006) that provided suggestions for the subsidence in longitudinal direction, and Russo and Nicotera (2022) that provided a combined function aimed at describing the tridimensional development of settlements around the excavation, to be calibrated with the value of maximum vertical displacement, deduced with another method.

- Hydraulic conditions: when the depth of water level is such that it interacts with excavation activities, the displacements produced by excavation operations are generally greater. If the support structure is embedded in an impermeable layer, the extraction of water from the excavation does not produce filtration movements, and the increase in displacement is simply because the system fails to achieve equilibrium between the hydrostatic thrust upstream and downstream of the structure itself. In this case, one refers to “direct effects” of the presence of groundwater. When an impermeable base layer is not present, however, a filtration movement directed from upstream to downstream is triggered in the vicinity of the excavation, responsible for what is known as “indirect effects”. As a result, upstream of the retaining structures, neutral pressures are reduced, effective vertical stresses increase, and consequently, settlements increase. Downstream, on the other hand, neutral pressures increase, effective vertical stress is reduced, and passive resistance can sometimes decrease significantly; in this case, local breakage phenomena may occur, producing horizontal displacements of the soil below the bottom of the excavation and a further lowering of the ground level.

- Stiffness of the retaining structures and excavation method: many observations from real cases (*e.g.*, Mana and Clough, 1981; Clough and O'Rourke, 1990) show that the entity of horizontal displacement of retaining structures is of the same magnitude of vertical displacement of soil behind. Therefore, it is possible to infer that increasing the stiffness of retaining structures (by installing anchorage system, eventually prestressed, designing a greater structural section, increasing the embedment depth or reducing the spacing between panels or piles) reduces horizontal and vertical displacements. As an example in Figure 15 the relationship between the maximum lateral displacement of the support structure, safety coefficient with respect to the lifting of the excavation bottom, and the flexibility ratio of the support system $EI/\gamma_w h^4$ proposed for excavations in clay by Clough, *et al.* (1989) is reported.

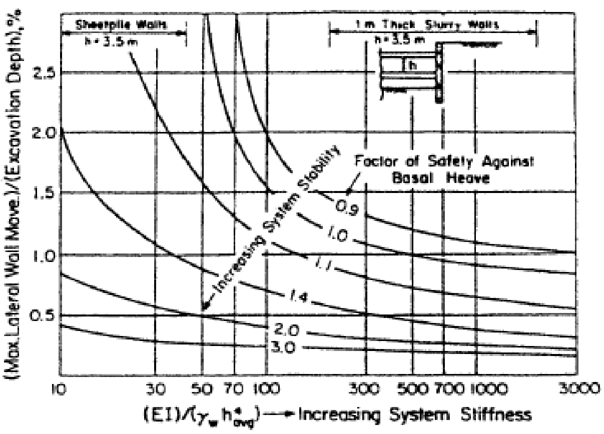

Figure 15. Maximum lateral displacement against flexibility parameter, as the safety coefficient against basal heave varies. (Clough et al., 1989, for excavations in clays).

As for settlement forecast, usually the methods for a first evaluation are based on the collection of data from real cases. The already mentioned contribution by Peck (1969) is the first systematic collection of data from case histories of open pit excavations, with different supporting and anchorage systems. Thanks to those data Peck produced the abacus shown in Figure 13 where, depending on the soil stiffness characteristics, three zones with different soil behavior are identified, where vertical downward displacements (*i.e.*, settlements) are reported with distance from excavation in direction orthogonal to the bulkheads development. As a general observation, as the soil becomes softer and the stability number against basal heave increases, the settlement magnitude at a given distance from the excavation increases and the presence of excavation is noticeable at greater distances, up to 3 or 4 times the excavation depth. The dataset proposed by Peck was significantly improved by O'Rourke and coworkers starting from the 1970s until the 1990s with data of braced excavations carried out in the city of Chicago. This work led to a comprehensive publication (Clough and O'Rourke, 1990) where vertical movements of soil and lateral displacements of retaining structures are reported as a function of excavation depth for different retaining systems (Figure 16). The considered soils are stiff clays and sands, that usually exhibit no problems of basal heave stability. According to Peck, lateral movements of retaining system in these kinds of soils averages around 1% of excavation depth, *H*; Goldberg *et al.*, (1976) suggest instead a value of 0.5% of *H* for lateral displacements estimation. The new data added by Clough and O'Rourke allow for a less conservative initial estimation of lateral displacement, that can be taken equal to 0.2% of *H*, while the vertical movements tend to average around 0.15% of H, with a roughly linear trend indicating that soil masses are behaving approximately as an elastic material.

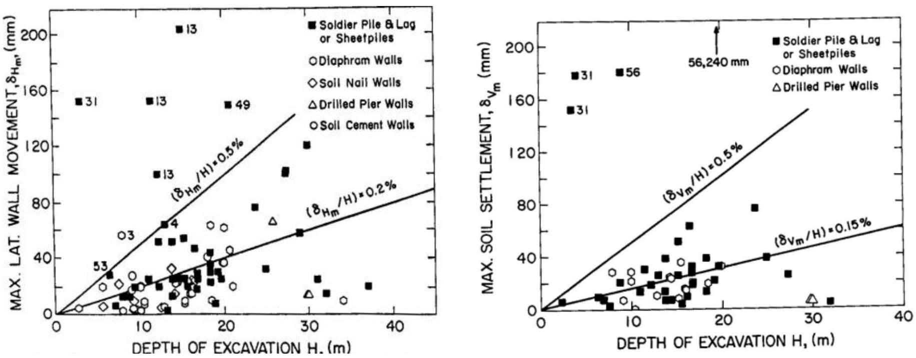

Figure 16. Dataset of vertical and lateral displacements versus excavation depth (after Clough and O'Rourke, 1990).

The data show ample scatter, more pronounced for lateral movements, but no significant differences are found among different retaining structures. Soil stiffness, instead, is found to have an impact, as shown in Figure 17 where results of numerical analyses carried out under the assumption of linear elastic behavior of the soil are reported. The results confirm what was already found by Peck (1969).

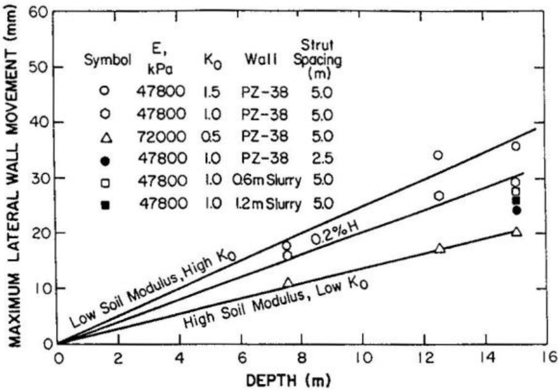

Figure 17. Results of numerical simulations about stiffness variation (after Clough and O'Rourke, 1990)

The dataset of Figure 16 has been organized also differentiating the trends of settlements with distance from excavation for type of soil, finding what is shown in Figure 18, for sands, stiff and soft clays.

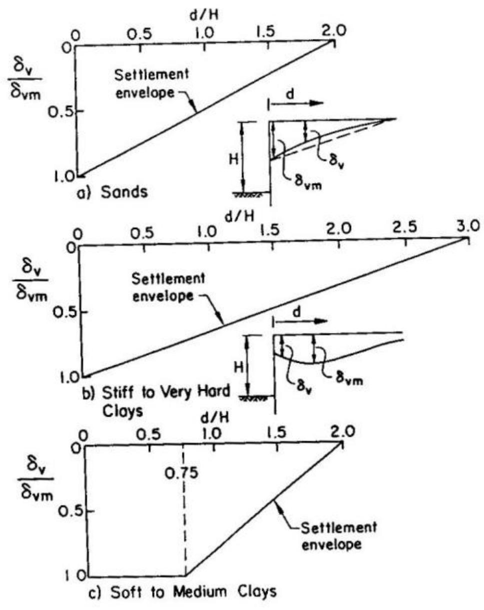

Figure 18. Trends of settlements with distance from excavation for different types of soil (after Clough and O'Rourke, 1990).

The authors pay attention to lateral movements as well, distinguishing different phases and diverse profiles occurring while excavation is proceeding and linking the shape of lateral movements to that of settlements (Figure 19).

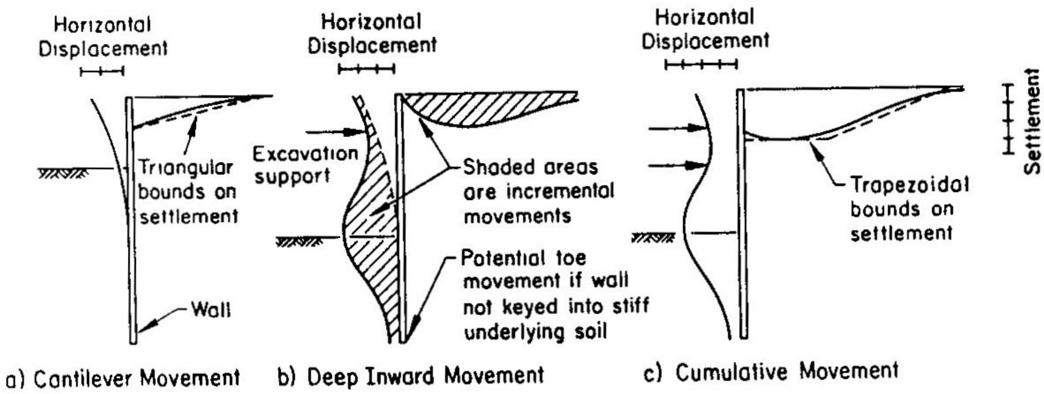

Figure 19. lateral and vertical displacements at different excavation stages (after Clough and O'Rourke, 1990).

The wall, initially without struts, starts deforming like a shelf, consequently, the settlements will exhibit a triangular distribution (Figure 19a), as the excavation proceeds struts or tieback anchors are installed, the upper part of the wall is constrained by the anchor system, while deep inward movement of the wall occurs (Figure 19b). In Figure 19Figure 19c the cumulative displacements of shelf deformation and deep inward movement are reported.

The issue of relation between vertical and lateral displacement had been already addressed by Mana and Clough (1981) who, based on empirical data, proposed the following relations, later confirmed by Ou (2006):

$$\delta_v = \delta_h \; for \; clays \qquad (8)$$

$$\delta_v = 0.5\delta_h \; for \; sands \qquad (9)$$

The methods presented so far are solely based on organization of field data and are intended to provide a useful and fast tool for estimating the expected magnitude of settlements, still used in practice nowadays. However, with the development of numerical tools in the last decades it became way easier than before to integrate empirical methods with information deduced by numerical analyses. This condition allowed for more refined methods to be used also in preliminary design stages. Among other topics, the tridimensionality of displacement field induced by excavation activities, neglected until then, was taken into account and Ou, in 1996, for the first time mentioned the so-called corner effect. The research was then able to focus not anymore only on the maximum value of settlement, but also on the shape of the settlement profiles. Roboski and Finno (2006) focused on the settlements in a direction parallel to the excavation support wall, as shown in Figure 20, producing, by reworking data from case histories, a closed form solution to its forecast to be calibrated with a maximum lateral displacement or settlement derived in another way, like a semi-empirical method or, indeed, numerical analyses, and with the geometrical dimensions of the excavation.

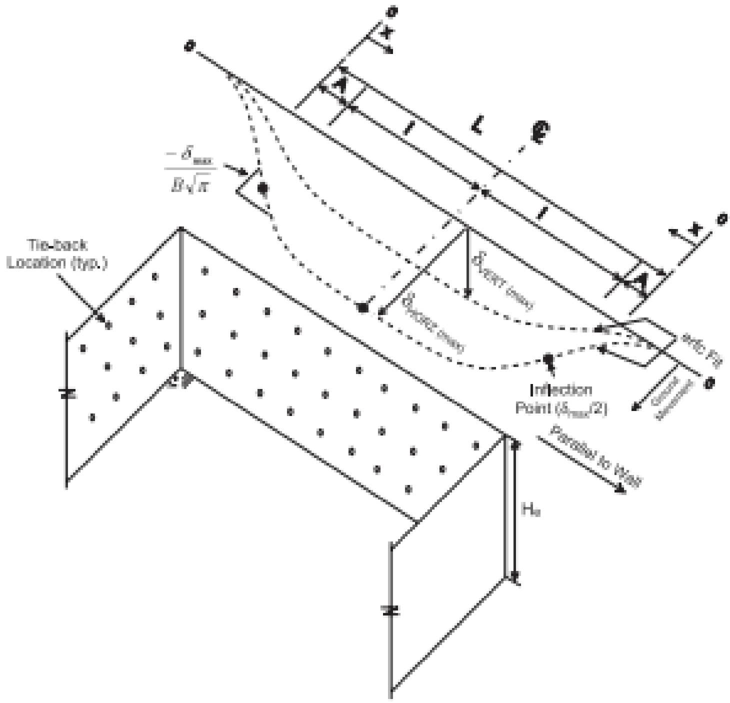

Figure 20. Derived fitting parameters for the complementary error function. $\delta_{VERT,}$ settlement; $\delta_{HORIZ,}$ lateral movement (after Roboski and Finno, 2006).

The method proposed by Roboski and Finno, in turn, is based on that of Hsieh and Ou (1998) for the estimation of the maximum settlement at the distance of interest from the excavation. Hsieh and Ou, in fact proposed a method that links lateral and vertical displacement profiles, as follows:

1. Determination of the shape of the trough. The authors calculate the ratio between the area associated with the cantilever deformation, A_c, and that associated with the concave deformation, A_s, considering $A_c = \max(A_{c1}; A_{c2})$, as represented in Figure 21. The lateral displacement profile is considered concave or linear depending on the ratio reported below:

$$\frac{A_s}{A_c}\begin{cases} < 1.6 \rightarrow linear\ profile \\ \geq 1.6 \rightarrow concave\ profile \end{cases} \qquad (10)$$

2. Abacus choice: depending on the ratio, the corresponding abacus should be used. If A_s/A_c is lower than 1.6, the spandrel shaped abacus will be used, reported in Figure 22, vice versa otherwise. The settlements shown in Figure 22 are dimensionless with respect to the maximum settlement that can be obtained using one of the empirical methods described above, or, alternatively, using a spring method.

3. Evaluation of the influence zone: the Influence Zone of the settlements, *IZ*, can be calculated as: $IZ = SIZ+PIZ$.

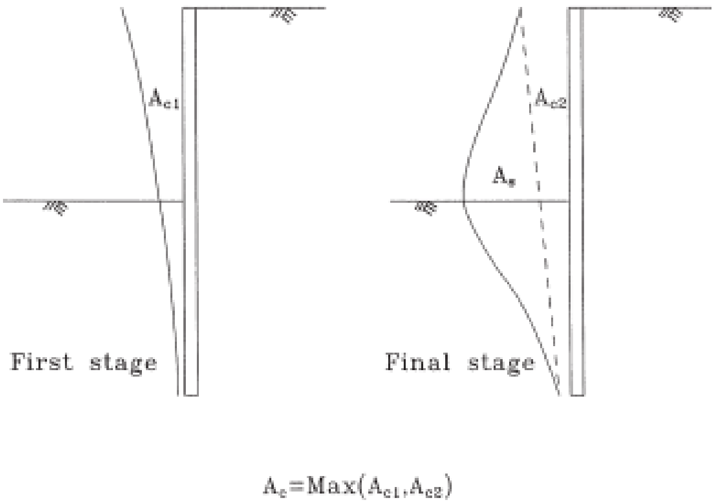

Figure 21. Deformed shape of excavation supporting walls(after Ou and Hsieh, 1998)

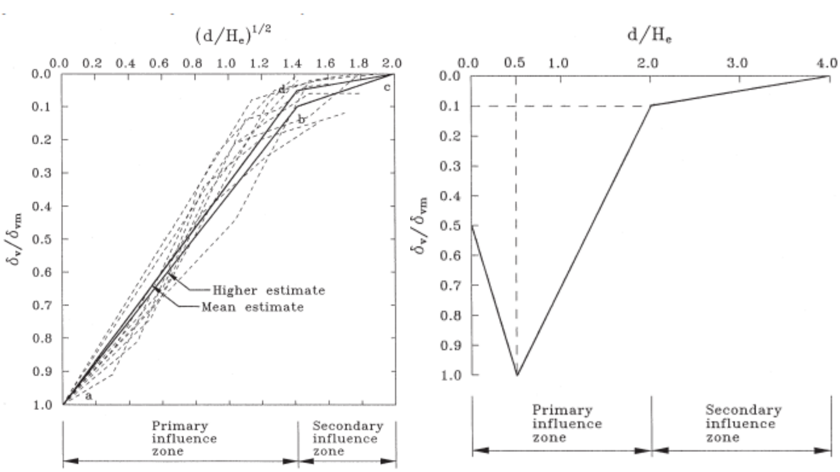

Figure 22. Shapes of bidimensional settlement trough orthogonal to retaining walls (after Ou and Hsieh, 1998)

Where PIZ is the Principal Influence Zone, *i.e.*, the zone where the most significant settlements occur because the soil volume is potentially susceptible to a failure mechanism; SIZ, is the Secondary Influenced Zone, *i.e.*, the zone adjacent to PIZ and interested by lower settlements, therefore usually it can be disregarded and $IZ \cong PIZ$.
With the aim of providing a tool for estimating the tridimensional distribution of settlements around an excavation, Russo and Nicotera, in 2022, proposed a function, which combines modified two-dimensional semi-empirical methods, resulting in a two-variable subsidence function, that has the following form:

$$\frac{\delta_v(x,y)}{\delta_{v,max}} = f(y) \cdot g(x) \qquad (11)$$

where *g(x)* represents the 2D settlement pattern in the direction parallel to the supporting wall while *f(y)* represents the 2D shape function for transversal settlement pattern. The first member of the equation is the function $\delta_v(x,y)$ describing the 3D settlement trough, divided by the maximum measured settlement, $\delta_{v,max}$. The authors give suggestions on the values of the fitting parameters to be used for different soils and anchorage systems.
The availability of tools for the accurate description of settlements around the excavations is useful for the assessment of the risk associated with damage of buildings and facilities interacting with the displacement field induced by this kind of works. Some methods useful for damage assessment are described in section 0 of this chapter.
To keep subsidence and displacements under control a monitoring plan is required with the primary aim of verifying that the project forecasts, derived from both semi-empirical methods and numerical analyses, are confirmed by measurements. The preparation of a monitoring plan, which includes the installation of instrumentation, the definition of the frequency of readings, attention and alarm thresholds, and the actions to be taken if these thresholds are reached, is therefore an operation that must be carried out prior to excavation and specifically for each construction site. The definition of attention and alarm thresholds becomes fundamental in the context of an observational approach (OM). Introduced by Peck (1969b) and taken up in Eurocode 7 (Jappelli, 1996), this approach consists in reviewing the project during its realization based on a comparison between the project forecasts and the monitoring results, to obtain economical advantages. The method proposed by Peck is referred to as OM *ab*

initio and in this case the initial design is made using the "most probable" properties of the soil, which is a reasonable but not too cautious estimation that can be based on a mean value of site and laboratory tests results. In this case the initial design itself forecasts the possible occurrence of a scenario where the displacements are greater than expected and some additional measures can be taken to minimize displacements in progress (*e.g.*, struts). OM has been the object of further research in the last years and in 2017 Gaba *et al.*, incorporated it in Ciria recommendations (Ciria C760) for bulkheads design individuating four different OM: "most probable properties" can be chosen for design, in this case OM is used adding anchors to counteract eventual excessive displacements and it is referred to as active *ipso tempore*; if "most conservative" properties are used at the design stage, and very low displacements are registered during construction, in this case it is passive *ipso tempore* approach.

Building damage criteria

Most contributions to this topic, mainly consisting in empirical methods for estimating differential settlements critical values, date back to the second half of the 20th century, and they are based on the general assumption of plane behavior of buildings (Smith, 2010), which is acceptable if no significant settlements are registered at the corners.

The issue of how structures respond to differential settlements has been addressed in different ways depending on the type of structure and, to explore the topic the interesting quantitites are illustrated in Figure 23.

The related definitions, first introduced by Skempton and MacDonald (1956), Polshin and Tokar (1957) and Burland and Wroth (1975) are listed below:

- Rotation or slope θ is the change in gradient of a line joining two reference points. The angular strain α is defined in Figure 23.
- Relative deflection Δ is the displacement of a point relative to the line connecting two reference points on either side.
- Deflection ratio (sagging ratio or hogging ratio) is denoted by Δ/L where L is the distance between the two reference points defining Δ.
- Tilt ω describes the rigid body rotation of the structure or a well-defined part of it.
- Relative rotation (or angular distortion) β is the rotation of the line joining two points, relative to the tilt ω. It is very important not to confuse relative rotation β with angular strain α.

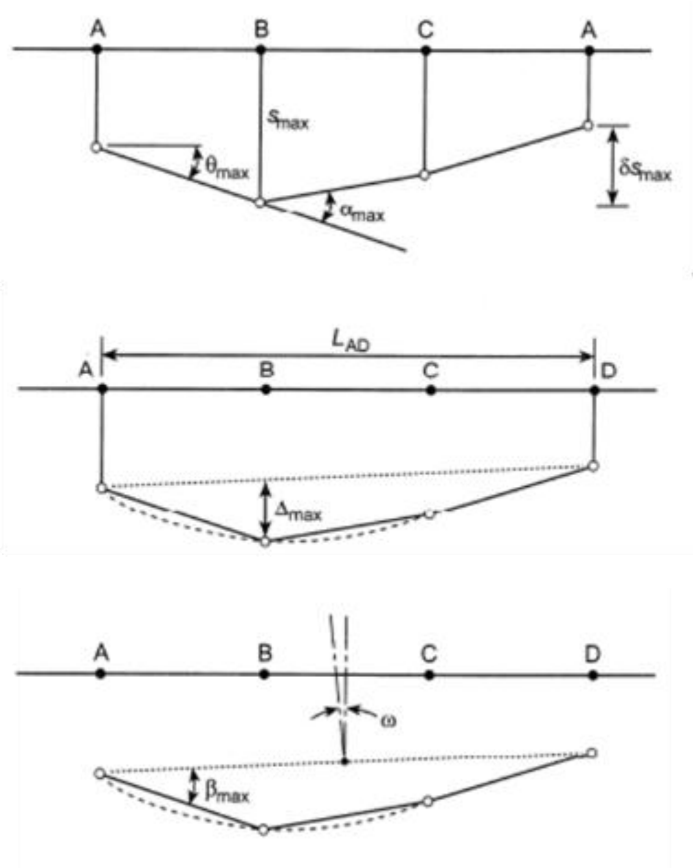

Figure 23. Parameters for describing differential settlements (after Burland and Wroth, 1975).

A macro-difference between masonry structures and RC, or framed, structures can be made. In the first case, because of the very low level of tensile resistance of masonry, tensile strain and deflection ratio are used as damage indicators; for RC buildings, usually more ductile, relative rotation as defined above is used for the estimation. In general, a first estimation of ground movements is made under the assumption of greenfield conditions, *i.e.*, without considering the buildings, in terms of weight or stiffness. However, the interaction depends on weight of the building, ground/structure relative stiffness, and interface between foundations and soil (Prosperi, 2025).
First, Meyerhof (1947) studied the impact of differential settlements on structures analyzing the interaction between a 2D frame and the soil, and calculating the effect produced on stress within the structure. Starting from the work of Skempton and MacDonald (1956), the approach to the problem changed: they, as later Grant *et al*., (1974) did, measured the differential settlement and corresponding damage, from real

cases, on existing buildings and suggested differential settlement limits. The authors reported that angular distortion will cause cracking in infills if greater than 1/300, and they will cause structural damage if greater than 1/150. More recently, the Eurocode 7 Annex H (2004) recommended two ranges of β based on Burland *et al*., (1977), to prevent the occurrence of a serviceability limit state (SLS) for the structure: for open framed structures, infilled frames and load bearing or continuous brick walls the maximum relative rotations should be comprised between 1/2000 an 1/300; for many structures, a maximum relative rotation $\beta = 1/500$ is acceptable for SLS and $\beta = 1/150$ for ultimate limit state (ULS); for normal structures with isolated foundations, total settlements up to 50 mm are often acceptable (Frank, 2007). For what concerns masonry structures, Potts and Addenbrook (1977) introduced relative stiffness definition, for axial and flexural load, and the modification factor MD that describes the ratio between deflection ratio of building and that in greenfield conditions. As the stiffness of building decreases with respect to the soil, MD decreases as well, and the building tends to deform following soil movements. It is important to remember that the response of the structures is not constant, but it is influenced by their non-linear behavior: the bending stiffness of the building progressively changes with the progression of cracking, and so the interaction between the soil and the structure is influenced. With the accumulation of damage a reduction of stiffness occurs, thus, in turn, the building may be able to better follow the ground deformation.
Despite this, many methods available in literature and used by practitioners for estimating the level of damage induced by vertical displacements on masonry buildings, assume that they can be regarded as an elastic beam that can be subjected to two main modes of deformation:

- Sagging occurs when the structure is subjected to a field of displacement with concavity facing upwards, which happens when the central settlement is greater than the lateral settlement.
- Hogging, on the other hand, is the opposite situation, *i.e.*, deformation with concavity facing downward, and is the most unfavorable condition for masonry buildings in which tensile strength is very low, if not zero, and the upper fibers of the equivalent beam are in extension.

Burland *et al*., (1977) introduced a classification of damage levels which was later modified by Boscardin and Cording in 1989, and Boone *et al*., (1999), based on a generalized crack width. Boscardin and Cording in 1989 provided damage assessment method based on the evaluation of horizontal strain and angular distortion. Horizontal tensile strain, already used as an indicator of damage by Burland and Wroth (1975) is the parameter at the base of the so-called limiting tensile strain method (LTSM). The method, widely used by practitioners in its various forms, is based on the following assumptions:

- The building is regarded as a weightless, rectangular and isotropic elastic beam in two dimensions.
- The behavior of this equivalent beam is governed by length L, height H, Young's modulus E, and shear modulus G.

The method assumes the full transfer of the ground movements to the structure, neglecting the effect of soil-structure interaction. The procedure of LTSM involves subsequent steps:

I. The calculation of the greenfield ground movements, neglecting thus the presence of the building.
II. The greenfield displacements are imposed on the simplified linear-elastic beam model representing the building.
III. The strains of the equivalent beam model are computed by means of analytical formulations and related to a possible damage level.

Among other LTS methods, the one proposed by Boscardin and Cording (1989) is still widely used in engineering practice. The method consists in the evaluation of tensile horizontal strain and angular distortion and the comparison of obtained values with limit ones reported in an experimentally-derived abacus. The latter is obtained for *L/H* = 1 and Poisson coefficient equal to 0.3 which means *E/G* = 2.6, and the neutral axis supposed at the bottom of the beam. The abacus reported horizontal tensile strain versus angular distortion and divided the state of damage into 5 levels. Son (2003) and, later, Son and Cording (2005) continued this work obtaining a generalized damage criterion which is not dependent on L/H and E/G, nor on the position of the neutral axis. The method is based on the evaluation of the maximum principal tensile strain ε_P as the combination of β and lateral strain ε_L at a point or in a building unit (Equation 12).

$$\varepsilon_P = \varepsilon_L \cdot cos\theta_{max}^2 + \beta \cdot sin\theta_{max} \cdot cos\theta_{max} \qquad (12)$$

$$\tan(2\theta_{max}) = \frac{\beta}{2\varepsilon_L} \qquad (13)$$

With θ_{max} direction of cracks formation and the angle of the plane on which ε_P acts, measured from vertical plane. The application of the method is then linked to the presence of visible cracks. A building unit can be a section between two columns, two cross walls, two different building geometries or stiffnesses, or two different ground displacements gradients. The classification is based on a wide set of case histories, numerical simulations and physical modelling, where the chosen damage parameter is the critical tensile strain ε_c, whose value describes the passage from one state of damage to another.

2.3. Soil-structure interaction under seismic loads

2.3.1. Introduction to seismic soil-structure interaction

Soil structure interaction (SSI) under seismic excitation has been widely investigated starting from the early XX century, with a considerable increase of research in the 60s and 70s in large part because of the seismic design of Nuclear Power Plants. SSI problems belong to a class of coupled contact problems where action and reaction along the contact surface are functions of each other. Its main objective is to determine the dynamic response of the structure interacting with the soil in terms of stresses and displacements and, to a less extent, of the soil itself. In Figure 24a (Wolf, 1985), the horizontal vertically propagating seismic waves are represented in the case of structure founded on rock and in the case of structure founded on soil. For the structure on rock the input motion can be applied directly at the base of the structure and the seismic response will depend only on the properties of the structure itself. When it comes to the structure founded on soil, the excavation and the installation of basement and lateral walls of the structure modify the free field motion, making it necessary to evaluate the interaction effects. The soil-structure interaction analysis can conceptually and practically split into a first step consisting of determining the free field motion of the soil at the site (site response analysis), and a second one where the free field motion is modified to take into account the interaction occurring when the structure is inserted into the seismic environment of the free field. Figure 24b and c represent the case of motion at the outcrop, and that where there is soil above the bedrock (free field), which produces a reduction in seismic motion at the point C and a modification (usually an amplification, but it depends on the frequency content of the excitation) of motion towards the free surface (points D and E). In the latter case the interaction exists, and it can be split into two different contributions: kinematical and inertial interaction (Figure 24d and e).

Kinematical interaction: the rigid base will experience some average horizontal displacements and a rocking motion that in turn will result in accelerations and inertial loads for the structure. The rigid foundation, in fact, acts as a filter for high frequency components of the translational motions and introduces rotational motions (rocking and torsion in the general case) (Kausel, 1974). The geometric averaging of the motion at the base of the structure is referred to as kinematical interaction. This type of interaction is greatly predominant for embedded structures.

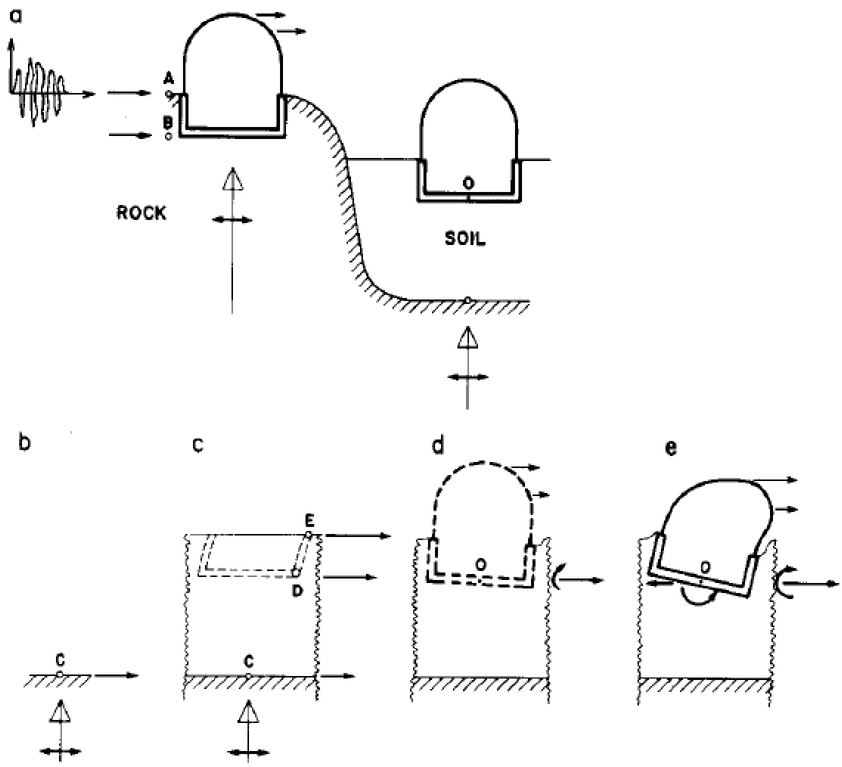

Figure 24. Seismic response of structure founded on rock and on soil: a) site; b) outcrop; c) free field motion; d) kinematic interaction; e) inertial interaction (after Wolf, 1985).

Inertial interaction: inertial loads applied to the structure will lead to an overturning moment and a transverse shear acting at the base (point O). This will cause deformation of the soil and, again, modification of motion. This is called inertial interaction. This phenomenon is pronounced for heavy structures such as dams and nuclear power plants, and it is typically responsible for period elongation and enhancement of its effective damping ratio. This leads to conclude that SSI can only be beneficial for structures, since it moves the working point towards a portion of the design spectrum with lower levels of intensity. Though, Mylonakis and Gazetas (2000) underlined that this is not always the case and that SSI can have a detrimental effect on structures in some cases.

Aim of the study of soil-structure interaction is the solution of dynamic equations of motion that, in matrix notation, can be written as follows:

$$[M]\{\ddot{r}\} + [C]\{\dot{r}\} + [K]\{r\} = \{R\} \qquad (14)$$

Where $[M]$ is the mass matrix, $[C]$ is the damping matrix, $[K]$ the stiffness matrix, $\{r\}$ is the displacement vector and $\{R\}$ is the load vector. Both the vectors are time dependent. When a harmonically varying load is applied:

$$\{R\} = \{P\} \cdot exp(i\omega t) \qquad (15)$$

$$\{r\} = \{u\} \cdot exp(i\omega t) \qquad (16)$$

With $\{P\}$ and $\{u\}$ are complex amplitudes of loads and displacements, respectively. By substituting equations (15) and (16) in equation (14) we obtain:

$$[S] \cdot \{u\} = \{P\} \qquad (17)$$

Where $[S]$ is the dynamic stiffness matrix:

$$[S] = [K] + i\omega[C] - \omega^2[M] \qquad (18)$$

In equation (14) a viscous damping term appears: the energy radiation due to the wave propagation away from the region of interest belongs to this type of damping. Material damping, which belongs to soil and structure, instead is a hysteretic damping, not frequency dependent that can be introduced in the solution, in frequency domain, through the correspondence principle: the damped solution can be obtained from the elastic solution by replacing the elastic constants with complex quantities. In this case the dynamic stiffness matrix, disregarding the hysteretic damping term, can be written as follows:

$$[S] = [K](1 + 2\xi i) - \omega^2[M] \qquad (19)$$

Where ξ is the damping ratio.

Two general methods of analysis were developed and are used for seismic analyses including soil-structure interaction:

- The direct approach allows inertial and kinematical interaction to be considered together, and material non-linearities can be considered as well. It is possible thanks to the use of advanced numerical methods. The direct solution procedures require in all cases the specification of the seismic input at the base of the soil model. There was a need therefore to obtain motions at the depth of the model's base compatible with the design earthquake specified at the free surface of the soil or at a hypothetical rock outcrop. This was referred to as a deconvolution analyses (Seed and Idriss, 1970). The direct approach presents the drawback of very long time of calculation.

- The three steps or substructure approach (Figure 25) proposed by Kausel in 1974. It works under the assumption of linearity because it is based on the superposition of effects. The three steps are as follows:

I. Calculation of free field motion at the interface points (empty circles in Figure 25).

II. The unbounded soil is analyzed as a dynamic subsystem: the dynamic stiffness coefficients (force-displacement relationships) of the interface nodes are determined. These dynamic stiffnesses can be interpreted as a spring-dashpot system.

III. The structure, supported by the spring-dashpot system, is analyzed for the loading case derived from the free field motion applied at the base of the spring.

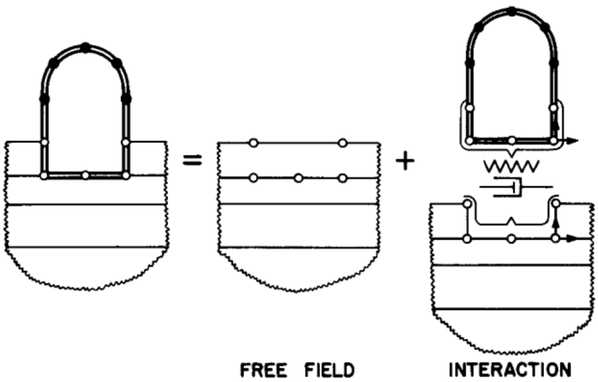

Figure 25. Substructure approach (after Wolf, 1985).

In the frame of substructure approach, writing the equations of motion in total displacements for a system composed by two substructures, namely an excavated volume of soil and a structure with embedded foundation, and developing them, leads to conclude that the load acts only on the soil-structure interface nodes: it is, in fact, the difference between the properties of the removed portion of soil and those of the embedded structure to determine the entity of the soil-structure interaction for the embedded part of the building (Wolf, 1985). For this reason, the main problem consists in modelling the contact between the two substructures, which is made via the definition of complex dynamic stiffness matrices, and much effort has been made in the last decades to produce impedance functions suitable for a variety of problems, often referring to foundations, both shallow and deep (*e.g.*, Gazetas, 1991).

The approaches to study SSI can be classified also based on other criteria (Anand and Kunar, 2018):

- Discrete or continuum modelling

- Linear or non-linear analyses
- Frequency or time domain analyses

However, the possibility to build appropriate impedance functions is strictly connected to the understanding of the phenomena happening during earthquakes and the generated mechanisms. In the case of underground structures this understanding is very limited, probably due to the very few well documented cases of important damages during strong earthquakes. Therefore, neither seismic increment of stress nor adequate impedance function can yet be calculated (Pitilakis and Tsinidis, 2013). This is the reason why very often numerical methods are used to address these problems.

2.3.2. Increase in lateral earth pressure due to seismic soil-structure interaction

Underground structures are known to perform better than aboveground ones under earthquake excitation and cases of collapse are quite rare (Finno, 2010; Lew *et al*., 2010), moreover often static design of such structures provide sufficient seismic resistance under low level of ground shaking (according to Seed and Whitman, 1970, up to PGA of about 0.3 g; according to Clough and Fragaszy, 1977, a cantilever retaining structure with an adequate factor of safety for static forces will have enough reserve to resist dynamic loads up to an acceleration of at least 0.4 g). Nonetheless, some severe collapses (*i.e*., the collapse of Daikai station during the Kobe earthquake in 1995, whose mechanism was discussed in Iida, Hiroto *et al*., 1996 and Parra-Montesinos *et al*., 2006, among others) is a reminder for engineers that in seismic areas even underground structures need to be designed according to seismic requirements to account for change in acting load. This is generally characterized in terms of deformation and strains imposed on the structure by the surrounding soil (Hashash *et al*., 2001) as a conservative design method. However, it is important to underline that a kinematic interaction between soil and the rigid structure exists, and it should be considered for a correct evaluation of seismic performances of the underground structures.

Probably due to the difficulty encountered in generalizing deep multi-propped excavation work, they are scarcely investigated in seismic conditions, while attempts have been made to characterize seismic behavior of different structural typology - namely tunnels, box culverts or embedded retaining structures without anchorage- that are shallower, with only one or without intermediate strut levels, more often interacting with a single soil layer.

The evidence collected by different studies regarding seismic damage of underground facilities (among the others Owen and Scholl, 1981; Sharma and Judd 1991; Iida *et al.*, 1995; Power *et al.*, 1998) lead to some general observation:

- underground structures are generally less vulnerable to seismic shaking than aboveground structures, and their vulnerability decreases as the overburden increases (this observation clearly is not directly applicable to deep open excavations, which develop in depth and in general have very little or no overburden at all).
- The observed damage is greater in soils with respect to rocks (which can be related to the observations by Wang, 1993 and Penzien, 2000 about the influence of soil-structure relative flexibility and interface properties, briefly discussed in §2.3.4).
- The ratio wavelength-tunnel diameter, when it is comprised between 1 and 4, is recognized to increase the vulnerability of the tunnel to the incident seismic wave.

However, there are many uncertainties related to the soil-structure interaction problem in seismic conditions, which makes it quite complex to evaluate the distribution and the magnitude of the seismic earth pressures on an embedded structure.
Several methods are available in the literature for the seismic design of tunnels and large underground structures (*i.e.*, Wang, 1993; Penzien, 2000; Hashash *et al.* 2001; Hashash *et al.*, 2010, among others). Based on the way that the seismic loading is described and modeled, they can be classified in three general categories: force-based methods, displacement-based methods, numerical methods where the structure and the soil are analyzed as a coupled system using different numerical techniques (finite elements, finite differences, etc.). In force-based methods the seismic load is applied as a static equivalent force to the structure, computed with peak ground acceleration or an equivalent seismic coefficient k_h. These parameters are obtained from the simplified analysis of local site effects. Moreover, an important distinction is made between:

- displacement – or yielding – walls (*e.g.*, gravity walls or cantilever walls)
- non-displacement walls, which is the case of propped retaining structures

Displacement walls

Among the different studies it is impossible not to mention the limit equilibrium Mononobe-Okabe method (1926-1929) where the applied inertia force results in rotation of the principal stress (angle θ in Figure 26), enlarging the Coulomb active wedge (or decreasing it, for the passive case) at limiting equilibrium. The M-O method is based on the work of Okabe (1926) and Mononobe and Matsuo (1929) following the great Kanto Earthquake of 1923 in Japan. Mononobe and Matsuo performed 1-g shaking table tests, paving the way to numerous experiments, both in shaking table and in centrifuge, aimed at the same scope. The method was originally developed for gravity walls retaining cohesionless backfill materials and today it is the most common simplified approach to determine seismically induced lateral earth pressures on a variety of structures (Sitar *et al.*, 2012). The M-O method is based on the Coulomb wedge theory, and it was developed under the following assumptions, considering the contribution of both horizontal and vertical component of seismic motion that are applied to the Coulomb active or passive wedge:

- The wall is a "yielding" or a "displacement" wall, that is: the wall yields sufficiently to produce minimum active pressures.
- When the minimum active pressure is attained, a soil wedge behind the wall is at the point of incipient failure and the maximum shear strength is mobilized along the potential sliding surface.
- The soil behind the wall behaves like a rigid body.

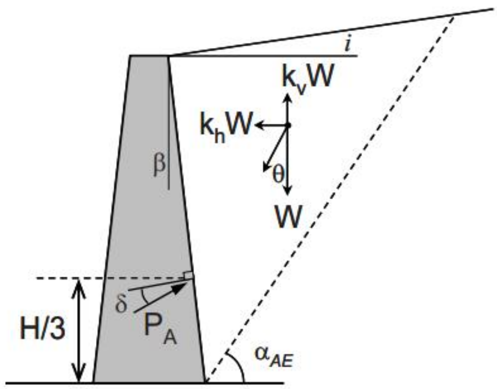

Figure 26. Forces involved in equilibrium in M-O method

The pseudo-static soil thrust is obtained from the force equilibrium of the wedge, as represented in Figure 26. In addition to those under static conditions (whose resultant is P_A), the forces acting on an active wedge in a dry cohesionless backfill wedge are constituted by horizontal and vertical pseudo-static forces whose magnitudes are related to the mass W of the wedge by the pseudo-static acceleration $a_h = k_h g$ and $a_v =$

$k_v g$. The total active thrust can be expressed in a form similar to that developed for static conditions, that is:

$$P_{AE} = \frac{1}{2}\, k_{AE} \gamma H^2 (1 - k_V) \qquad (20)$$

With the dynamic active earth pressure coefficient k_{AE} given by:

$$k_{AE} = \frac{cos^2(\phi - \mathrm{q} - \beta)}{\cos(\mathrm{q}) \cdot cos^2(\beta) \cdot cos^2(\delta + \beta + \mathrm{q}) \cdot \left[1 + \sqrt{\frac{\sin(\phi + \delta) \cdot \sin(\phi - \mathrm{q} - i)}{cos(\delta + \beta + \mathrm{q})\cos(i - \beta)}}\right]^2} \qquad (21)$$

Moreover:

- γ is the unit weight of the soil;
- H is the total height of the wall;
- ϕ friction angle of the soil;
- $\mathrm{q} = tan^{-1}[k_h/(1 - k_v)]$
- β slope of the wall relative to the vertical;
- δ angle of wall friction;
- i slope of the backfill relative to the horizontal;
- k_V and k_H are the vertical and horizontal acceleration in g, respectively.

It is worth noticing that when it comes to the passive thrust, the dynamic increment acts in the opposite sense with respect to the static thrust, thus reducing the available passive resistance.

The M-O analysis provides a useful way of estimating earthquake-induced loads on retaining walls. A positive horizontal acceleration coefficient causes the total active thrust to exceed the static active thrust (horizontal acceleration against the backfill) and the total passive thrust to be less than the static passive thrust (horizontal acceleration directed away from the backfill) (Whitman, 1991). Since the stability of a particular wall is generally reduced by an increase in active thrust and/or a decrease in passive thrust, the M-O method produces seismic loads that are more critical than the static loads that act prior to an earthquake. According to the M-O method the total thrust is applied at H/3 above the base of a wall of height H, however, despite a substantial agreement about the load shape, an agreement has not been reached among researchers about the appropriate point of application of the dynamic increment, since experimental results suggest that dynamic active thrust increment ΔP_{AE} acts at a higher points than H/3.

As an example, Seed and Whitman (1970) divided the total active thrust into a static component, P_A, and a dynamic increment, ΔP_{AE}, and they proposed a simplified expression for ΔP_{AE}:

$$\Delta P_{AE} = \frac{1}{2}\,\Delta k_{AE}\gamma H^2 \qquad (22)$$

With:

$$\Delta k_{AE} = \frac{3}{4}k_h \qquad (23)$$

They introduced the concept of “inverted triangle” distribution, suggesting that the point of application should be H/6 for the dynamic increment. Other suggestions, deriving from different studies, both analytical and experimental, were all comprised between these two values. However, it must be mentioned an inherent unconservative error in the M-O method when $\delta>0.5\phi$: it derives from Coulomb theory which assumes a linear failure surface while it is curved (see also section 2.2). This is why EC8 completely ignores wall friction. More recently Mylonakis *et al.*, (2007) proposed a modification of M-O method introducing a single formula valid for both active and passive thrust, more conservative since it underestimates passive pressure and overestimates the active one.

Non displacement walls

When it comes to “non displacement” walls (*i.e.*, which remains in an essentially elastic state during an earthquake) like basements, or box structures, that are founded on a firm soil or rock stratum, and, of course, propped retaining walls, the assumption of “displacement walls”, *i.e.*, the developing a displacement such that the soil is in plastic conditions, is unlikely to be satisfied and the M-O method is considered to be unsuitable for many walls of this type due to kinematic constraints.

Static equivalent analyses

In the frame of static equivalent analyses Wood (1973) first addressed the topic of dynamic earth pressure on non-displacement retaining structures founded on rigid soils in his PhD thesis. Under the assumption of rigid structure, modulus constant with depth and foundation on rock, and linear elastic behavior of soil, based on numbers of analytical and numerical analyses, he suggested a dynamic increment of active thrust, applied at 0.58H, to be calculated as:

$$\Delta P_{AE} = F k_h \gamma H^2 \qquad (24)$$

Where F is a reduction factor for horizontal acceleration, that according to Whitman (1991) can be posed always equal to 1, essentially finding the approach for displacement walls to be unconservative for non-displacement systems (see Eq. (22)). However, further studies with finite element simulations, again within the scope of methods derived from the Coulomb wedge, seem to indicate that the thrust depends on the soliciting frequency (Sitar *et al.*, 2012) and that when this approaches the eigen-frequency of the soil layer the active thrust increases up to 1.8 the static value (Whitman, 1991).

In EC8-5 (latest release of Eurocodes for seismic geotechnical design) some suggestions are given for the calculation of active and passive thrust coefficient in seismic conditions. In the formulation proposed the intensity parameter, in the form of horizontal acceleration at the site (stated as described in section 2.1.3 of this chapter), is introduced into θ_{eq} parameter, being the angle that the volume forces due to seismic excitation form with the vertical direction. It should be noted that the direction of the pseudo-static actions must be chosen in such a way as to maximize the active thrust acting on the wall: in the case of the horizontal component, the most severe condition is undoubtedly that of seismic action directed towards the retaining structure.

F-R methods

In non-displacement retaining systems, the soil-structure interaction, mainly in the form of kinematical interaction, assumes great importance as testified by the studies of Wang (1993) and Penzien (2000) related to box-type structures. In the transverse direction these structures undergo racking deformation (Figure 27).

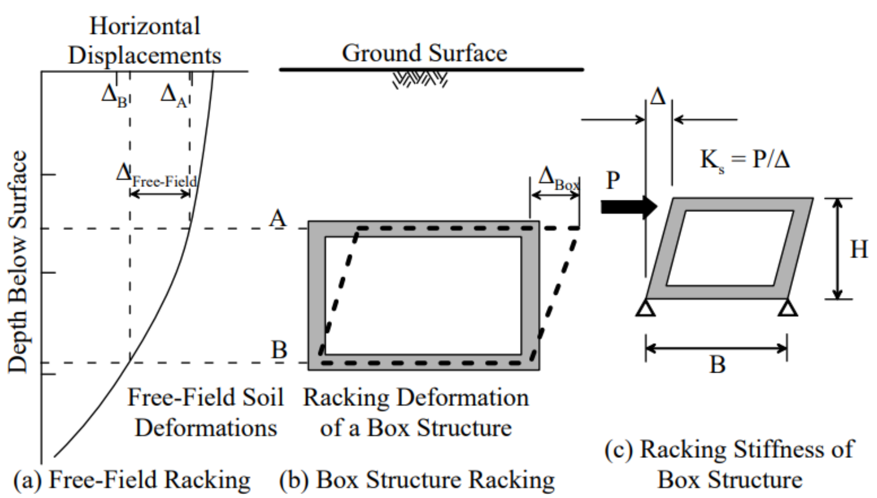

Figure 27. Racking deformation mode

The parameters that play the most significant role in the transfer of stresses to the structure are:

a. Soil/structure relative stiffness

It is expressed through the flexibility ratio F structure/soil, which, according to Wang (1993) for rectangular structures can be computed as:

$$F = \frac{G_m \times W}{S \times H} \qquad (25)$$

Where G_m is the soil shear modulus, W is the width of the structure, H is the height of the structure and W is the required force to cause a unit racking deflection of the structure, estimated through a simple static elastic frame analysis.
A structure with stiffness comparable to that of the soil will exhibit deformations similar to those of free field, whereas a structure that is much stiffer than the soil will modify the free field deformation, but at the same time will be subjected to greater loads. The contribution of relative stiffness can be quantified through the racking ratio R (structural/ground distortion). Wang (1993) related R to F using results from full dynamic analyses of soil-tunnel systems, while Penzien (2000) correlated the two ratios based on a pseudo-static approach.

b. Properties of the interface.

A rough interface will give rise to strong interaction between soil and structure and will be able to absorb high shear stresses with limited deformations. This implies, on the one hand, high stresses on the structure and, on the other, low deformations of the soil which, constrained to the structure by the roughness of the interface, will also exhibit a small decay of the shear modulus. A smooth interface, on the other hand, produces a sort of kinematic disconnection between the soil and the structure: the soil is free to deform, producing a significant decay of the shear modulus and lower stresses on the structure.

Effect of relative stiffness and interface properties can be considered together in graphs like the one reported in Pitilakis and Tsinidis (2013) and represented in Figure 28.

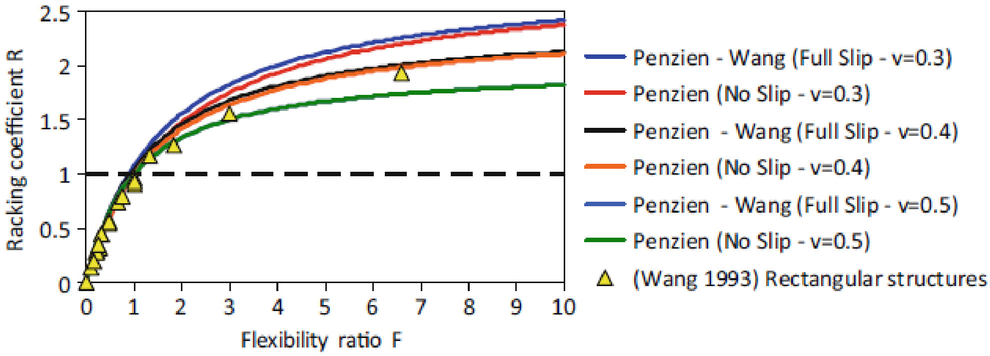

Figure 28. Racking coefficient against flexibility ratio for different interface conditions (after Pitilakis and Tsinidis, 2013).

Then, knowing the free-field motion Δ_{ff}, the motion of the structure can be computed as $\Delta_{str} = F \times \Delta_{ff}$. Lastly, the equivalent forces acting on the structure can be derived and applied as concentrated (*P* in Figure 27) or distributed loads to compute the internal forces induced by the earthquake, to be added to those statically induced.

Recent developments: analytical and numerical tools

More recently, Brandenberg *et al*. (2015) referred to U-shaped retaining structures, embedded into a soil layer with non-varying shear wave velocity, to interpret the increment of lateral earth pressure as a combination of inertial and kinematic soil-structure interaction (the latter is greatly predominant in embedded structures), in the frame of linear elasticity, enlightening the substantial incorrectness of the soil wedge approach which is not able to capture the modification of motion caused by interaction phenomena, responsible for the relative displacement produced during earthquake occurrence between soil and structure. In the paper, frequency-dependent stiffness expressions for the contact between soil and vertical walls and soil and horizontal foundation are introduced and used to determine the increment in horizontal force and bending moment acting on the wall as a result of the kinematic interaction, due to the impossibility for the rigid wall to follow the soil motion u_{g0}, represented in Figure 29. The increment pressure deriving from kinematic interaction is found to have a strong dependency on the normalized wavelength l/H (Figure 29).

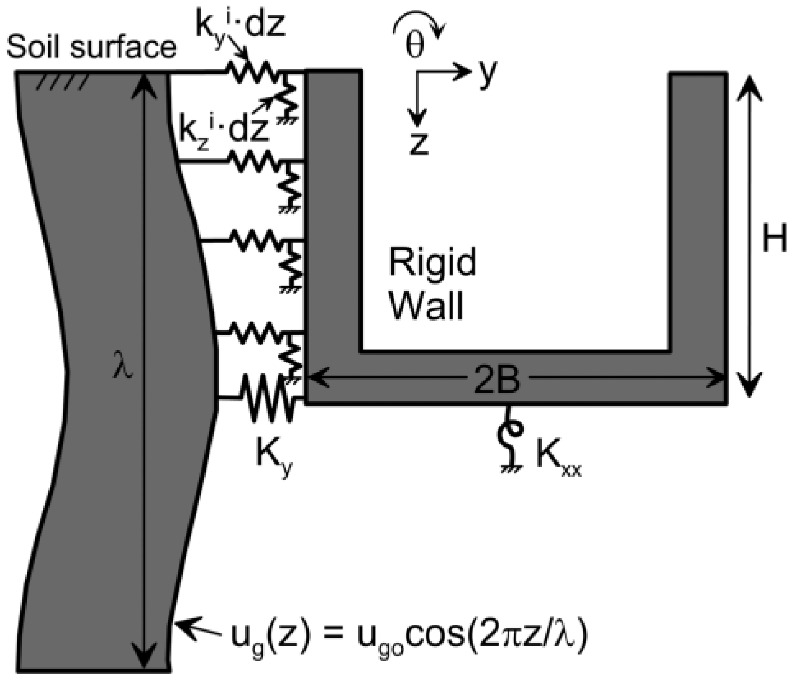

Figure 29. Embedded rigid strip foundation excited by vertically propagating shear wave (after Brandenberg et al., 2015)

The approach provides a unified means to evaluate increment of pressure and allow to explain some inconsistencies in the results of previous experimental studies, *i.e.*, the lower than M-O seismic earth pressure increments observed by Al-Atik and Sitar (2009, 2010), and the higher than M-O pressure increments computed by Ostadan (2005), Veletsos and Younan (1994), and others. Nonetheless, it suffers from many simplifying assumptions such as Winkler assumption (the stiffness terms act independently from one another) and that of non considering soil non-linearity. Callisto (2024) accounts for soil nonlinearity addressing a topic rarely investigated: the computation of dynamic forces acting on a propped retaining wall, via a static non-linear analysis that is pushover analysis, widely used for structural analysis, it consists in constructing the capacity curve of the structure in terms of acceleration related to the displacement registered. The use of this tool for geotechnical application had already been suggested by Visone and Santucci de Magistris, 2007. The mechanical behavior of the soil is described by a non-linearly elastic perfectly plastic model, having a Mohr-Coulomb plasticity criterion. The structure is solicited starting from the end of the construction stage and applying to the system horizontal inertial forces obtained multiplying the nodal masses by a uniform acceleration $k_h \times g$ that is progressively increased, eventually leading to the collapse of the system. For each value of the seismic coefficient, the push-over analysis provides the distribution of the internal forces in the structural elements and the intersection of elastic spectrum (corresponding to a damping obtained with a few iterations) with capacity curve (in S_a-S_d plane) gives the performance point of the structure. The bending moments resulting from the pushover, performed with FLAC2D, are compared with those of dynamic analyses where the acceleration time histories were applied at the base of the model resulting in a satisfying agreement. *It is instructive to note that the ordinate of the performance point is significantly larger than the PGA, which is the first spectral ordinate. This means that by neglecting the deformability of the soil-structure system the internal forces in the structural members would be largely underestimated* (Callisto, 2024).

2.3.3. Structure-soil-structure interaction: coupling among foundations

The study of SSI paved the way to another research branch that is structure-soil-structure interaction (SSSI) accounting for structures close enough to each other to mutually influence their seismic response. The first studies on this topic have been conducted by MacCalden back in 1969 who investigated both analytically and experimentally the transmission of steady-state vibrations from one rigid circular foundation to another through the soil. Two years later, Warburton *et al*. (1971) studied the response of two cylindrical masses on an elastic half-space, excited by a harmonic force applied to one of the masses. They showed that the interaction between the masses is maximized at frequencies close to their resonances. Luco and Contesse, in 1973, published a study named "*Dynamic structure-soil-structure interaction*", introducing the term SSSI. In the paper, a closed form analytical solution for the problem of two shear walls on rigid semi-circular foundations embedded in the half-space, subjected to vertically and oblique incident harmonic SH-waves, was presented and the seismic response of the two walls was compared with that of an isolated structure. The comparison showed a modification of the fundamental frequencies of the structures, with respect to the single shear wall. Important interaction effects were observed in the case of a small shear wall structure located close to a larger one, with the response of the small structure being significantly affected by the presence of the larger structure. Moreover, due to waves reflected and diffracted by the foundation, the ground motion resulted modified depending on inertia and excitation frequency, at distances at least one order of magnitude greater than the characteristic length of the foundation.

Analytical solutions

In the very beginning of SSSI, attempts were made to produce analytical solutions of simple problems, *e.g.*, the model for the motion of a single rigid circular foundation on an elastic half-space or the equations for the response of two geometrically identical cylindrical bodies, attached to the surface of an elastic half-space, developed by Warburton *et al.*, 1969, or the mathematical solution of the dynamic subsoil-coupling between circular and rectangular foundations, developed by Triantafyllidis in 1987. These types of solutions, though, present numerous drawbacks: they are developed for foundations placed on linear elastic half space, they are strongly dependent on the assumed geometry, often very simple, and they show discrepancies with experimental results (Lou *et al.*, 2011). Moreover, according to Seed *et al.*, 1975, an elastic half-space can be used to analyze shallow foundations, while it is not suitable for deep foundations where damping phenomena become important.

Numerical analyses

This topic kept being studied in later decades mostly because of nuclear power plants, composed of a reactor building adjacent to a turbine and a control building, or referring to very crowded and densely built urban environments (in this case, the study of more complex scenarios than two adjacent foundation is usually referred to as *city effect* or *site-city interaction*, Ghergu and Ionescu, 2009), thus the main focus has been about coupled effects of adjacent above-ground structures. Numerical methods (FEM, BEM, FDM) are, and were, widely used to overcome some of the problems highlighted in the analytical approaches. Some factors that had emerged as important after Gonzalez (1977) (*i.e.*, vertical displacements of the foundation related to horizontal force) and Lysmer *et al.*, (1977) (*i.e.*, the embedment of the foundations) were further and systematically investigated by Lin *et al.*, (1987) adopting a coupled analytical-numerical (FE) method, where the near field, with all geometric irregularities and material inhomogeneities incorporated, was modelled with discrete elements, while the far field was modelled with semi-discrete transmitting boundaries: the modes of vibration were modelled in vertical direction with discrete elements and in horizontal with continuous functions.

In the study three parameters were varied: embedment of the foundation, distances among foundations, and position of the foundations in a Cartesian coordinate system (x, y, z) in order to investigate their influence on:

- the magnitudes of several elements of the dynamic compliance matrix of the system of foundations in comparison with the corresponding elements of the dynamic compliance matrix of one of the foundations in the absence of the other;
- the magnitudes of the displacements and rotations of the foundations due to ground motion in each of the coordinate directions with free-field displacement of unit magnitude on the surface of the stratum compared with the corresponding quantities for each of the foundations in the absence of the other.

The embedment of the foundation is found to amplify the interaction, as well as short distances between two foundations, but what's more interesting is that the interaction also gives rise to coupling between horizontal and vertical displacements, between rocking and torsion, etc., that would not appear for a single foundation; this finding was later confirmed by different studies, among them Qian and Beskos (1996). They also found that the additional inertia of one of the structures will lower the resonant frequency of the other. In the following years many finite elements and finite difference software were employed to study SSSI effects incorporating non-linearities of soil. It was found that structural inertia and geometrical configuration of the system are very influent in increasing interaction effects that were studied mainly in terms of design parameters, such as acceleration at the base, base shear and induced displacements. It was found that the base shear can increase up to +120% because of SSSI (Yahyai *et al.*, 2008).

FE analyses have been very useful in modelling real case scenarios, with respect to analytical models, but, despite their versatility, it is difficult the accurate modelling of the infinite or semi-infinite soil domain due to wave reflections at the mesh boundaries. BEM models overcome this problem; in fact, they satisfy automatically the radiation condition without any need for using special non-reflecting boundaries (Stamos and Beskos, 1995). Therefore, BEM has been used as well, even if it presents another shortcoming, being the impossibility of using it in non-linear problems.

<u>Experimental observations and site city effect</u>

Some attempts have also been made in performing experimental analyses of SSSI phenomena with both shaking tables and centrifuges, as well as measurements on full scale buildings (Lou *et al.*, 2011; Vicencio *et al.*, 2023). Particularly interesting is the work made by Schwan *et al.*, (2016) treating a theoretical, numerical and experimental crossed-analysis to qualify and quantify the complex multiple SSSIs occurring in urban environment through the design of an elementary case study.

<u>Summary of results in SSSI</u>

SSSI is something to consider when multiple buildings are very close to each other in seismic areas. The main factors influencing the interactions are:

- Distance between buildings
- Inertia of buildings
- Direction of the alignment of building's centers
- Depth of foundations embedment: the interaction increases as the embedment increases

The main effects are:

- Coupling between horizontal forces and vertical motion
- Rocking motions
- Lowering of eigen-frequency of the structure, the most affected structures are not tall and rigid.
- Increase in base shear.

The research is based both on numerical methods, and experimental tests. Even though they helped in the initial understanding of the phenomenon, analytical methods cannot replicate the complexity of real cases, and thus they result inadequate at this stage of research where some real cases, especially related to nuclear power plants, need to be analyzed.

However, the stage of research is still very far from a conclusion, also due to the multitude of parameters that the problem depends on and the almost complete absence of experimental data. Therefore, SSSI is not yet included in guidelines and national codes.

2.3.4. Interaction between underground structures and surroundings under seismic excitation

When it comes to the interaction between underground and above-ground structures, the comparison with the findings previously exposed is not straightforward for different reasons, and further research is required. Among others, some differences are: the predominant type of interaction occurring between soil and underground structure is kinematical, while inertial interaction is minimized; the effect of the frequency content of the soliciting dynamic signal is not interpretable in the same way as before, in fact, the dynamic characterization (*i.e.*, individuating the eigen-frequencies) of an embedded structure cannot be made disregarding the soil, in contrast it strongly depends on the soil response and vibration modes (some work in individuating the natural frequency of the soil-structure system has been done on underground tunnels referring to the individuation of damage in tunnel linings -*e.g.*, Jiang *et al.*, 2016-, but, to the author's knowledge, there is not a standard procedure for the identification of dynamic properties of soil-structure systems, that is still delegated to complex 3D analysis, when taken into account); the depth of the embedment is much greater and not comparable with that of in-elevation structure foundations; they constitute an empty volume, thus a discontinuity, into the soil and their construction produces a change in the stress state of the soil along all the depth of embedment, connected with excavation process and bulkheads installation. This kind of interaction can be considered a subtopic of SSSI, scarcely investigated and not present at all in national codes and Eurocodes, but of increasing interest since the number of embedded structures in the city centers, such as metro stations, tunnels and parking spots is constantly rising. The complexity of the interaction phenomena that characterize this kind of system makes it necessary to operate some simplifying assumptions, which can consist in operating analyses in 2D, using elastic constitutive models to describe soil behavior, or dividing the SSSI system into two sub-problems (*i.e.*, influence of buildings on underground structure and vice versa) and addressing one of them at a time. Following this latter interpretative key the following paragraphs are organized.

2.3.1. Modification of seismic response in the underground structure surroundings

The presence of an underground excavated structure can affect the seismic response of the environment because of two main reasons. On one hand the structure acts as a discontinuity in the continuity of the medium soil producing deviation of the seismic waves along their path; on the other hand, the work made to realize the structure – *i.e.*, installation of bulkheads, soil removal – induces a displacement field around the excavated area, which affects the soil properties and in turn its response to the seismic input.

Modification of wave propagation due to underground cavities

Seismic waves can undergo diffraction, reflection and refraction phenomena (Figure 30) due to the presence of inclusions and discontinuities within the propagation medium, or surface irregularities. A brief description of these phenomena is:

- Reflection: when a wave meets a boundary, it can be reflected or transmitted. Reflection can be partial or complete, and it can also involve a phase flip (change of phase of 180 degrees.)
- Refraction: refraction occurs when a wave crosses a boundary separating two different media. A wave entering a medium at an angle will change direction while crossing the boundary.
- Diffraction: this refers to the "bending of waves around an edge" of an object. Diffraction depends on the size of the object relative to the wavelength of the wave.

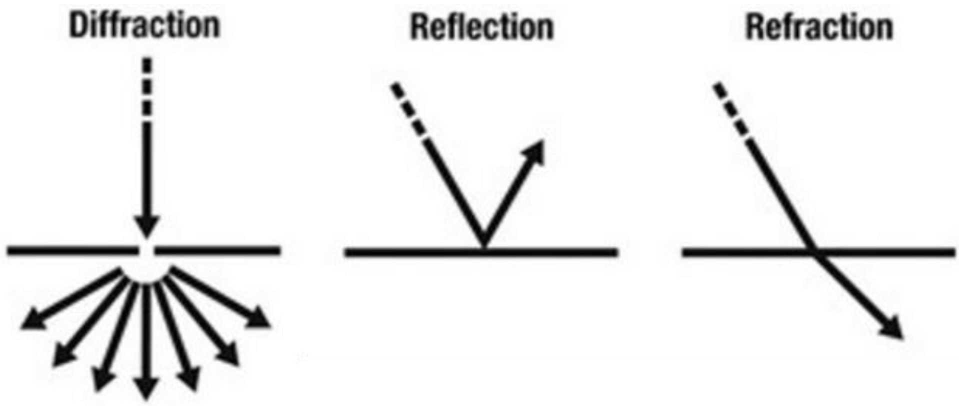

Figure 30. Schematic illustration of phenomena occurring to a wave when it encounters an obstacle along its path.

While numerous studies have been developed on the effects induced by valleys and topographies and implemented in seismic norms as well (see *e.g.* Part 5 of Eurocode 8), understanding and quantifying the effects of underground irregularities, such as buried cavities, tunnels or box stations, is still at a research stage. The first systematic studies about the diffraction of seismic waves were conducted by Lee and coworkers and are testified by numerous publications addressing the issue under the assumption of plane waves (P, SV, and SH) propagating through an elastic half-space (plane waves are a mathematical approximation of real problems, where the wave front can be assumed to be flat if the source is sufficiently distant) and perfect bonding at the interface between the elastic domain and the inclusion. First, a solution for the problem of diffraction of elastic plane waves by a hemispherical canyon was presented; the same method of analysis was then used in studying the motions of a hemispherical rigid inclusion and the scattering and diffraction of plane waves induced by the presence of a hemispherical alluvial valley into a half-space (Lee, 1984). The problem is set by writing the wave equation, using as an input a harmonic wave so that the equation can be rewritten in the form of Helmholtz equation:

$$\nabla^2 f = -k^2 f \qquad (26)$$

where, when applied to the propagation of waves, k has the meaning of wave number, and Eq. (26) is a time-independent wave equation. The solutions are found in terms of displacements at the free surface that result from the superposition of effects of waves scattered and diffracted by both the free surface and the inclusion. When both the plane free boundary and the hemispherical alluvial valley are considered, in fact, the incident and reflected plane waves will be scattered and diffracted around the valley, and the scattered spherical waves from the valley will be reflected into the medium from the plane free surface. The resulting displacement at the free surface is given by:

$$u\,(0) = u^i + u^r + u^s + u^R \qquad (27)$$

Where the contributions of incident waves (u^i), waves reflected from the free surface (u^r), waves scattered (u^s) and waves refracted (u^R) by the inclusion are added together. Being the problem studied in a tridimensional space, the displacements resulting from the interaction phenomenon are studied in *x, y* and *z* coordinates, separately for each of the three considered waves.
Ten years later, in 1996, Manoogian and Lee developed the studies by Lee and Trifunac (1979) and Lee and Karl (1992) related to transversal sections of circular cavities (in 2D), applying the method to cavities of arbitrary shapes. In the same year Luco and De Barros (1994) proposed an indirect boundary integral method to describe the problem of SV and P waves incident on a cylindrical infinite cavity in a visco-elastic half space, in terms of total displacements and stresses on the cavity surface, overcoming the limitations of previous studies on these types of waves. Lastly, in 1999, Lee *et al.* studied the combined problem of a canyon in an elastic half-space interacting with a circular cavity under the excitation produced by steady harmonic plane waves. The existence of a circular inclusion and of a canyon (schematized as hemi-spherical cavity) is recognized to potentially amplify the displacements induced at the free surface that, depending on the adopted configuration, varies between +100% and +300% with respect to a free-field condition at a certain distance from the cavity; immediately above the cavity instead a de-amplification is observed in that that is referred to as "shadow zone" (Yiouta-Mitra *et al.*, 2007; Moghadam and Baziar, 2016). Moreover, the pattern and amplitudes of surface displacements depend significantly on the direction of incident waves and the material properties of the valley (that in the study are simply

represented by wave velocity), and the ratio of the diameter of the inclusion to the wavelength of the incident plane waves determines the extent to which the effects are developed. A similar approach has been used by Smerzini *et al*. (2009) under the same assumptions of Lee and coworkers. They applied it to study three kinds of inclusions under incident SH waves: an unlined cavity, a lined tunnel and a filled cavity, conducting parametric studies by varying transversal dimension, depth, frequency content of the input, angle of incidence, distance from the cavity axis. The response of the system is studied in time and frequency domain: in time domain the sequence of arrival of incident, reflected and transmitted waves can be appreciated; the frequency domain allows to quantify the modification of motion (spectral amplitude). It results that the dominant wavelength associated with the motion along the cavity axis is approximately equal to 6H (with H embedment depth of the cavity axis). The results of the parametric analysis show that significant amplification of motion (in terms of displacement and acceleration at the ground level) is found only for the unlined tunnel, placed at small depths, and for small distances from it (less than three times its radius). In addition, the authors conclude that the presence of underground cavities is expected to induce significant effects on surface ground motion limited to the low period branches of the acceleration response spectra.

Unfortunately, analytical methods, despite their accuracy, are not useful when it comes to modelling real problems, because of many simplifying assumptions needed to solve analytical equations. More recently BEM methods have been employed to study the phenomenon, assuming a linear elastic behavior of the soil. Alielahi *et al*., (2015) and Alielhai and Adampira (2016) used 2D boundary element method in a parametric study conceptually similar to that performed by Smerzini *et al*., but focused on the propagation of SV and P waves, not only aimed at qualitatively describing the diffraction phenomena, but also at providing some useful guide for design, stating that "*considering each site as a simple one-dimensional site without any underground structure is very irrational and non-conservative*". The results are essentially presented in terms of vertical and horizontal displacement amplification, and a linear function of the tunnel depth ratio (depth/radius) is proposed to identify the distance from the tunnel at which the maximum amplification happens. In contrast to the findings of Smerzini *et al*., Alielahi *et al*. conclude that with incident waves with short predominant frequencies (longer period bands), the ground motion tends towards greater amplification, while short period contributions tend to be de-amplified. Other conclusions are instead in agreement among different studies, like the fact that the amplification effect decreases as the embedment depth increases (Lee, Smerzini, Alielahi); that the portion of soil overlying the tunnel undergoes a de-amplification of motion (Panji and Ansari, 2017; Alielahi *et al*., 2015; this finding has been confirmed also by finite element analyses as will be discussed later, *e.g*., Sica *et al*., 2014); that within a certain distance from the axis of the tunnel clear amplification of motion is registered (in terms of displacements by Smerzini *et al*., 2009; Alielhai *et al*., 2015; Panji *et al*., 2017, and in acceleration by Liang *et al*., 2012; Smerzini *et al*., 2009). The methods used in the studies presented here, although useful for physically an qualitatively description of the phenomenon, are only valid in idealized situations, where non-linearities are not taken into account, the waves are harmonic (only Smerzini and coworkers validate their study using a real accelerogram), cavities are often unlined, and the shape of the cavity is circular, differing only in terms of embedment depth and radius, so that only pipelines and circular tunnels can be studied (Stamos and Beskos, 1999).

Effects on seismic behavior of buildings due to deep excavations induced deformation

The contributions related to this aspect are fewer than those about the deviation of seismic waves. However, a couple of works, particularly focused on building damage, testify the importance of considering the correct displacement field induced by excavation activity, before studying the seismic response of the system. The first one is that by Mo and Hwang (1997) aimed at characterizing the influence of different steel and concrete types on the seismic behavior of a framed building in proximity to a deep supported excavation. The analyses were carried out in 2D with the FE software SOIL-STRUCT. The static analyses, consisting of sequential phases of soil removal (excavation) and support installation, were calibrated on experimental results in terms of horizontal displacements, and the settlements were derived as a consequence. Focus of the study was on the displacement history produced at the building's roof. It was computed by using a single input, and allying it at different excavation stages (*i.e*., with the building subjected to settlement profiles with different maximum values) and to a system subjected to different settlement shapes (*i.e*., smooth or concave asymptote). The displacement time histories appear to be affected by settlement types and entities, but no attempt is made in the paper to interpret the observed behavior.

More recently, Mangir *et al*., (2023) and Van Nguyen *et al*., (2024) highlighted the importance of considering the settlement pattern for the evaluation of the seismic performances of framed buildings. Van Nguyen *et al*., (2024) produced a comprehensive work on this topic analyzing in 2D with ABAQUS the seismic performances of buildings with different heights (5 and 15 floors, respectively) and comparing them in two scenarios: with excavation (ESSI) and without excavation

(SSI). The effects of the interaction are evaluated in terms of acceleration, shear floor forces, inter-story drift and horizontal displacement at the floor levels. As a general conclusion, excavation produces a decrease in acceleration and shear floor forces and an increase of displacement and inter-story drift in the ESSI system with respect to the SSI one. This observation is motivated claiming that the induced settlements are responsible for lower rigidity in the soil-structure system, which in turn means more displacement and lower forces. However, although eleven different accelerograms were used for the analyses in time domain, only mean values of the results are reported so that no influence of the accelerogram characteristics can be considered.

Experimental and numerical evidence

Recently, increase in number of underground works, mainly due to improvement of public transportation in the city centers, has been testified in literature by an increasing interest in SSI and SSSI phenomena involving aboveground and underground structures (and not only unlined cavities, like those addressed with analytical solutions), which has been made simpler by the development and improvement of computational tools. Numerical (FEM and FDM) and, to a less extent, experimental investigations were carried out in the last decade contributing to an initial description of the modification of seismic motion induced by the presence of tunnels and excavations in real case scenarios and the interaction occurring between adjacent structures embedded into the soil, which was not allowed by analytical methods and, in some extent, neither by BEM. As already mentioned in previous sections most of the literature contributions treat circular, horseshoe or box tunnels. In 2007 Yiouta-Mitra *et al*., were among the first to study the influence exerted by a lined tunnel on the propagation of harmonic shear waves (SV) with a finite difference plane model (in FLAC 2D) validated against the analytical solution proposed by Luco and De Barros (1994) by comparing the free surface displacements. The study is conducted by varying embedment depth, diameter and relative flexibility of the tunnel, frequency content and soil properties, with the soil treated like an isotropic homogeneous visco-elastic material, and displacement time histories are reported at increasing distance from the tunnel axis. Together with the already mentioned Smerzini *et al*., (2009), this paper constitutes a benchmark in this field, because it gives some rules of practical utility, *e.g*., the tunnel can amplify the motion at the ground level, until a distance equal to three times its radius, moreover wavelength input greater than the characteristic length of the structure result in negligible interaction effects. However, the discussion is made under many simplifying assumptions, and the results, presented only in the form of free surface displacement amplifications, are a useful indication about the physical phenomenon but they are not the only, neither the first, parameter to consider in designing above-ground structures. Numerical methods in subsequent years were then applied in parametric studies to characterize, under diverse assumptions and different configurations, variations of base shear forces (Wang *et al*., 2013; Yeganeh *et al*., 2015), interstory drift (Guo *et al*., 2013; Yeganeh *et al*., 2015; Castaldo and de Iuliis, 2014) and peak ground acceleration, PGA, (Wang *et al*., 2013; Moghadam and Baziar, 2016; Abate and Massimino, 2017a and 2017b; Abuhajar *et al*., 2015; Sun *et al*., 2019; Isari *et al*., 2021) – due to soil interaction with tunnels and excavations –, that are design parameters widely adopted nowadays in the codes. In the following some of the parameters that are found to be significant in this kind of problem are listed and analyzed.

Arrangement of structures with respect to input motion direction

Wang *et al*., (2013) introduced buildings in a FE model (ANSYS) of a box station, to study the SSSI system, and investigated different arrangements of ground (GS) and underground structure (US) under incident S waves by varying distances and GS orientation with respect to the station and the input direction. The amplification ratios of peak ground acceleration of the different configurations, with respect to the free field condition, are presented in frequency domain and lead to conclude that the worst case scenario (*i.e*., highest amplification) is that represented in Figure 31.

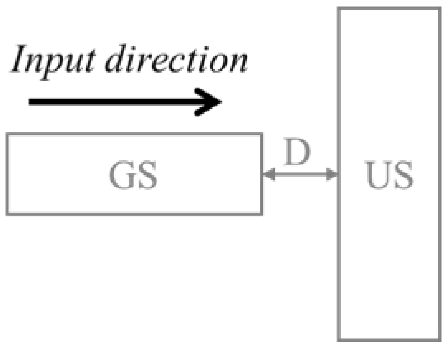

Figure 31. Configuration that produces the highest amplification ratio, according to Wang et al., 2013.

Therefore, Wang and coworkers highlighted the importance of distance among structures and direction of input motion, in addition to an analysis of the role of input frequency content, depth of the structure and number of floors.

Distance from the underground structure

The effect of distance from the underground structure has been further investigated with numerical methods by Guo *et al*., (2013), Sun *et al*., (2019), Miao *et al*., (2020) among

others. Guo and coworkers used the generalized interstory drift spectral method to run 2D analysis on pre- and post-excavation models by varying building-station distance and building's structural period. Low period structures and small distances from the station axis led to higher interstory drift, used in the paper as damage indicator.
Sun *et al.*, with FLAC 2D, used Daikai station as a reference to study shear wave velocity, dimensionless period together with distance effect on PGA and shear strain. The analyses were run under two different hypotheses on soil behavior:

- Linear visco-elastic
- Viscoelastic model in conjunction with the soil shear stiffness degradation (equivalent linear)

Both the models predict a maximum amplification of PGA at dimensionless distances comprised between 1 and 1.5, while a de-amplification along the axis of the station (as already found by Yiouta-Mitra *et al.*, 2015; Moghadam and Baziar, 2016; Sica *et al.*, 2014) is only predicted by the analysis that accounts for the non-linear behavior. Lastly, shaking table tests performed on a circular tunnel embedded below a framed building, were numerically simulated by Miao *et al.*, (2018 and 2020) in ABAQUS (3D FE software). The investigated distances, L, span between 5 and 50 m from the tunnel wall: for both interstory drift and peak ground acceleration, L = 5 m (corresponding to a dimensionless distance of 0.7) represents the worst scenario and, starting from L = 30 there is no influence of tunnel anymore. Similar results are also reported by Isari *et al.*, (2021) who found maximum PGA at x/B < 1, with B semi-length of the station. The existence of the already discussed shadow zone, instead, is confirmed by diverse researches, both experimental and numerical (Moghadam *et al.*, 2016; Abate and Massimino, 2017b; Hong *et al.*, 2025).

<u>Burial depth of the tunnel</u>

The influence of tunnel depth has been investigated by Moghadam and Baziar (2016), who performed shaking table test to analyze the effect of a box shaped tunnel on the PGA in the surroundings; the experiments were then analyzed with FDM (FLAC 2D), no buildings were modeled and together with the embedment depth, the flexibility ratio of the lining and the dimensionless period of the input l/D (as defined by Alielhai *et al.*, 2015) were varied. The tunnel is studied under seismic excitation at different dimensionless burial depths x/a (1.5-4) finding results similar to those obtained by Yiouta-Mitra *et al.*, (2015), with the maximum PGA amplification occurring when x/a < 3, *i.e.*, for shallow structures. Abate and Massimino (2017a and 2017b) starting from a case study in Catania (2017a) carried out a parametric study in a 2D FE model (ADINA) (2017b): a circular tunnel and a framed building are studied in different configurations (building and tunnel vertically aligned, or with a spacing *d* between their axes, different depths of the tunnel). Both tunnel and building produce de-amplification in maximum acceleration profiles. The de-amplification due to the tunnel happens at the tunnel depth and propagates towards the surface; it is related to the deviation of seismic waves already discussed in previous sections. For what concerns the building, Abate and Massimino claim the compaction of the soil due to the building's load. A similar result is also reported in Wang *et al*., (2018) and Abuhajar *et al*., (2015). A more pronounced de-amplification of PGA is found for shallower depths of the tunnel, as already found by Baziar *et al*., (2016) and Yiouta-Mitra *et al*., (2007). The results are extracted along the tunnel and the building axes (when different), so that no information about the eventual amplification in other locations, far from the disturbance, is given.

Relative flexibility

The relative flexibility between soil and structure can be investigated by varying the section dimensions of the structure. Abuhajar *et al*., (2015) investigated the effect of lining thickness during centrifuge experiments on a box culvert: 6.35 mm and 3.18 mm (scale factor equal to 60) of thickness were used to simulate thick and thin box culverts. The effect in terms of PGA seems negligible.
The already-cited works of Yiouta-Mitra and coworkers (2007) and Moghadam and Baziar (2016) make use of the flexibility ratio (*F*) definition given by Wang (1993):

$$F = \frac{2E_s(1-{\nu_l}^2){R^3}_l}{E_l(1-{\nu_s}^2){t^3}_l} \qquad (28)$$

Where pedicles *l* and *s* stand respectively for lining and soil, while *R* and *t* are radius and thickness of the lining. The results of both studies go in the same direction, *i.e*. an increase of stiffness produces reduction in amplification of motion. However, while in Yiouta-Mitra *et al*., the topic is only mentioned, Moghadam and Baziar make a more detailed discussion providing data relative to four significative values of *F*:

- $F = \infty$ (unlined cavity): highest amplification at the ground surface (1.4)
- $F > 1$: values of amplification higher than 1 (with F=2419, 100 and 4 result in the amplification ratio of 1.3, 1.25 and 1.16, respectively).
- $F = 1$: the amplification is 1 and the effect of tunnel at the ground surface is eliminated

- *F <1*: the tunnel de-amplifies the PGA with respect to the free field, in fact it acts as a barrier in the propagation path of the incident shear waves.

Dimensionless period and frequency content of the input

It is well known, by many research fields, that the interaction between incident waves and matter occurs when the characteristic wavelength of the incident waves is comparable with the characteristic dimension of the object of interest.
Considerations about wavelength can be deemed equivalent to those about frequency content of the input, which is recognized to have an effect in SSSI systems. In this sense according to Yiouta-Mitra *et al*., (2007) higher dimensionless frequencies produce greater amplifications in the range 0.05-1; Wang *et al*., (2013) reported that frequency effect on the interaction between underground and aboveground structures, is only visible for $f > 1\ Hz$, but mentioning correlations with the structure dimension that, instead is found to be significant when one refers to the dimensionless period defined as λ/D, with λ wavelength of incident wave and D diameter of the tunnel or cavity. Alielahi *et al*., in 2015, found that the tunnel effect could be ignored in the case of incident waves with wavelengths shorter than the diameter of the tunnel; in case of incident waves with wavelengths of 2–8 times greater than the diameter of shallow tunnels, the amplification factor at the ground surface would usually be greater than unity and in most cases, the maximum amplification will occur for incident waves with greater wavelengths. Instead, the ground surface response would be approximately the same as the free-field motion if deeper tunnels are impinged by incident waves with wavelengths much greater than the tunnel diameter. Lastly, Moghadam and Baziar, confirming what already found by Smerzini *et al*., (2009) for circular unlined cavities and in substantial agreement with Alielhai and coworkers, state that the effect of λ/D exists and it is maximally visible for $\lambda/D = 6$ for shallow tunnels.

Filtering effect of the underground structure

Research has revealed the filtering effect that box shaped and circular tunnels can have on the applied input, thanks to parametric studies conducted using different inputs and frequency domain data processing of acceleration time histories. Different studies agree about the fact that the presence of tunnels tends to amplify long period (or low frequencies) and to de-amplify short periods (or high frequencies). Among others Baziar *et al*., (2014) found the result during a numerical parametric study in FLAC2D, firstly aimed at replicating centrifuge experiments and then at investigating the effect of the frequency content of the applied input motion, using both simple sinusoidal signals and real earthquakes; Abate and Massimino (2017b) solicited the numerical model with 30 different input signals, dividing the response of the system based on the value of f_s/f_m ratio, with f_s being the first natural frequency of the system (retrieved with a modal analysis carried out with ADYNA) and f_m the mean frequency of the input motion; in addition to what already found by other, they observed also a reduction of the natural frequencies of the system due to the aboveground buildings; lastly, equivalent results were found by Hong *et al*., (2025) during shaking table tests experiments.

Open pit excavations

Very few contributions are available in literature about seismic effect of open pit excavations. With respect to tunnels and box culverts, deep open excavations are less suitable to be generalized; in fact, their geometrical dimensions and design of retaining structures are strongly dependent on site conditions. This makes almost necessary and very important to refer to a case study, which allows for taking into account also the displacement field induced during excavation. Yeganeh *et al*., (2015) and Castaldo and de Iuliis (2014) are among the few researches who treated the topic, based on a case study, thus simulating the static stages before applying the seismic loads, paying particular attention to the damaging effects on adjacent buildings. Castaldo and de Iuliis use the case study of San Pasquale station (Line 6 of Napoli underground) to build a bidimensional model in Plaxis where both the excavation and the building are present. The calibration of soil parameters and the static stages are performed based on Castaldo *et al*., (2013), and are followed by a coupled dynamic analysis on the same system. The focus is mainly on the damage parameters of the modeled building expressed as interstory drift and ductility demand. Both parameters are significantly increased by excavation. However, the conclusions drawn by this study are affected by several choices: the constitutive model that doesn't account for hysteretic damping (Hardening soil model), the choice of acceleration input (Irpinia earthquake, registration of Sturno, is used), the station structure that is an old design version and it is quite different from that actually realized (for example, vertical drains, represented in the model, have not been realized). Moreover, similar studies conducted by Yeganeh and coworkers lead to the opposite result, with the reduction of interstory drift on the building at the excavation side reduced by 28%. However, it must be noted that in Yeganeh *et al*., (2015) the building is perfectly adjacent to the excavation, while in Castaldo and de Iuliis (2014) it is 15 m away from the wall. Applying the findings about propagation of seismic waves in presence of tunnels and the distance effect, the differences could be explained. Other parameters, such as settlements or base shear force are not investigated by Castaldo and de Iuliis, thus not comparable.

Together with the quantities mentioned so far, other parameters have been investigated, such as:

- effect of PGA on kinematical interaction (Abuhajar *et al.*, 2015)
- relative density of the soil (Abuhajar *et al.*, 2015),
- shear wave velocity of the propagation medium (Yiouta-Mitra *et al.*, 2007; Wang *et al.*, 2013; Sun *et al.*, 2019),
- damping of soil (Sun *et al.*, 2019).

The results obtained are less easy to summarize but citing them helps to give an idea of the complexity of the phenomenon and the multitude of parameters on which it depends.

2.3.2. Influence of buildings on the underground structure

The other side of the interaction phenomenon is the effect that above-ground buildings produce on underground structures. Navarro in 1992 outlined that the simplified methodologies available for seismic design of underground structures are no longer conservative when massive buildings are near the buried structures. In fact, vibration characteristics of the soil-underground subway station system can be changed by the ground structure (Long *et al.*, 2012).

<u>Dynamic stresses</u>

Among the first to address the problem in recent years there are Pitilakis *et al.*, (2014) who conducted a parametric study on a transversal cross section of a circular tunnel with and without elevation buildings, modelled as SDOFs. They studied the effect of burial depth, relative flexibility, distance of buildings from the tunnel and constitutive models for the soil finding that usually buildings worsen the seismic response of tunnels increasing normal stress and bending moments in the lining (which is confirmed by Yeganeh *et al.*, 2015 for a fully modelled structure founded on piles), and horizontal accelerations at the tunnel depth, finding that the effects are more pronounced for shallower and stiffer structures (the opposite is found by Hashash *et al.*, 2018, for box tunnels). The study was then extended by Tsinidis (2018) who, following a similar methodology, investigated the role played by burial depth of circular tunnels, number of high-rise, massive buildings (m = 400 t) and their relative position to the axis of the tunnel, and response of two twin tunnels. In both cases the authors use two different soil models (a visco-linear elastic law, the second is a visco-elastic plastic model) and compare the results. Deformations, stresses and forces on the lining exhibit residual values after shaking, meaning that the soil underwent plastic deformations, which makes it advisable to use a constitutive model incorporating plasticity. In addition to results already exhibited in the previous study, Tsinidis finds that the higher the number of buildings the higher the increment of stress on the lining (confirmed by Miao *et al*., 2020), that is even worsened, in most cases, when the buildings are placed exactly above the tunnel: the number and disposition of buildings-SDOFs at the ground surface, in fact, affects the extent of the soil yielding area around the tunnel and hence the residual dynamic earth pressures developed around the tunnel. Earth pressure under dynamic loads has been also investigated by Hashash *et al*., (2018), who performed tridimensional dynamic FE simulations (LS-DYNA) of centrifuge experiments conducted on SSSI systems where the buried structure is, from time to time, a rectangular tunnel and an open pit excavation, and the ground one has 13 and 42 floors. Two parameters, particularly useful for design purposes, are investigated: dynamic earth pressure on the excavation wall and shear base force of the ground structure, which are found to be connected to each other. Envelopes of dynamic earth pressure are reported and found to be non-linear with depth (behavior that is not reflected in standard design procedure). The envelopes show a significant increase on the building side of the wall due to the base shear of adjacent tall buildings, which is found to be more consistent for open excavation (+71%) and less for tunnels (+67%), because a portion of the building's base shear can be transmitted to the soil mass above, while there is no overlying soil in open excavations.

Peak ground accelerations

Wang *et al*., (2017) extend the investigation carried out in 2013, using the same FE model and configurations of buildings-underground structures system, but focusing on the effect produced by aboveground buildings on underground station quantified by amplification parameters describing the increase of acceleration at the ground level due to interaction among structures. As a general conclusion ground structures are less sensitive to the presence of underground ones that the opposite, but the configuration causing the highest amplification is the same represented in Figure 31.

Frequency response

For what concerns the frequency response of buried structures, according to Hashash *et al*., (2001) they follow the behavior of the surrounding soil mass. However, in Hashash *et al*., (2018) the authors find that presence of the high-rise buildings amplifies the spectral response of underground structures at short periods (0.3-05 s) and attribute the result to kinematic constraints provided by the basement and the confining pressure of the structure. Instead, Qiu *et al*., (2021) propose a novel approach to describe the interaction dividing it into kinematical and inertial contributions, the latter becoming important in dense urban environment. The presence of adjacent buildings significantly augments the seismic responses of subway stations at the first-order natural frequency of buildings, and this is attributed to the inertial interaction effect induced by the vibrations of adjacent buildings.

2.4. Summary and concluding remarks on existing literature

In the first sections of the present chapter an attempt of presenting a quite organic and organized discussion has been made referring to static effects in terms of displacement and stresses acting on underground structures, reviewing available technologies, prescription of Eurocodes and national code, empirical methods for the prediction of induced movements, design approaches to calculate earth pressures and stresses acting on the structures, even if pointing out the difficulty of determining the behavior of hyperstatic structures like multi-strutted excavations, and the work still required for a more rationale, less conservative and more economical design. The task has become less easy in approaching the increment of earth pressures due to seismic loading since very few experimental evidence is available, and the analytical methods that practitioners can count on are developed for box or circular shaped tunnels, while very few contributions are related to strutted excavations.

When the discussion focuses on the literature about underground-soil-aboveground structures the text contents are more fragmented and definite statements are difficult to express. This is partially due to a shortcoming on the part of the author, on the other side some observations are due: this is a quite new research field, in fact nearly all the papers related to this topic have been published in the last twenty years, all of them stating the importance of considering the interaction effects for seismic design purposes. However, the problem has been addressed by investigating the effects of underground structures on buildings, or vice versa, using different tools: experimental campaigns with centrifuge or shaking table; numerical experiments with FDM or FEM, in 2D or 3D conditions. The soil has been modeled as viscous-linear elastic, elastic-perfectly plastic (Mohr Coulomb), or, rarely, non-linear elastic-plastic material, leading to results not always comparable since effect of plasticity can significantly influence SSSI. Moreover, different kinds of structures and soil conditions are treated and, most important, the studies present in output diverse parameters (displacements, stresses, accelerations, frequency content, relation between seismic input and soil response, interstory drift, base shear forces), and the amplification ratios used to characterize the effect of considering SSSI are greater or less than unity depending on many factors including distance from the disturbance and frequency content of the input. All this makes it very complicated to summarize the findings by giving design suggestions and paves the way to further investigation. In Table 2 a summary of the existing literature about the effect of underground structures on aboveground ones, and the methods applied to study it, is reported.

Table 2. Summary of literature on underground-soil-aboveground structures

Paper	*Structure type*	*Method/soil behavior*	*Burial depth (m)*	*Depth (m)*	*Width/Radius (m)*	*Output*	*Varying parameters*
Mo & Hwang, 1997	open pit*,**	FEM 2D non-linear elastic	-	13.9	31.2	building's roof displacements	Depth of excavation, material properties
Castaldo & de Iuliis, 2014	open pit*,**	FEM 2D non-linear elastic plastic (HS model)	-	27	24	interstory drift, ductility demand	presence of excavation
Yeganeh et al., 2015	open pit*,**	FDM 2D elasto-plastic (Mohr Coulomb)	-	12.5	-	base shear force, interstory drift, settlement profile at the ground level	presence of excavation, type of structural model
Youta Mitra et al., 2007	circular tunnel	FDM 2D linear viscous-elastic	not specified	1R-7R	5-20	ground displacements	burial depth, diameter, frequency content, relative flexibility
Moghadam & Baziar, 2016	circular tunnel	Shaking table + FDM 2D linear viscous-elastic	2-12	-	8	PGA	dimensionless period, embedment depth, flexibility ratio
Wang et al., 2018	circular tunnel**	Shaking table	2	10	-	peak acceleration and frequency content	characteristics of the input
Miao et al., 2020	circular tunnel**	Shaking table + FEM 3D non-linear elastic plastic (Davidenkov)	5-30	14	22.4	interstory drift of the buildings	burial depth, location of buildings, number of stories and of buildings
Baziar and Moghadam, 2014	rectangular tunnel	Shaking table + FDM 2D elasto-plastic (Mohr Coulomb)	10	7.4	10.7	peak acceleration, peak frequencies	input PGA
Abate & Massimino, 2016a	horseshoe tunnel**	FEM 2D linear viscous-elastic	18	11	7	acceleration in time and frequency domain	configuration of the system (4 models)
Abate & Massimino, 2016b	horseshoe tunnel**	FEM 2D 2D linear viscous-elastic	12 - 18	11	7	acceleration in time and frequency domain	input, depth, horizontal distance building-tunnel
Wang et al., 2013	box culvert**	FEM 3D linear viscous-elastic	2	12.5	21.2	base shear force, amplification of acceleration (vs free field)	location of buildings, input frequency content and direction, shear wave velocity, damping, burial depth, stories number
Guo et al., 2013	box culvert**	Interstory drift spectral analysis 2D elasto-plastic (Mohr Coulomb)	2	12.4	-	Interstory drift	distance between buildings and station, fundamental period of buildings
Abuhajar et al., 2015	box culvert	Centrifuge+FDM 2D	7.7	4.7	4.7	PGA, acceleration amplifications	culvert thicknesses, soil densities, input characteristics
Sun et al., 2019	box culvert	FDM 2D 1. linear viscous-elastic, 2. non lineare-viscous elastic	4.8	7.2	17	PGA,spectral ratios, Housner intensity, peak shear strain	dimensionless distance, dimensionless period, shear wave velocity, section dimensions
Isari et al., 2021	box culvert	FDM 2D hysteretic damping model	4.8	7.2	17	PGA, vertical acceleration profiles, frequency content	thickness of the central column of the station

Cheng et al., 2023	box culvert**	Shaking table	3	15	27	peak acceleration profiles, modes of vibration	input, configuration of the SSSI system
Hong et al., 2025	box culvert**	Shaking table	6	21.24	23.94	acceleration in time and frequency domain	configuration of the SSSI system, frequency content of the input

**excavation stages simulated, **buildings included in the simulation*

Chapter 3

Chiaia station case study

3.1. Description of the case study

The case study presented in this chapter refers to the construction of *Chiaia* station realized between 2009 and 2017, preceded by two investigation campaigns for the geotechnical characterization of the excavation site. *Chiaia* is part of Line 6 of Napoli's public transport, the most recently completed metro line (it was opened in July 2024).

3.1.1. Line 6 of Napoli underground

The project of Line 6 originated in the 1980s under the name LTR (*Linea Tranviaria Rapida*) and stemmed from a project developed for the 1990 football world cup. The project involved the construction of a metro-tram line, with characteristics halfway between a tram and a classic underground railway, which would have crossed the city from east to west, namely from *Fuorigrotta* to *Ponticelli*, passing through the city center (*Municipio* Square). The section was completed in time for the world cup, but technical problems prevented it from opening.

The project was shelved until 2002, when work resumed, albeit limited to the western section. The idea of a metro-tram was also abandoned, and the project was modified to a light metro, entirely underground, as defined by the UNI UNIFER 8379 standard. Line 6 can be considered a subsystem divided into two parts built in different periods with geological and site conditions rather variable along the path (*e.g.*, water table), which led to diverse solutions for the excavations:

- First the *Mostra-Mergellina* section was realized. It is 2.2 km long with four stations (*Mostra, Augusto, Lala, Mergellina,),* two of which are interchange hubs: at *Mostra* it connects with Line 2 and Line 7, and at *Mergellina* with Line 2.

- The *Mergellina-Municipio* section is approximately 3.3 km long, in addition to *Mergellina* it includes 4 other stations: *Arco Mirelli, San Pasquale, Chiaia, Municipio*. The terminus station, *Municipio*, is an important interchange hub with Line 1 and the port where connections to the islands depart.

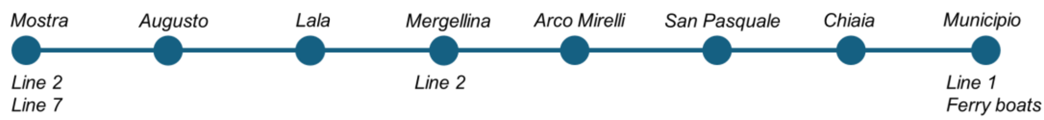

Figure 32. Stations of Line 6 and interchange hubs.

From a geological point of view the city is located in the Campanian Plain, a deep graben filled with pyroclastic and alluvial deposits associated with frequent marine and marsh deposits. Furthermore, its geology and geological structure have also been influenced by the tectonic processes and volcanic events of the Phlegraean Fields and Somma-Vesuvius. The morphological element Naples was built on, is Neapolitan Yellow Tuff (NYT), covered by pyroclastic layers and fill material. The subsoil of the south-western part of the city has a complex structure, the result of many geological and volcanic vicissitudes, which has been overlaid by human activity over the centuries. The area interested by the route of Line 6 can be divided into four homogeneous zones:

- *Fuorigrotta* plain
- *Posillipo* hill
- Coastal arc from *Mergellina* to *san Pasquale*
- *Pizzofalcone* hill, where Chiaia station is located, and the subsequent stretch up to *Municipio*.

In the *Fuorigrotta* plain, the works involve mainly loose pyroclastic products (pozzolans, pumice, sand) of Phlegraean origin; in terms of altitude, the route is located a few meters above the free surface of the water table. The section below the *Posillipo* hill to just beyond *Mergellina* station, affects the lithoid tuff formation above the water table and only in the final part it passes through loose materials below the water table. The section from *Mergellina* to *san Pasquale* mainly involves loose soils of pyroclastic origin (pozzolans, pumice, sands). The most superficial layers are reworked by water and sedimented in a marine environment. Near the surface there are anthropic fill materials, with thicknesses reaching up to about 10 m.

Both the pyroclastic soils and the fill materials are characterized by a medium-high degree of compaction and medium or high permeability. The loose soil mass is bounded at the bottom by a substrate of lithoid tuff with rather variable permeability. In the section between *Arco Mirelli* and *san Pasquale* stations, the roof of the tuffaceous substrate has a top elevation that reaches 6 m above sea level (asl). In this area, the line tunnel affects the tuffaceous formation for a certain distance. The ground surface is flat and lies a few meters above mean sea level; therefore, the free surface of the water table, located at an elevation of 1÷1.5 m asl, is found at a shallow depth. In this area, the tunnel and stations are located below the water table.

Figure 33. Excerpt from the geological map of Napoli (sheet 187). Yellow circles indicate the location of the station mentioned in Figure 32.

Finally, the section from *san Pasquale* to *Municipio* again affects the lithoid tuff formation. The tunnel initially climbs up to *Chiaia* station (*Pizzofalcone* hill), where it is still completely immersed in the water table (+ 3÷4 m asl), and then continues slightly downhill to *Municipio* station.

3.1.2. Geotechnical characterization

Chiaia station has been excavated starting from *Santa Maria degli Angeli* square, located at an elevation varying between +40.2 m asl, at the access point to the square from *Nicotera* Street, and +37.4 m asl, at the access point from *Gennaro Serra* Street (see Figure 34). Three investigation campaigns were carried out in the area, the first dating back to 2005, followed by two additional campaigns in 2007. During the campaigns 21 boreholes were executed along the perimeter of the station and inside the supposed excavation area (their locations are represented in Figure 34), 6 of which were integrated with standard penetration tests (SPT). Lugeon permeability tests were also performed within the boreholes showing that the maximum permeability values are on the order of 10^{-6} m/s. The highest values vary in the rage 2-4 × 10^{-6} m/s, and the geometric mean of all available values is slightly less than 0.9 × 10^{-6} m/s. The boreholes show an irregular stratigraphy and a non-horizontal NYT top boundary; it must be mentioned anyway that not all of the boreholes reached the tuff. In Table 3, depth and elevation of NYT top boundary are reported for the boreholes that reached it. The stratigraphy, quite variable until the depth of NYT, has been summarized in three main layers with geological and geotechnical features fairly homogeneous, represented in Figure 35. The figure shows the soil stratigraphy consisting of a series of pyroclastic deposits with geological and geotechnical characteristics typical of the urban area of Napoli and its surroundings (*e.g.*, Pellegrino 1967; Picarelli *et al*. 2007): the top thin layer consists of a few meters of sandy artificial ground (layer A); some intermediate layers of pyroclastic silty sands alternating with levels of ashes and pumices and a base layer consisting of the NYT formation subdivided in two different facies: an upper unlithified, commonly referred as NYT pozzolana (merged, in the stratigraphic model, with the above sandy layer B), and a bottom lithified facie which consists of the soft rock identified as Neapolitan yellow tuff (layer C).

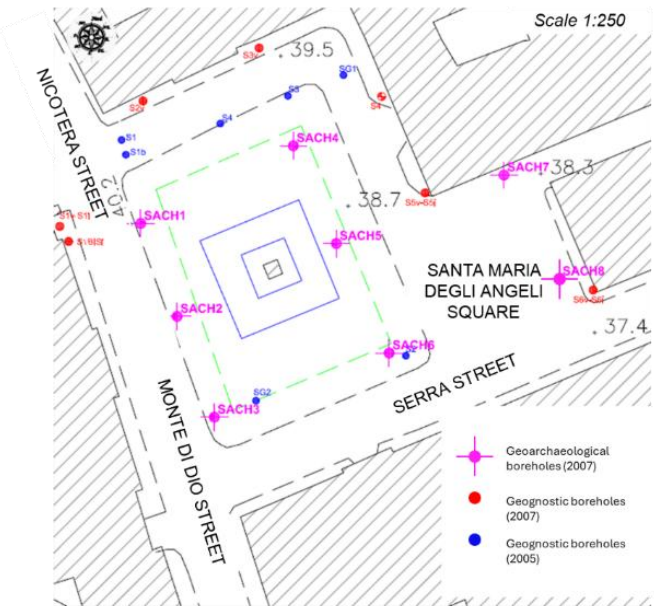

Figure 34. Plan view of the station and location of boreholes.

As deduced from the boreholes, the elevation of the NYT top boundary is located between +25 and +16 m asl (contour lines of tuff elevation are reported in Figure 36). Twenty tuff samples were retrieved and subjected to uniaxial compression tests and tests for the determination of unit weight. In Figure 35 the Unconfined Compression Strength (UCS) of the NYT specimens and N_{SPT} for the upper sandy layer are reported. The SPT blow count, as expected, shows a certain variability, but overall testifies an increasing trend. UCS, in contrast, show a slight decrease with depth.

Table 3. Elevation and depths of NYT top boundary reconstructed by boreholes

Borehole	Ground level elevation	Depth top boundary NYT	Elevation top boundary NYT
	m asl	m bgl	m asl
		Campaign 2005	
S1bis	35	16	24
S2	26	21.5	16.5
SG1	27	17	23
SG2	22	22.5	17.5
		Campaign 2007 I	
S1v	40.5	15.5	25
S2v	40	15.5	24.5
S3v	39.5	20.7	18.8
S4v	39	22.5	16.5
S5v	38.5	22.2	16.3
S6v	37.5	21.5	16
		Campaign 2007 II	
SACH1	40.2	16.8	23.4
SACH2	40.3	18.5	21.8
SACH3	40.5	17.1	23.4

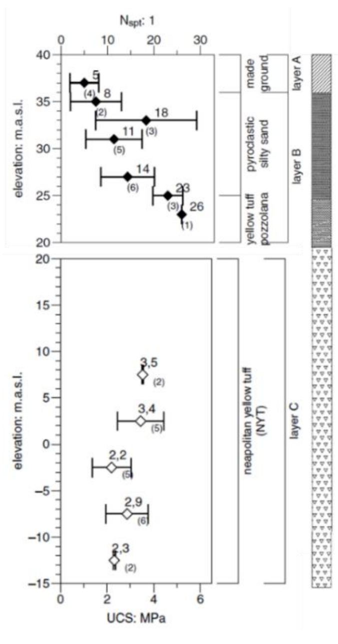

Figure 35. Standard penetration tests and UCS lab tests of soil samples, by sampling elevation.

3.1.3. Structural aspects and monitoring instruments

Chiaia station is placed in a complex urban context which has determined different design choices, among them the depth and the unusual shape of the station plan. Figure

36 is a plan view of the square where the excavation began. It is bordered on the four sides by masonry buildings: a school on the north side, two residential buildings (E11 and E11A) on the east side, an ancient Basilica on the west, dating back to the XVII century, and the Military Court, south of the square. It must be mentioned that the school building doesn't have its foundations at the elevation of the square, because the building continues below, and it is founded on *Chiaia* Street, whose elevation is +25 m asl (15 m lower than the square). The existence of this particular condition means that the wall of the excavation on the north side doesn't receive any pressure because there is no soil in the back. Another peculiarity, which made necessary locally modify the anchorage system, is the presence, on the same side, of *Chiaia* bridge and of the foundations of an elevator connecting *Chiaia* Street and *Santa Maria degli Angeli* Square.

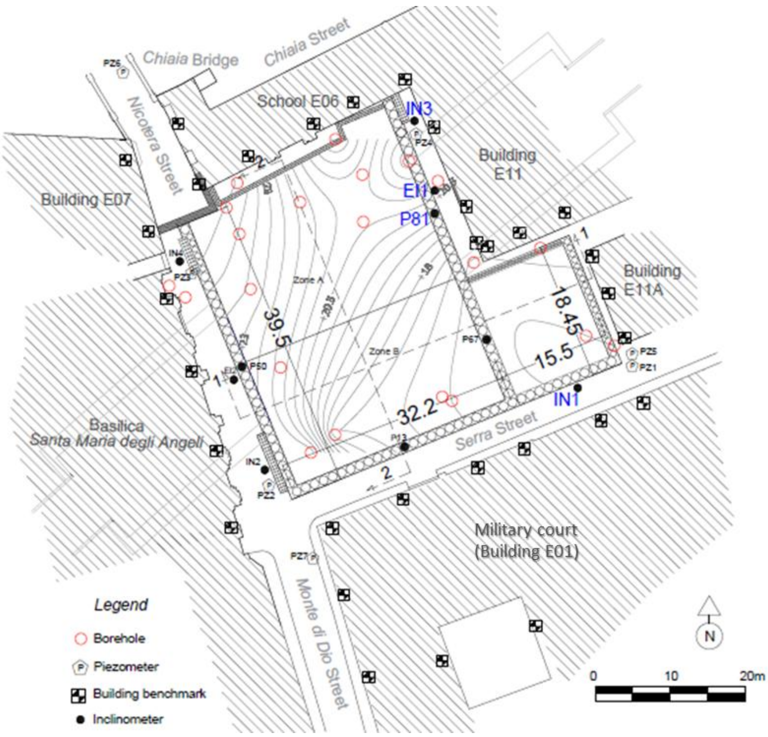

Figure 36. Plan view of the station, location of the in situ investigations, and elevation contours of soft bedrock NYT in m asl (Russo et al., 2024).

The excavation, whose plan view is reported in Figure 36, is composed by two nearly squared open pits: the main pit, with dimensions 32.2×39.5 m^2 and 48 m deep, and the adjacent access shaft, 18.45×15.5 m^2, 21 m deep. The great and unusual depth of the station is due to the necessity of connecting the pit with the tunnel already excavated

with TBM (Fabozzi *et al*. 2017; Bilotta *et al*. 2017), whose axis approximately coincides with the water level, this is the reason why a double entrance to the station is provided: from *Santa Maria degli Angeli* Square and from *Chiaia* Street.
The main excavation sides are sustained by contiguous pile walls installed before the excavation began. The piles have diameters of 800 and 1200 mm and lengths between 16 m and 23 m, on three out of four sides of the main shaft (see sections 1-1 and 2-2 in Figure 37); in front of the school micro-piles were realized, instead. Since the excavation first passes through the sandy layer and then descends approximately 30 m into rock (NYT), the contrast system has been differentiated. In sands, tieback anchors were installed on the walls of the main shaft as the work proceeded, while in tuff no additional support was provided and only rock bolts were installed to prevent detachments. Due to the non-horizontal stratigraphy, the anchorage system is composed of three or four levels of pre-stressed anchors, depending on the thickness of the loose soil (Figure 37).

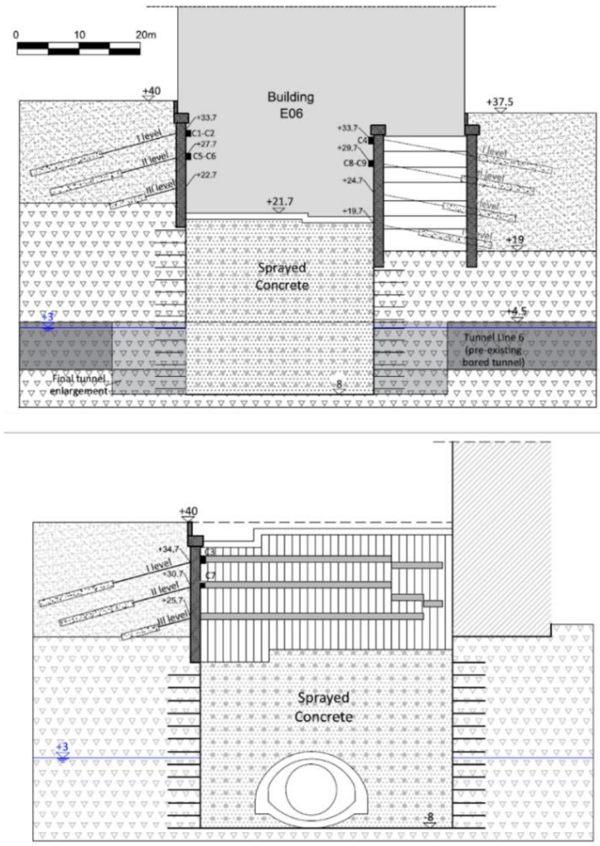

Figure 37. Sections 1-1 (figure above) and 2-2 (figure below) (see Figure 36).

Along the school side (Building E06) clearly no anchors were installed; moreover, near the school, due to the foundations of the elevator and those of Building E11, it was impossible to realize the first level of anchors that were substituted with two steel props 30 m long with a diameter of 1000 mm and a thickness of 12 mm. The props and the connection beams of the tie-back anchors are visible in Figure 38.

Figure 38. Pictures taken during excavation.

Lastly it is worth mentioning three anthropic cavities interfering with the excavation, whose existence affected the execution of the work, requiring the adoption of a particular sequence in the excavation stages, mainly consisting of the early excavation of Zone B and a later excavation of Zone A (Figure 36). A large cavity (number 1 in Figure 39), not known before the start of the excavation, with a bell-shaped section with the floor level at elevation +6.70 m asl and the vault ridge at an elevation of +21 m asl, was found next to foundation of the Chiaia bridge during the execution of borehole S1. The other two cavities were registered, instead, and they consist of: an irregularly shaped cavity (number 2 in Figure 39) occupying the central part of the station main pit, just south of the school building; the footing of this cavity was at an elevation ranging from +6.00 to +7.00 m asl, and the vault was at an elevation of +18.00 m asl; a smaller cavity interfering with the east side of the station platform tunnel (3 in Figure 39), with the footing at an elevation of about +5.00 m asl and the vault at an elevation of +12.00 m asl.

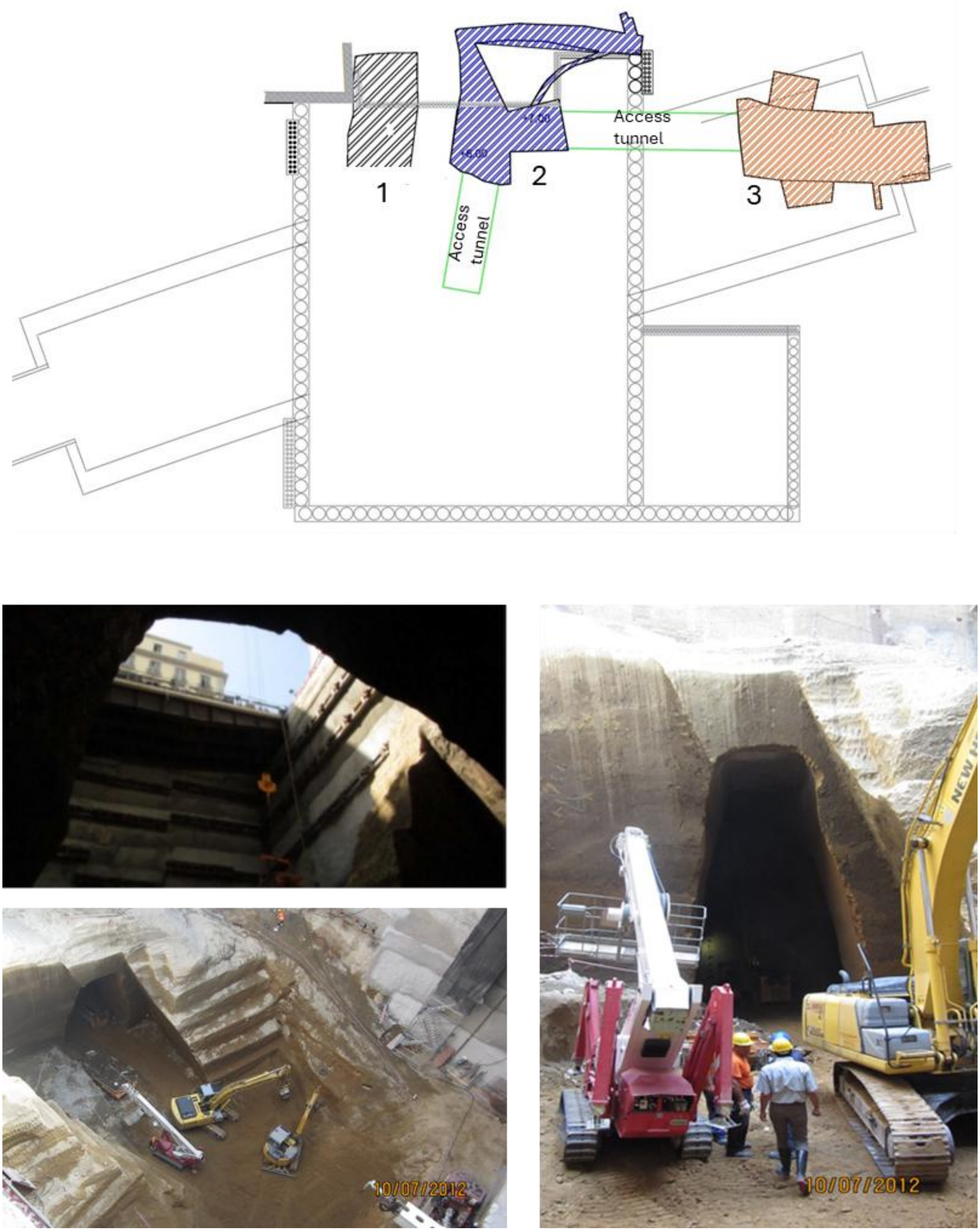

Figure 39. Above: plan view of the station with the indication of anthropic cavities, and below: pictures of the cavities interfering with the work.

Due to the proximity of buildings all around the station (average distance of about 4 m from the edge of the shaft) – some of these are of historical and artistic interest – a variety of monitoring instruments were installed to control displacements and stresses (their location is reported in Figure 36):

- Benchmarks on buildings and sidewalks for optical levelling
- Inclinometers embedded into the soil up to a depth of 50 m
- Inclinometers installed into the piles
- Piezometers (to control the effect of the water table draw-down)
- Load cells at the point of attachment of pre-stressed tie-back anchors

A summary of the installed instrumentation is in Table 4. The monitoring activities went on during all the duration of the work and after, for a couple of years.

Table 4. Summary of instrumentation

Instrument	Total number	Depth/Length/ elevation (m)	Average Frequency	Monitoring period
Inclinometers in the piles	4	20	1/week	9 years
Inclinometers in the soil	6	50	1/week	9 years
Load cell	10	I – II level Variable depth	4/day	9 years
Benchmarks on buildings	32	2.5 m above the ground surface	2/week	9 years
Benchmarks on sidewalks	32	0.3 m below the ground surface	2/week	9 years
Piezometers	7	50	1/week	4 years

It is worth noticing that measurements of displacements on buildings do not significantly differ from those retrieved by benchmarks on sidewalks, therefore in the following no distinction will be made between the two sets of readings.

3.1.4. Work stages

For what concerns the actual sequence of the work, it has been carried out with a bottom-up procedure alternating excavation stages and installation of anchor levels during the excavation phase, then, once reached the bottom of the excavation, impermeabilization membrane was installed and internal structures were built. After the installation of pile walls, the chronological sequence in which the work was carried out is reported in Table 5. The monitoring system was kept in place for 9 years and some data are reported versus time in Figure 40 where the main stages of works can be recognized.

Table 5. Sequence of work carried out.

Stage	Duration	Excavation depth (main shaft)	Other works
1	05/05/2009 - 23/04/2010	4 m (archaeological excavation)	Excavation of access shaft (depth = 21m)
2	24/04/2010 - 22/04/2011	8 m	Construction of internal walls of access shaft
3	23/04/2011 - 24/06/2011	10 m	Installation and tensioning of 1st level anchor rods and struts
4	25/06/2011 - 23/09/2011	-	Installation and tensioning of 2nd level anchor rods
5	24/11/2011 - 30/03/2012	21 m	Installation and tensioning of 3rd level anchor rods
6	31/03/2012 - 08/03/2013	35 m	Installation and tensioning of 4th level anchor rods and water level draw-down, tunnel segment demolition
7	09/03/2013 - 29/11/2013	48 m (End of excavation)	Realization of the foundation and of the station platform
8	30/11/2013 - 12/12/2016		Shutdown of the drainage pumps, removal of temporary struts, de-tensioning of anchor rods, realization of the internal walls, completion of internal structures.

The environmental temperature with nearly 8 full-year cycles and some residual measurements covering the last 2 years as a long-term check is reported in Figure 40a. The excavation depth in the main shaft reached its maximum value (- 48 m bgl) in the first half of 2014. The accession shaft was excavated first, and the main shaft was excavated following slightly different schedules for the northern part (Zone A) and the southern part (Zone B) represented in Figure 36. Casagrande piezometers, installed outside the excavation, monitored the water level before, during, and after the dewatering stage. During dewatering the water level was maintained slightly below the bottom of the excavation. There was an evident influence of distance, *i.e.*, the farther the piezometer, the lower the water table level reduction (see Figure 40c). When the pumps were stopped, the water level quickly returned to its undisturbed original value (about +3.5 m asl).

Horizontal displacements versus time are also reported in Figure 40d: inclinometers will be treated in more detail later, given that their measurements have been used as a benchmark for the back-analysis. Lastly, settlements of all the monitored buildings are

reported in Figure 40e and f, where a black line marks the average value, clearly affected by effect of temperature cycles.
The excavation was completed during the first half of 2014 and, in fact, the biggest part of vertical displacements are exhibited by the half of 2014; the station structures, instead, were completed by the end of 2015; finishing installation took until 2017. During those years monitoring went on, showing an increase of subsidence even after the end of excavation, probably due to creep phenomena. Differences between *end of excavation* and *end of observation* (last reading in 2019) are not insignificant and a comparison between the values is reported in Figure 41. The highest values of vertical displacements are recorded at the military court (Building E01) close to the center of the building façade overlooking the excavation. It also has the highest differential settlements, as will be shown in next section. The buildings with the minimum average settlement, about 5–6 mm, are E06 and E07, located on the north side of the shaft, and both have their foundations deeply buried at the level of the tuff bedrock or very close to it. Lastly, the stresses in the prestressed anchors were monitored until the end of construction using load cells installed in the first two levels of anchors. The loads are plotted over time for two anchors in the first and second levels (Figure 42). The cutting of the anchor tendons occurred on different dates as the internal structural box of the station was progressively built.

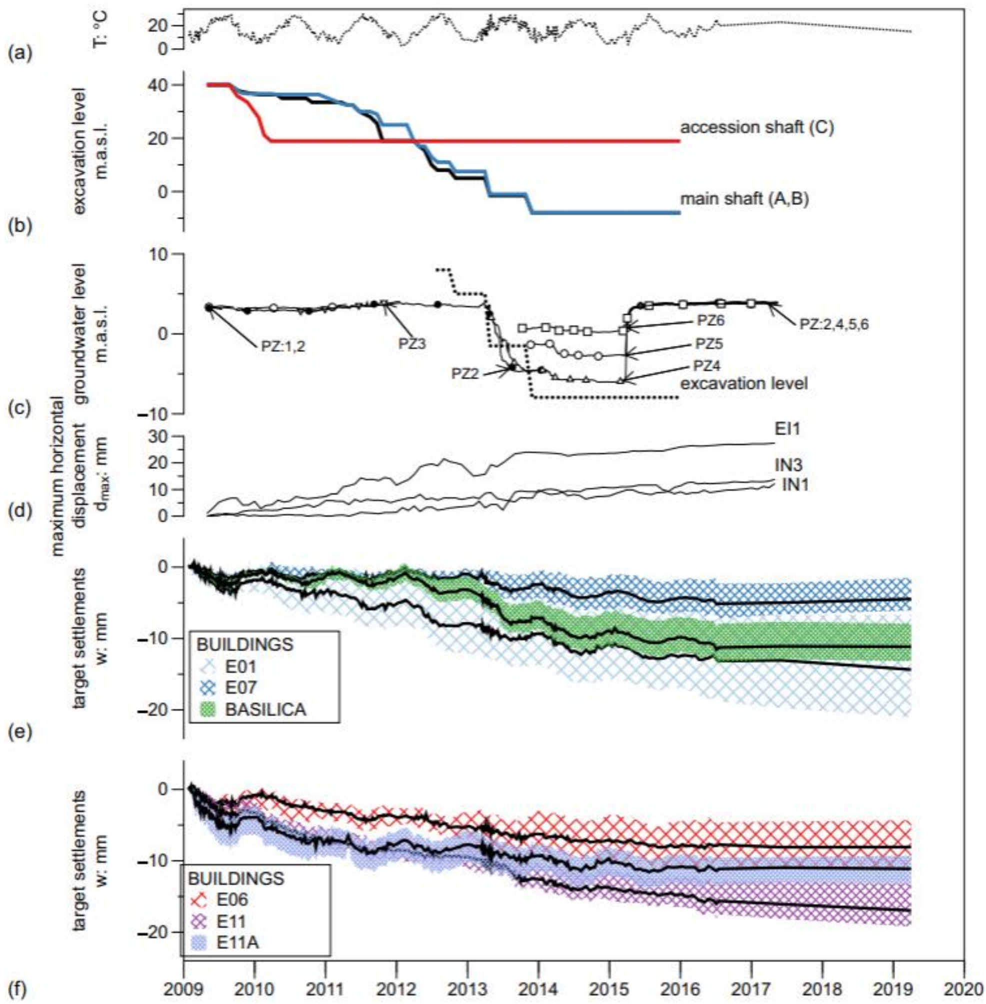

Figure 40. Measurements versus time: (a) temperature; (b) depth of the excavation; (c) groundwater table; (d) horizontal maximum displacement in several inclinometer pipes; and (e and f) settlement measured at the building benchmarks versus time (Russo et al., 2024).

As expected, the ground anchors of Level 1 (*i.e.*, the shallowest level) carried a lower load than the ground anchors of Level 2 depending on the estimated earth pressure at different depths. The two anchors of Level 2 on the side of Building E11 were set up with a lower prestress than the other anchors on Level 2 because Building E11 has a two-level basement, and as a consequence the earth pressure on the diaphragm wall was lower than that on the other sides of the excavations. In general, the anchor loads remained nearly constant and were equal to the imposed design prestress even with the downwards progress of the excavation, as already observed by Russo and Viggiani

(1998), Fenelli and Ramondini (1997), Zhu *et al*., (2022), among others, for the case of ground anchors with a relatively low axial stiffness compared with the high bending stiffness of the diaphragm wall.

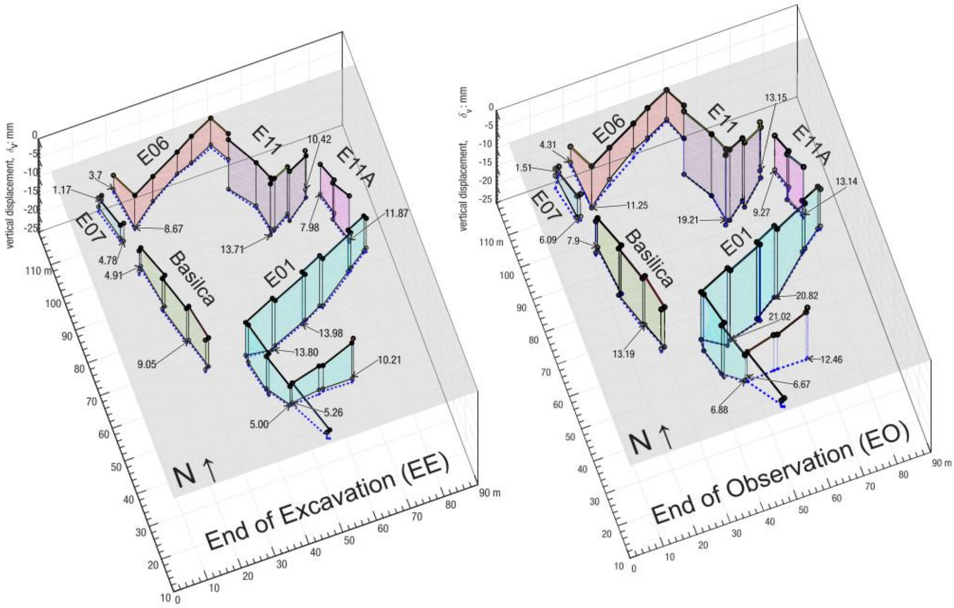

Figure 41. Axonometric view of the building façade footprints and the corresponding settlements at the end of excavation and at the end of observations (Russo et al., 2024).

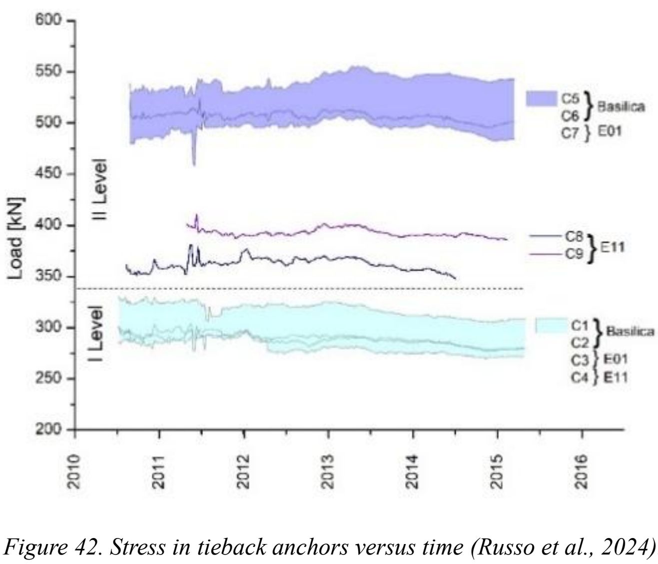

Figure 42. Stress in tieback anchors versus time (Russo et al., 2024).

3.2. Static back-analysis

The back-analysis was carried out on FE software Plaxis 3D Ultimate 2022. The model has dimensions 140×90×70 m^3 and it is composed of 146880 10-node tetrahedral elements and 250564 nodes. On the model boundaries, far enough from the excavation to make its effect to fade away within the model, normal fixities were imposed (*i.e.*, only displacements out of plane are constrained). The numerical model is represented in Figure 43. On the northern side of excavation, the model boundary coincides with the side of the main shaft. The boundary, in fact, is placed in correspondence with the discontinuity in the ground surface elevation already mentioned in section 3.1.3. The choice, driven by the consideration that on that side no interaction between soil and retaining structures would occur since only the lower stories of Building E06 are present, among different alternatives allowed a better control of the movements and stresses computed on this side of the model, taking into account the fact that the earth pressure on the opposite site (*i.e.*, the side of Building E01) along Serra Street during the excavation was absorbed independently by the four levels of ground anchors.

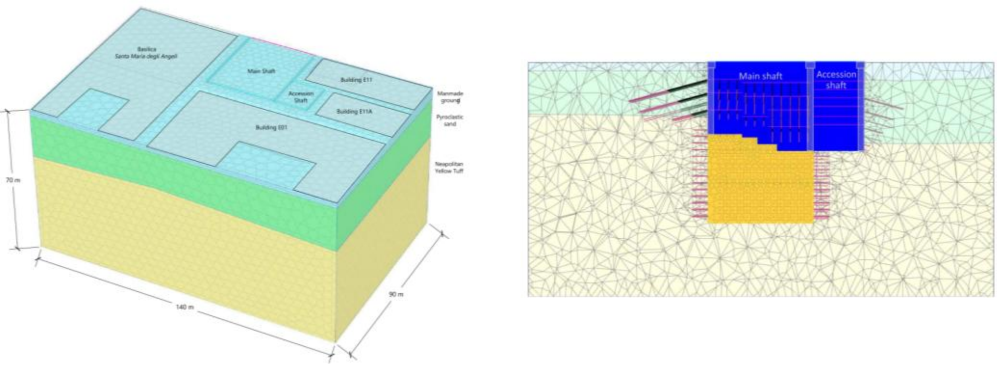

Figure 43. Left: FEM model perspective view of the excavation shaft of the Chiaia Station; right: section of the model with activated structures (Russo et al., 2024).

3.2.1. Choice of the constitutive model and soil characterization

The stratigraphy reproduced in the model is derived from the available soil characterization previously illustrated in this chapter. Three layers of soil were described in the model: manmade ground (0-4 m bgl), pyroclastic sands and NYT. The non-horizontal tuff surface, whose elevation varies between +16 and +24 m asl, was reproduced in the model with the definition of boreholes according to data reported in Table 3. The well-known Hardening Soil (HS) model (Schanz *et al.*, 1999) was chosen to model sandy layers. It is a constitutive model implemented in Plaxis 3D, particularly suitable for describing mechanical behavior of dry sands during excavation processes. It is a hardening elastoplastic model with a stress dependent law governing the evolution of stiffness with stress state.

$$E = E_{ref}\left(\frac{c \cdot cos\phi - \sigma'_3 \cdot sin\phi}{c \cdot cos\phi + p^{ref} \cdot sin\phi}\right)^m \qquad (29)$$

E_{ref} is the generic stiffness modulus at the reference pressure p^{ref} that has been set equal to 100 kPa. Exponent *m* has been set equal to *0.5*, that is a value suitable for sands when no more detailed information is available.

The model is characterized by three strength parameters (cohesion c', friction angle ϕ' and dilation angle ψ) and three elastic moduli: oedometric modulus E_{oed}, secant modulus at 50% of deviatoric stress ultimate value in a triaxial path, E_{50}, and unloading-reloading modulus E_{ur}, which allows to differentiate the stiffness of soil during a first-loading path from that of an unloading-reloading path. Because of the scarcity of in situ tests, in this case E_{50}^{ref} was calculated based on SPT data, E_{oed} was set equal to E_{50}^{ref}, and E_{ur} equal to $3E_{50}^{ref}$.

The only tests available on NYT were UCS carried out on samples taken at different depths (Figure 35). Archive data in terms of initial stiffness E_0 and UCS were compared with the field data available in *Chiaia* site. Because of the similarity emerged from the comparison, some results from archive data were considered valid for the site of *Chiaia* as well. Therefore, the strength of the Chiaia tuff was described by means of the Mohr–Coulomb strength envelope plotted in Figure 44; in particular, a friction angle value equal to that derived from the archive tests (φ = 29.82°) and a cohesive intercept (c = 825 kPa, calculated as $\sigma_c/2\sqrt{k_p}$), based only on the values of the uniaxial compressive strengths measured in the Chiaia samples, were adopted. The modulus E_0 of the NYT formation was assigned with a range of 1–2.5 GPa derived by considering the E_0–UCS relationships obtained by local strain measurement and the UCS data limited to the tuff samples of the *Chiaia* station.

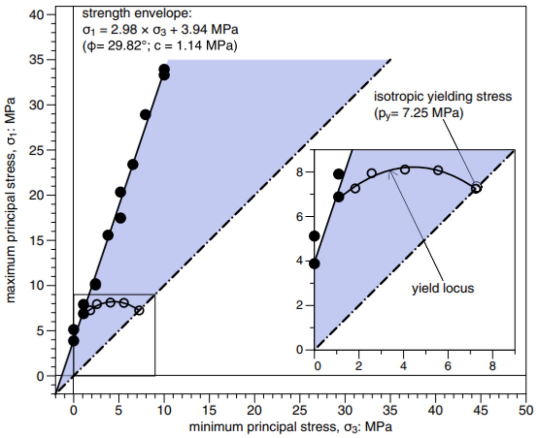

Figure 44. NYT strength envelope and yield locus (Russo et al., 2024).

Figure 44 individuates the *locus* in principal stress plane, where the behavior of NYT is essentially elastic. This makes it possible to significantly simplify the constitutive model adopted for the description of NYT when the state of stress is expected to fall into the yield locus, which is the case for the problem of interest. Therefore, Neapolitan yellow tuff has been modelled with elastic perfectly plastic Mohr-Coulomb's constitutive model. The main mechanical parameters adopted for the three layers are reported in Table 6.

Table 6. Main soil properties deducted by site and laboratory investigations.

Layer	Depth	Unit weight	c'	ϕ'	E'_{ref}	E_{ur}^{ref}	E_{50}^{ref}	E_{oed}^{ref}
	m	kN/m^3	kPa	°	GPa	MPa	MPa	MPa
A (superficial sand)	0-4	18,00	0	36	-	90	30	30
B (pyroclastic silty sand)	4-16/20	16,00	0	36	-	90	30	30
C (NYT)	>16/20	16,00	825	29.82	1.0-2.5	-	-	-

3.2.2. Modelling of structural elements

The 50 m deep pile walls of the main shaft and those, shallower, of the access shaft were reproduced in the numerical model with orthotropic linear elastic plate, with two equivalent stiffnesses, E_1 in the longitudinal direction and E_2 in the transverse direction, which were determined considering the spacing and the diameter of the bored piles connected at the head by a top belt beam, with the longitudinal direction of piles characterized by higher stiffness (E_1), more details about the procedure of stiffnesses calibration can be found in *Appendix 1*. Prestressed anchors were modeled as node-to-node anchors for the free length portion, and as embedded beams for the grouted part, where a pullout force T_{skin} must be defined to characterize the properties of soil/concrete interface. The steel props close to the ground surface were modeled as elastic beams, and the steel bolts grouted in the tuff were modeled as embedded beams. Table 7 summarizes the geometrical and mechanical features of the retaining structures. Among the simplifications introduced in the numerical analysis, the building considered in the model are E11, E01 (Military Court) and the ancient Basilica of *Santa Maria degli Angeli*. To consider the stiffness of buildings, without modeling the entire structure, orthotropic plate elements with equivalent thickness have been adopted. The weight of the buildings, applied as uniformly distributed load on the plate, was estimated from the number of floors and thickness of the masonry walls (made of NYT bricks). The stiffness was estimated by relying upon the major role of the masonry walls parallel to the excavations and adopting the suggestions of Pickhaver (2006) as modified by Netzel (2009), which essentially consider the masonry wall stiffness in bending and shear, reduced to take into account the openings. In this case, the *L/H* ratio of the masonry walls considering the overall development of the buildings is very close to, or larger than, the critical value of 3, and thus the equivalent stiffness is dominated by the amount of the openings. The reduced inertia of the equivalent elastic plate was obtained by considering a reduced height H very close to the net height of the walls that are not affected by the openings. The main properties assigned to structural elements are summarized in Table 7 and more details on the adopted procedure are reported in *Appendix 1*.

Table 7. Diaphragm walls, tieback anchors, tuff bolts and building equivalent plate properties.

Structure	Model	E_1	E_2	Thickness,	T_{skin}	Prestress	Load
		GPa	GPa	m	kN/m	kN	kPa
Diaphragm wall 1200	Plate	36.5	0.365	0.94			
Diaphragm wall 800	Plate	36.5	0.365	0.63			
Diaphragm wall 250	Plate	36.4	0.364	0.50			
Top belt beam	Beam	31	31	1-1.96			
Ground anchors	Beam	25	25	0.14-0.2	90-105	280-860	
Rock bolts	Beam	205	205	0.026	185		

Basilica plate	Plate	3	3	6	120
Building E01	Plate	3	9	8	130
Building E11	Plate	3	9	7	70

3.2.3. Numerical analyses

During the calculation the excavation sequence described in previous sections was reproduced as accurately as possible. After the initial phase, where initial stress state is calculated (with a k_0 procedure), plates and surface loads used for buildings' modelling are activated first, and then pile walls as wished in place, which implies disregarding the possible effect of installation on the surrounding assuming that at the distances of buildings' façades they have no significant influence (L'Amante *et al*., 2012). After that, the stages described in Table 5 have been split into 18 calculation phases where soil removal is followed by installation of anchors at the reached depth. Since the recorded displacements are small, and in the first stages of excavation they are close to the instrument sensitivity, attention was dedicated to the last stages, when displacements are bigger and easier to interpret and reproduce. Namely, referring to Table 5, attention will be paid to Stages 5, 6, 7 (stage 8 is not included in the back-analysis). The analyses carried out are three, they differ from each other for the approach of modelling buildings and for the properties assigned to the tuff: details are reported in Table 8.

Table 8. Differences among the cases analyzed with FE model.

Analysis	Buildings	$E'_{ref,\ NYT}$
Case 1	Surface loads	1 GPa
Case 2	Surface loads	2.5 GPa
Case 3	Surface loads + plate (stiffness considered)	2.5 GPa

In Case 1 the stiffness of NYT was set equal to the lower bound value deduced by archive data, however the comparison with inclinometer measurements indicated that the stiffness modulus should increase, thus in Case 2 it was set equal to the highest value of the experimental range, *i.e*., 2.5 GPa. The horizontal displacements extracted in the locations corresponding to those of IN1, IN3, E11 and P81 (Figure 36) by Case 2 perfectly overlapped with those of Case 3 analysis, certifying that the influence of the stiffness of the buildings on the horizontal measured displacement was negligible.
The displacement profiles measured by inclinometer IN3 in each stage are reported in Figure 45 and compared with the corresponding calculation results. Case 1, Stage 7

(continuous black line) significantly overestimated the measured horizontal displacement at the tuff level. The profiles calculated in Case 2, with a stiffer NYT layer for all three relevant selected stages, provided a better match with the corresponding profiles measured from the bottom of the pipe to the top boundary of the tuff layer, here located at about +18 m asl. The better agreement of Cases 2 and 3 confirms the validity of the selection of the higher stiffness of the NYT. In the shallow sandy layers, Stage 6 of Cases 2 and 3 had very good overall agreement, whereas in Stage 7 there were differences, although they were within a few millimeters on inclinometer, the overall length of which is about 55 m. Similar comparisons of observed and computed displacement profiles are plotted in Figure 46 and Figure 47 with reference to Inclinometers EI1 and IN1. For the sake of completeness in these figures, the calculated profiles for Cases 1 (reported only for Stage 7) and 2 are reported, confirming that profiles from Case 2 better reproduce the measured displacements. Inclinometer IN1 was located in front of the small and shallow access shaft, the maximum excavation level of which was about +19 m asl, therefore it is much less affected by the main excavation. Even for these 55-m-deep inclinometers, the horizontal measured displacements, with a maximum value in the range 1–2 cm, were rather small and very close to the known range of precision of an inclinometric measurement.

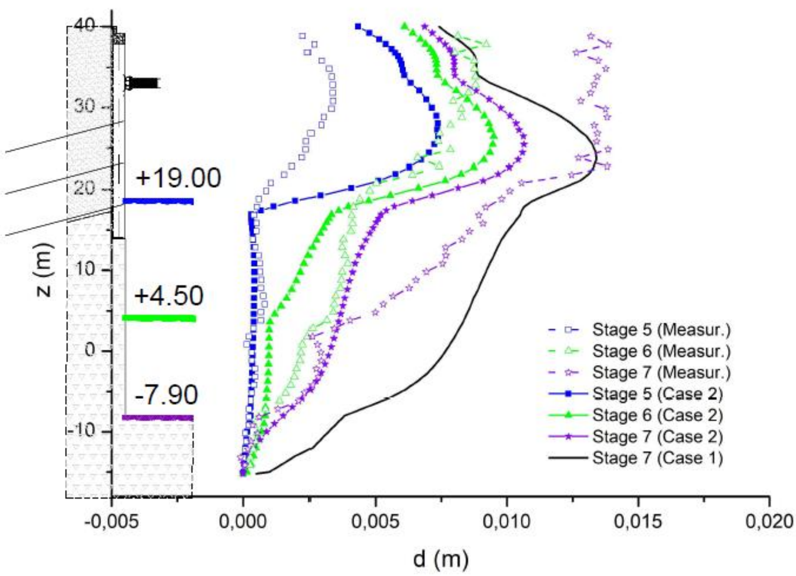

Figure 45. Calculated vs measured inclinometric profile of IN3 (see Figure 36)

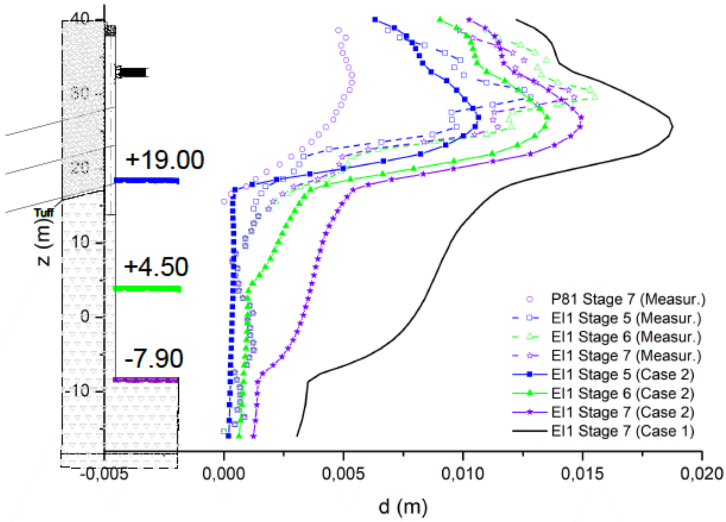

Figure 46. Calculated vs measured inclinometric profile of EI1 (see Figure 36)

The comparison of recorded inclinometric profiles with the numerical ones of Case 1 and 2 made it possible to calibrate the stiffness of NYT since no experimental information was available from the site, thus settlements below buildings presented below relate only to Cases 2 and 3, whose comparison allows us to appreciate the effect of building stiffness on the shape and the extent of vertical displacements.

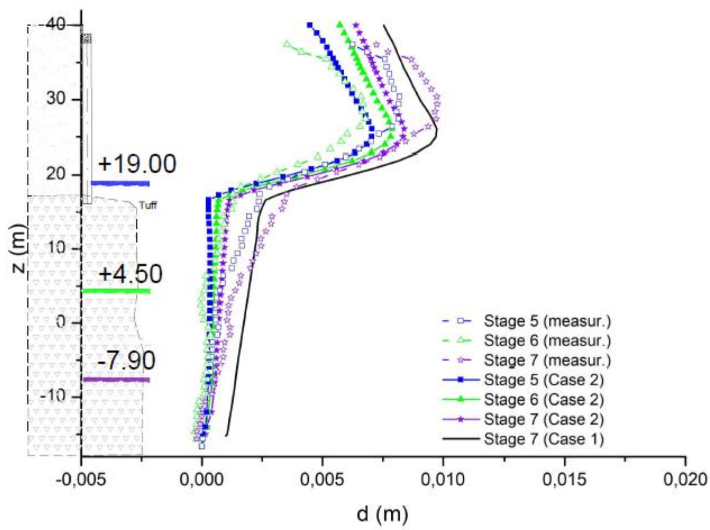

Figure 47. Calculated vs measured inclinometric profile of IN1 (see Figure 36)

Building main façade settlements are reported in Figure 48 and Figure 49. Two shaded areas for each monitored alignment are shown. They represent the envelope of the calculation results for Stages 5, 6, and 7 of Case 3 and the corresponding measurements. Calculated settlements at the last simulation Stage 7 for Case 2 also are reported for comparison. It is evident from the plot of the façade of Building E01 along Serra Street (Figure 48) that the greenfield profiles of Case 2 do not match the measured profiles due to the absence in the model of any element reproducing the building stiffness, whereas the average settlement is rather satisfactorily reproduced. A very satisfactory agreement between calculations and measurements for the main stages of the construction process (*i.e*., Stages 5, 6, and 7) was obtained by introducing in the FEM model the orthotropic plate previously described occupying the building foundation area. The stiffness of the wall was spread over the area of the plate, with direction 2 (stiffness E_2) corresponding to the long side of the building and direction 1 (stiffness E_1) orthogonal to direction 2.

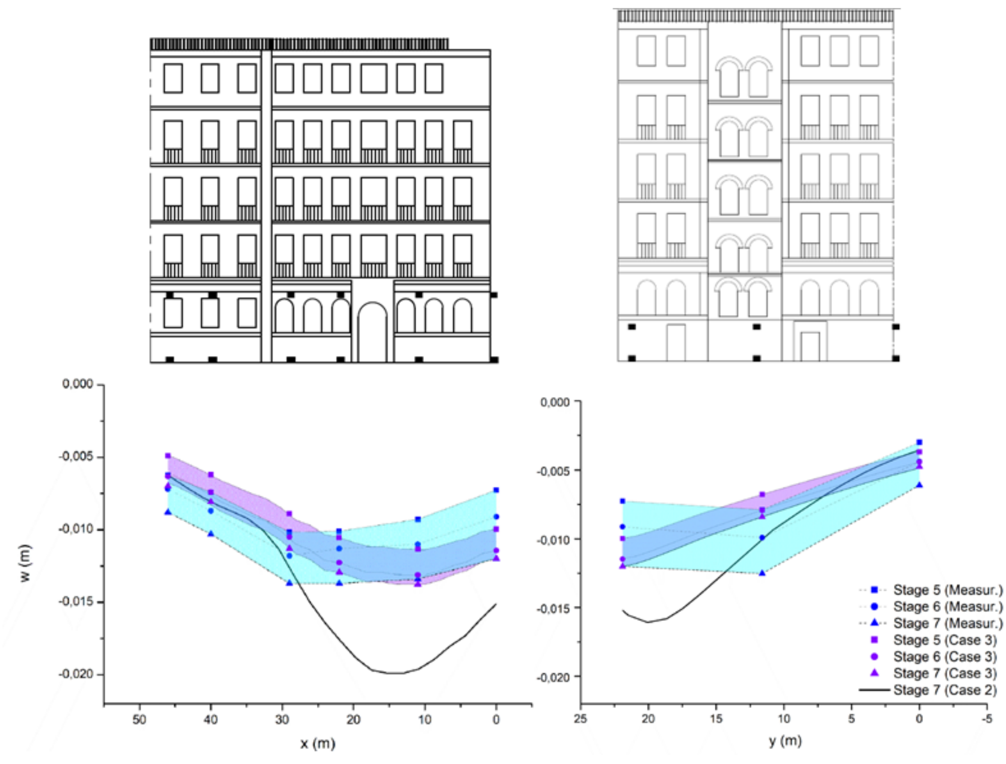

Figure 48. Settlements calculated and measured along Military Court (building E01) on Santa Maria degli Angeli square side (on the left) and on Monte di Dio Street side (on the right) (after Russo et al., 2024).

For the main façade of Building E01 (Figure 48, left), the computed deflection ratio of the main façade was reduced substantially from the greenfield value 0.200‰ for Case 2 to 0.083‰ for Case 3, which incorporated the building stiffness. The observed deflection ratio was 0.09‰, a very good agreement with the computed value. On the other façade along Monte di Dio Street (Figure 48, right), the comparison of calculations and measurements also was rather satisfactory. The introduction of the building stiffness in Case 3 improved the agreement between measured profiles and computed profiles on both the edges of the building, with some differences for the central benchmark in the range of 2–3 mm. The same was true for the Basilica *Santa Maria degli Angeli* (Figure 49), for which the computed deflection ratio in Case 3 was 0.069‰, which compares very well with the value of 0.058‰ obtained from measurements, but with a slight clockwise rotation of the overall façade, which is not detectable in the measured profiles. This may be due to the aforementioned mentioned complex boundary behavior at the right side of the Basilica, where the layered foundations of the seventeenth-century Chiaia Bridge also are located. In this case the greenfield computed deflection ratio was about 0.170‰.

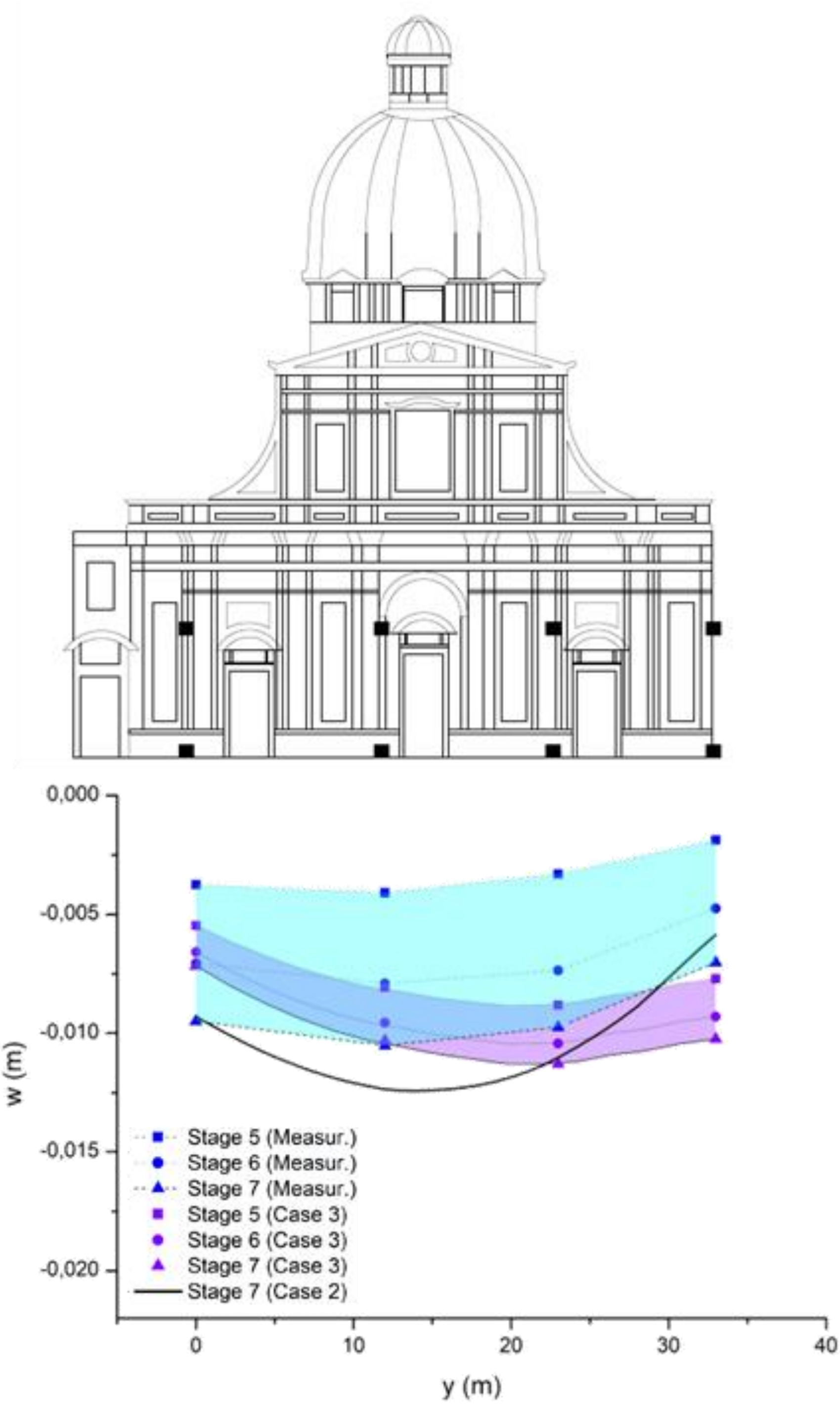

Figure 49. Settlements calculated and measured along the façade of Santa maria degli (after Russo et al., 2024).

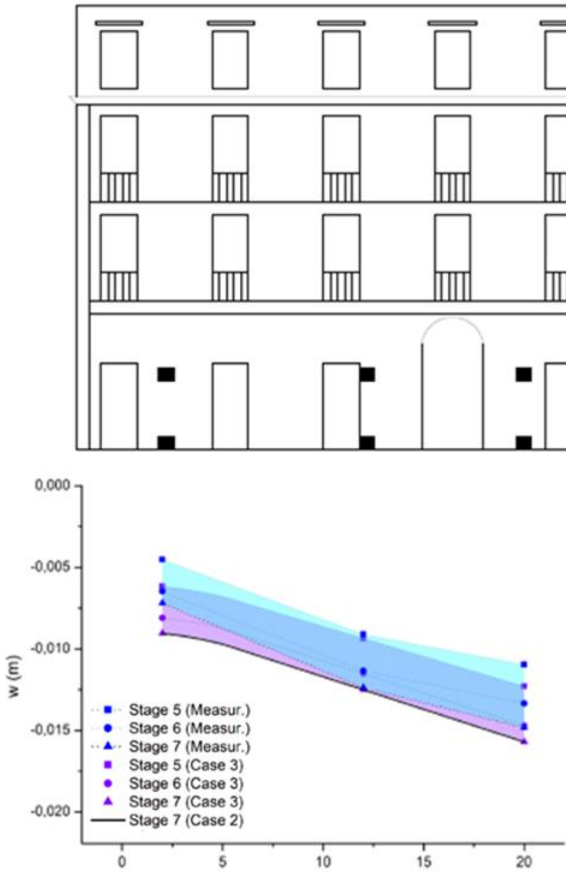

Figure 50. Settlements calculated and measured along the façade of Building E11 (after Russo et al., 2024)

Finally, the settlements of the façade of Building E11 are plotted in Figure 50, which compares the results of the FEM model with the measured profiles. In this case both deflection ratios were very small (*i.e.*, 0.0523‰), and there was no significant difference between greenfield Case 2 and Case 3. In all buildings, the maximum settlement observed at the end of excavation was rather small, in the range 5–15 mm. Lastly, the loads on the ground anchors were studied. In such a work with no symmetrical earth pressure distribution on the four sides of the station shaft, and with the shallow pile wall completely underexcavated, the role of the ground anchors was very important. They were pretensioned at design load, and, as shown by the results in Figure 42, they mainly kept a constant load until the end of their temporary use, which lasted about 5 years. Only a few had a very small decrease at a very low rate, probably due to some creep. Figure 51 presents the change of load over time for the measurements (solid black line) and the calculation results obtained in Cases 1 and 2 (*i.e.*, with the two different tuff stiffness values; results of the Case 2 and Case 3 calculations completely overlap) for two load cells placed on opposite sides of the excavation. Results of Case 2 (and Case 3) do not differ significantly from Case 1. Furthermore, for ground anchor C1 the measurements indicate an initial decreasing trend of the load, probably due to some slip at the locking system, which was entirely recovered with the prosecution of the excavation. This increase of the load is confirmed by the computations, which after Stage 5 indicate a slightly decreasing value of the load on the ground anchors. For Load cell C4, the measurements indicate a practically constant value very similar to the applied prestress, which is quite different from the calculation results, which indicate an increase of the stress between the prestress application and Stage 5. However, the evolution of the computed load in the long term agreed with that of the measured load in the following stages.

In general, no visible damages were recorded, and the observed settlement trough with the recalled deflection ratios substantially agrees with such a finding. Furthermore, the observed ability of the 3D model to reproduce the order of magnitude of the horizontal and vertical displacements and the general pattern of the observations with the depth and the distance from the ground surface was only the final result of a rather huge effort to reproduce even minor details in the staged construction process of the Chiaia Station shaft.

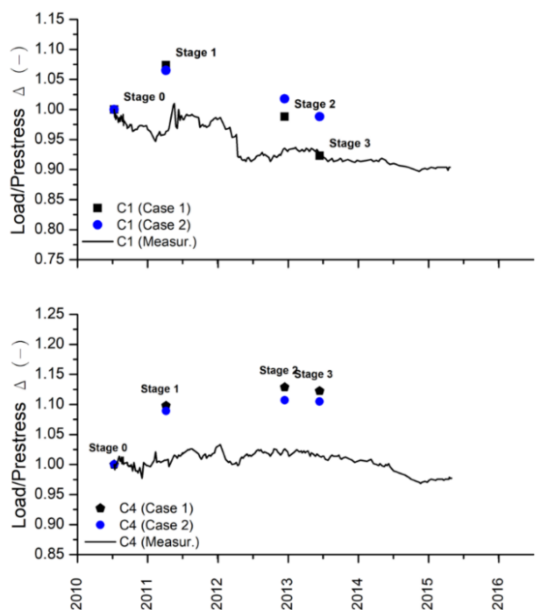

Figure 51. Time evolution of load in ground anchors load cells.

3.3. Coupled dynamic analyses

The calibration of the static model described in previous section served also as a benchmark for the numerical model to conduct coupled dynamic analyses. Aim of these analyses is to understand if and how the presence of a deep excavation can affect the seismic risk of the surrounding environment, including soil, existing buildings and facilities. To carry out dynamic analyses the model was modified with respect to the static one, according to requirements related to geometry and soil behavior. The main modifications are listed below.

- The soil domain has been enlarged to avoid reflection of waves around the station.
- The soil constitutive model was changed (Hardening Soil model with small strain stiffness was adopted) to consider hysteretic damping, not included in the HS.
- The internal structures of the station, including slabs and columns, were modeled as well, to carry out the analyses on a model representative of the current situation at the site; the construction sequence of the station was simplified, instead, assigning to the slabs the role of struts and avoiding the modelling of the huge number of tieback anchors.
- Among buildings, only the Military Court and the Basilica were accounted for in the new model.

In Figure 52 a section of the final aspect of the station is represented.

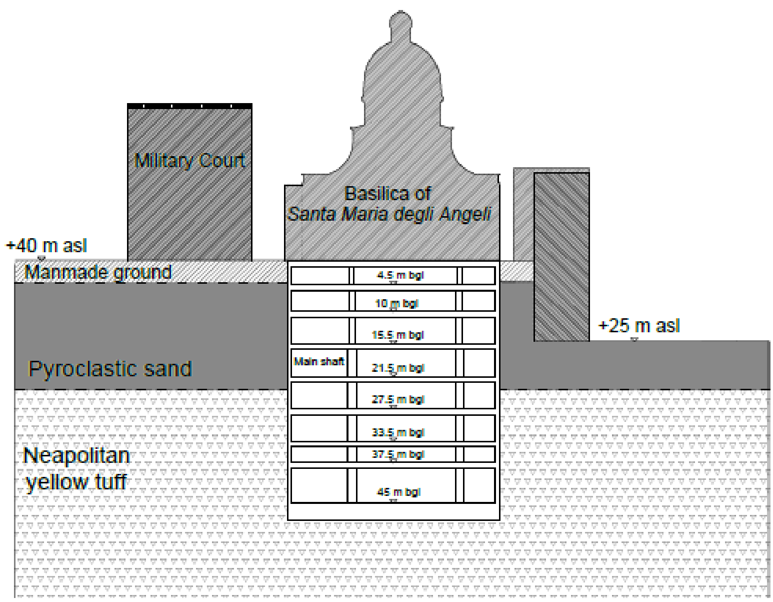

Figure 52. Section 2-2 (see Figure 36): station and lift shafts, main buildings.

3.3.1. Accelerograms selection

Seven horizontal acceleration time histories were adopted as seismic inputs for the parametric study. These were initially extracted based on the spectro-compatibility criteria set out in the Italian National Code (Ministero delle Infrastrutture, 2018) and available in software designed for seismic activity in Italy (REXEL, Iervolino *et al.*, 2010). The Ultimate Limit State (ULS) elastic response spectrum was derived for the Chiaia site in Napoli (latitude = 41.9541°, longitude = 15.0012°), using the following input data:

- subsoil class A (rock; V_S, 30 ≥ 800 m/s)
- topographical category T1 (flat horizontal ground surface)
- design working life V_N = 50 years
- class of importance II
- unscaled, original recording.

which all provided a return period T_R = 475 years and a customary value of ξ = 5 % for the structural damping ratio. Based on the above reference spectrum, the seven horizontal acceleration time histories whose characteristics are listed in Table 9 were extracted from the European Strong-motion Database (ESD) (Luzi *et al.*, 2020) for a moment magnitude M_w = 6 ÷ 7 and an epicentral distance R_{ep} = 0 ÷ 15 km. These values were obtained following site-specific seismic hazard and disaggregation analyses of the horizontal peak ground acceleration (PGA), considering a rather cautious value of M_w with respect to that provided by the above described procedure. In fact, according to the disaggregation the most significant contribution to the hazard in terms of moment magnitude was associated with values of 4.3 ÷ 5.8. It is worth noting here that PGA refers to the location where the bedrock formation emerges, *i.e.*, the outcrop. As the time traces were recorded at the outcrop, they were deconvoluted using 1D equivalent-linear analyses (Idriss and Seed, 1968) performed with the code MARTA v 1.2.0 (Callisto, 2015) which assumes a visco-elastic constitutive relationship for the soil layers. The resulting ground motions at bedrock depth were then low-pass filtered using an eight-order Butterworth filter at a maximum frequency f_{max} = 10 Hz, thus fulfilling Kuhlemeyer & Lysmer (1973) aforementioned requirement regarding the maximum distance between adjacent nodes along the main propagation direction of the seismic waves (*i.e.*, the vertical direction in this case). Finally, the filtered acceleration time histories were baseline-corrected using a cubic polynomial to achieve zero horizontal velocity and displacement at the end of the time history, after an initial check on these last quantities obtained by integration of the original acceleration time history. The main properties of the seismic inputs obtained in this way are listed in Table 9. Here, $a_{max,input}$ is the peak horizontal acceleration at the bedrock; f_p and f_m are the predominant and mean frequencies, respectively, as determined from the Fourier amplitude spectrum (Rathje *et al*., 1998; Kramer and Stewart, 2025); and $D_{5\text{-}95}$ is the strong-motion duration (Trifunac and Brady, 1975), calculated based on the time interval between the 5th and the 95th percentiles of the Arias intensity, I_A (Arias, 1970).

Table 9. Main properties of the input motions applied in the 3D FE analyses.

Event	000149xa	000471ya	004675xa	006326xaya	006332xa	006335xa	007142ya
location	Friuli*	Vrancea	South	South	South	South	Bingol
date	15/09/1976	30/05/1990	17/06/2000	21/06/2000	21/06/2000	21/06/2000	01/05/2003
$a_{max,input}$ (g)	0.09	0.01	0.08	0.07	0.21	0.08	0.16
f_p (Hz)	8.3	0.7	0.4	0.4	3.2	3.2	0.4
f_m (Hz)	6.7	2.3	3.7	2.5	4.3	2.1	3.7
$D_{5\text{-}95}$ (s)	6.61	13.73	5.70	5.60	3.50	5.78	8.78
I_A (m/s)	0.08	0.002	0.05	0.07	0.28	0.08	0.24

**aftershock*

3.3.2. Numerical model

The analyzed domain, represented in Figure 53, has dimensions 140×140×70 m^3 and contains 168.209 ten-noded tetrahedral elements characterized by a second-order displacement approximation, linear strain interpolation and four Gauss points. The elements have an average dimension of 2.6 m, with a finer mesh in the upper layers (sandy soils) where the shear wave velocity V_S is lower than in the underlying NYT. These dimensions are consistent with the recommendations of Kuhlemeyer and Lysmer (1973) regarding the ratio of minimum wavelength to shear wave velocity. The station and lift shafts are located approximately in the middle of the plan domain; the morphological vertical discontinuity between *Santa Maria degli Angeli* square and *Chiaia* Street is simulated behind the northernmost side of the excavation by introducing a horizontal displacement constraint and removing a 15 m-thick layer of soil (Figure 53). The internal structures of the shafts (*i.e.* walls and slabs) are modelled using linear elastic isotropic plate elements, the mechanical properties of which are reported in Table 10. Interface elements were used to disconnect the nodes of the plate elements used to model the shaft walls from the surrounding soil nodes. These interfaces are zero-thickness bidimensional elements whose normal and shear stiffnesses are determined based on the stiffness characteristics of the adjacent solid elements as well as on a virtual thickness which is the product of the average size of the mesh elements and a dimensionless virtual thickness factor, *vtf* (Bentley, 2024). The shear and the normal stiffness of the interface elements are inversely proportional to *vtf*. A default value of *vtf* = 0.1 is adopted to ensure the efficiency of the numerical solution algorithm, because too low values could lead to incorrect solutions or difficulty in convergence. However, a different value of *vtf* can be specified to vary the interface stiffness without changing the stiffness of the surrounding soil.

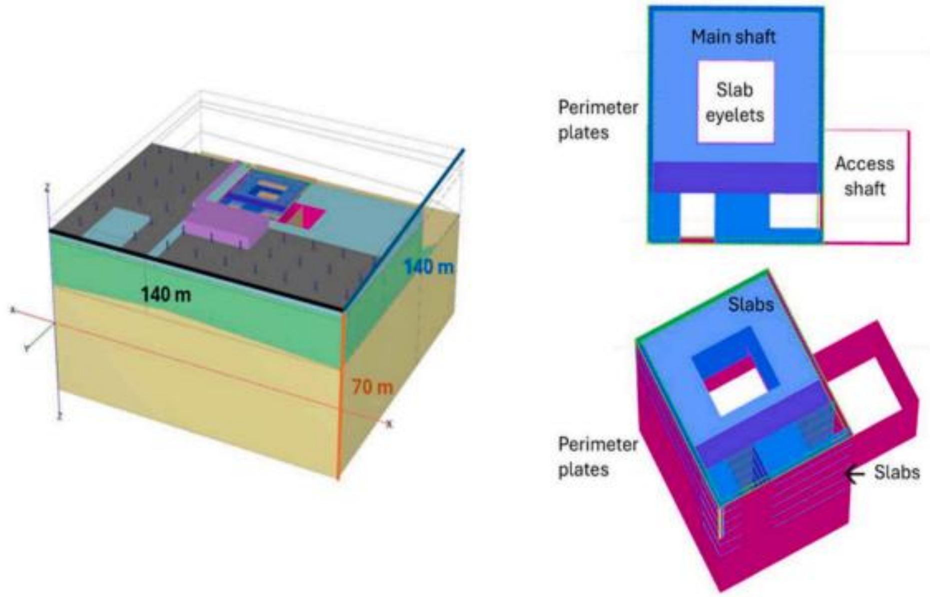

Figure 53. Perspective view of the 3D FE model with dimensions (left), plan view and perspective view of the structural box of the station (right) (after Esposito et al., 2026)

Table 10. Stiffness and thickness of the station structures

Structure	E	G_{12}	d	γ
	GPa	GPa	m	kN/m^3
Top Slab	30	12.5	1.1	24
Other slabs	30	12.5	0.35	24
Internal walls	30	12.5	0.8	24

Regarding the buildings surrounding the station shaft, two parallelepiped solid elements were built extending to the foundation level, at a depth z = 2 m bgl: the first, 8-m high and 2-m wide in plan is aligned with the Basilica façade; and the second, 6-m high, extends over the entire Military Court plan. In the case of the Basilica, the parallelepiped simply represents the front wall, which was only simulated after careful consideration of the Basilica's relatively low stiffness in the direction perpendicular to the main façade. Describing the correct relative soil-structure stiffness is clearly fundamental to obtaining more accurate information about the real displacement field (Franzius *et al*., 2006). Specifically, when a structure is included in a numerical model for soil-structure interaction analysis with its own stiffness, the predicted damage intensity increases compared to the surcharge method (*e.g*., Yeganeh *et al*., 2015). The Jointed Rock Model implemented in Plaxis 3D (Bentley, 2024) was chosen to mimic the orthotropic behavior of the main masonry walls, in fact the model permits to assign two distinct stiffness moduli along two planes, oriented with a user managed angle (in this case 0° and 90°, respectively). The model was used in this case to assign the same stiffness used in the static back-analysis for orthotropic plates, to characterize solid elements. For the Military Court, the stiffness module ratios in the two orthogonal directions were set to describe the bending stiffness of the entire structure. Simple surface loads were also introduced to account for the impact of the remaining portions of the Basilica and the adjacent buildings (*i.e*., the Basilica aggregate) and those adjacent to the Military Court (*i.e*., the Military Court aggregate) on the excavation shaft. The uniformly distributed vertical loads applied to the surfaces have values of 120 and 130 kPa, respectively. The weights and stiffnesses assigned to the solid elements are summarized in Table 11. The weight of the building was selected to reproduce the average estimated foundation pressure for the modelled volume, according to information reported in Ferraro (2010). The static part of the simulations consisted of an initial phase in which the stress field due to the weight of the soil was generated using a k_0-procedure. Then the buildings (loads and structural elements) were activated followed by the plates representing the excavation walls (wished in place). Hence, the shaft construction process was simulated in thirteen simplified calculation phases where slabs served as anchorage system, and they were installed during the stage following soil removal at the corresponding depth.

Table 11. Modelled buildings' properties.

Building	Type	E_1	E_2	G_{12}	γ
		GPa	GPa	GPa	kN/m^3
Basilica	Solid	3	3	1.2	20
Military Court		3	9	3.6	16.25

The accuracy of the predicted initial condition was verified by comparing mainly the deformation state with the results of a static analysis of the complete construction process which considered all the details (Russo *et al*., 2024). As an example, in Table

12 the maximum settlement and deflection ratio computed along the basilica façade are reported for the two static analyses, and compared with the monitoring data (Russo *et al.*, 2024).

Table 12. Main parameters of the subsidence trough: comparison of the quantities computed with the simplified model (*), with the FEM back-analysis and monitoring results.

w_{max}*	$w_{max,}$ Russo *et*	$w_{max,measured}$
8.0 mm	11.3 mm	9.0 mm
Δ_{max}*	$\Delta_{max,}$ Russo *et*	$\Delta_{max,measured}$
0.09 ‰	0.069 ‰	0.058 ‰

Boundary conditions

The FE model was first validated under dynamic conditions through preliminary 1D soil column analyses. This allowed the required mesh refinement and related boundary conditions to be determined. The computed profiles of maximum horizontal accelerations and shear strains were in very good agreement with those obtained from ground response analyses carried out using the linear-equivalent method (with code MARTA – Callisto, 2015), confirming the accuracy of the numerical model set up for dynamic calculations. During the dynamic calculation stages, tied-node boundary conditions were imposed at the lateral boundaries in the direction in which the seismic input was applied (Zienkiewicz *et al.*, 1989) using node-to-node anchor elements with high axial stiffness (10^9 kN) crossing the soil domain in the direction of the input application. The initial horizontal effective stress profile was applied at the vertical boundaries perpendicular to the seismic input (y-z plane in Figure 55) after the static boundary conditions (normal fixities) were removed (Gaudio and Rampello, 2019). The selected acceleration time histories were applied to the bottom of the numerical domain along the x-direction, which implies assuming an infinitely rigid bedrock: the finite stiffness of the bedrock formation was already included in the deconvolution process. The time step for time integration was assumed to be equal to the sampling interval of the acceleration time histories (Δt = 0.01 s), and the unconditionally stable average-acceleration time integration scheme (α = 0.25 and β = 0.50) was adopted in the dynamic calculations (Newmark, 1959). A lumped-mass matrix was assumed in the analyses (Bathe, 1996).

Selection and calibration of Hardening soil with small strain stiffness model

As already mentioned, dynamic analyses required a different constitutive law to be adopted for the soil layers with respect to static calculations. Namely, the Hardening Soil model with small strain stiffness (HSss) was chosen (Benz, 2007) for all the three layers already described in section 2 (static back-analysis). In addition to the parameters required in the definition of Hardening soil model, in fact, the initial shear modulus at a given reference pressure, G_0^{ref}, and the shear strain γ_{07} (corresponding to the shear strain where the value of shear modulus is equal to 72% of the initial value) are required to replicate the decay curve of initial shear modulus. HSss is a model particularly suitable for static calculation of excavation problems (Benz *et al.*, 2009), thanks to the addition to the Hardening soil model of the decay curve of G_0, which allow to replicate in a more accurate way the behavior of soil at very low level of strain (i.e., ranges of strain usually attained during excavation with very stiff retaining structures, like that under consideration); moreover, it is deemed suitable, and widely used, for dynamic calculations as well since a hysteretic damping ratio ξ is inserted into the model, whose evolution with shear strain is geometrically calculated from the values of secant and tangential shear stiffness; a cut-off is assumed in shear strain, $\gamma_{cut\text{-}off}$, that depends on the ratio G_0/G_{ur}, where G_0 is a free parameter of the model, and G_{ur} (shear modulus of unloading-reloading) is obtained from E_{ur} with the Poisson coefficient. If $\gamma > \gamma_{cut\text{-}off}$, damping is not expected to increase anymore but it assumes a constant value (Brinkgreve *et al.*, 2007). The calibration of additional parameters was made based on experimental decay curves available in Fabozzi *et al.*, (2017) and on G_0 profile obtained with the relationship between G_0 and N_{SPT} proposed by Schnaid *et al.* (2004) (Figure 54a and b).

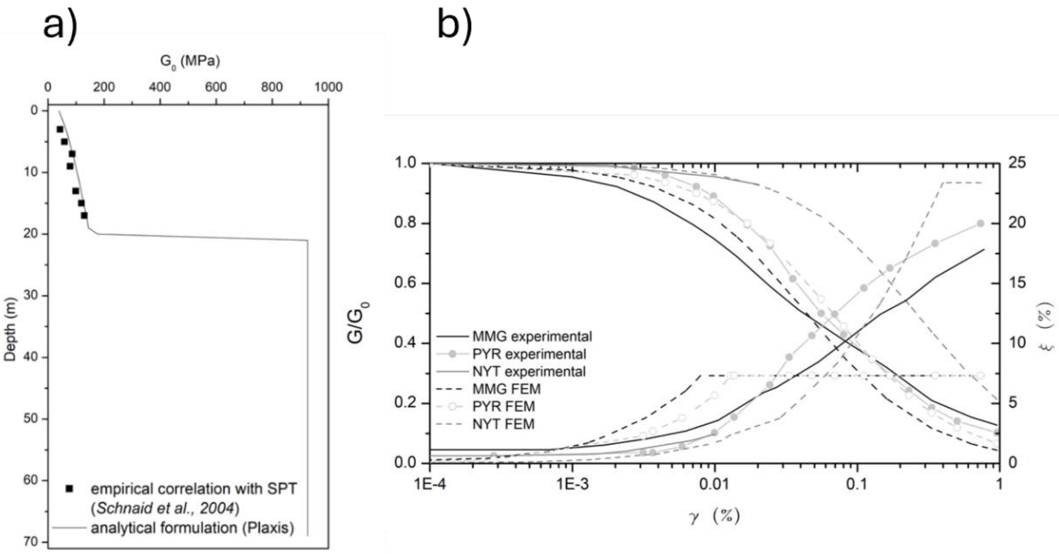

Figure 54. a) G_0 profile from SPT.; b) decay curves, experimental and numerical (FEM)

Since the shape of decay curve is managed by the ratio G_0/G_{ur}, E_{ur} was modified (with respect to Table 6) to better reproduce the laboratory curve, while E_{50} and E_{oed} were maintained as in the previous calibration. The resulting parameters of the three defined soil layers are reported in Table 13 and the comparisons between experimental and numerical decay curves and G_0 profile are reported in Figure 54a and b.

Table 13. Soil parameters for the calibration of HSss model in Plaxis 3D

Soil	Model	γ_{sat}-γ_{unsat}	ν_{ur}	φ'	c'	E_{50}^{ref}	E_{oed}^{ref}	E_{ur}^{ref}	G_0^{ref}	γ_{07}	*m*
		kN/m^3	-	°	kPa	MPa	MPa	MPa	MPa	%	-
MMG	*HSss*	17-15	0.3	36	1	30	30	146.4	112.6	0.17E-3	0.64
PYR	*HSss*	16-14	0.3	36	1	30	30	146.4	112.6	0.26E-3	0.64
NYT	*HSss*	16-14	0.35	27	820	83.33	83.33	250	925.9	1E-3	0

As the *HSss* model does not provide damping at very small strain levels, a viscous Rayleigh damping ratio ξ = 1% was added to eliminate spurious high-frequencies components. The relevant Rayleigh coefficients, α_R and β_R, were calibrated using the procedure suggested by Amorosi *et al*. (2010).

3.3.3. Fully coupled dynamic analyses

Three different cases were considered in comparison. The first case, referred to as the without excavation case (WE), consisted of a series of dynamic analyses in which only the buildings were activated, and the excavation was not present at all. This case was used as a benchmark for comparison. In the second and third cases, referred to as the excavation (E) and excavation with soft interface (E-SI) cases, the presence of the excavation was considered. However, the E-SI case was designed to examine the impact of interface stiffness on model predictions. It was deemed necessary to verify how the technological construction detail of the contact between the walls of the final structure and the walls of the excavation could influence the dynamic interaction with the surrounding soil. In practice, the presence of the waterproofing layer implies that sort of gap exists between the structure and the walls of the excavation; due to the effective thickness of the gap, the contact stiffness is likely reduced with respect to the case of perfect contact between the structure and the wall of the excavation. In this instance, the interface stiffness was reduced by approximately one third by setting *vtf* = 0.3. Figure 55 shows a vertical section of the two models, E and WE, crossing the boundary representing the morphological discontinuity. Two different limit conditions were considered in the models for the nodes belonging to this boundary: vertical displacement was either free to occur (u_z = free) or perfectly fixed (u_z = 0). It was then assumed that the actual response of the system was somewhat intermediate. With reference to the same boundary, it is worth recalling that horizontal displacement along the y-direction was fixed in both static and seismic stages, while the nodes were left free to move along the x-direction (*i.e.*, the direction of application of the seismic input).

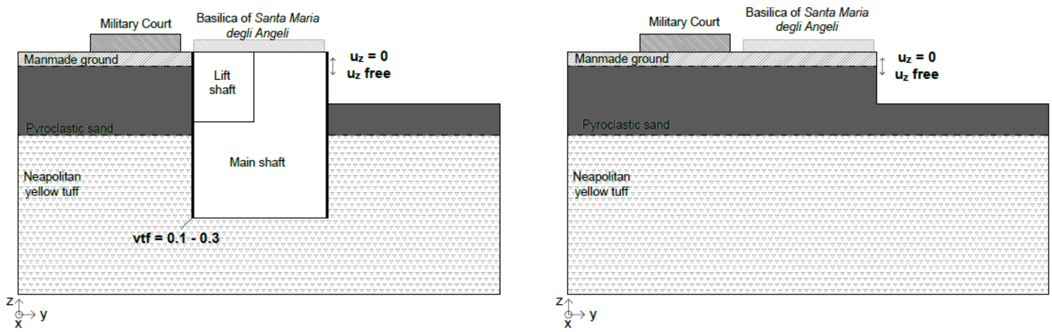

Figure 55. Illustration of a cross section (nearly corresponding to Section 2-2 of Figure 36) of analyzed cases (with and without excavation, different interface thickness, different boundary conditions on vertical displacements) (after Esposito et al., 2026).

Analysis of the eigenfrequencies of the system

In order to make a rational choice of inputs for the analyses, an analysis was carried out with a frequency sweep input applied at the bottom of the numerical model. The amplitude was kept constant over a frequency range of 0–10 Hz, with the frequency increasing at a given step of 0.1 Hz/s over time. A total duration of 100 s was therefore selected. The input amplitude was kept constant and relatively small (0.001 m) to ensure that the soil response remained within its elastic regime. The analysis aimed to determine the eigenfrequencies of the entire soil-excavation system. The results were extracted at a depth of 2 m below the model top surface in six different points, indicated in plan in Figure 56. Figure 57 shows the Fourier amplitude of horizontal displacement time history for the selected points.

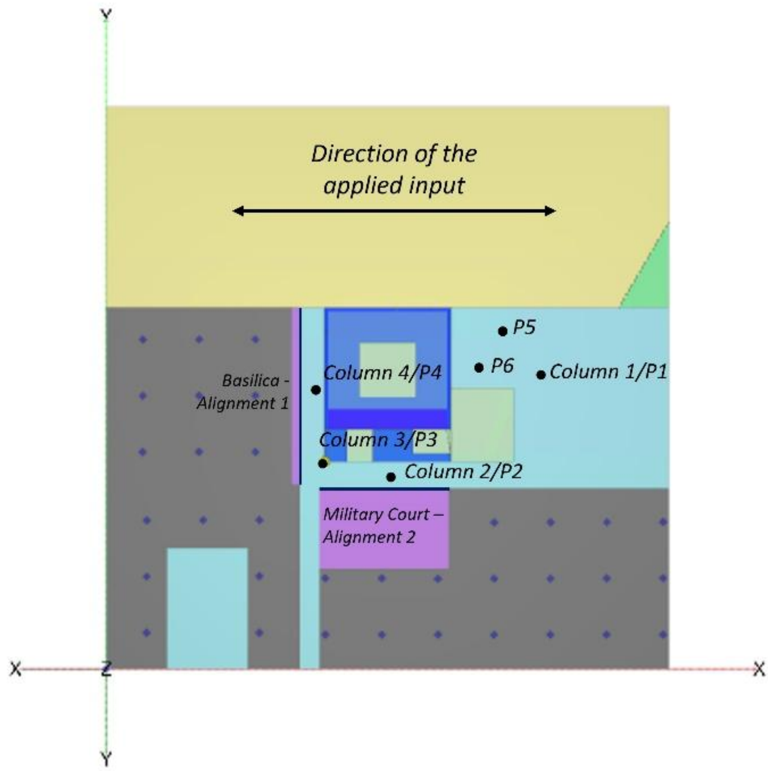

Figure 56. Plan view of the FEM model with the location of the presented results (after Esposito et al., 2026)

The analysis was first conducted with the 1D FE column and then with the WE 3D model (Figure 57a). Finally, the same sweep analysis was performed using the 3D model with the simulated excavation for comparison (Figure 57b, c, d). Figure 57a shows that the 1D column exhibits a primary peak in the Fourier amplitude at a frequency of 2.1 Hz, and a secondary peak at 3.0 Hz with significantly lower intensity. The WE model produces a slight shift in these two frequencies, which become 2.2 Hz and 2.7 Hz, respectively. Notably, the second eigenfrequency exhibits an intensity close to that of the primary frequency. Lastly, the excavation case was analyzed using the same input, yielding peak frequencies of 2.3 Hz and 3.0 Hz, for all analyzed points. This demonstrates that these two frequencies are inherent properties of the geotechnical system, with the presence of excavation having only a minor impact. The results of the frequency sweep analysis have been compared with the Fourier spectrum and mean frequencies of the seven selected input.

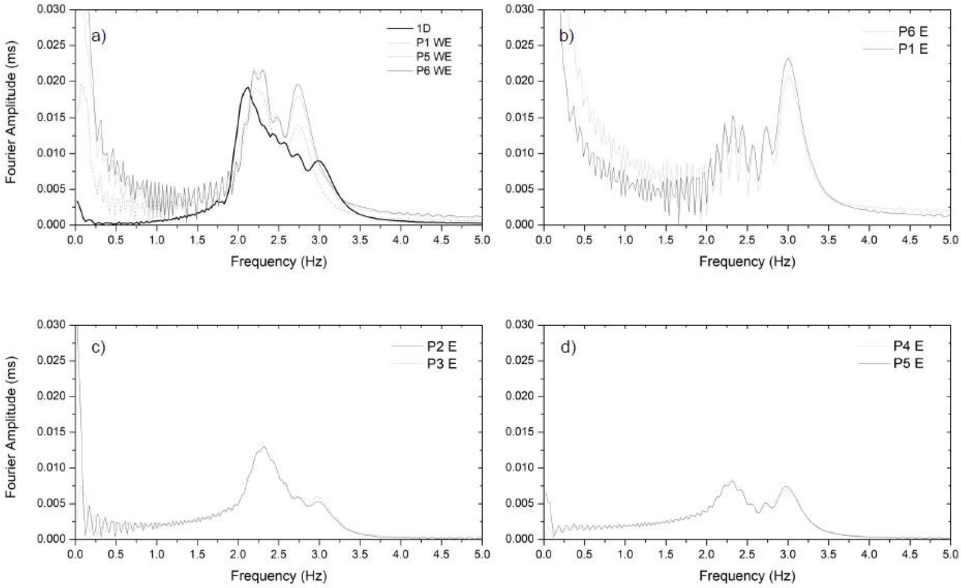

Figure 57. Sweep results for the selected points represented in Figure 56.

Based on the input properties reported in Table 9 and the comparison with the findings of sweep analysis, three accelerograms were selected for the fully coupled dynamic analyses, with varying intensity and frequency content. The first two were signals 000149xa and 004675xa, which have very similar peak acceleration ($a_{max,input}$) of 0.09 g and 0.08 g, respectively, but different frequency contents, f_m being 6.7 Hz and 3.7 Hz, respectively. The third was accelerogram 006332xa, which has a peak acceleration of 0.21 g and a mean frequency f_m of 4.3 Hz. The time histories of the three selected horizontal accelerograms are plotted in Figure 58. In Figure 59, Fourier spectra of the three selected inputs are represented and compared with the eigenfrequencies deduced by the frequency sweep analysis. It is clear that the first and the second modes of the soil-excavation system are both activated by ground motion 006332xa. This dynamic coupling is expected to amplify the effects of this ground motion on the soil-excavation system, due to its high Arias intensity (Table 9). The opposite holds true for inputs 000149xa and 004675xa. Nevertheless, the mean frequency of the input 004675xa is close to the second eigenfrequency of the system. This aspect is not negligible in terms of amplification.

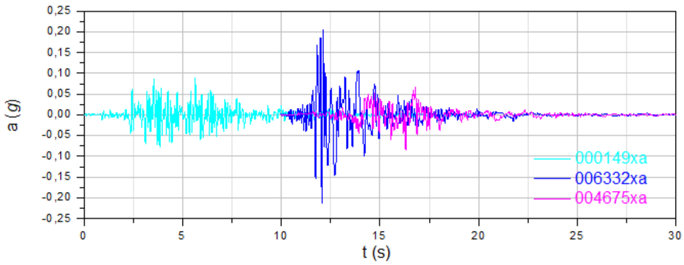

Figure 58. Acceleration time histories used as an input for the full 3D analyses.

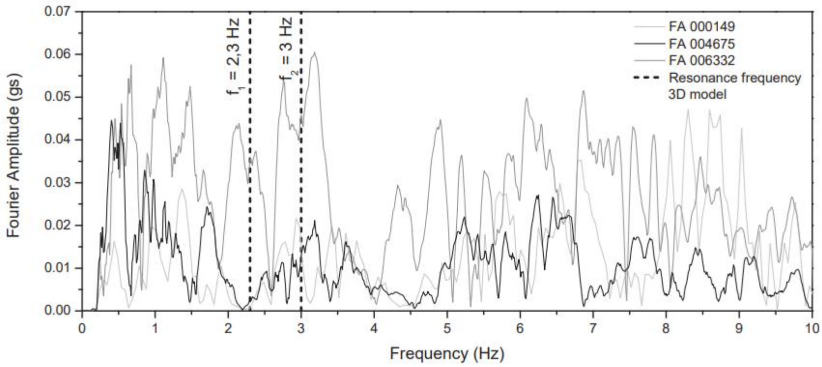

Figure 59. Fourier Amplitude spectra of the three selected seismic inputs, together with the eigen-frequencies of the system.

Results and discussions

The results of the analyses are presented in terms of amplification factor (the maximum soil horizontal acceleration at a given depth divided by the maximum input acceleration, $a_{i,max}/a_{max,input}$), ground-level vertical displacements and the related deflection ratios along two alignments parallel to the building façades. The location of the extracted results is shown in the plan view of the model in Figure 56. C*olumns 1* and *4* were chosen because they are aligned with the direction of input application with the excavation between them. C*olumn 4*, placed only 1 m far from the excavation edge, is also located very close to the area where the stiffness of the main façade of the Basilica and the distributed load of the entire religious building are modelled; *column 2* is, instead, at a greater distance from the excavation (20 m apart). For these reasons, the effects of the seismic action are expected to differ between the two columns. Finally, *column 4* is located two meters from the deep excavated shaft, with the NYT at a depth of 16 m, while *column 1* is located where the tuff layer is deeper (z = 24 m) and at a greater distance from the excavation edge (20 m apart). Conversely, c*olumns* 2 and *3* are aligned along the direction of the input application, on the same side of the excavation. Both columns are very close to the excavation, with *column 3* next to the corner and *column 2* nearly in the middle of the south side. These locations were selected to evaluate the possible differences between the corner zone, which is expected to be stiffer, and the mid-side zone. The results are reported in the following in terms of peak acceleration profiles, acceleration time histories and vertical displacements at the ground level along buildings' façades. The effect of location, stratigraphy, frequency content and peak acceleration of the input are discussed.

Peak accelerations

The nodes selected to construct the column profiles are spaced an average distance apart, which increases with depth. Starting from 2.5 m below ground level, this distance increases to 10 m in the NYT, which is not expected to provide a noticeable dynamic response because of its high stiffness. Regarding acceleration, the profiles discussed below have been filtered using an eighth-order low-pass Butterworth filter with a cut-off frequency of 5 Hz, since soil excitation occurs almost exclusively within this frequency range. The profiles have been elaborated in two ways. Figure 60 and Figure 61 show the amplification factor obtained for inputs 006332xa and 004675xa, respectively, for the cases WE and E.

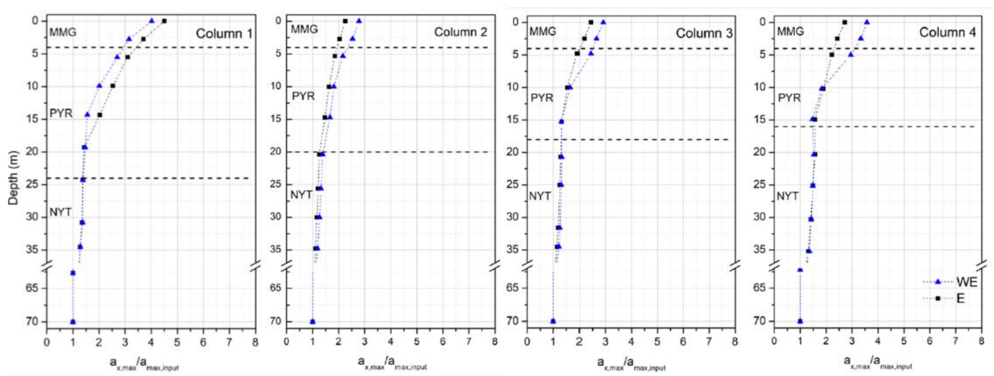

Figure 60. Maximum acceleration profiles obtained from analyses carried out with input 006332xa: E vs WE

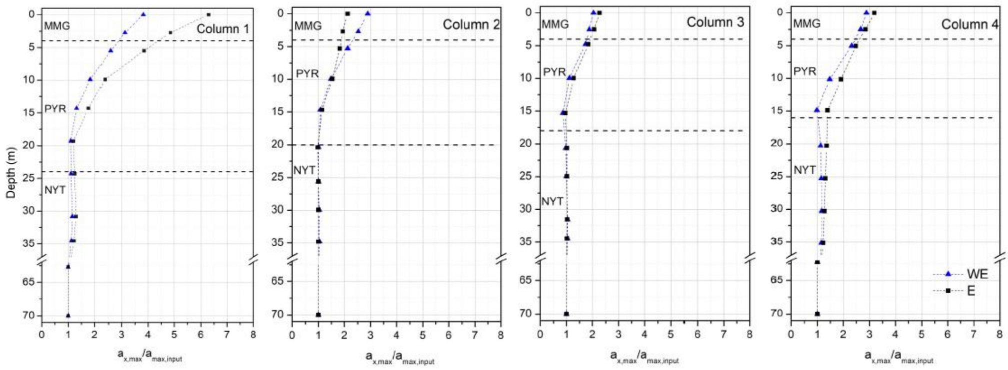

Figure 61. Maximum acceleration profiles obtained from analyses carried out with input 004675xa: E vs WE

The figures clearly show that the presence of the excavation and its supporting structure in *column 1* is responsible for significant amplification, which is much larger than in the WE case. The greater amplification at ground surface can be quantified as approximately +10 % for input 006332xa (Figure 60) and almost +60% for input 004675xa (Figure 61).

In Figure 62 the amplification factor computed at *columns 1, 3* and *4* are compared for the three input signals adopted in the parametric study.

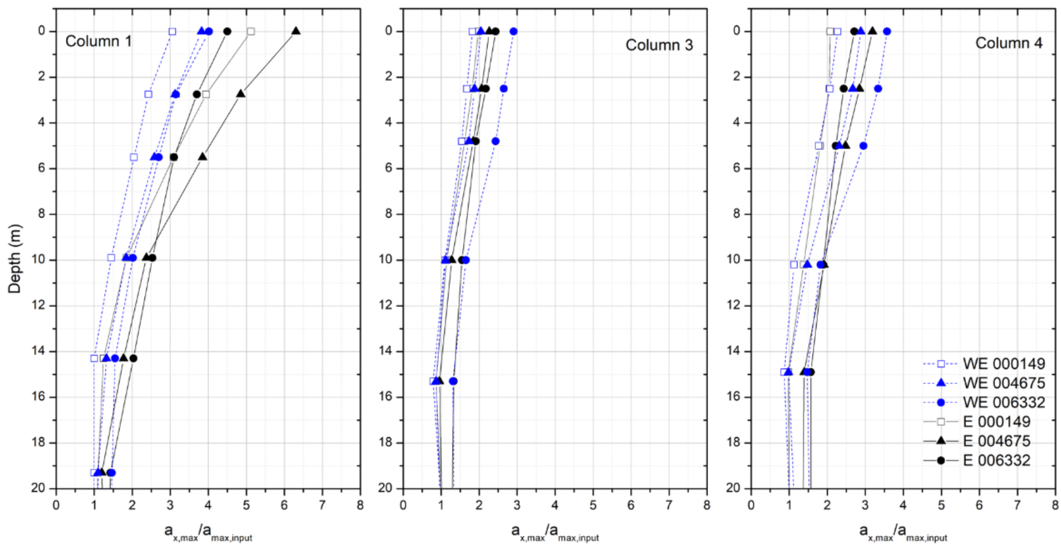

Figure 62. Maximum acceleration profiles: Excavation (E) vs Without Excavation (WE) for all three analyzed inputs.

It should be noted that in the case of input 006332xa, the maximum ground surface acceleration is about 4.5 times greater than the maximum input acceleration, whereas for input 004675xa this ratio exceeds 6. These results were somewhat expected when considering the mean frequency of the two inputs, f_m, rather than their predominant frequency, f_p, (see Table 9), compared to the eigen-frequencies of the overall system (Figure 57 and Figure 59). However, by comparing them to the results obtained by Sun *et al*. (2019), greater insight can be gained. The study, investigating the seismic effects of a box culvert built on the model of the Daikai station, shows that the maximum horizontal acceleration amplification occurs due to the presence of the underground structure at a dimensionless distance $x/B = 1$ from the excavation, where x is the horizontal distance from the edge of the excavation and B is half the excavation width in the same direction. For lower and higher values of x/B, the amplification is reduced. In the present study, *column 1* ($x/B = 2$) exhibits greater amplification than columns positioned nearer to the edges of the excavation. This finding is consistent with that of Sun *et al*. (2019), considering that column 4 is positioned at $x/B = 0.05$. However, it should also be noted that the depth of the underground structure under investigation, $z = -48$ m, is much greater than that considered in the aforementioned study. Furthermore, studies on tunnels of different radii (Youta-Mitra *et al*., 2007; Moghadam and Baziar, 2016) suggest that the area affected by the presence of a tunnel is proportional to its radius, with the distance of maximum amplification increasing accordingly. The differences between the results of *columns 1* and *4*, suggest that the distance from the edge of the excavation and the influence of the loaded area of the Basilica aggregate may indeed play a role. Considering *columns 2* and *3*, it can be seen that the presence of a close excavation with its support structures (E) produces a slight reduction in amplification for both adopted inputs. Figure 62 plots the comparisons for three out of four columns, considering the results produced by all three input signals. The same discussion presented for signals 004675xa and 006332xa can be applied to input 000149xa.

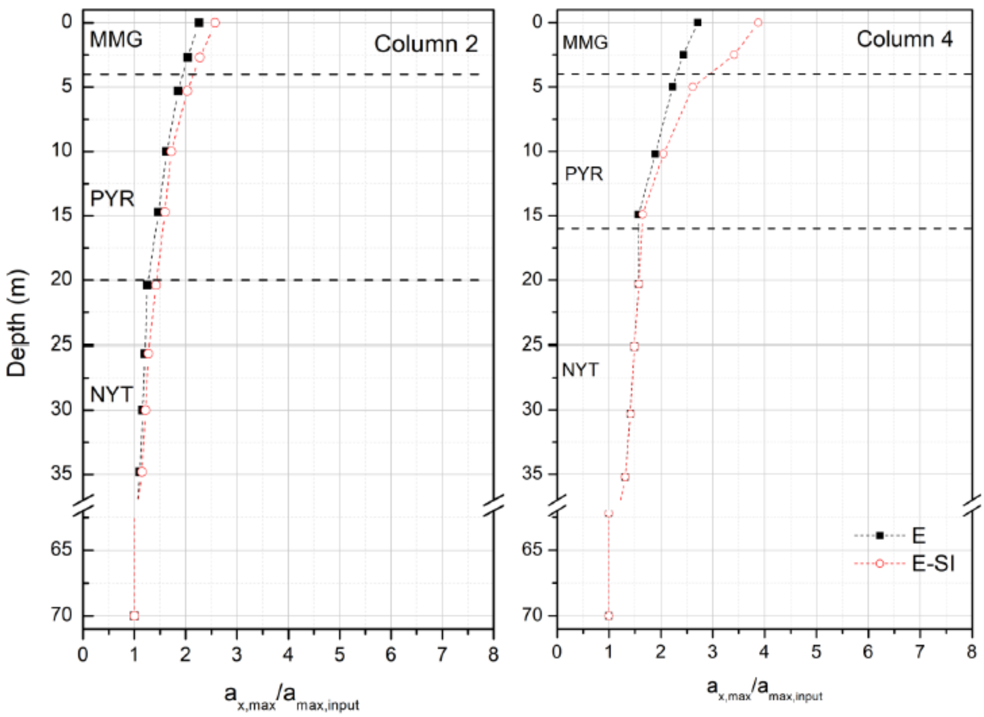

Figure 63. Effect of the interface thickness along Column 2 and 4 (input 006332xa)

Figure 63 and Figure 64 plot the results for *columns 2* and *4* obtained with signals 006332xa and 004675xa, comparing the amplification obtained with the excavation (E) while varying the stiffness of the interface (E-SI). Both columns are close to the excavation (they are placed 1 m from the retaining structure, and *x/B* is 0.05 and 0.07 respectively) and are located midway between the two perpendicular sides of the excavation shaft. It can be seen that introducing a soft interface produces greater amplification in the upper layer, which is more evident at ground surface, in both cases. The increase is much larger for *column 4* than for *column 2*, which can be attributed to *column 4* being located at equal distance from the shaft to *column 2*, but close to the shaft wall orthogonally stressed by the earthquake. The increase in peak acceleration in the E-SI case compared to the E case is significant, ranging from +45% for input 006332xa to nearly +66% for input 004675xa. These findings are consistent with those of Wang *et al*. (2013) who emphasized that an input motion applied perpendicular to a building usually has the most noticeable effect. Whether this results in amplification or de-amplification depends on the layout of the buildings.

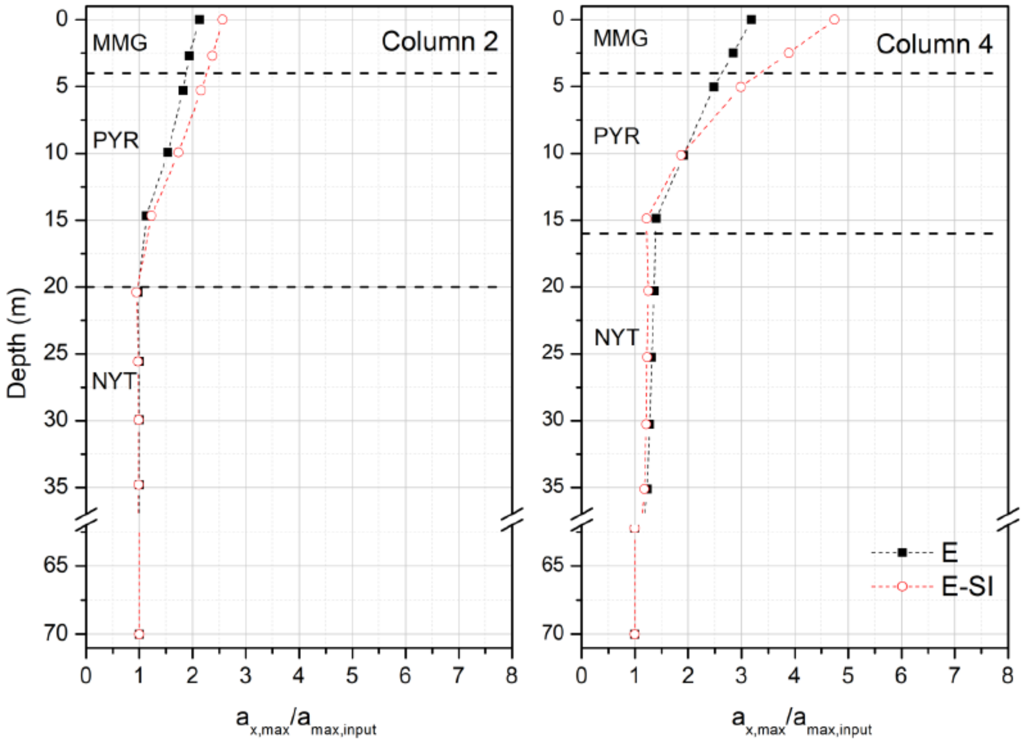

Figure 64. Effect of the interface thickness along Column 2 and 4 (input 004675xa)

Effect of excavation and interface stiffness on Arias intensity

To gain a better understanding of the differences in maximum acceleration reported in the previous section, a time interval of 10 s of the acceleration time histories calculated at ground level for specific locations are here reported and discussed for each accelerogram. Figure 65 shows a comparison of the two target situations with (E) and without (WE) excavation for the nodes at z = 0 m in *columns 1* and *4*, considering all the inputs. As can be seen from the figure, the amplification at ground level in *column 4* is lower than in *column 1*. This is also confirmed by the Arias intensity values reported in Table 14, which express the energy content of these time histories. Furthermore, it can be seen that the E analysis produces a higher acceleration than the WE analysis for column 1, not only for the relevant peak values, but also throughout the entire input signal duration. This indicated significant amplification of the input motion, corresponding to an increase in Arias intensity ranging from 130 % to 240 %. This is confirmed for all analyzed inputs. Conversely, analyses E and WE for *column 4* produce similar acceleration results, except for a few spikes, where the WE analysis shows higher values. This confirms that the results discussed in the previous section (Figure

60-Figure 64) tend to overlap throughout the entire input duration. This observation is quantitatively confirmed by the respective Arias intensity values (Table 14). Figure 66 finally illustrates the effect of the interface properties for the node at the ground surface belonging to *column 4*, which is located approximately 1 m from the edge of the excavation. The general trend exhibited here confirms the results presented in the previous section: the acceleration produced at ground level by analysis with a rigid soil-structure interface (E) is significantly lower than that produced by analysis with a soft interface (E-SI). In such cases, the Arias intensity increases between 200% and 280%.

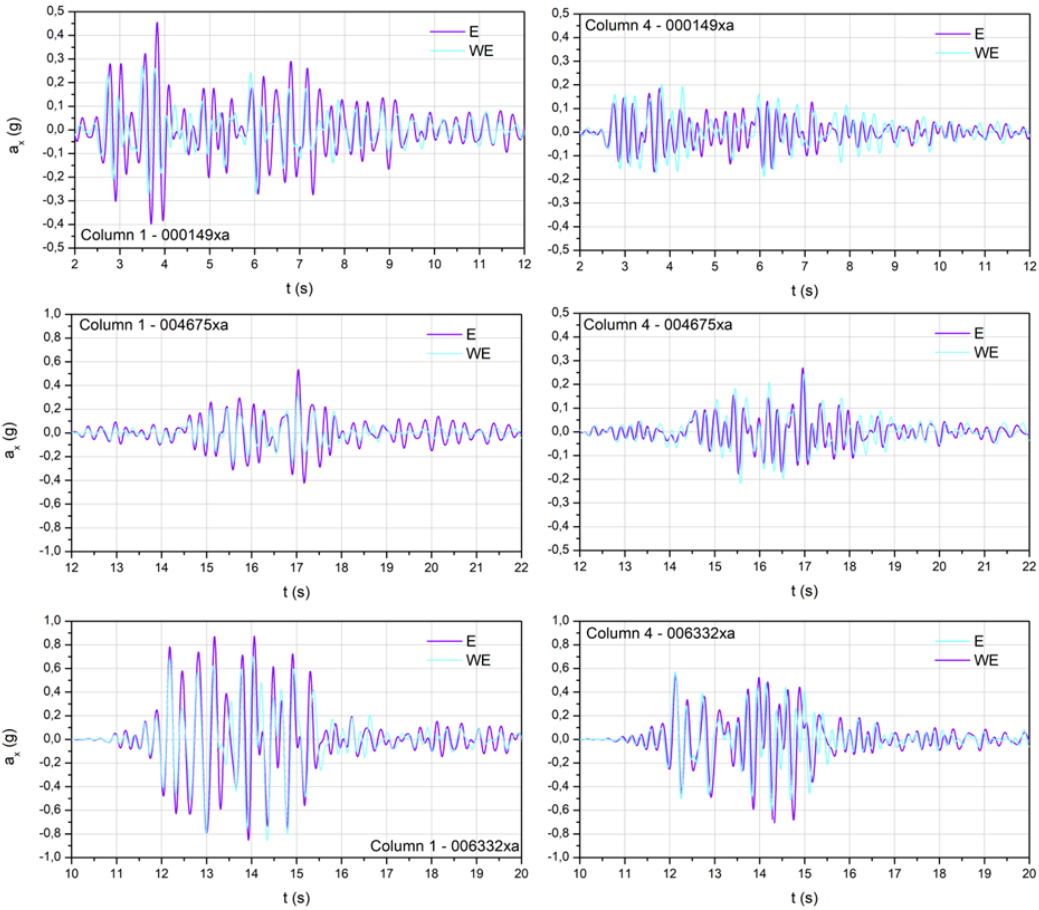

Figure 65. Acceleration time histories at the ground surface (z = 0) for columns 1 and 4 (Figure 56), recorded during the three input signals in the two target conditions E and WE

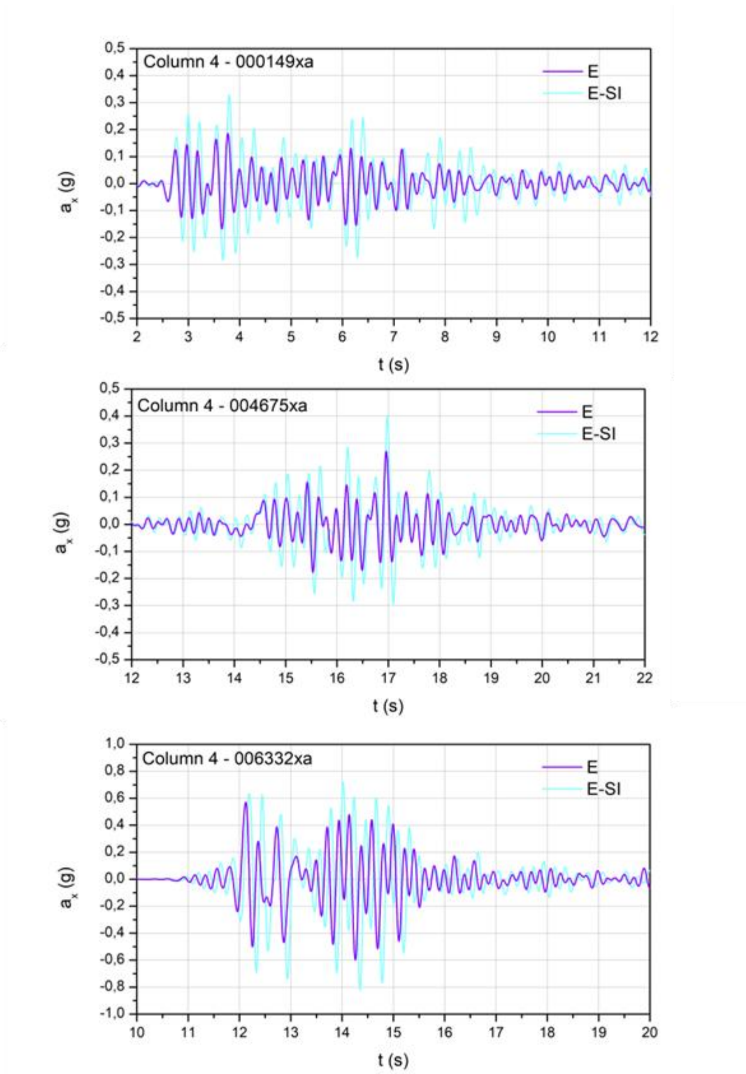

Figure 66. Acceleration time histories at the ground surface (z = 0) for column 4 (Figure 56), recorded during the three input signals: comparison between E and E-SI analyses

Table 14. Arias Intensity of the acceleration time histories computed at the ground surface

		Arias intensity (cm/s)		
Column	Analysis	000149xa	004675xa	006332xa
1	WE	99.7	88.6	860.9
	E	229.7	213.7	1141.8
4	WE	65.4	60.0	457.1
	E	48.3	45.3	382.8
	E-SI	137.5	111.6	767.9

Vertical displacements

The impact of excavation and its supporting structures on the seismic behavior of the surrounding area has been investigated even in terms of maximum displacements registered along buildings' façades, modeled as described in section 3.2.2 of this chapter. The maximum vertical displacements of the buildings along alignments 1 and 2 (see Figure 56), which correspond to the main façades of the Basilica and the Military Court, are plotted in Figure 67 and Figure 68 respectively, for the input signals producing the most significant effect (004675xa and 006332xa).

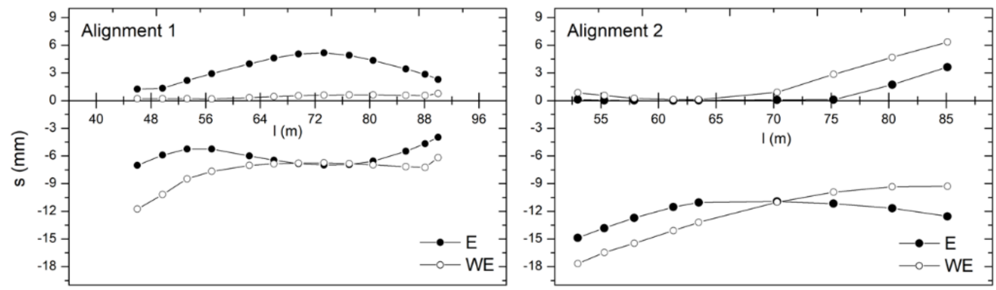

Figure 67. Maximum vertical displacements along alignment 1 and 2 (in Figure 56) exhibited during the input motion 006332xa (after Esposito et al., 2026).

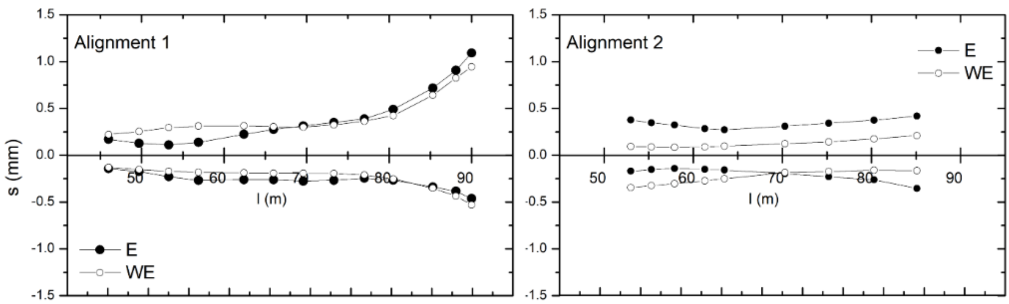

Figure 68. Maximum vertical displacements along alignment 1 and 2 (in Figure 56) exhibited during the input motion 004675xa (after Esposito et al., 2026).

The settlement is clearly affected by the aforementioned assumption regarding the boundary conditions of the model (vertical displacements are either free or fixed at the northernmost side of the excavation), so the plotted settlements are calculated as an average of the two extreme conditions. As can be seen from the Figure 67 and Figure 68, the higher accelerations of input signal 006332xa are responsible for the larger settlements of the two alignments, with maximum values ranging from 7 to 12 mm (alignment 1) and from 15 to 18 mm (alignment 2). For both alignments the larger values are computed in the case WE. In other words, the presence of the excavation and its stiff supporting structures seems to reduce the maximum seismic induced settlement. The opposite generally occurs when upward movements are considered, with a maximum value of around 4 mm being observed. It should be noted that these values represent the maximum vertical displacement recorded over time during the application of the inputs. It is worth recalling that the maximum settlement recorded during construction, and calculated, as reported in 3.2.3, was of a similar magnitude, at approximately 10 mm for the alignment 1 (see also Table 12) and 20 mm for the alignment 2. The maximum tensile strain ε_{max} was checked for all the instantaneous settlement profiles calculated. As the buildings were modelled using an equivalent deep beam approach, it is possible to estimate earthquake-induced damage using methods based on this assumption. Assuming the buildings behave as a shear beam, as modelled, the ε_{max} (Eq. (30)) was computed as the maximum value between the maximum flexural $\varepsilon_{f,max}$ and the maximum shear $\varepsilon_{t,max}$ strain, respectively defined in Eqs. (31) and (32):

$$\varepsilon_{max} = max(\varepsilon_{f,max} \,;\, \varepsilon_{t,max}) \qquad (30)$$

where:

$$\varepsilon_{f,max} = \varepsilon_h + \frac{\frac{\Delta}{L_i}}{\frac{L_i}{12t} + \frac{3EI}{2tL_i HG}} \qquad (31)$$

$$\varepsilon_{t,max} = 0.35\varepsilon_h + \left[0.65{\varepsilon_h}^2 + \left(\frac{\frac{\Delta}{L_i}}{1 + \frac{H{L_i}^2 G}{18EI}}\right)^2\right]^{0.5} \qquad (32)$$

with H denoting the height of the entire building, L_i the length of the analyzed building segment, I the moment of inertia of the equivalent beam cross section, and G and E the shear and Young's moduli of the building, respectively. The deflection ratio $\frac{\Delta}{L_i}$ is computed for every triplet of points in a single alignment, at each instant of time during the application of the input, and only the maximum value was considered when evaluating the damage condition. Similarly, the maximum value of the horizontal strain ε_h (Eq. 31) is taken from all the values computed along the alignment for each instant of time. These values were then compared with the tensile strain ranges identified by Son and Cording (2005) in order to estimate the level of damage, which ranges from 0 (negligible damage) to 5 (severe or very severe damage). The worst condition resulting from this procedure is associated with settlements and flexural behavior in hogging mode. These are reported in Table 15 for *alignment 1* only, *i.e.* the alignment corresponding to the Basilica façade.

Table 15. Damage parameters of buildings deformed shapes under seismic excitation

Alignment	Analysis	$\frac{\Delta}{L_i}$ (%)	ε_h (%)	$\varepsilon_{h,max}$(%)	Damage
Basilica	006332xa - E-SI	2.34×10^{-2}	0.042	0.062	1
Basilica	006332xa - WE	8.86×10^{-3}	0.055	0.060	1
Basilica	006332xa - E	1.22×10^{-2}	0.034	0.043	0

The class of damage obtained and reported in Table 15 ranges from 0 to 1. These classes are both referred to as nearly negligible damage, involving only a few capillary cracks that can affect the plaster covering the masonry. It is important to note that the excavation seems to improve performances under seismic action, since the damage class changes from 1 to 0. Only in the case of E-SI is the damage class practically confirmed, as in the case of an earthquake acting without excavation (WE).

3.4. Conclusions

This chapter presents the case study of Chiaia station, a very deep excavation in the old center of the city of Napoli. The case study was replicated in two numerical models, constituting the starting point for two sets of analyses that in this chapter have been presented and discussed:

1. The first, aimed at replicating the measures of monitoring instruments collected during the excavation.
2. The second one served to investigate the possible scenario of earthquake occurrence and the effects produced by the excavation on the buildings surrounding it.

The two models are differentiated based on their scopes, but strictly connected since the first one allowed for the calibration and verification, in static conditions, of the second.

The one calibrated for static analyses achieves the goal of reproducing very satisfactorily the data recorded during construction. Due to the limited information available from site and laboratory tests, a back-analysis also based on literature data, was due to establish NYT stiffness, known for being widely variable and that significantly affected horizontal displacements. Moreover, particular attention was paid to modelling the buildings, investigating the differences encountered in simulating them using different simplified approaches. Since they are old masonry buildings with very stiff bearing walls, soil structure interaction (*i.e.*, the displacements exhibited during station excavation) is found to be significantly affected by the modeling of the orthotropic stiffness that characterizes them, due to the arrangement of the walls.

The very good agreement between calculation and experimental results allowed for the calibration of another model, simplified under certain aspects with respect to the static one, but still giving good agreement with monitoring data. This second model allowed for the investigation of the effect produced by the excavation on the seismic risk associated with the buildings surrounding it. Although the problem, as highlighted in section 2.3.4 of *Chapter 2*, depends on many factors, some conclusions can be drawn:

- The eigen-frequencies of the geotechnical system composed of soil domain, underground and above-ground structures are not significantly influenced by the presence of the excavation.
- The excavation produces an increment of peak accelerations at the ground level at a distance comparable with its plan dimensions and a general decrement within 1 m from its edge.

- In the same way that in static conditions, the location near the corner of the excavation seems to be less affected by the excavation itself than locations placed in the middle of the retaining walls.
- This observation can be interpreted together with others regarding the effect of interface stiffness – also investigated in the analyses –, the input direction with respect to the orientation of the retaining wall and the sensitivity to input characteristics (frequency content and peak acceleration) that could lead to conclude that effect of excavation is more pronounced where the stiffness of soil-structure system is lower.

The results presented here shed light on the complex mechanisms involving underground-soil-aboveground structures interaction during earthquakes, when it comes to deep pits with very stiff retaining structures, and some of them are found in substantial agreement with findings related to tunnel effect discussed in *Chapter 2*. However, because of what is already discussed about excavations and some inherent limitations of the work under consideration, the results must be intended as related to the single case study and the influence of more parameters needs to be analyzed to draw more general and widely applicable conclusions.

Chapter 4

San Pasquale station case study

4.1. Description of the case study

San Pasquale station is part of Line 6 of Napoli Underground (see section 3.1.1) located in the *Riviera di Chiaia* Street, near *San Pasquale* Square (Figure 69). The seaside is very close to the excavation area so that it was carried out under water, which determined some design choices regarding retaining structures, sequence of work and dewatering system. The ground level is nearly horizontal, at a mean elevation of +2.5 m above sea level (asl), and the water level is found at a depth ranging between 1 and 2 m bgl. Over the years, the project underwent some modifications regarding geometries of the excavations and dewatering systems; its plan and retaining system in the definitive configuration are reported in Figure 70.

Figure 69. Surroundings of San Pasquale station, aerial view (Google earth, 19/09/2022).

The characteristics of soils, the properties of the internal structures, sequence of works, and results of monitoring activities for the control of induced displacements have been the subject of several publications (L'Amante *et al.*, 2012; Castaldo *et al.*, 2013; Russo *et al.*, 2014; Russo *et al.*, 2016; Russo *et al.*, 2019) and three doctoral thesis (Licata, 2015; Autuori, 2016; Fabozzi, 2017) treating different aspects of the case study. However, for the sake of completeness of the work here presented, these aspects are concisely discussed in the following sections.

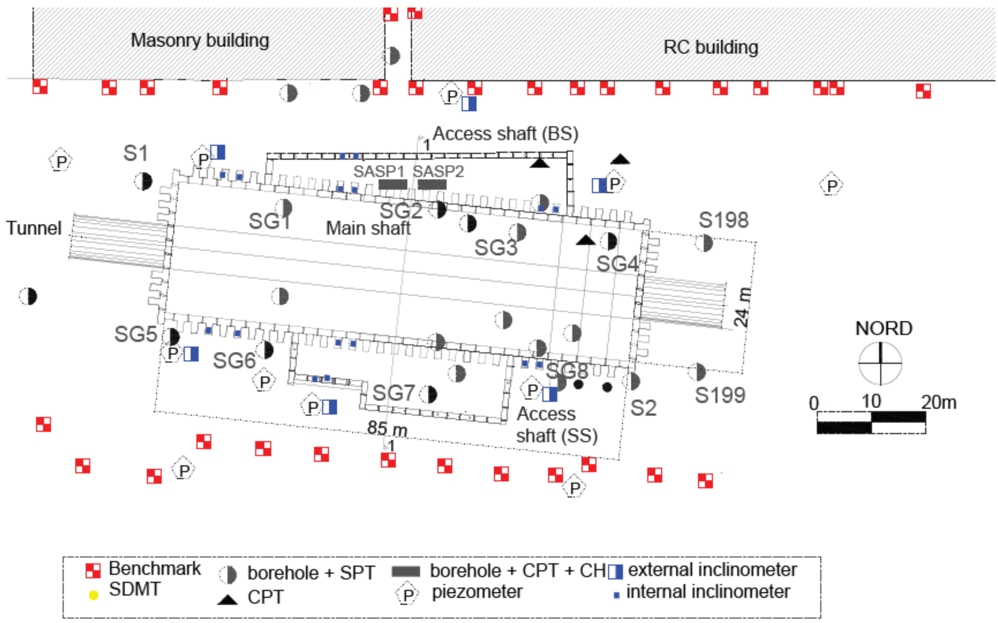

Figure 70. Plan view of the station, site investigations and monitoring instrument locations.

4.1.1. Geotechnical characterization: site and laboratory investigations

In the years between the station's first project (dating to 1980s) and its actual construction (that began in 2008) different investigation campaigns were carried out, the first in 1990 and, later, other three in 1999-2000, 2005 and 2008. A total of 27 boreholes, most of them using continuous coring, were carried out in the excavation area (see Figure 70) and integrated by SPT, Cone Penetration tests (CPT), Seismic Dilatometer Tests (SDMT) and Cross Hole (CH), whose locations are shown in Figure 70. The results of the tests useful for the characterization of the soil are reported in Figure 71. N_{SPT} show increasing values with depth; CPT, CH and SDMT results, instead, indicate a significant variability of soil properties and make the transition from one layer to another quite evident. Regarding V_s profiles, CH and SDMT have a good agreement in sandy layers, with the values retrieved from SDMT slightly higher than those from CH. This difference is probably due to test execution: with SDMT, the soil is locally displaced and compressed by the dilatometer, while in the CH, the soil expands after drilling the holes.

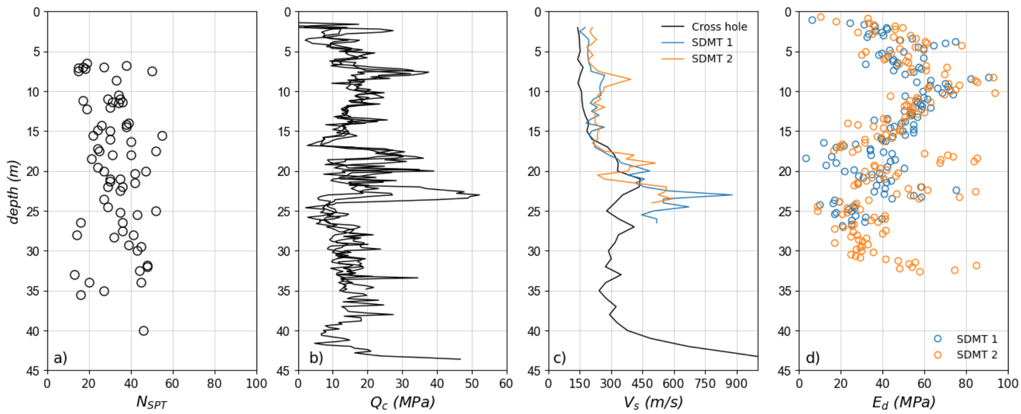

Figure 71. a) NSPT, b) tip resistance of CPT, c) shear wave velocity retrieved by CH and SDMT tests, d) dilatometric modulus from SDMT.

During the first campaign, 4 samples were collected and subjected to stratigraphic recognition and laboratory tests involving determination of water content, unit weight, triaxial tests at different confining pressures. The properties derived by laboratory tests are reported in Table 16.

Table 16. Laboratory tests, investigation campaign 1990

Sample	Average depth	Soil	w	γ_{sat}	S_r	γ_s	Triaxial test	
							σ'_3	σ_1-σ_3
	m		%	kN/m^3		kN/m^3	kPa	kPa
1	11.45	Marine	0.49	16.38	0.92	11		
2	15.75	Marine	0.23	19.24	0.94	15.63		
	15.75		0.23	19.49	0.97	15.85	150	968
	15.75		0.23	19.55	0.98	15.85	300	1674
	15.75		0.23	19.51	0.98	15.84	450	2497
3	23.7	Pyroclastic	0.36	17.43	0.96	12.81		
	23.7		0.37	16.78	0.90	12.21	200	686
	23.7		0.37	17.14	0.93	12.55	300	997
	23.7		0.35	17.08	0.91	12.65	400	1350
4	24.75	Pyroclastic	0.35	17.11	0.90	12.69		
	24.75		0.36	17.22	0.92	12.71	200	714
	24.75		0.35	17.15	0.91	12.67	300	1003

24.75	0.34	17.25	0.91	12.86	400	1536

The boreholes were pushed down to a depth of 60 m, which allowed for the reconstruction of tuff roof surface along the perimeter of the excavation area. The knowledge of the tuff top surface, that is strongly not horizontal varying between -32 and -47 m asl, was aimed at establishing the minimum depth of diaphragm walls (the tuff depths are reported in Table 17). Other tests were carried out at shallower depths, reaching a maximum of 45 m.

Table 17. Depths of tuff according to boreholes carried out in excavation area (see Figure 70).

Borehole	Ground level	Depth top boundary	Elevation top
	m asl	m bgl	m asl
		1990 campaign	
S198	2.3	40.2	-37.9
S199	2.3	38.5	-36.2
		2005 campaign	
S1	2.2	34.2	-32.0
S2	2.1	41.0	-38.9
SG1	2.3	40.7	-38.4
SG2	2.3	44.5	-42.2
SG3	2.3	47.5	-45.2
SG4	2.3	38.0	-35.7
SG5	2.0	36.0	-34.0
SG6	2.4	40.0	-37.6
SG7	2.3	36.5	-34.2
SG8	2.0	45.5	-43.5
		2007 campaign	
SASP1	2.1	42.0	-39.9
SASP2	2.3	49.5	-47.2

Based on geological knowledge of the interested area, and according to the boreholes results, a geological section has been realized (see Figure 72). The stratigraphy consists of a thick layer of cohesionless soils, including made ground, the underlying marine sands, remolded ashes and in situ *pozzolana*, laying on the bedrock of Neapolitan Yellow Tuff (Russo *et al*., 2012; L'Amante *et al*., 2012; Autuori, 2016). The first 2-3 meters of NYT have reduced mechanical properties, and the resulting rock material is known as *cappellaccio*. Apart from various inclusions, two main layers can be recognized, that are marine sands and pyroclastic soils. By comparing Figure 71 and Figure 72 it is evident that the marine sand deposit shows quite different stiffness characteristics along its depth, while the pyroclastic layer, although containing ash inclusions, is fairly homogeneous in mechanical properties, that decrease significantly with respect to the upper layer.

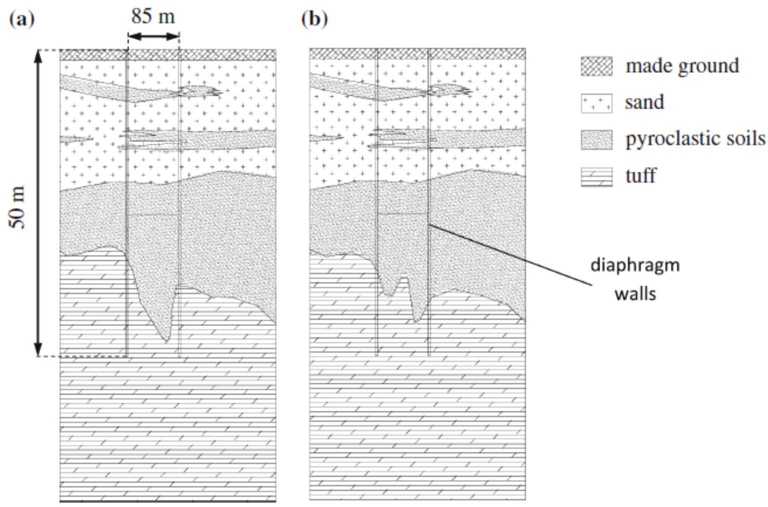

Figure 72. Geological section of San Pasquale (after L'Amante et al., 2012).

In addition to the already mentioned investigations, in conjunction with the boreholes, *in situ* permeability tests were carried out on both sandy layers (Lefranc tests) and NYT (Lugeon tests) at different depths. Lefranc and Lugeon tests, measuring the permeabilities along horizontal direction, return the following values for the three main layers of soil, calculated as the geometric mean of the measures at different depths:

1. Marine sands: 6.8×10^{-7} m/s
2. Pyroclastic layer: 1.8×10^{-7} m/s
3. *Cappellaccio* and NYT: 4.15×10^{-7} m/s

Later, after the construction of the diaphragm walls, a dewatering test was carried out in the excavation area, which allowed the pumping system to be sized and the excavation to be carried out in dry conditions. A total of six pilot wells were installed in the station area within the existing diaphragm walls. The wells were 600 mm in diameter, and they were deep enough to get into the NYT deep layer. The results of the dewatering tests suggest significantly higher values of permeabilities for all the considered layers of soil with respect to site and laboratory investigations (Mormone *et al*., 2013). Moreover, the flow induced by this type of test is tridimensional, thus it suggests some considerations about the anisotropic behavior of the subsoil, especially for the tuff formation. A back-analysis of the test was conducted by Russo *et al*., (2014) where the permeability values of the soil layers were back-calculated by means of two bidimensional finite element models, representing longitudinal and transversal sections of the excavation. Isotropic permeability is suitable for describing the behavior of sands (sand deposit and pyroclastites), whereas for cappellaccio and NYT the best fit with field data was found assigning different permeabilities in horizontal and vertical directions; the resulting set of parameters is reported in Table 18.

Table 18. Permeability values producing the best fit with field data according to Russo et al., (2014).

Sand deposit		Pyroclastites		Cappellaccio		NYT	
10^{-6} m/s		10^{-6} m/s		10^{-6} m/s		10^{-6} m/s	
horizontal	vertical	horizontal	vertical	horizontal	vertical	horizontal	vertical
800	800	400	400	7	70	7	70

In addition to the already mentioned site and laboratory investigations, an extensive investigation campaign was conducted by Licata (2015) on soil samples collected on the same site at a depth of approximately 18 m bgl, corresponding to the soil overlying pyroclastites. It was aimed at studying the effect of particle fragility, relative density and confinement on the liquefaction potential of the sampled soil. In fact, according to Evangelista (2006) who reported data in terms of distribution of the liquefaction potential index (Iwasaki *et al*., 1982), Neapolitan costal area results characterized by a medium-high susceptibility to liquefaction. In Licata (2015) the sampling of the soil tested with cyclic triaxial tests was made by taking undisturbed block samples from the excavation front. Their size was large enough to consider specimens carved from the center of the block as undisturbed. Other material was subjected to grain size analyses. All the tested samples can be classified as sandy soil characterized by a variable silty fraction ranging between 10% and 45% and a gravelly fraction not exceeding 35%. The comparison of the grain size curves with the limit curves – suggested by the NTC 2008 for a preliminary screening of the liquefaction potential for soil (Tsuchida, 1970) –, shows that the entire fuse obtained falls within the limits characterizing the liquefiable soils with uniformity coefficient UC>3.5. In addition, before carrying out laboratory tests, assessment of liquefaction potential was made using semi-empirical methods for the estimation of cyclic resistance ratio (CRR) based on N_{SPT}, Q_c and V_s (appropriately corrected transforming them into normalized values, *i.e.*, $N_{1,60}$, Q_{c1} and V_{s1}, respectively, for an overburden stress equivalent to the atmospheric pressure) according to the formulations proposed by Idriss and Boulanger (2004). The functions described by the mentioned equations predict an increase of CRR with increasing values of the considered parameter, until an asymptotic value ($N_{1,60}$=30, Q_{c1}=180 and V_{s1}=215, respectively) considered as a threshold beyond which no liquefaction is expected. According to this semi-empirical evaluation San Pasquale site results susceptible to liquefaction if penetrometer data are considered. V_s-based assessment, instead, leads to conclude that no liquefaction will occur on the site. The latter has the advantage of using values coming from non-destructive tests, and generally leads to a more reliable estimation of *CRR* with respect to method based on CPT and SPT.

4.1.2. Structural station box and monitoring plan

The main shaft, 27 m deep, has rectangular plan (85×24 m^2), and in the middle of the long sides two – shallower – access shafts are realized (Figure 70); the excavation is bordered by a 5-story masonry building and a 8-story RC building on the north side (in the following it will be referred to as "building side" or BS), whose façades have a slope of approximately 6° with the tunnel axis and they are located at distances spanning between 19 and 28 m from the edge of the excavation and only 12 from the access shaft; on the south side ("sea side" or SS) the public park runs along the edge of the excavation.

The access shaft on the building side has trapezoidal shape and goes down up to 8 m bgl; the one on the seaside has rectangular shape and reaches 13 m bgl. Their retaining structures, realized before the excavation, consist of rectangular panels 22 m deep. Below the bottom of excavations jet grouting treatment were realized to ensure hydraulic isolation. The internal structures of access shafts have been realized with a bottom-up procedure. A graphical representation is given in Section 1-1 in Figure 73.

For what concerns the main pit, due to the water level placed at 1-2 m bgl, it has been built with a top-down procedure. The RC t-shaped diaphragm panels were installed, before the excavation began, reaching a depth of 50 m to achieve a penetration into the tuff necessary to ensure stability. The panels were placed at a center distance of 2.65 m, with a wing width of 2.8 m and a height of 3.2 m, and a wing and core thickness of 1.2 m, for a total of 6,7 m^2 in plan. Because of the huge dimension and depth of the panels (Figure 73), hydro-mill and bentonite slurry were used for excavating and sustaining the walls. Moreover, before the panels were constructed, the first 10 m of soil were treated using Cutting Soil Mixing (CSM) to improve mechanical properties of the soil.

The work lasted 6 years, from September 2008 until July 2014, except for architectural installations and finishes. The construction of the station went on with subsequent steps of excavation and installation of RC slabs, non-continuous, but equipped with eyelets to make possible the movement of excavating machines. The water level was constantly kept at least 5 meters below the current excavation bottom with a pumping system, sized based on the dewatering tests cited before. The internal walls of the station were built during the ascent phase, adjacent to the temporary retaining structure, without structural connections between them.

The construction phases, schematically listed in Table 19, are grouped in three main stages (Stage 1, Stage 2, Stage 3) corresponding to:

1. end of archaeological excavation, installation of diaphragm walls and TBM passage;
2. end of excavation of main and access shafts;
3. shutting down of the pumping system.

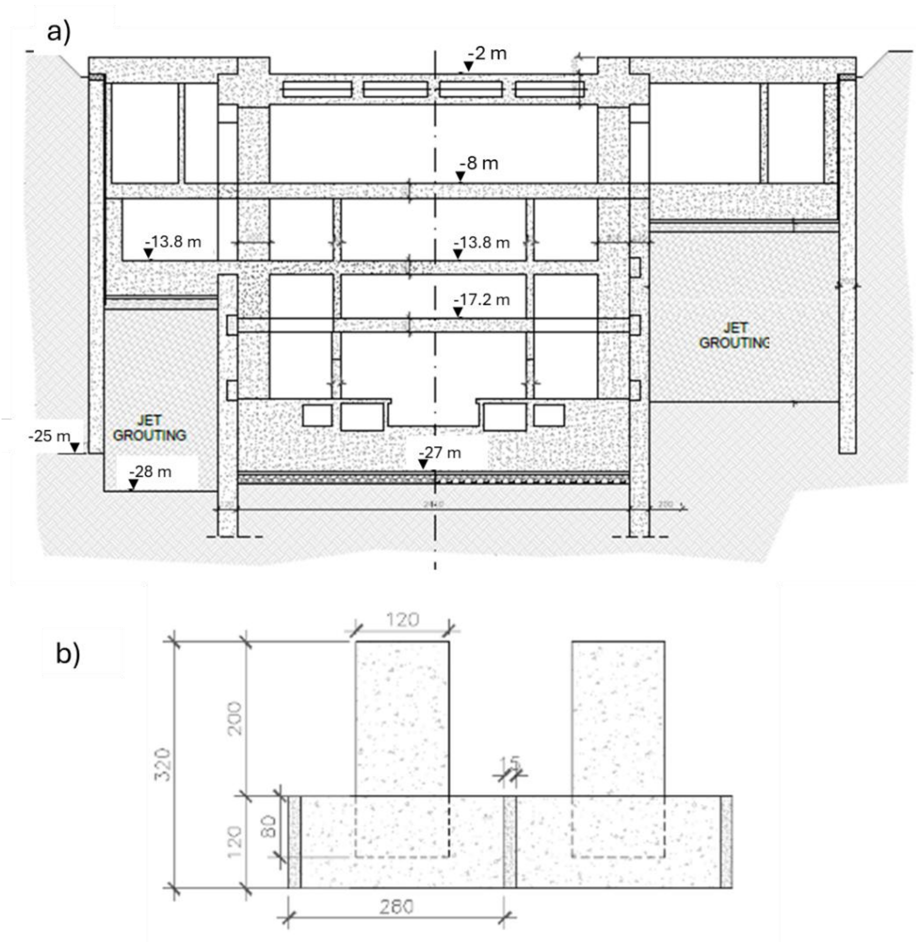

Figure 73. a) Section 1-1 (see Figure 70); b) cross section of diaphragm panels. Depths are reported in m bgl, dimensions of structural elements are expressed in cm.

The effect of this kind of work is interpretable looking at the effects on the surroundings and on the retaining structures of the shaft itself. Dewatering and excavation activities are both causes of subsidence around the excavation site. The water level inside and outside the excavation was constantly kept under control through monitoring of piezometers. The piezometers installed externally to the excavation at different distances from it, are affected by the dewatering, but they reflect relatively small values of groundwater lowering. Each piezometer has two measuring points where piezometric head is measured, at 15 and 30 m bgl respectively. The time histories of measured groundwater heads are represented in Figure 74, where the deep and superficial trend of external piezometers is reported together with the mean trend of the internal piezometers. Clearly the area outside of the excavation is scarcely influenced by the water level drawdown, whose effect is more visible for the deeper measuring points during the stages where the water level was lowered at -25 m asl and -30 m asl.

Table 19. Main stages of work

Stage	Duration	Excavation depth (main shaft)	Water level	Other Work
	15/09/2008 – 26/08/2009	-	undisturbed groundwater level	installation of diaphragm panels and formation of jet-grouting beneath the access shaft
	27/08/2009-10/07/2010	4 m (archaeological excavation)	4 m	archaeological excavation in access shaft areas, dewatering test in the main shaft
Stage 1	11/07/2010-22/03/2011	9 m	12 m	TBM passage and top slab casting
	23/03/2011-23/12/2011	11 m	14 m	casting of slab at 8 m bgl
	24/12/2011-20/01/2012	14 m	20 m	casting of slab at 13.8 m bgl
	21/01/2012-11/09/2012	17 m	25 m	casting of slab at 17 m bgl
	12/09/2012-28/09/2012	27 m (end of excavation)	30 m	-
Stage 2	29/09/2012-27/12/2012	-	30 m	excavation access shaft
	28/12/2012-22/10/2013	-	25 m	placement of a waterproof membrane at the shaft base and casting of the bottom slab

Stage 3	23/10/2013-24/07/2014	-	undisturbed groundwater level	Partial removal of intermediate slabs, completion of internal structures and cessation of groundwater lowering

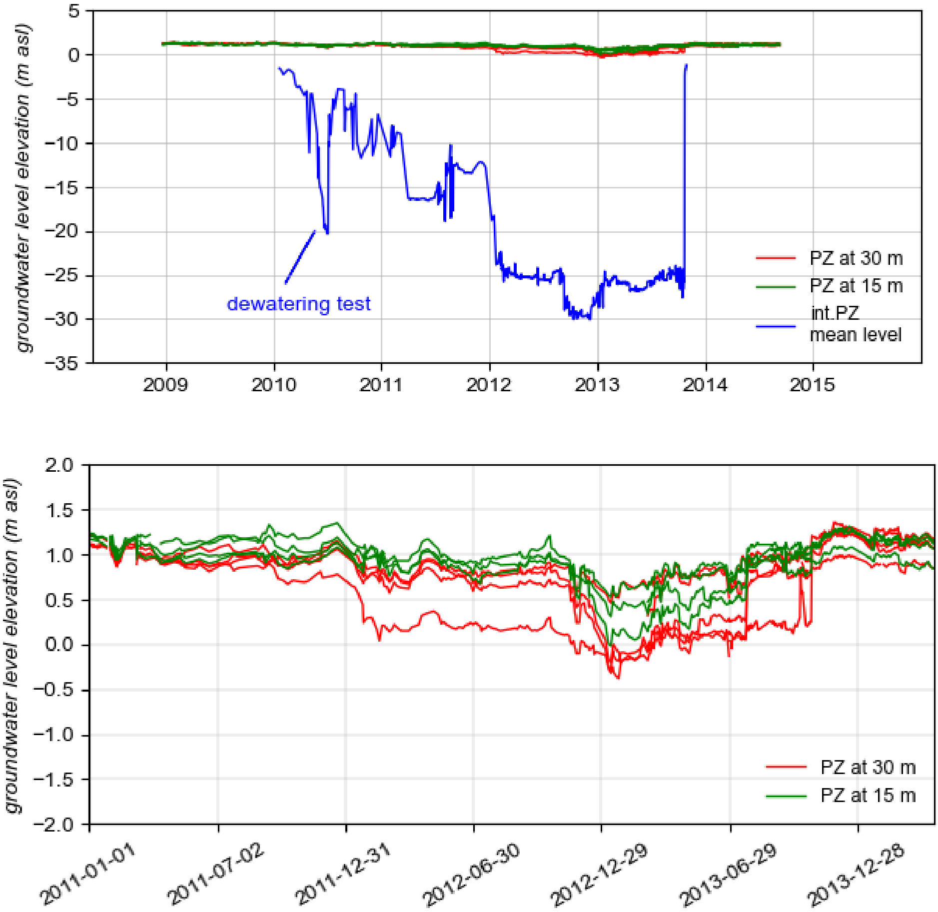

Figure 74. Upper: time history of groundwater head inside and outside of the excavation. Lower: zoom of the groundwater elevation registered by external piezometers between January 2011 and December 2013.

Benchmarks and leveling brackets were installed along the two alignments BS and SS, on buildings and sidewalks (their plan locations are indicated in Figure 70) to measure settlements of the buildings and of the ground level. In Figure 75 the settlement time histories registered during excavation, corresponding to some of the installed benchmarks, are reported as an example. The considered benchmarks are those exhibiting maximum settlement on each alignment (filled markers), placed in correspondence with the centerline of the excavation, and those placed in correspondence with the corner of the excavation on the west side of the station (empty markers). Settlements increase as excavation deepens, reaching a maximum of approximately 25 mm measured on the building side and of 17 mm on the seaside (Autuori, 2016; Russo *et al*., 2019); as expected the settlements are linked to the water table, in fact the minimum water level outside the station shaft was reached at the end of the excavation and it is approximately -0.5 m asl (Figure 74), which corresponds to maximum settlements. Then, the settlements decrease when the dewatering pumps are turned off. The comparison between the vertical displacements at the centerline and at the corner is aimed at highlighting the corner effect (Ou *et al*., 1996), strictly connected with the tridimensionality of the displacement field, which produces a diminishment of settlements around the corner of excavations. Similar trends are exhibited by the benchmarks placed in correspondence of the corner on the east side.

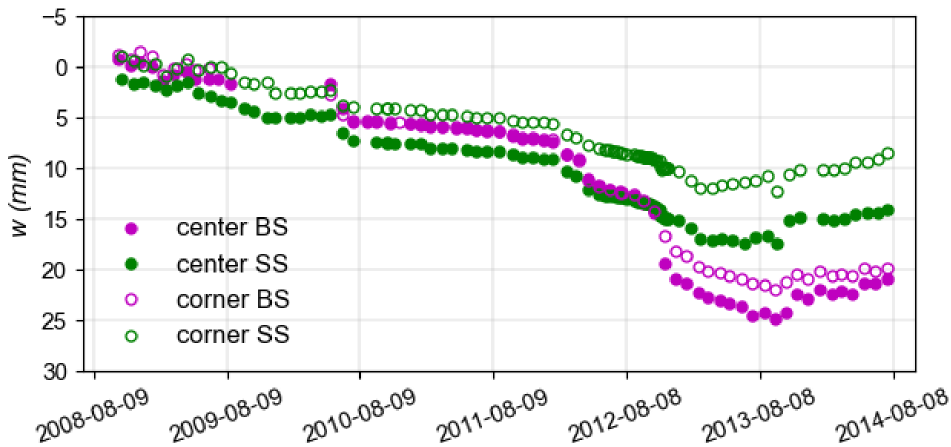

Figure 75. Time history of settlements registered by some benchmarks during the duration of works.

The displacement of soil produces, in turn, stresses and horizontal displacements on the retaining system. To monitor the displacements external and internal inclinometers, both represented in Figure 70, have been installed and monitored. In Figure 76 three monitoring sections -AA’, BB’ and CC’-, individuated by the positions of internal inclinometers, are represented, together with the inclinometer profiles related to Stage 1 and Stage 2 (see Table 19). The entity of maximum registered horizontal displacement is 35 mm in the centerline section on the building side. In general, the profiles exhibit similar shapes (with the only exception being the inclinometer belonging to section CC’-BS, Figure 76, which shows anomalies probably due to incorrect installation of the inclinometer tube) and values that decrease toward the edges of the shaft, which is further evidence of the three-dimensional nature of the deformation problem.

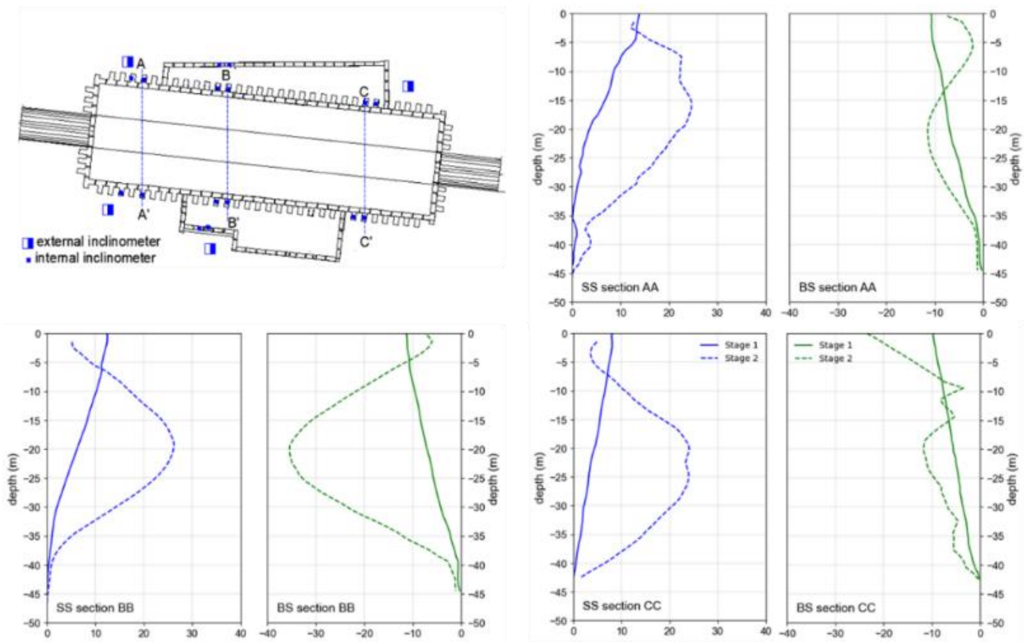

Figure 76. Monitoring sections and inclinometer profiles in stages 1 and 2 (Table 19).

4.2. Static back-analysis and damage of buildings

The static back-analysis of the excavation was carried out on the FE software Plaxis 3D (Bentley, 2024 – Plaxis 3D, Ultimate), where the soil domain, the station structures and the buildings were modelled using information available from site and laboratory tests, and literature. The model (Figure 77), has a plan dimension of 200×140 m² and a depth of 70 m and consists of 346417 ten-node tetrahedral elements with an average size of 3.26 m, with a total number of nodes equal to 539451; the mesh size is differentiated with smaller elements in the immediate vicinity of the excavation and larger ones further away. First, a so-called free field analysis (*i.e.*, without buildings) was carried out to calibrate the model by comparing the results with the already exposed monitoring data. After, the two buildings overlooking the excavation (see Figure 69 and Figure 70) have been modeled in detail to explore the interaction of the structural system with displacement field induced by excavation and dewatering. A total number of 20 calculation phases was defined in the software attempting to respect as closely as possible the sequence of operations carried out on site, albeit with the necessary simplifications. Three main operations are simulated which are:

1. Excavation
2. Installation of slabs
3. Lowering of the water level and the resulting filtration motion

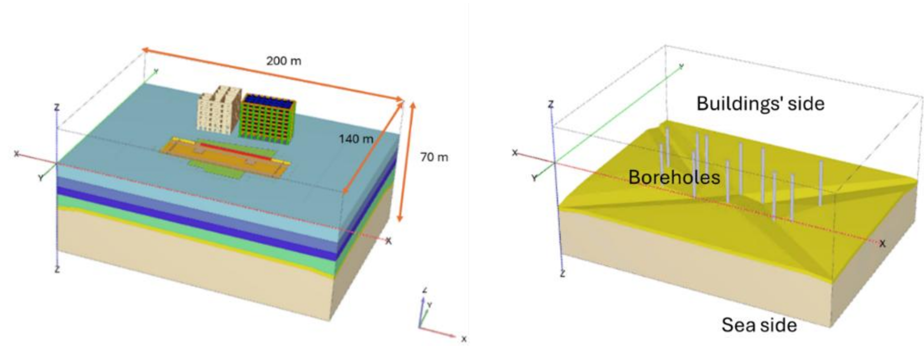

Figure 77. Left: perspective view of the numerical model; right: cappellaccio (and NYT) top surface.

4.2.1. Numerical model: soils

The non-linear elastic-plastic *Hardening soil model with small strain stiffness* (HSss) (Benz, 2007) was adopted for the sandy soils of the upper layers (marine sands and pyroclastic layer), while in this case the elastic perfectly plastic Mohr-Coulomb law, because of the small deformation registered, was deemed suitable for the description of the underlying soft rocks: *cappellaccio* and NYT. For what concerns the stratigraphy of the soil domain built in the numerical model, it is schematized assuming that marine sands can be divided in three layers with different stiffness characteristics, below them a layer of pyroclastic sands is found lying on cappellaccio and NYT, as represented in Figure 78.

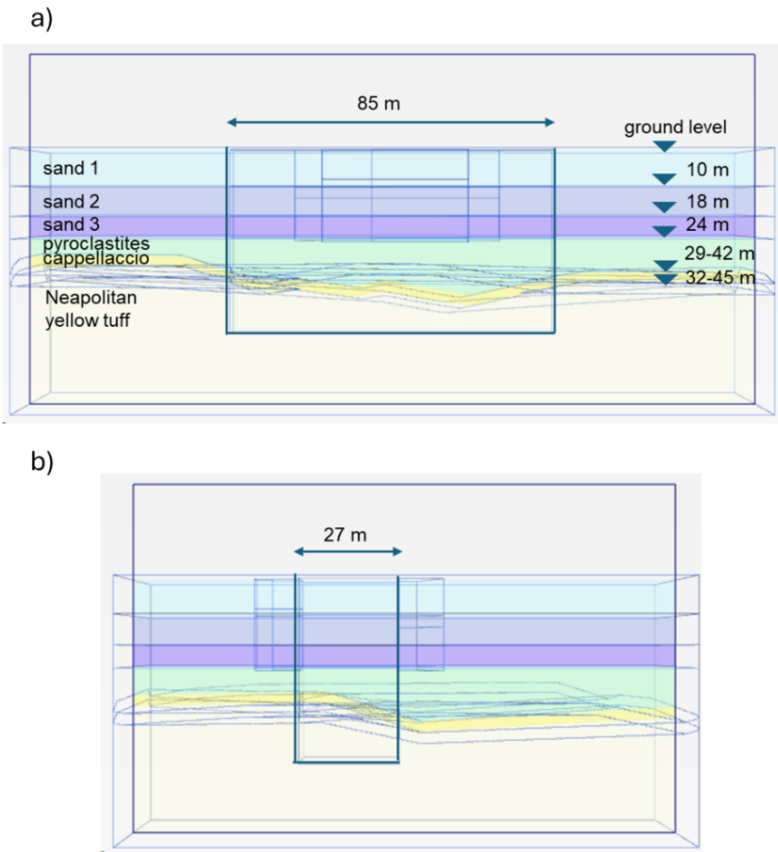

Figure 78. Longitudinal (a) and transversal section (b) of the numerical model with visible stratigraphy and structure contours.

The layers of marine sands are horizontal in the model, whereas the non-horizontal surface of *cappellaccio* and NYT has been replicated using information from boreholes (Table 17), linearly interpolated by the software itself in the middle between two boreholes. The three layers of marine deposits have been identified based on CH and SDMT results, already presented in Figure 71. The same assumption on the marine deposits' layers had already given good agreement with monitoring data in L'Amante *et al*., (2012), where the same software had been used to study horizontal displacements induced by the installation of a diaphragm panel in the site of San Pasquale, and a calibration of soil properties had been done by using SDMT. In that case, however, the Hardening soil model (HS) (Shanz, 1998), instead of HSss model, was used. HS, neglecting the stiffness of soil at small strain level, tends to overestimate horizontal displacements of retaining walls, and settlement troughs can be obtained that are too flat and extended (Benz *et al*., 2009). HSss, already presented in *Chapter* I of this thesis, describes the decay curve of initial soil shear modulus, thus it requires two additional parameters, being G_0, the initial shear modulus, and γ_{07}, that is needed to calibrate the decay curve, being the shear strain corresponding to a decay of shear modulus of 28% with respect to its initial value. Then, stiffness parameters required to describe a soil with HSss model are 4, in addition to those related to strength (c' and φ'). All of them are listed in Table 20.

Below the bottom slab of two access shafts, volume of an impermeable soil material simulating jet grouting treatment are activated during the calculation. In Table 21 the parameters of Mohr Coulomb materials are reported. *Ad hoc* interface elements were also created for *cappellaccio* and NYT, with cohesion values reduced by a factor 10, to prevent the structures from sticking to the ground; interfaces of sandy soils are defined, instead, by reducing strength properties of the adjacent soil by a factor 3 ($R_{interface}$ = 0.67).

Table 20. Mechanical properties for soils described by HSss model.

soil/parameter	γ_{unsat}-γ_{sat}	E_{50}^{ref}	E_{oed}^{ref}	E_{ur}^{ref}	ν_{ur}	G_0	$\gamma_{0.7}$	c'_{ref}	φ'
	kN/m³	MPa	MPa	MPa	-	MPa	%	kPa	°
Sand 1	17-18,5	37,0	37,0	110,0	0,2	51,0	0,02	0	38,8
Sand 2	17-18,6	24,8	24,8	74,3	0,2	74,0	0,02	0	38
Sand 3	17-18,7	15,4	15,4	46,10	0,2	220,0	0,02	0	38
Pyroclastites	14-16	9,4	9,4	28,0	0,2	140,0	0,02	0	37,2

Table 21. Mechanical properties for soils described by Mohr Coulomb model.

soil/parameter	γ_{unsat}-γ_{sat}	E'_{ref}	ν'	c'_{ref}	φ'
	kN/m³	MPa		kPa	°
Cappellaccio	14-16	800,00	0,3	150	27
TGN	14-16	2160,00	0,3	500	27
Jet grouting	16	50,00	0,3	200	36

E_{ur}^{ref} , E_{oed}^{ref} and E_{50}^{ref} are the elastic moduli of unloading-reloading, oedometric and that secant corresponding to 50% of ultimate deviatoric stress, q, in a q/ε plane, respectively, defined at a given reference mean stress p_{ref}, by default equal to 100 kPa. They have been derived from oedometric modulus, M, with the elastic relationship described in Eq. (33):

$$E_{ur}^{ref} = \frac{(1+\nu)(1-2\nu)}{(1-\nu)} M \qquad (33)$$

M, in turn, is retrieved by SDMT (Figure 71) as a function of the dilatometric modulus E_D, through the dilation index I_D. E_{50}^{ref} and E_{oed}^{ref} are set equal to $E_{ur}^{ref}/3$ (after parametric analyses carried out by L'Amante *et al*., 2012). The initial shear modulus G_0 is retrieved as a mean value of the data from SDMT and CH elaborated as shear wave velocity; for depths greater than 30 m only CH values are available. Lastly, shear strain γ_{07}, is obtained by decay curves already presented in the previous chapter (Figure 54b).

Based on the experimental and numerical results already exposed in section 4.1.1, values of permeability for all the soil materials have been set and are reported in Table 22. The anisotropy of NYT is due to the existence of vertical fractures called *scarpine*.

Table 22. Permeability of soil materials.

Sand 1, Sand 2, Sand 3			Pyroclastites			*Cappellaccio*, NYT		
m/day			m/day			m/day		
k_x	k_y	k_z	k_x	k_y	k_z	k_x	k_y	k_z
52	52	52	0.9	0.9	0.9	0.65	0.65	6.5

4.2.2. Numerical model: structures

Bulkheads and slabs are rendered in the numerical model with plate elements, whose properties have been derived based on what already exposed in section 1 of this chapter. Therefore, isotropic elastic materials have been used for the rectangular shaped bulkheads of access shafts, and slabs; orthotropic elastic material with an equivalent thickness, instead, is used for main shaft bulkheads in order to replicate the anisotropic behavior linked to the t-shape of diaphragm panels, some more details about the adopted procedure are reported in *Appendix 1*. Main properties of the structural members are reported in

Table 23.

Table 23. Mechanical properties and equivalent thickness of slabs and bulkheads

Plate element	d	E_1	E_2
	m	*GPa*	*GPa*
Slabs	0,90	30,00	30,00
Perimetral bulkheads (main shaft)	2,16	49,50	5,14
Perimetral bulkheads (access shafts)	1,00	30,00	30,00

Lastly, the bottom slab has been modelled as a solid element 3 m thick with the properties of reinforced concrete (unit weight of 25 kN/m^3, E = 30 GPa).

4.2.3. Numerical model: buildings

The RC building (Figure 69 and Figure 70) facing the excavation dates back to 1950s, has a rectangular plan of 34×15 m^2, with nine columns on the long side and four on the short side. It consists of eight stories, which measure 3.2 m in height, except for the ground floor, with a height of 4.2 m. According to Castaldo and de Iuliis (2013), the external beams are emerging beams with a cross-section of 0.3×0.5 m^2, while the internal beams are thick beams with a cross-section of 0.3×0.3 m^2. The internal columns have a cross section of 0.5×0.5 m^2, the external ones of 0.5×0.8 m^2. Beams and columns are reproduced in the model with linear elastic beam elements, with equivalent rectangular cross sections and an elastic modulus E of 20 GPa (which is a typical value for concrete used in those years) and the Poisson coefficient equal to 0.2.

No information is available about slabs or foundations, however, according to code prescription on maximum allowed inflexion, the height of the slabs should be approximately 30 cm, derived by dividing the maximum length by 25. In the numerical model joists and hollow bricks were not simulated, instead a rectangular isotropic plate was used to simulate slabs; therefore, an equivalent thickness of 10 cm of solid reinforced concrete was assumed, with a Young's modulus equal to 25 GPa. Foundations have been assumed to be shallow, thus a plate with equivalent thickness of 1 m has been used to simulate it, with E = 20 GPa. Unit weight of 25 kN/m^3 was assigned to all the materials representing reinforced concrete. Front and perspective view of the building in the numerical model are represented in Figure 79.

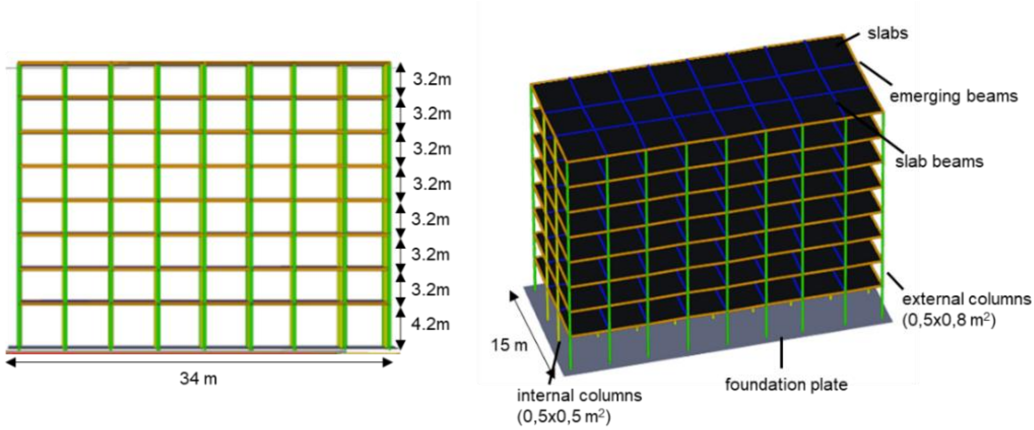

Figure 79. RC building as schematized in the numerical model with dimensions, front (left) and perspective (right) views.

The masonry building overlooking the excavation is a historical building, built in 1689, named Ludolf Palace, built with bricks made of Neapolitan yellow tuff very common in Neapolitan architecture until the end of the 1800s. The knowledge of its plan and geometrical details about the disposition of bearing walls and masonry bands comes from Ferraro (2012); in the model the structural system has been simplified, disregarding stairs and slabs. In Figure 80 a perspective and a plan view of the building as modelled are given, together with dimensions of interest. Masonry has an anisotropic behavior due to the presence of strong elements (stone blocks or bricks) and weak joints (mortar or dry joints), where more likely fracture happens. To make it possible to accurately study the distribution of stresses induced by displacements in masonry elements, the user defined Jointed Masonry Model JMM (Lasciarrea *et al*., 2019) implemented in Plaxis 3D has been used as constitutive law. It is formulated in the context of simplified multilaminate linear elastic-perfect plasticity to account for the anisotropic irreversible behavior of the material while assuming isotropic elasticity (Amorosi *et al*., 2021). The model allows identification of three preferred planes of discontinuity along which the behavior of the masonry is described using a modified Mohr-Coulomb criterion, where a tension cut off can be set to consider the weakness of the joints. The model assumes initial isotropic elastic behavior, followed by an anisotropic plastic phase linked to discontinuities between blocks. The failure surfaces are characterized by very limited shear strength and tensile strength (or none at all in the case of dry masonry). The elastic properties of JMM are derived using homogenization techniques that consider the mechanical characteristics of both blocks and mortar joints (De Felice & Malena, 2019). The definition of discontinuity direction is made with two angles (Figure 81):

- Dip angle indicates the inclination of the plane with respect to the horizontal plane (xy). This parameter is essential for correctly describing the orientation of head joints which can be arranged with different geometries depending on the masonry texture used.
- Strike angle defines the orientation of the plane with respect to a reference axis (usually the x axis). This parameter is particularly useful for modeling bed joints.

In order to model the behavior of walls parallel and orthogonal to the building façade, two materials were defined, with different dip and strike angles (the angles set consider the inclination – of 6° – of the building alignment with respect to the excavation main axis). Main parameters adopted for the JMM materials are reported in Table 24 and Table 25.

Table 24. Jointed masonry model – brick properties

Brick properties					
G	v	c_{mc}	ϕ_{mc}	ψ_{mc}	$tens_{mc}$
kPa	-	kPa	°	°	kPa
1.03E+06	0.18	1090	29.8	0	376

Table 25. Jointed masonry model – masonry properties

Masonry of main façade						Masonry of orthogonal façade					
Plane 1						Plane 1					
$1{:}\ \alpha_1$	$1{:}\ \alpha_2$	c_1	ϕ_1	ψ_1	$tens_1$	$1{:}\ \alpha_1$	$1{:}\ \alpha_2$	c_1	ϕ_1	ψ_1	$tens_1$
°	°	kPa	°	°	kPa	°	°	kPa	°	°	kPa
95.85	90	100	21.8	0	29.5	5.85	90	100	21.8	0	29.5
Plane 2						Plane 2					
$2{:}\ \alpha_1$	$2{:}\ \alpha_2$	c_2	ϕ_2	ψ_2	$tens_2$	$2{:}\ \alpha_1$	$2{:}\ \alpha_2$	c_2	ϕ_2	ψ_2	$tens_2$
°	°	kPa	°	°	kPa	°	°	kPa	°	°	kPa
0	0	100	21.8	0	29.5	0	0	100	21.8	0	29.5

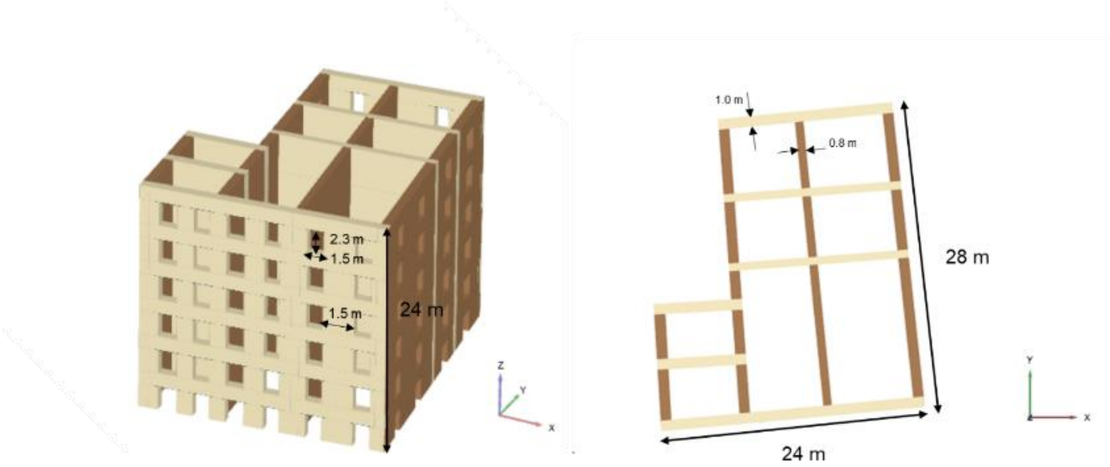

Figure 80. Masonry building in the numerical model with dimensions, perspective (left) and plan (right) views (different colors indicate different material, with different dip and strike angles).

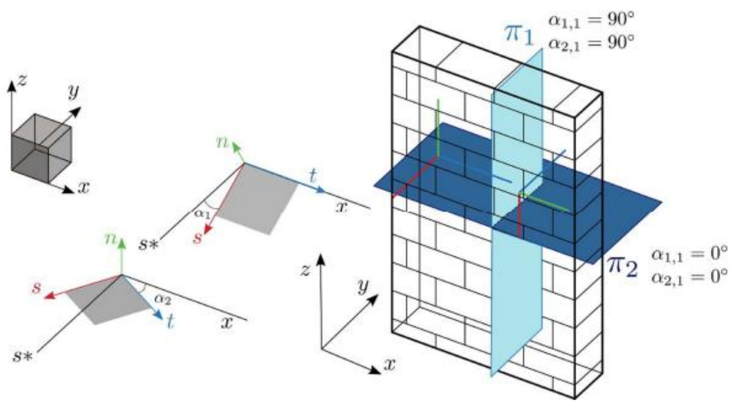

Figure 81. Definition of plane of discontinuity (after Pepe et al., 2020)

4.2.4. Numerical model: water table management

The water table in the model is placed 1 m below the horizontal ground level. The lowering of the water table, and the resulting filtration motion, have been obtained creating a user defined water table only in the area occupied by the main shaft and imposing a steady state groundwater flow during the phases where water level was lowered. Regarding access shafts, the water level was lowered during the archaeological excavation of the main pit; during the excavation they are hydraulically isolated by jet grouting caps. In Figure 82 a picture of the model is reported: the global water table (pink surface) is placed at 1m bgl and three different user defined water tables are created in the excavation area, at 13, 24 and 30 m bgl respectively.

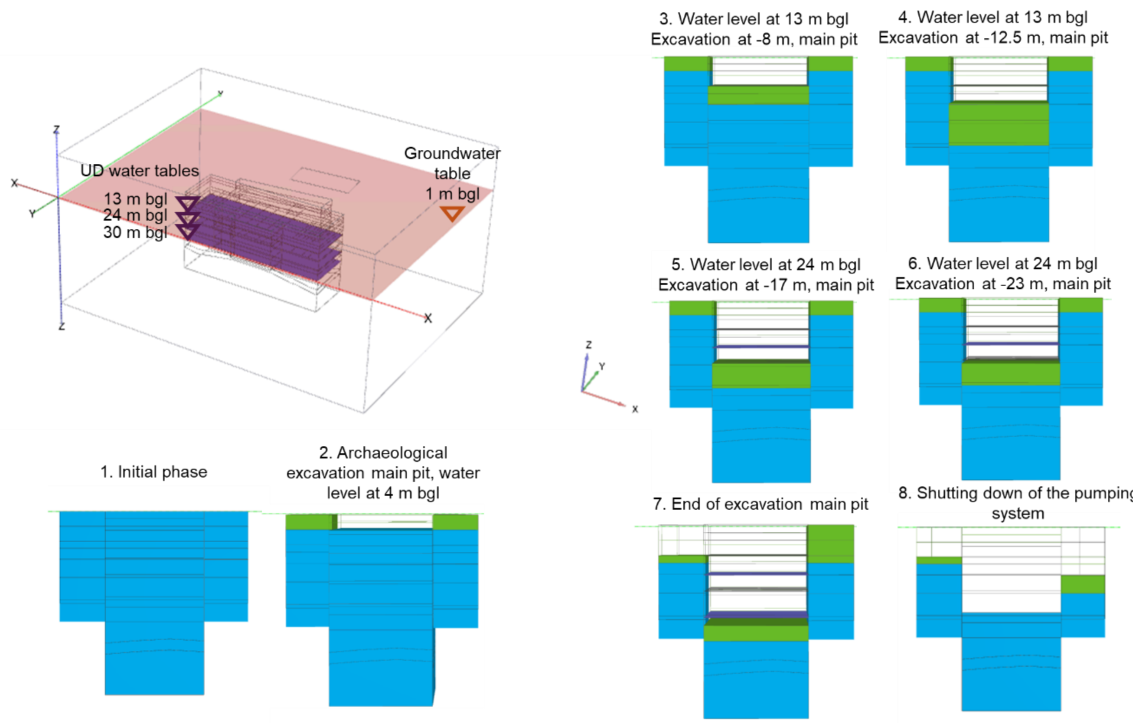

Figure 82. Upper left: numerical model with indication of global water level and user defined (UD) water level. Lower left, and right: soil volumes corresponding to access and main shafts in sequential calculation phases, green color indicates soil volumes where no water pressures are defined, blue color indicates saturated soil.

4.2.5. Computed and field displacements

Settlements and horizontal displacements

The first analysis was conducted in free field conditions using the mechanical properties reported Table 20 for sands. For NYT and *cappellaccio*, instead, higher values of stiffness E'_{ref} were used, respectively equal to 6.5 GPa and 1 GPa, calculated using V_S from SDMT and CH (L'Amante *et al.*, 2012). The comparison of the numerical results and field data, especially inclinometer profiles, suggested to lower these values, and, through a trial-and-error procedure, the values reported in Table 21 were defined and used in the subsequent analyses. The change of tuff stiffness produces an effect mostly on horizontal displacements, while ground level vertical displacements are not affected by it.

The three main stages under consideration correspond respectively to: (*1*) archaeological excavation (-4 m bl), (*2*) excavation of the main shaft down to -15 m bgl, (*3*) reaching the bottom of the excavation (-27 m bgl), where field data register maximum settlements. Figure 83 shows vertical displacements computed by the free-field numerical model at the end of the excavation of the main shaft (*3*): settlement troughs mainly develop along the long sides of excavation, with maximum values concentrated on the building side and comprised within 30 mm, it is clearly visible the tridimensional distribution of displacements that fade away near the corners.

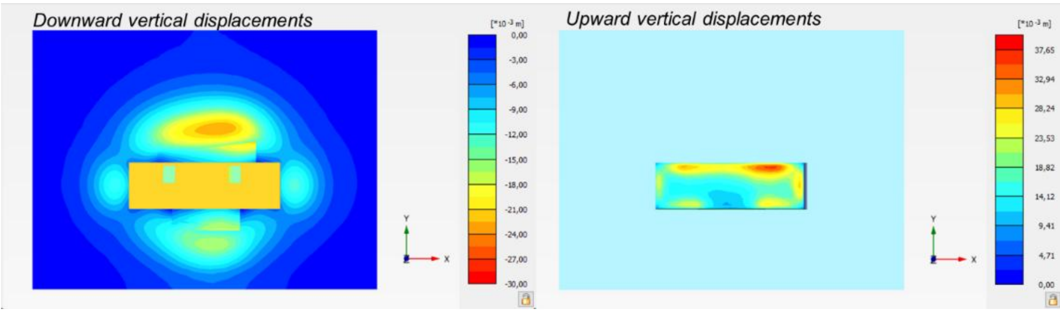

Figure 83. Left: downward displacements at the ground level at the stage (3). Right: upward displacements at the bottom of the excavation (stage (3)).

In Figure 84 seaside and building side settlement troughs at different excavation stages in free field (FF) conditions are reported. The curves are extracted at model coordinates corresponding to the alignments of benchmarks. The numerical curves are compared, in figure, with the field data (empty markers). The agreement between recorded and calculated data is very good, with maximum values perfectly captured by the software, which only slightly overestimates the displacements in (*1*). The rotation attributable to the angle between excavation shaft and buildings' facades is also well reproduced. However, a rather evident flattening of the curve can be observed on building side field data in stage (*2*) due to the stiffness of buildings, which, obviously, is not reproduced by the calculations but can assume its own importance when it comes to the evaluation of deflection ratio for the assessment of buildings' damage.

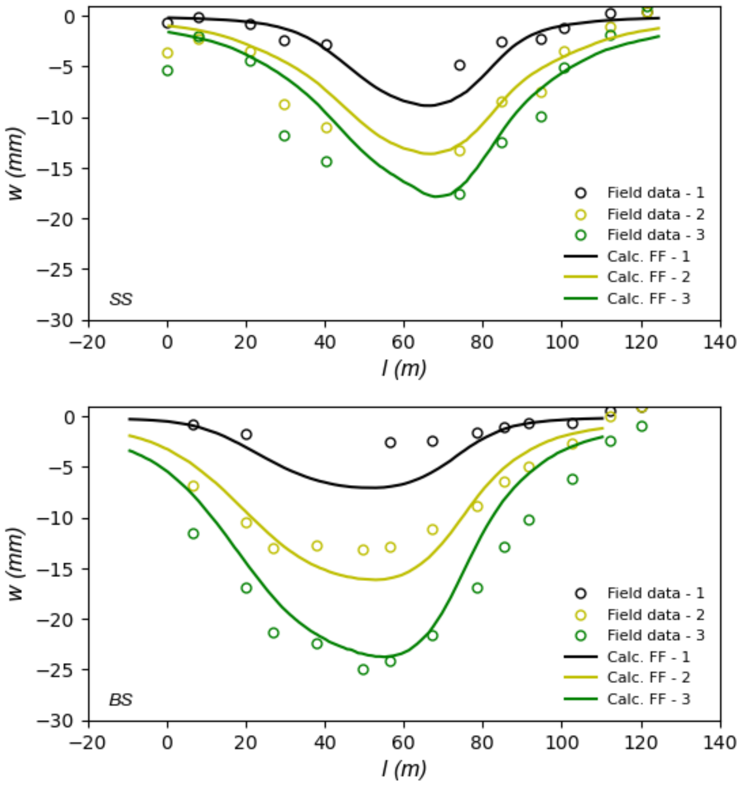

Figure 84. Seaside (SS) and building side (BS) settlement trough

Therefore, in Figure 85 the plan view of downward displacements produced by the model with the buildings considered is reported: the settlement trough appears more distributed and extended than in FF conditions and the maximum values are encountered right below the facade of the buildings.

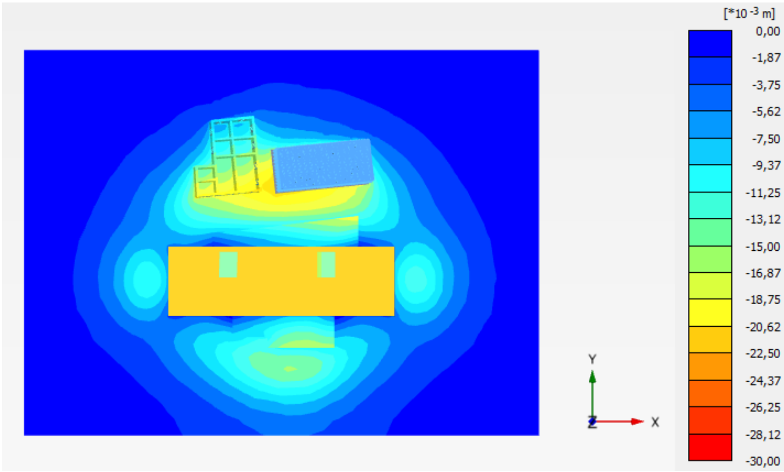

Figure 85. (stage 3) vertical downward displacements, plan view of the model with buildings.

In Figure 86 the settlements retrieved by the numerical model accounting for the buildings are reported and compared with experimental data. The flattening obtained by introducing the buildings is consistent with field measurements, even if the rather sharp discontinuity marking the end of the two buildings is not found in recorded data, since other buildings are present, that are not considered in the model.

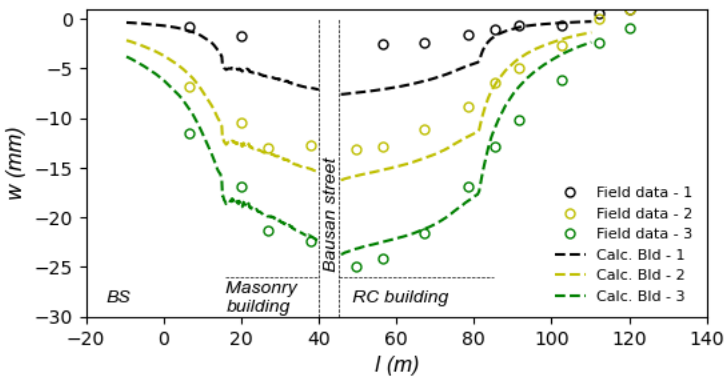

Figure 86. Settlement trough from the calculation with the buildings considered (Calc. Bld in figure)

Because of the good agreement between numerical and experimental data, it is possible to assume that even for settlement curve retrieved in direction orthogonal to the excavation is reliable, even if no experimental evidence is available. A comparison between curves obtained with and without buildings along the lateral side of the buildings (along *Bausan* Street) are reported in Figure 87. While along the main façade introduction of buildings produces only a flattening of the settlement profile, in addition to a slight reduction of maximum settlement, along the building side the shape changes, leading to a translation of the concavity change at a greater distance from the excavation edge in the analysis carried out with buildings, because of the wider distribution of settlement induced by building's stiffness.

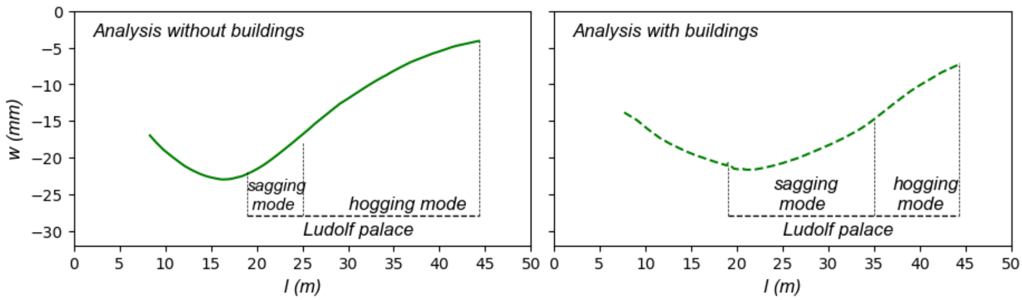

Figure 87. Settlement trough along the direction orthogonal to the excavation. Left: free field analysis. Right: analysis with buildings

A correct evaluation of both maximum value and shape of the settlement trough is the basis for the assessment of eventual damage of buildings connected to differential settlements. In this case the conjunction of tridimensional analysis and the use of a constitutive model suitable for masonry allowed an evaluation of the state of damage expected with these levels of displacements.

In Figure 88, Figure 89 and Figure 90, horizontal displacement profiles are reported. The figures are related to sections AA', BB' and CC' as represented in Figure 76. The calculation results, referring to stage *1* and *3*, are compared with the experimental data already represented in Figure 76. Except that for section AA' and CC' (where inclinometer measurements may be affected by an incorrect installation of the pipe) on the building side, numerical analyses underestimate recorded displacements of approximately 50% in *2*. None of the represented profiles show a significant effect of the struts, and the displacements are overall small and comparable with the observed settlements, as expected based on literature data reported in *Chapter 2* and with recorded data of similar works in the city of Napoli. However, since some years passed between installation of diaphragm walls and excavation, it was deemed acceptable to consider creep of concrete which, under static loads, produce a decrease of stiffness that can be estimated as a reduction factor of concrete Young modulus, according to Italian building code NTC 2018.

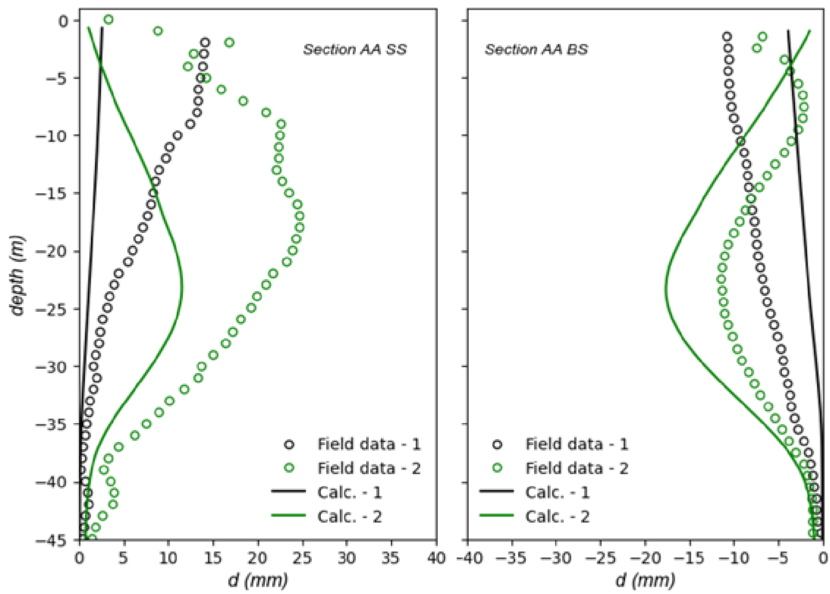

Figure 88. Horizontal displacements section AA' (see Figure 76)

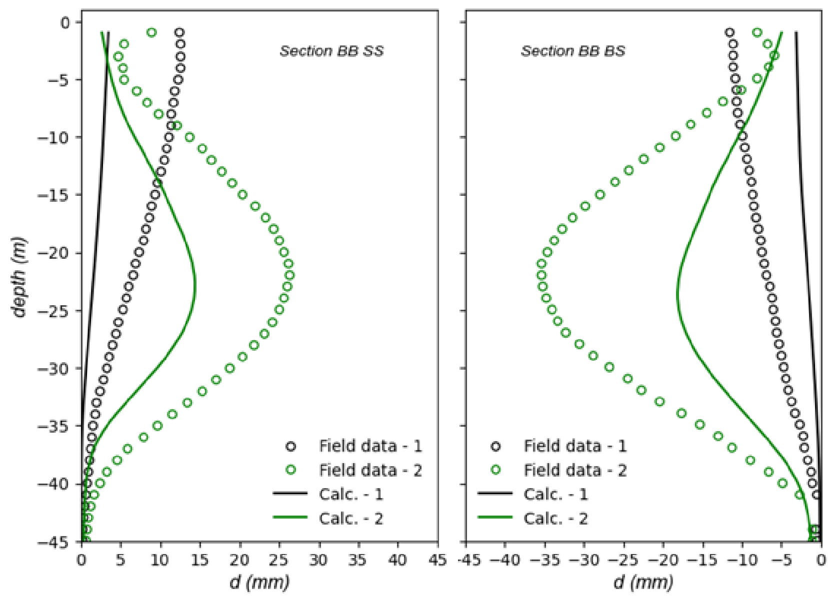

Figure 89. Horizontal displacements section BB' (see Figure 76)

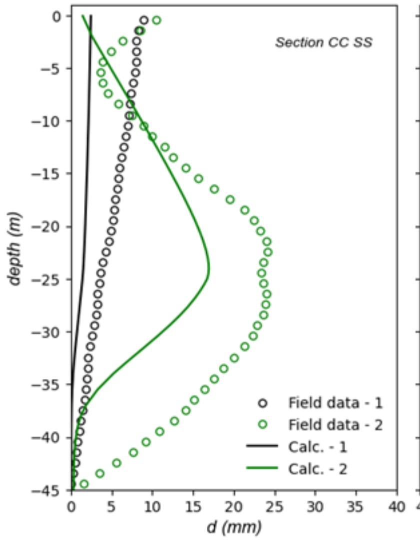

Figure 90. Horizontal displacements section CC' (see Figure 76)

Therefore, in the FE analysis a coefficient of 2 was used to reduce *E* of concrete: the agreement between calculated and recorded data improved significantly in horizontal displacements adjacent to the diaphragm walls, and results for section BB (the one presenting the most significant discrepancies) are reported in Figure 91. The discrepancies are significantly reduced, and the agreement is completely satisfactory, which indicates the importance of considering creep effects.

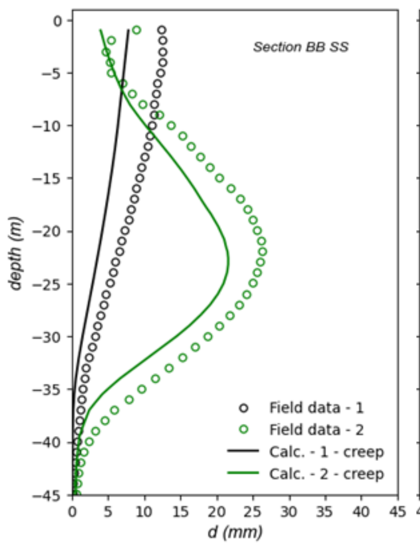

Figure 91. Horizontal settlements in section BB': calculated vs measured. Creep effect included in calculations.

Considering creep effect in the material properties, however, produces an increase of displacements in the immediate vicinity of the retaining walls, while settlements at the distance corresponding to the building facades, are not affected by it.
Lastly, the water flow at the excavation bottom corresponding to different water level drawdown into the main pit are plotted in Figure 92. The results are in agreement with the value of 25 l/s measured in site at the end of the excavation.

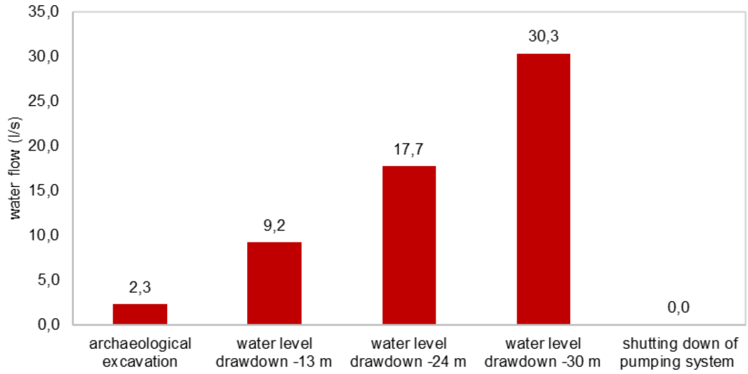

Figure 92. Vertical water flow at the bottom of the excavation, different stages

Evaluation of damage induced on Ludolf Palace and the adjacent RC building

In the present paragraph an assessment of damage based on limiting tensile strain method (LTSM) is used for evaluating the state of damage related to excavation-induced displacements on Ludolf Palace. The method in its various forms, already introduced in *Chapter 2* and applied in C*hapter 3*, schematizes the building as an equivalent isotropic elastic beam with a planar deformation mode, therefore it must be applied separately along the two directions. The assessment of damage state is based on the evaluation of maximum principal tensile strain of a building unit (as defined by Son and Cording, 2005) and the comparison of the obtained values with experimentally obtained damage classifications, like the one presented by Son and Cording (2005). Eqs. (30), (31) and (32) reported in C*hapter 3*, are applied here for the calculation of maximum principal horizontal tensile strain (Burland and Wroth, 1975), according to the general assumptions of the method, (*Chapter 2*) and the assumption of neutral axis at centerline of the section in case of sagging, or at the bottom of the beam in case of hogging, and Poisson coefficient equal to 0.3. This formulation, with respect to that proposed by Son and Cording (2005) allows to overcome the necessity of visible cracks to calculate θ_{max}. The horizontal strain ε_h of Eq. (31) is the calculated as the maximum difference between horizontal displacements retrieved by numerical analyses of two consecutive points of four total for each side, arbitrarily chosen along the building wall, so that they are nearly equally spaced, as indicated by red squares in Figure 93. The assessment was conducted on two sides of the building (main façade, overlooking the excavation, and lateral side along *Bausan* Street, where subsidence was computed and compared with the field data). Consistently with the elastic assumption about building behavior at the base of the approach, the free field settlement profile of the last excavation stage (3) was used for the estimation of strain, incorporating effect of masonry stiffness with the elastic moduli *E* and *G* reported in the formula above.

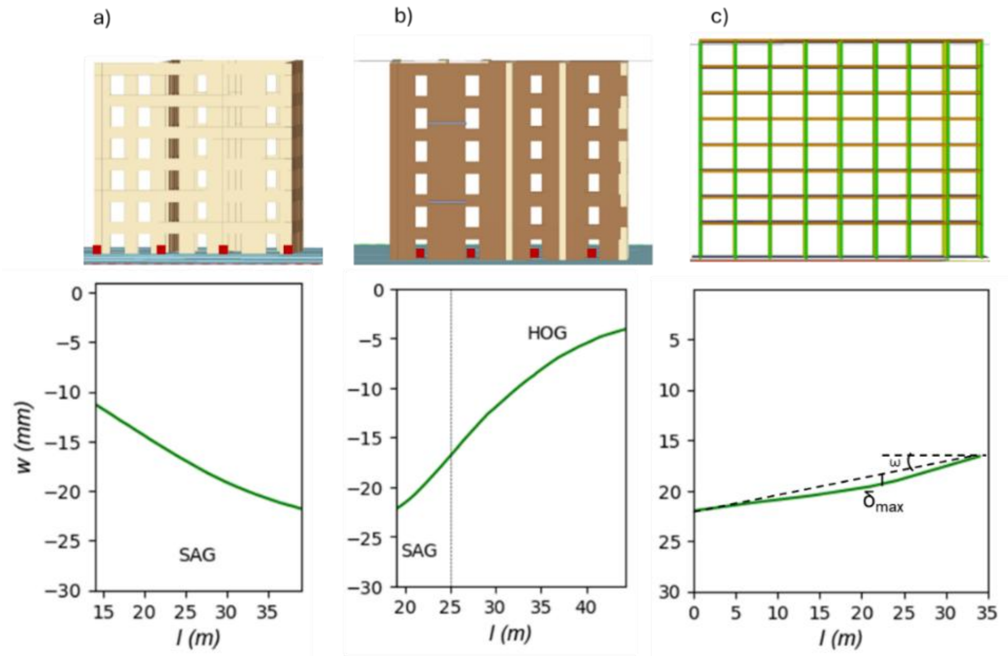

Figure 93. a) main façade of Ludolf palace; b) lateral side of Ludolf palace; c) framed structure.

The heigh of the equivalent elastic beam was kept equal to the total heigh of the building (24 m), therefore elastic moduli were recalculated with the aim of obtaining equivalent values, reduced with respect to those attributed to the masonry material in FE model, to take into account openings within the assumption of continuous equivalent elastic beam:

$$E = 1696\ MPa$$

$$G = 652.3\ MPa$$

The main façade undergoes a sagging deformation, along all its length (Figure 84 and Figure 86); the lateral side, instead, exhibits a small upward inflection (sagging mode) in the portion closer to the excavation for a length of 10 m, in the remaining part it is in hogging mode deformation (Figure 93), for a length of 18 m. Along both the alignments, however, flexural total strain constitutes the maximum one, and in Table 26 values of maximum tensile strain for the two sides of the building are reported.

Table 26. Differential settlement parameters for damage estimation according to Son and Cording (2005).

Alignment	Deformation mode	$\frac{\Delta}{L_i}$ (%)	ε_h (%)	$\varepsilon_{h,max}$(‰)	Damage
Main façade	Sagging	8×10^{-3}	0.07	0.80	2
Lateral side	Sagging	0.096×10^{-3}	0.019×10^{-3}	0.08	0
Lateral side	Hogging	0.14	0.065×10^{-3}	1	2

Son and Cording (2005) proposed a classification of damage dividing the level of damage in five ranges of critical tensile strain values, going from a "*negligible*" state of damage (indicated as 0 in Table 26) to "*severe or very severe*". Level 2 indicated in Table 26 corresponds to "*slight*". It is worth recalling that structural damage can occur even without cracking, with other occurrences such as jammed doors or loss of joist bearing.

Referring to framed structures, instead of inflexion *Δ/L*, the parameter usually taken as an indicator of damage is angular distortion or relative rotation *β*, as defined in chapter 2. Shape of settlements under the framed building overlooking the excavation is represented in Figure 93, where also maximum value of differential settlement δ_{max} is indicated. It is however small, being equal to 0.00003, which is two orders of magnitude lower than the lower limit proposed by Skempton and MacDonald (1956) for architectural damage (*i.e.*, damage to infills) in RC buildings.

4.3. Coupled dynamic analyses

Dynamic analyses, also here, as in the case of Chiaia station (C*hapter 3,* section 3.3), were conducted on a slightly different numerical model, simplified with respect to that used for static back-analyses. The reason of this simplification is twofold: on one side practical considerations suggest to simplify models for fully coupled dynamic analyses as much as possible due to very long calculation time, that are made even longer if mesh problems (like those induced by very small elements created in correspondence of sharp edges) are encountered; on the other side a simpler model, still accounting for the main aspect of the case study regarding soil properties and construction sequence of the station, can be useful for drawing observations of practical and more general applicability. The simplifications and main modifications adopted are listed below:

- Access shafts are not considered in the model: the presence of irregular excavations makes it quite difficult to standardize a parameter of the analysis known to be significant, *i.e.* the distance from the excavation edge. Moreover, their shallow depth and reduced plan dimensions can be considered relatively irrelevant in the modification of seismic wave propagation with respect to the effect produced by the main excavation.
- The soil layers have been modeled as horizontal assuming that the tuff top surface is placed at a depth that is approximately the mean value of that retrieved by boreholes (42 m bgl): considerations about the mesh at the boundaries, where soil-dependent surface loads have been created, have driven this choice. Moreover, unlike static analyses where the effects of excavation are concentrated in its vicinity, for the aim of dynamic analysis the stratigraphy trend far from excavation is relevant, but no information is available, therefore it has been preferred avoiding complicated automatic interpolation, which would have led to incorrect and slower simulations.
- Two, instead of three, layers of marine sand deposits have been individuated: being the reference decay curve for marine deposits only one, there was no reason for distinguishing them in three layers.
- Points 2. and 3. led to a slightly modified thickness of the soil layers. The new stratigraphy is presented in detail in section 4.3.1.
- Buildings are not modelled.
- The excavation is placed in the center of the model (whose dimensions are $200\times120\times70$ m^3) to ensure conditions that are as symmetrical as possible (internal structures of the station have nonsymmetrical openings).

The imposed boundary conditions are the same as those described in Chiaia station case study, on lateral boundaries and at the bottom, where it is assumed that a rigid bedrock is found. In this case, because of the geometry of the case study, it was possible for the accelerometric inputs to be applied along two directions, separately. The analyses have been carried out modelling the soil in two ways:

1. An analysis performed with all the sandy layers modelled with HSss, and cappellaccio and NYT with Mohr-Coulomb, was used as a comparison with the results of the static model to assess if the magnitude of displacements and the associated state of stress was comparable with the static back analysis. With this model a first set of dynamic analyses were conducted. Licata (2015) showed that the soil layers surrounding the tunnel are unlikely to be subject to liquefaction under the seismic actions considered, therefore it was deemed acceptable to run the first set of analyses disregarding cyclic accumulation of pore water pressure.
2. In the second set of analyses, instead, marine sand deposits were modelled with UBC3D PLM, suitable for predicting liquefaction. For static stages, a calibration of the model was made based on the results of the simplified model with HSss; for dynamic stages, instead, some parameters were changed trying to capture the dynamic characteristics of the upper layers of soil as described in Licata (2015).

Both the set of analyses were conducted with three different accelerometers, derived from the same disaggregation analysis used in the case of Chiaia. For this site the choice of accelerograms to use for coupled dynamic analyses was made, based on their characteristics in terms of peak acceleration and frequency content (Table 27), after deconvolution of the seven spectrum-compatible accelerograms with 1D linear equivalent code STRATA. Namely, the following inputs were chosen: 006332xa because of its highest peak acceleration, 006326xa because its mean frequency is the closest to the first fundamental frequency of the soil column, and 000149xa, whose mean frequency is close to the second eigen-frequency of the soil column. All the three inputs have a peak frequency of about 2 Hz. The dynamic characteristics of the soil column were studied performing a frequency sweep analysis in Plaxis 3D and analyzing the amplification function at the free surface: the first two eigen-frequency of the defined stratigraphy resulted $f_1 = 1.6$ Hz and $f_2 = 4.5$ Hz (see Figure 94). The frequency sweep analysis investigated a range of frequencies going from 0 to 10 Hz, with a sinusoidal input of constant amplitude (0.001g) aimed at maintaining the soil within its elastic regime. The frequency sweep was applied to two soil columns, to test both the constitutive models, leading to identical results.

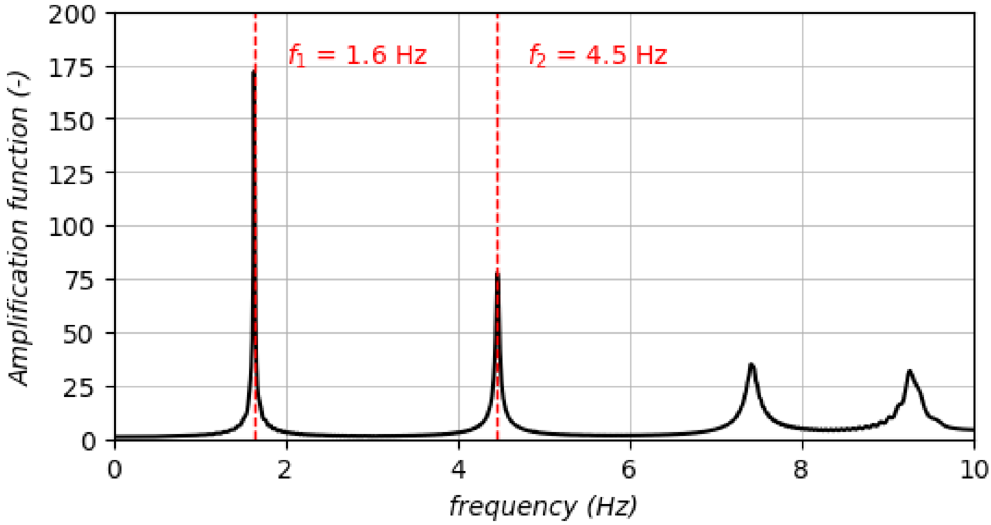

Figure 94. Amplification function retrieved by frequency sweep analysis for both the constitutive models.

The inputs chosen for fully coupled dynamic analyses are such that effect of peak acceleration and frequency content can be considered. Energetic content as defined by Arias intensity (Arias, 1970) is also varied (see Table 27).

Table 27. characteristics of the selected inputs, after deconvolution procedure

Parameter/Input	000149xa	007142	000471	004675xa	006335	006332xa	006326xa
f_p (Hz)	2.39	2.5	0.68	0.40	2.00	2.07	0.43
f_m (Hz)	4.88	2.25	1.95	2.04	2.00	2.50	1.73
T_p (s)	0.42	0.40	1.47	2.50	0.50	0.48	0.46
T_m (s)	0.36	0.74	0.93	1.04	0.88	0.51	1.01
a_{max} (g)	0.046	0.118	0.010	0.058	0.083	0,182	0.087
D_{5-95} (s)	7.10	8.23	11.70	5.53	5.35	3.00	4.26
I_A (m/s)	0.02	0.18	0.001	0.03	0.07	0.25	0.06

The analyses carried out are listed in Table 28. Main scope of the analyses was characterizing the influence of excavation on the propagation of seismic waves in the surroundings, therefore analyses with and without excavation were carried out. The conditions imposed to the model boundaries are such that they ensure a one-dimensional propagation of seismic waves.

Results for input along x and y direction will be presented separately for the model with the excavation; the model without excavation is just a large soil column, and applying the input in one direction or another doesn't make any difference.

Table 28. Analyses performed with HSss and UBC3D PLM

Input	006326xa	000149xa	006332xa
Constitutive Model	$f_{av}=f_1$	$f_{av}=f_2$	$a_{peak,pax}$
HSss	E, input along x E, input along y WE	E, input along x E, input along y WE	E, input along x E, input along y WE
UBC3D PLM	E, input along x E, input along y WE	E, input along x E, input along y WE	E, input along x E, input along y WE

4.3.1. Calibration of Hardening soil model for dynamic analyses

Hardening soil model with small strain stiffness has been used in this context disregarding the possible accumulation of excess pore pressure under dynamic loading and assuming undrained conditions during earthquake occurrence. In static analyses the calibration, mainly based on site test results, has given good results in comparison with field data. Here more care was invested in calibrating the parameters of the model governing small strain behavior, which also governs the damping trend and resulted in a slightly modified initial shear moduli G_0, with values derived from CH and SDMT tests, and elastic moduli of unloading-reloading E_{ur}. The newly defined stratigraphy, modified with respect to the static model as described in previous paragraph, is reported in Table 29 and Table 30, while the comparison between experimental and numerical decay curves is reported in Figure 95.

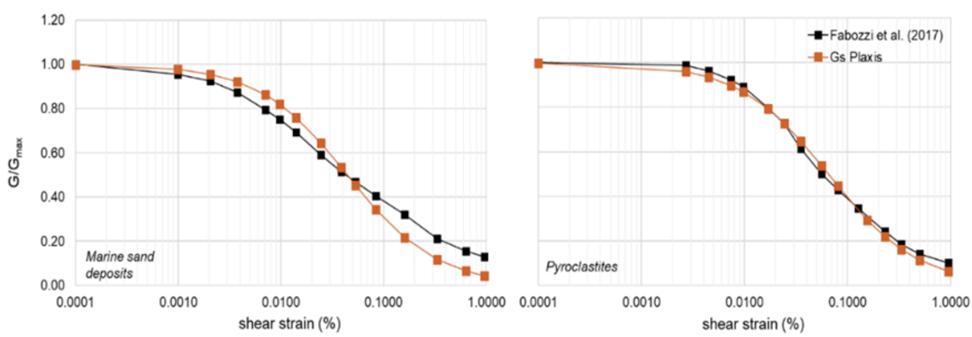

Figure 95. Experimental and numerical decay curves of initial shear modulus for the sandy soils.

Table 29. Mechanical properties for soils described by HSss model.

soil/parameter	Depth	γ_{unsat}-γ_{sat}	E_{50}^{ref}	E_{oed}^{ref}	E_{ur}^{ref}	ν_{ur}	G_0	m	p_{ref}	$\gamma_{0.7}$	c'_{ref}	φ'
	m	kN/m³	MPa	MPa	MPa	-	MPa	-	kPa	%	kPa	°
Sand 1	0-18	17-18,5	37,0	37,0	110,0	0,2	91,5	0.2	70	0,017	1	38
Sand 2	18-24	17-18,5	15,4	15,4	46,10	0,2	170,0	0	100	0,017	1	38
Pyroclastites	24-39	14-16	9,4	9,4	28,0	0,2	144,0	0	100	0,02	1	37,2

Table 30. Mechanical properties for soils described by Mohr Coulomb model.

soil/parameter	Depth	γ_{unsat}-γ_{sat}	E'_{ref}	ν'	c'_{ref}	φ'
	m	kN/m³	MPa		kPa	°
Cappellaccio	39-42	14-16	1810	0,3	150	27
TGN	42-70	14-16	5340	0,3	500	27

The newly defined model was validated against experimental data. Since it underwent some simplifications (see paragraph 4.3), scope of the comparison was that of reproducing just the order of magnitude of horizontal and vertical displacements occurred during excavation and dewatering of the main shaft. The objective was reached, and some results are reported as an example in Figure 96 and Figure 97, where settlements at the end of excavation on both the long sides of the shaft are compared with those determined at the end of the calculation (*i.e.*, maximum depth of excavation reached), and horizontal displacements of the centerline section of excavation are compared with inclinometric profiles in the same section, at the same stage of works. The displacements here presented are obtained with the concrete Young's modulus, reduced to take into account of creep effect, according to the better agreement found under this assumption and presented in section 4.2.5 of this chapter. The assumption is deemed valid only in static conditions.

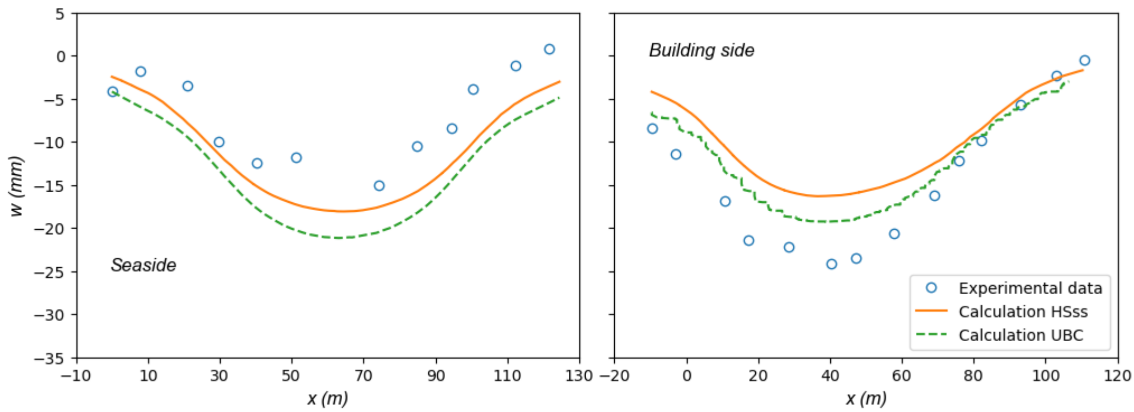

Figure 96. Buildings' side and seaside settlement trough.

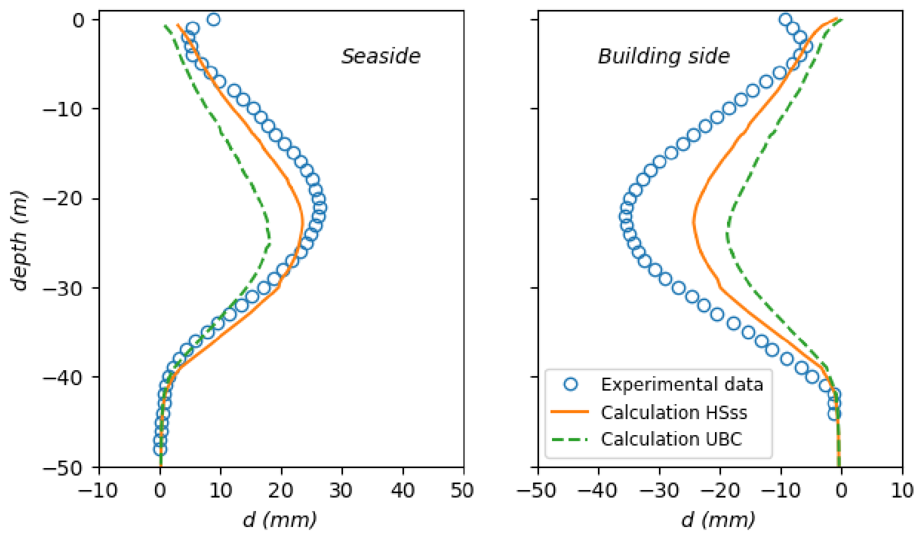

Figure 97. Horizontal displacements along section BB' (excavation centerline).

4.3.2. UBC3D PLM: description and calibration

Brief introduction to the model

UBC3D PLM is an effective stress elasto-plastic model implemented in Plaxis 3D to capture liquefaction phenomena, or cyclic accumulation of pore water pressure, eventually happening in saturated sands (Petalas and Galavi, 2012). It is the formulation in 3D principal stress space of UBCSAND (formulated in 2D) introduced by Puebla *et al*. (1997) and Beaty and Byrne (1988). Fundamental aspect of the model, for the generation of excess pore pressures induced during cyclic loading, is the densification law (Eq. (34)) introduced as follows: among the input parameters, the shear plastic modulus K_G^{*p} evolves during the application of the load, increasing with the number of cycles (n_{rev}). The increase in the plastic modulus simulates the process of densification of the soil under cyclic loads, which is the phenomenon underlying liquefaction.

$$K_G^{*p} = K_G^p \left(4 + \frac{n_{rev}}{2}\right) \cdot hard \cdot f_{dens} \qquad (34)$$

In Eq. (34) *hard* is a factor correcting the densification rule for loose soils dependent on SPT value, and f_{dens} is a user input parameter to adjust the densification rule.
The model is characterized by two yield surfaces that follow Mohr-Coulomb criterion, represented in *qp'* plane in Figure 98:

- The primary surface is activated when the friction angle mobilized is the maximum ever reached by the material, and the behavior of soil within the surface is non-linear elastic and governed by a hyperbolic hardening rule (as defined by Beaty and Byrne, 1988).
- The secondary surface is characterized, instead, by a kinematic hardening rule, and it is active during any load path in which the angle of friction mobilized has already been experienced by the soil. The evolution of K_G^{*p} with number of cycles (Eq. (34)), happens withing this surface, *i.e.*, during secondary loading.

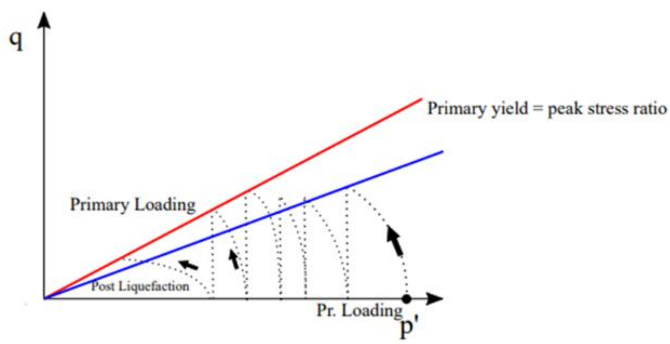

Figure 98. Primary and secondary yield surfaces in UBC3D PLM (Plaxis Manual, Bentley, 2025).

The elastic behavior which occurs within the yield surface is governed by a non-linear rule in turn governed by elastic bulk – *K* – and shear – G^e – moduli: the modules depend on the stress state with exponential laws, whose exponents (m_e for *K*, n_e for G^e) are user-defined input parameters; they must be defined at a given reference pressure usually taken equal to atmospheric pressure, through two dimensionless factors K_B^e and K_G^e. Once the stress state reaches the yield surface, plastic behavior is predicted as long as the stress point is not going back to the elastic zone. More specifically the hardening rule governs the amount of plastic strains depending on the mobilized friction angle. The flow rule proposed by Puebla *et al*., (1997) is used in this formulation of the model, and is formulated as follows:

$$d\varepsilon_v^P = sin\psi_m \cdot d\gamma_p \qquad (35)$$

$$sin\psi_m = sin\phi_m - sin\phi_{cv} \qquad (36)$$

Where $d\varepsilon_v^P$ is the increment of plastic volumetric strain, ϕ_{cv} the constant volume friction angle, ϕ_m and ψ_m mobilized friction and dilatancy angle, respectively. The stress ratios that lie below ϕ_{cv} are associated with contractive behavior, those above ϕ_{cv} with a dilatant behavior instead. For undrained behavior, the volumetric strains that would occur for drained loading are compensated by the generation of excess pore pressures. Pure elastic behavior is predicted by the model during unloading.

The input parameters of the UBC3D are summarized below:

- φ_{cv} is the constant volume friction angle
- φ_p is the peak friction angle
- c is the cohesion of the soil
- K_B^e is the factor of elastic bulk modulus of the soil in a reference level of 100 kPa. It can be derived from a drained triaxial test with a confining pressure of 100 kPa.
- K_G^e is the factor of elastic shear modulus of the soil in a reference level of 100 kPa.
- K_G^p is the factor of plastic shear modulus
- m_e is the elastic bulk modulus index and has a default value of 0.5
- n_e is the elastic shear modulus index and has a default value of 0.5
- n_p is the plastic shear modulus index and has a default value of 0.5
- R_f is the failure ratio
- f_{dens} is the densification factor. It is a multiplier that controls the scaling of the plastic shear modulus during secondary loading
- $N_{1,60}$ is the corrected SPT value of the soil.
- f_{post} is a factor that can be used to soft the behavior of the soil during the post liquefaction behavior.

For all the listed parameters, calibration based on SPT result is available and reported in Material Models manual (Plaxis, 2025).

Calibration of UBC3D PLM

Herein the constitutive law was applied only to the first two layers of sandy soil, namely the marine sand deposits that reach the depth of 24 m bgl, below whom it is not supposed to occur liquefaction. The model was used for the purpose of verifying the importance of pore pressure accumulation at the site of interest and comparing the results with the Hardening soil with small strain stiffness model, used until now. Even though results presented by Licata (2015) show that, under the tested conditions, corresponding to the cyclic stress ratio (CSR) expected at the site of interest, no liquefaction is expected to occur, capturing the soil behavior that induces pore pressure accumulation under dynamic loading, is still an important topic in fully coupled dynamic analyses.

UBC is a model specifically developed for saturated sands under dynamic loading, but it cannot describe static behavior as accurately as HSss does, first of all because it doesn't include a small strain formulation, very useful for describing soil behavior at the strain levels usually involved in excavation problems. However, in order to produce a state of stress in the soil comparable with that calibrated with HSss at the beginning of dynamic analyses, a static calibration, different from the dynamic one, was made for UBC as well, as follows:

- the elastic shear modulus G^e was regarded as a sort of G_0 from HSss. The assumed similarity was considered acceptable because of the parabolic relationship between stress and strain in the stress ratio/shear strain plane, characterizing both the constitutive models. G^e and G_0 also control the slope of the unloading curve of oedometric test simulated in Plaxis lab tool.
- Plaxis manual suggests a correlation between G^e and the elastic bulk modulus K, however it leads to a value of K corresponding to a Poisson coefficient very low (*i.e.*, 0.02). In fact, according to Hardin (1978) and Negussey (1984), Poisson coefficient has a significant variability with strain level, and it can range between 0 and 0.2 at small levels of strain. For this reason, for dynamic calculations a much lower Poisson's ratio can be used, the same way the small strain shear modulus is used (Makra, 2013). This value, though, is not suitable for static calculations, therefore the formulation proposed in the manual was modified to obtain a Poisson ratio equal to 0.2.
- The plastic shear modulus was set after a parametric analysis, from which the best fit with data was obtained with a modulus reduced by 30% with respect to that proposed by the manual and depending on N_{SPT} and G^e.
- For what concerns friction angles, φ_{cv} was deduced from data reported in Licata (2015), while φ_p comes from site characterization already used for HSss calibration. Moreover, it was verified that the correlation between φ_p and φ_{cv} based on SPT applied in this case with the values set as described.

- m_e, n_e and n_p were set equal to 0 (*i.e.*, no stiffness increment with stress state is expected) according to site investigations.
- Other parameters, explicitly made for adjusting the cyclic response of soil, were left with their default value, since they are not expected to play a role in static calculation.

The resulting calibration of UBC for Sand 1 and Sand 2 is reported in Table 32. Summary results of the static phases are reported in Figure 96 and Figure 97, compared with field data, together with HSss analysis results.
Regarding calibration for dynamic stage of calculation, it was made based on experimental data reported in Licata (2015) for the considered layers of soil, as follows:

- The hypothesis on the equivalence between G^e and G_0 was maintained, and values of friction angles were maintained as well.
- K was chosen so that $\nu = 0.02$, as suggested by Makra (2013).
- Other parameters (*i.e.*, R_f, f_{dens}, f_{post}) were chosen to match the laboratory curves reported in Licata (2015).

The experimental campaign carried out by Licata (2015) involved undrained cyclic triaxial tests, and it was possible to derive curves of cyclic stress ratio (*CSR*) vs number of cycles. In the thesis these curves have been used as a benchmark for the calibration of UBC3D PLM and a comparison between experimental and numerical trends is reported in Figure 99. Red triangles in Figure 99 correspond to numerical results obtained simulating undrained cyclic triaxial tests reported in Licata (2015) with the soil test tool implemented in Plaxis. In Table 31 confining pressure, σ'_r, and deviatoric stress cyclic increment, Δq, are listed.

Table 31. Parameters of cyclic undrained triaxial tests, confining pressures and increment of deviatoric stress.

CSR	*σ'_r (kPa)*	*Δq (kPa)*
0.3	100	60
0.35	100	70
0.4	100	80
0.5	100	100

The obtained agreement between experimental and numerical results is acceptable for higher stress ratios and low number of cycles, while tends to disagree for lower *CSR* where the numerical results underestimate the number of cycles required for liquefaction. This is a well-known shortcoming of the model, testified in different works (Makra, 2013; Vozza, 2017) consisting in the fact that the calibration of the fitting parameter f_{dens} depends on the level of stress applied, and then it is appropriate to fit the experimental results for the expected number of cycles. According to the chart reported in Idriss (1999) and Idriss and Boulanger (2006), a correlation exists between earthquake magnitude and equivalent number of equivalent stress cycles. Therefore, for the range of magnitudes here considered it was deemed appropriate to better capture the CSR/N_{cycles} agreement for low cycle numbers. The agreement represented in Figure 99 was obtained with the parameters reported in Table 32.

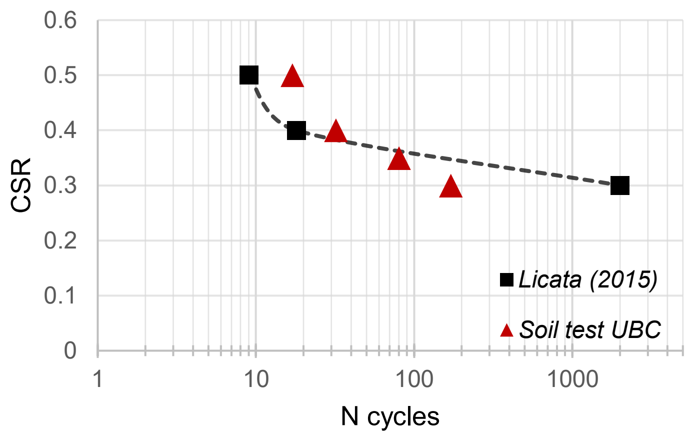

Figure 99. CSR vs number of cycles: comparison experimental-numerical

Table 32. UBC3D model parameters, for static and dynamic calibration

	k_B^e	k_G^e	k_G^p	c	ϕ_{cv}	ϕ_p	$N_{1,60}$	f_{dens}	f_{Epost}	R_f	me, ne, re
	-	-	-	kPa	°	°	-	-	-	-	-
Sand 1 (dyn)	640	915	5000	0.1	31	38	20	1	0.02	0.5	0
Sand 2 (dyn)	1400	1700	5000	0.1	31	38	23	1	0.02	0.5	0
Sand 1 (stat)	1220	915	700	0.1	31	38	20	1	1	0.95	0
Sand 2 (stat)	2266	1700	1546	0.1	31	38	23	1	1	0.95	0

UBC3D-PLM model has hysteretic damping, but the constitutive model over-produces hysteretic damping in the system because of the linear elastic unloading rule with constant shear modulus G_{max} (Petalas and Galavi, 2012). However, on very small cyclic shear strains the hysteretic damping is very small and it underestimates the real soil damping, therefore 1% of Rayleigh damping has been added with control frequencies chosen according to Amorosi *et al*. (2010).

4.3.3. Dynamic analyses results

Excess pore pressures and bending moments

The analysis of the system subjected to selected accelerometric inputs was carried out with the two numerical models described before, differing from each other only for the constitutive model adopted for simulating the two layers of marine sands. Although the difference relies only in the constitutive model adopted for the first two layers of soil, for the sake of simplicity the analyses will be referred to as HSss and UBC3D, respectively.

It is worth mentioning that a known bug in Plaxis version used for the analyses (version 2024.2) prevents dynamic calculations from being performed in partially drained conditions (with the option *dynamic with consolidation*) when plates are used in the model, leading to an error in the solution exceeding 10^2, thus all the dynamic analyses were conducted in undrained conditions. Free field analyses (*i.e.*, without excavation) performed with the calibration described in previous paragraphs do not give rise to liquefaction phenomena, except that some points at elevation z = 0, with any of the three inputs used. As an example two sections are reported in Figure 100, where liquefaction point history (*i.e.*, any stress point that has ever reached liquefaction during the calculation) at the end of dynamic calculation are reported. Only results for 006332xa input are reported, being the one with the highest peak acceleration.

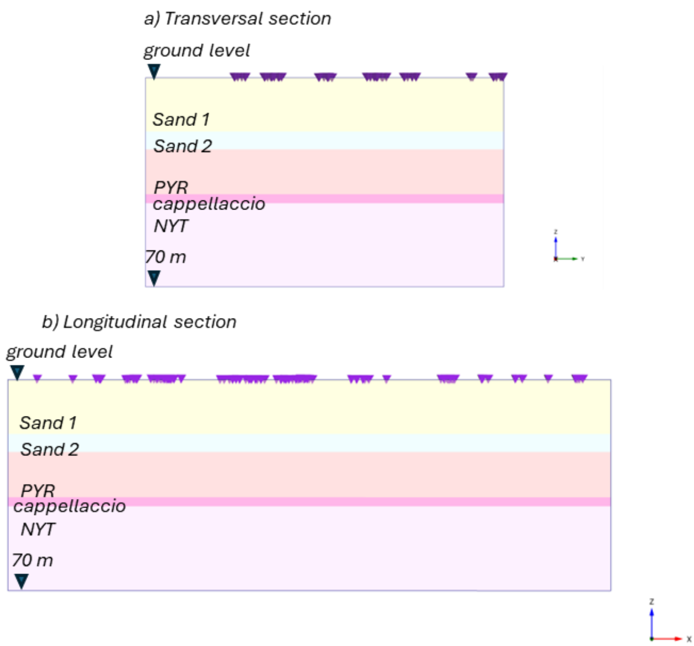

Figure 100. Liquefaction point (purple tringles) history at the end of 006332xa input.

Liquefaction is detected in Plaxis when $r_{u,p'}$ reaches value of 1, where: $r_{u,p'} = \frac{p'_0 - p'}{p'_0}$. Even though no significant liquefaction phenomena are expected from calculation (Licata, 2015), an accumulation of excess pore pressure is still predicted by UBC3D model, depending on intensity of seismic excitation. In Figure 101, Figure 102 and Figure 103 color maps of $r_{u,p'}$ are depicted for analyses with the three inputs. The images are cut at a depth equal to 24 m bgl (*i.e.*, bottom of Sand 2 layer), because $r_{u,p'}$ is a state parameter of UBC3D, while it is not available for HSss and Mohr-Coulomb. In each figure a cross section of the entire model, for *with* and *without* excavation cases are represented, in correspondence with the instant of peak acceleration and at the end of the significative duration ($D_{5\text{-}95}$). The value 1 is never reached (no liquefaction is detected by the software) but it can be observed that in every case $r_{u,p'}$ is close to zero in the entire soil domain in free field conditions; around the retaining structures, instead, an increment of $r_{u,p'}$, increasing with time, is detected, for all the analyses.

In more detail for the signal 006332xa, which is the one with highest peak acceleration, the maximum value of $r_{u,p'}$ is of the order of 0.2 both at the time of peak acceleration and at the end of $D_{5\text{-}95}$. These values occur close to the diaphragm wall, which is impervious, very stiff and neglecting the possibility of drainage at the interface with the soil being the analysis a fully undrained one. The same comments apply for the other two signals. However, both in the case of 006326xa and 000149xa the maximum values of $r_{u,p'}$ reaches highest values in the order of 0.3-0.4 but, again, these values are limited to a thin zone around the diaphragm wall. These two signals are characterized by a significantly lower maximum acceleration but they both have an average frequency content respectively closer to the first and second eigen-frequency of the soil column. As a further general comment, it should be noted that in all cases the zone of larger $r_{u,p'}$ values close to the diaphragm wall occurs at relatively large depth, *i.e.* in the range 15-25 m down from the ground surface. The comments above are indeed remarking the only significant differences between the analyses with and without the excavation.

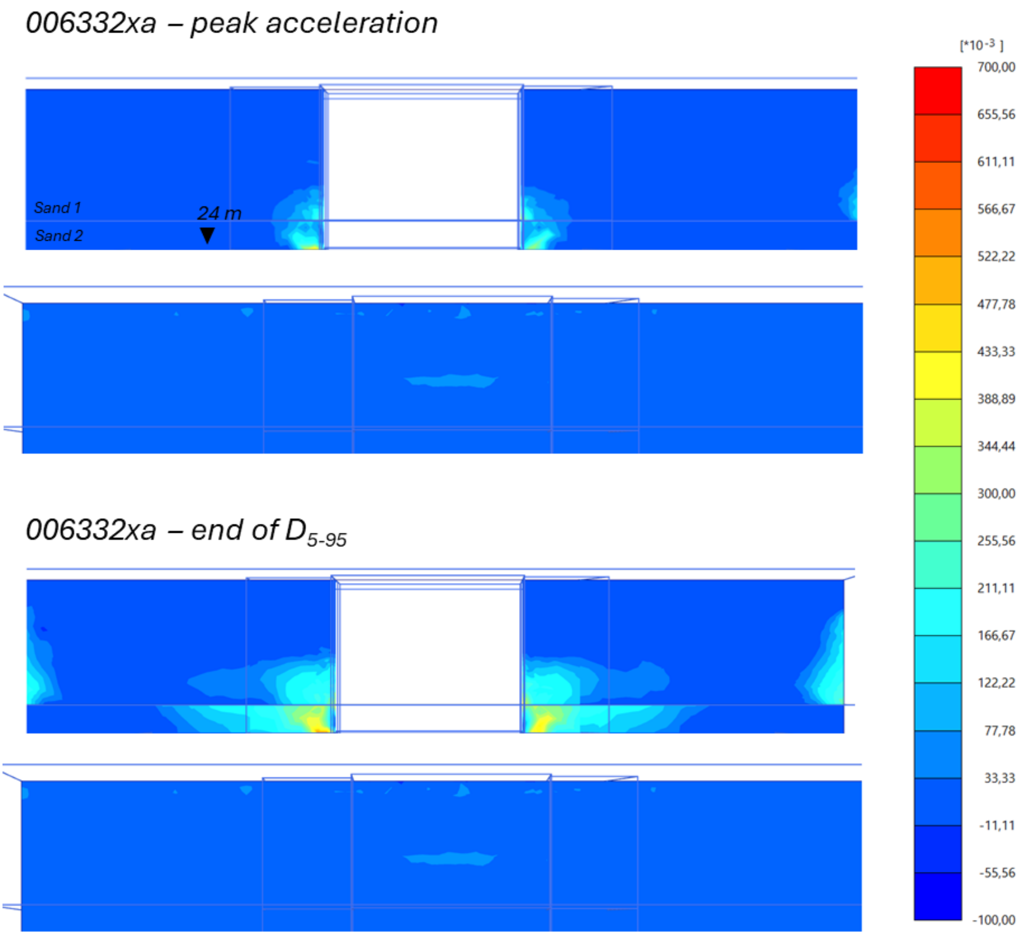

Figure 101. Color maps of excess pore pressure ratio in terms of mean effective stress p', for analyses with input 006332xa. Contour of volume elements are visible.

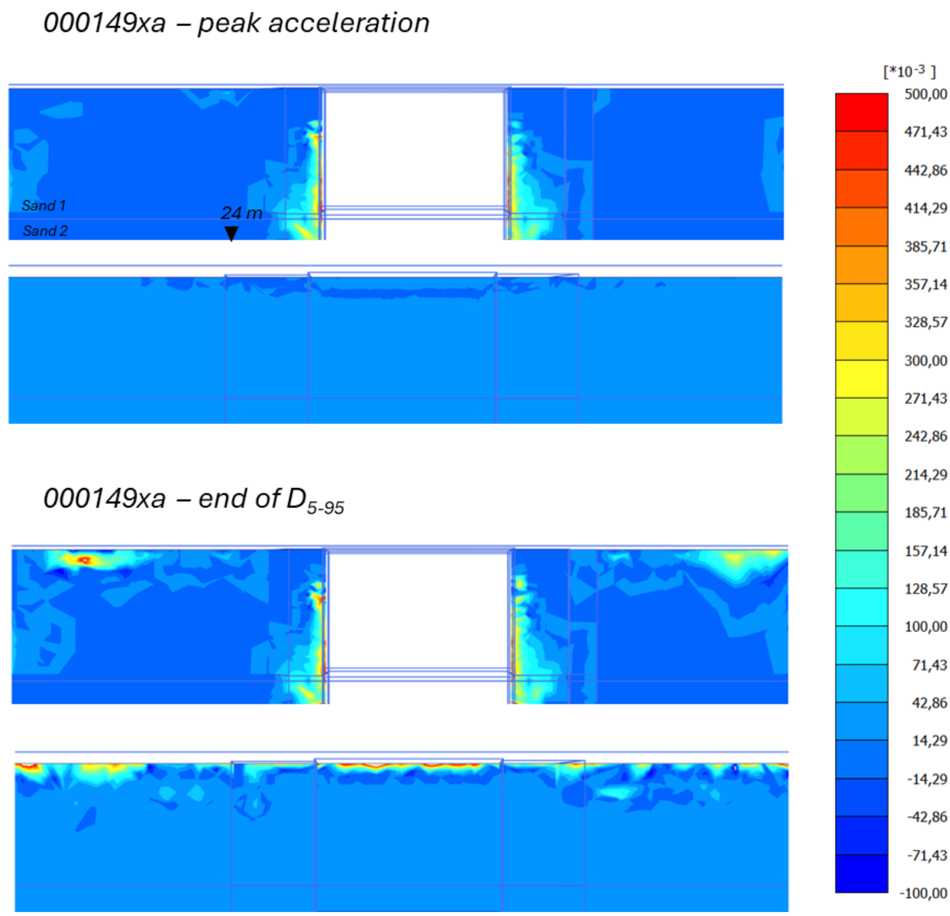

Figure 102. Color maps of excess pore pressure ratio in terms of mean effective stress p', for analyses with input 0001492xa. Contour of volume elements are visible.

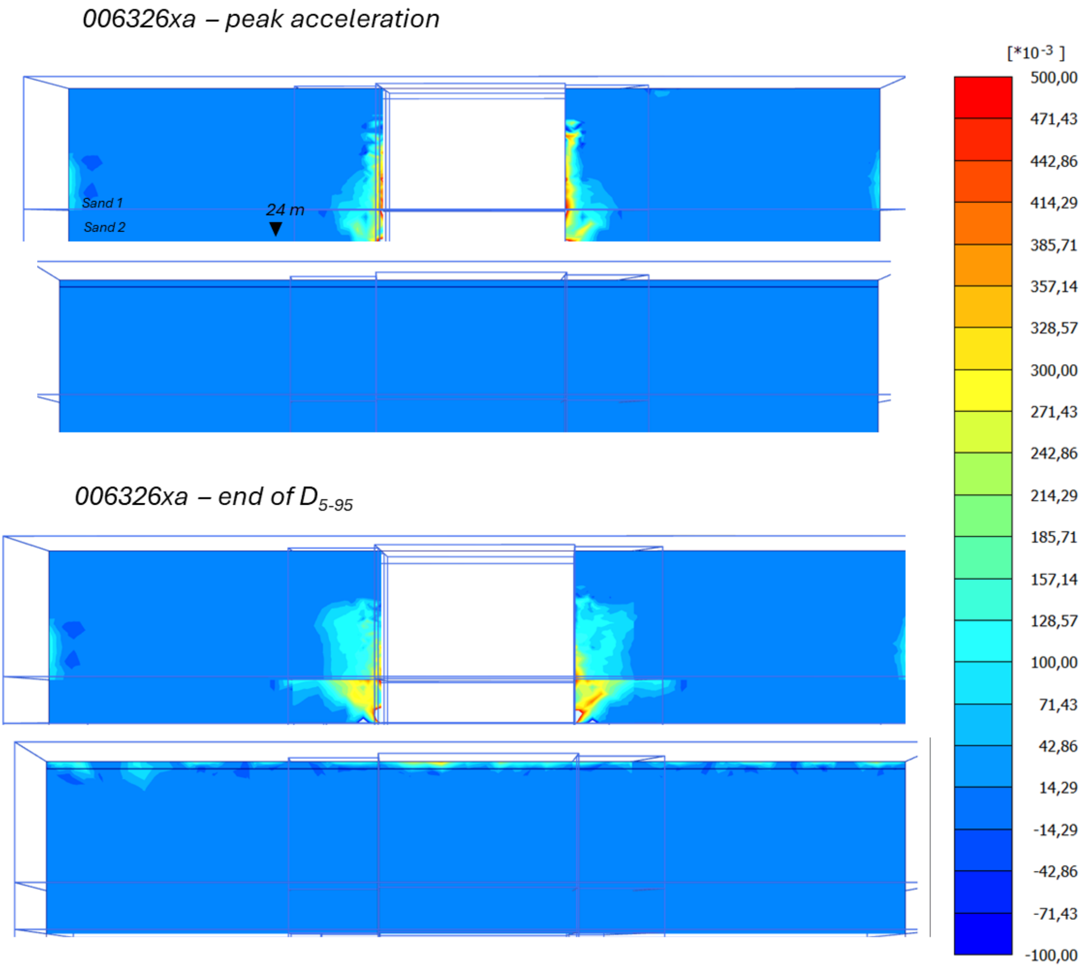

Figure 103. Color maps of excess pore pressure ratio in terms of mean effective stress p', for analyses with input 006326xa. Contour of volume elements are visible.

From the analyses, bending moments acting on bulkheads can be retrieved as well. Simplified methods to predict the increase in bending moment due to seismic excitation are not yet available or, at least, not widespread in practice, when it comes to such complex and multi-anchored structures; therefore, numerical analyses such those conducted in this case play an important role in collecting this kind of data.

In Figure 104 bending moments are represented for analyses conducted with input 006332xa applied along x (left graph) and y (right graph). For each graph both static (end of excavation) and maximum of dynamic calculations are reported, for analyses with UBC and HSss. Bending moments are represented along the center section of the excavation, on the building side. The effect of props is well visible, as well as that of foundation slab (between 24 and 27 m bgl). The comparison between the development of bending moments along the depth of the bulkheads with the input applied in two orthogonal directions highlights differences related to the constitutive model adopted for the soil, possibly attributable, in part, to the change in soil-structure relative flexibility, due to the differences of the models formulations, especially for what concerns the buildup of pore water pressure under cyclic loading. In the case of input applied in direction parallel to the bulkheads, the differences between static and dynamic bending moments, and those between constitutive models, are very limited. When the input is applied orthogonally to the bulkheads, instead, the hardening soil model keeps not producing noticeable differences between static and dynamic conditions; in contrast, UBC3D clearly produces an effect leading to a not negligible increase in the upper layers and a modification of bending moment distribution along all the length of the bulkheads.

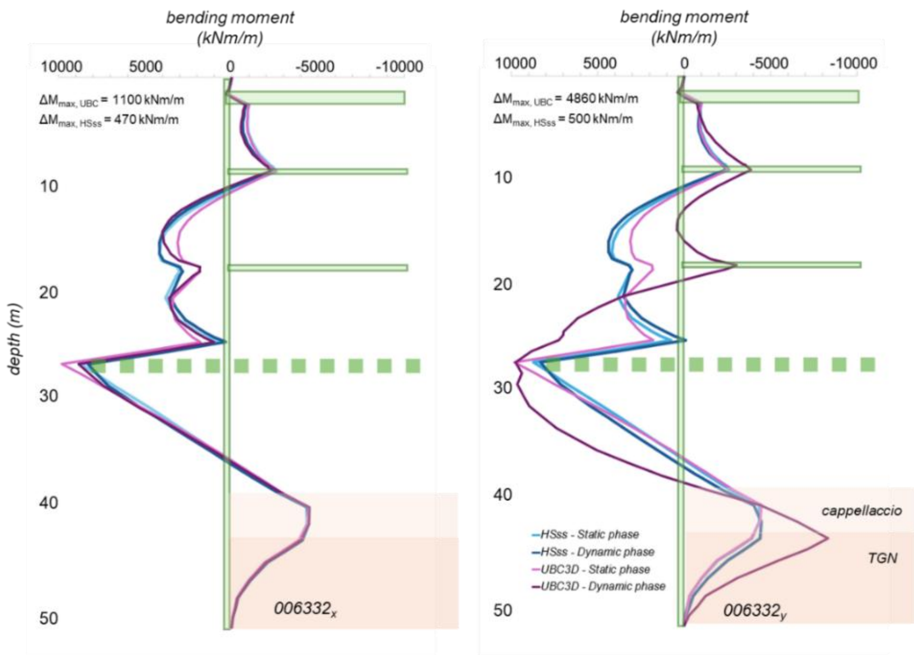

Figure 104. Center section of the excavation, BS: bending moments for analyses conducted with input 006332xa applied along x (left graph) and y (right graph). For each graph both static (end of excavation) and maximum of dynamic calculations are reported, for analyses with UBC and HSss.

Acceleration time histories, PGA and Arias intensity increments

In this section results of the analyses are presented and discussed; among various seismic parameters peak ground acceleration, PGA, is one of the most widespread measures of ground motion used in engineering applications and in setting building codes (Elenas, 2000; Liu *et al*., 2016), including Italian national code (NTC 2018). Therefore, results are here presented focusing on acceleration time histories and derived parameters, both in time and frequency domain, with particular interest in spatial distribution of the quantities and the effect obtained by soliciting the system in two orthogonal directions. In Figure 105 plan position of results presented in the following are reported. *Alignment 4* and *5* are solely intended to serve as a comparison for *alignment 1* and *2*: since the model is symmetric, except for internal structures of the station, the results are expected to be very similar along *1* and *4* and along *2* and *5*. The points along *alignment 1* and *2* are taken at increasing distance from the excavation edge: 2.5 m, 5 m, 15 m, 25 m, 35 m, 45 m for *alignment 1* and 0, 2.5 m, 5 m, 15 m, 25 m, 35 m for *alignment 2*. *Alignment 3* consists of four points at distances of 2.5 m, 5 m, 15 m and 35 m away from the excavation corner, along the direction inclined at 45°: the point at 2.5 m is taken for comparison with the corner column analyzed in Chiaia case study, and the other points are intended as a sort of free field alignment since not much effect of excavation is expected.

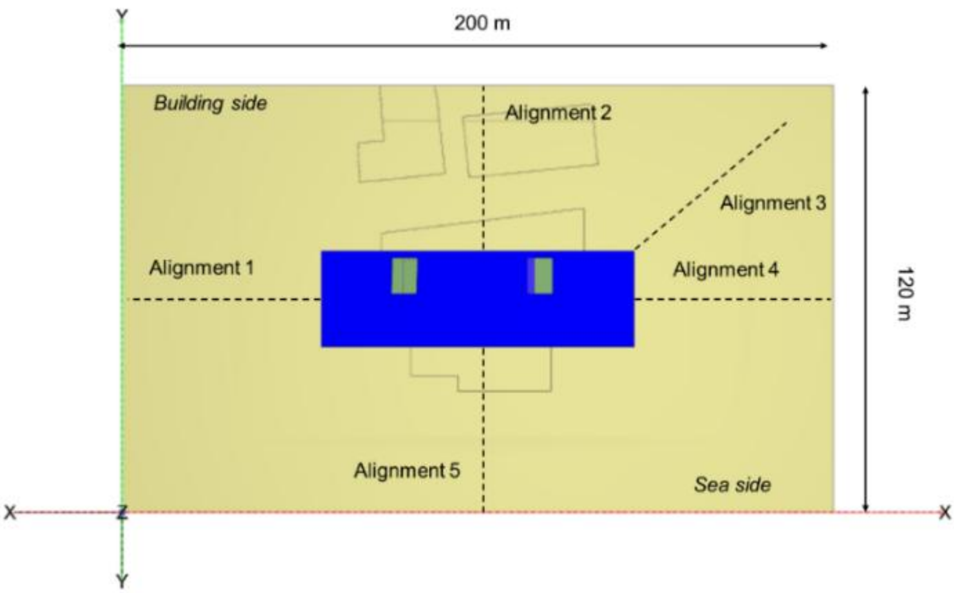

Figure 105. Plan view of alignment considered in presented results of calculation.

Discussion of the results is focused on increment – positive or negative – of the quantities of interest of Excavation (E) case, with respect to Without Excavation (WE) scenario. PGA increments, R_a, are obtained as:

$$R_a = \frac{PGA^E}{PGA^{WE}} \qquad (37)$$

Where PGA^E and PGA^{WE} are PGA of *with* and *without* excavation analyses, respectively. Acceleration time histories from where PGAs have been extracted underwent a filtering procedure with a lowpass Butterworth filter of 5th degree with highest frequency equal to 10 Hz, assuming that higher frequencies are not of interest in the problem, since PGA is studied here in relation to its use as a measure of seismic intensity for structural design. Because of the complex phenomena of refraction and reflection of waves happening when interacting with structures, individuating a clear trend of peak accelerations is not an easy task, especially since PGA is a parameter that describes motion in a single instant, without providing direct information on energy content. This is the reason why giving a look to other parameters can help in understanding the phenomenon. Therefore, Arias intensity, defined by Arias in 1970 as reported in Eq. (38), will be used as well.

$$I_A = \frac{\pi}{2g}\int_0^T a(t)^2\,dt \qquad (38)$$

I_A can be seen as the cumulative energy per unit weight of a set of single-degree-of-freedom oscillators without damping at the end of an earthquake. It reflects at the same time effect of amplitude and duration of the seismic event, which makes it a useful indicator of the potential destructiveness of an earthquake in the form of seismic slope failure (Jibson *et al*., 2000), structural damage (Cabanas *et al*., 1997), and soil liquefaction (Kayen and Mitchell, 1997). A correlation, based on regression on empirical data mainly related to slope failures, has been proposed between PGA and Arias intensity I_A and confirmed by different authors (Arias, 1970; Jibson, 1993; Romeo, 2000; Liu *et al*., 2015):

$$\log(I_A) = a + b \cdot log(PGA) \qquad (39)$$

Where *a* and *b* are regression coefficients. Eq. (39) has been further specified by Liu *et al*., (2016) who have taken into account effect of moment magnitude and site effect (namely, shear wave velocity). As a general rule Arias intensity tends to increase with increasing PGA and moment magnitude, and with decreasing shear wave velocity. As an example, in Figure 106 PGA increment – obtained with HSss analyses – versus the I_A increment are represented for the three inputs applied along x direction, and for alignments *1* and *2*: the general trend describes an increment of PGA with increment of I_A, however it can be seen that the correlation is not punctual and some scatters don't perfectly follow the main trend, meaning that in this case not always to an increase of PGA corresponds a higher energetic content.

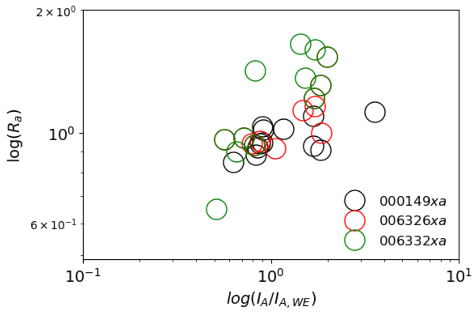

Figure 106. Dimensionless PGA vs dimensionless Arias intensity

Input characteristics and filtering effect of soil

First, to better interpret the results obtained as the input is varied, in addition to their characteristics in terms of mean and peak frequencies, duration and Arias intensity already reported in Table 27, Fourier spectra of the three accelerograms selected for the analyses are reported in Figure 107. It is quite evident that 006326xa input has a frequency content mainly concentrated in the range 0.4-3 Hz. Both 006332xa and 000149xa, even if with clear difference in intensity, have a richer frequency content, with a well visible peak around 2 Hz and not negligible contributions at lower and higher frequencies.

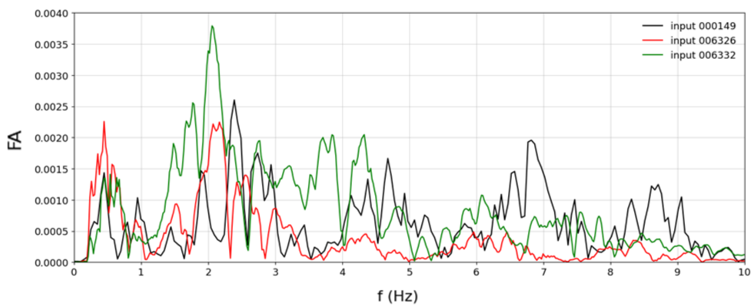

Figure 107. Fourier amplitudes of input 000149xa, 006326xa, 006332xa.

The Fourier spectrum of the input, however, is modified by the soil layers, which tend to amplify the first two eigen-frequencies (*i.e.*, ~1.5 Hz and ~4.4 Hz). In Figure 108 a comparison of Fourier spectra of acceleration time histories retrieved at the ground level in WE case is presented, and the two constitutive models adopted in the analyses are compared. In both cases and for all three inputs, the soil produces a shift of the peak frequency, and the peak at ~1.5 Hz, is clearly amplified. A second peak, around 4.4 Hz, is still identifiable but in a much clearer way in analyses performed with UBC. Comparing the constitutive models, the response is almost identical at low frequencies (*i.e.*, 1-3 Hz) for all three inputs, and it almost completely overlaps in the case of 006332xa analysis. At high frequencies (>5 Hz) only 000149xa input shows differences with a much higher peak around 7 Hz of HSss analysis than UBC does.

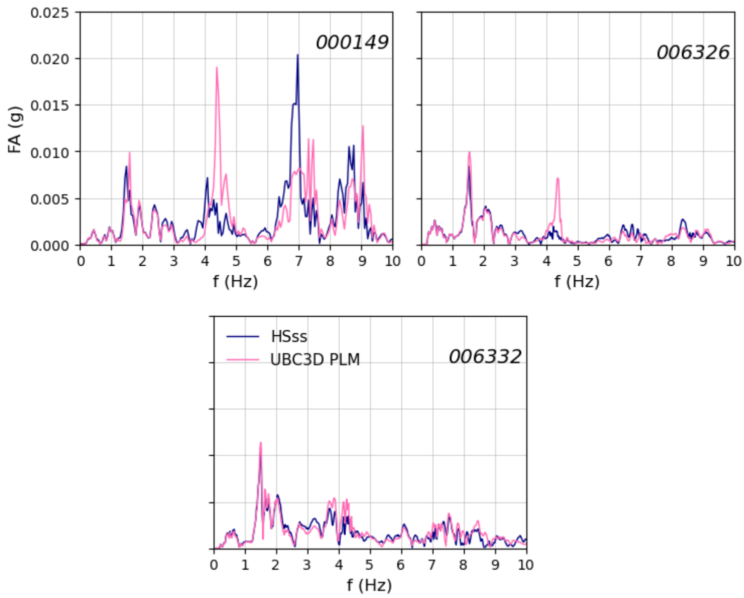

Figure 108. Fourier spectra of acceleration time histories at the ground level in WE analyses, for each input applied to the models (HSss and UBC3D).

Effect of distance and constitutive model

In Figure 109 and Figure 110 peak accelerations at the ground level obtained with both the models (UBC and HSss) for the analyses performed with input applied in x and y directions, respectively, are reported. The representation is made for alignments 1, 2 and 3, shown in Figure 105, at increasing distance from excavation. As a general observation, although with some exceptions that will be discussed later, in most cases the PGA is de-amplified with respect to WE case or, at least, it equals the WE value in the immediate vicinity of excavation. This reduction of PGA is usually recovered within 15 m of distance from excavation edge, which, referring to the case study, nearly corresponds to the minimum distance between excavation and buildings. At that distance, often an increment with respect to WE scenario can be appreciated. Although UBC3D and HSss present some differences, the increment remains always within

+100% of WE value, with mean values less than +50%. At a certain distance (between 25 and 45 m away from excavation, *i.e.*, same order of magnitude of the excavation depth and that of the retaining structures) the increment of PGA decreases going back towards values equal or similar to WE.

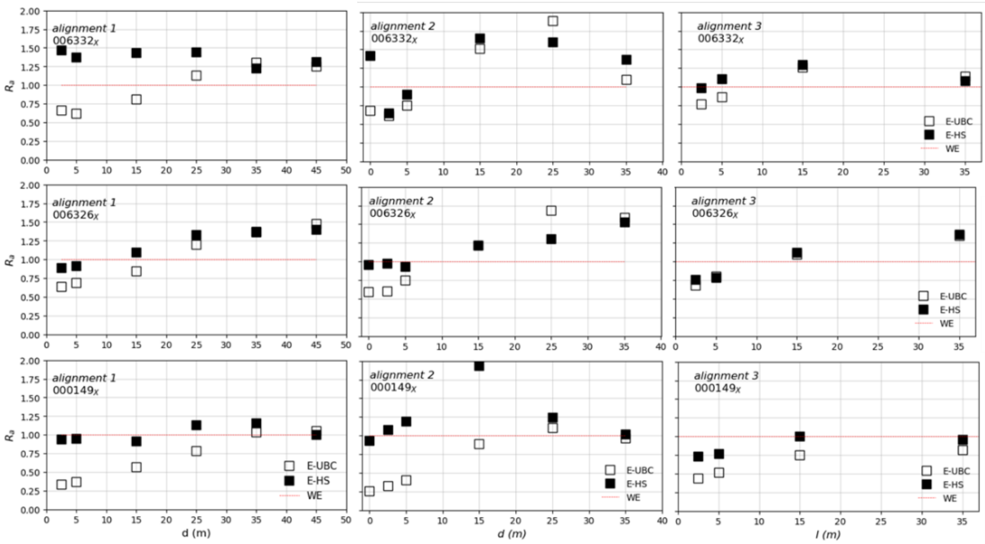

Figure 109. Peak ground accelerations at the ground level with input applied in x direction: 3 inputs, 3 alignments, two different constitutive models for marine sands.

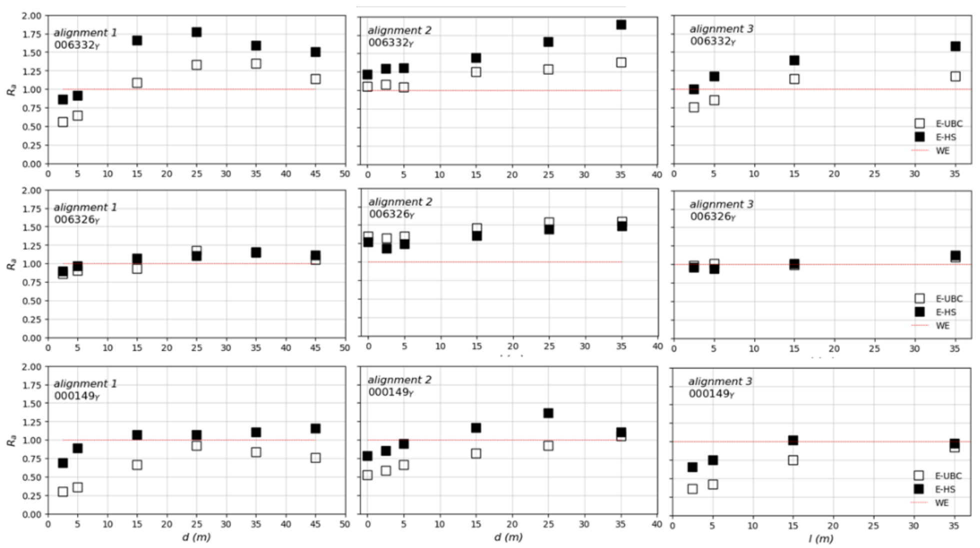

Figure 110. Peak ground accelerations at the ground level with input applied in y direction: 3 inputs, 3 alignments, two different constitutive models for marine sands.

Since in Figure 109 and Figure 110 the results of both the constitutive models are reported, and some evident differences are observed, in Figure 111 PGA for all the alignments and for input 000149xa, 006326xa and 006332xa, applied along x and y directions, are reported to make easier the comparison between the two constitutive models adopted. With distance, the already described trend of de-amplification, amplification and extinguishing of excavation effect is recognizable for both UBC3D and HSss, but it is quite evident that HSss produces overall higher R_a at the ground level than UBC3D does.

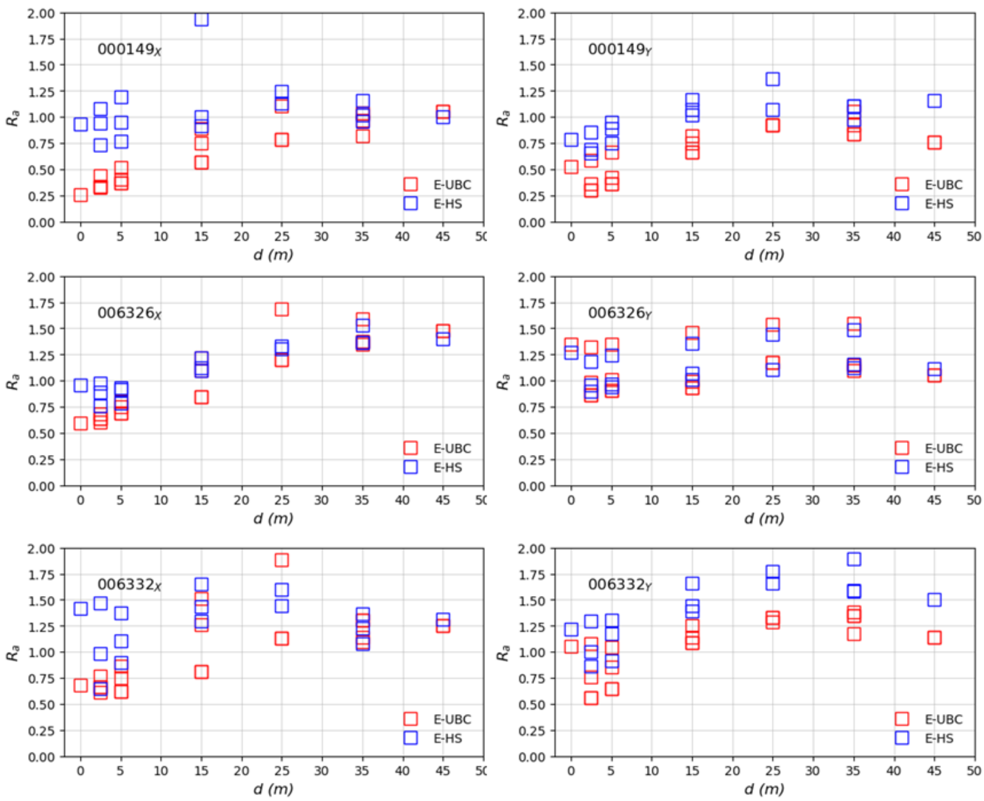

Figure 111 . Differences produced by variation of constitutive model on PGA increments.

It is worth noticing that, based on what discussed before about Arias intensity, a comparison of PGA increment with I_A increment is useful to understand the significancy and reliability in terms of energy content of the exhibited R_a profiles. In general, increment of I_A has the same profile of R_a; however, the point at $d = 0$ of alignment 2, 006332_x (see Figure 109) is found to have Arias intensity of E condition slightly lower than WE, confirming the trend already individuated, the same is true for the first two points ($d = 2.5\ m$ and $d = 5\ m$) of alignment 1 (Figure 112).

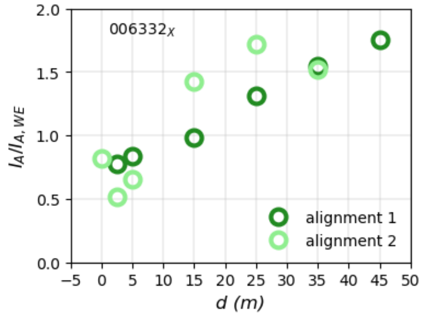

Figure 112. Arias intensity of analysis HSss with 006332xa, alignments 1 and 2.

A further comparison between models is based on maximum acceleration profiles in Figure 113 and Figure 114, which enable the comparison of soil response with depth. Maximum accelerations at $d = 2.5$ *m* and $d = 25$ *m* of alignment 1 are represented in Figure 113, for analyses performed with input in x (upper figures) and y (lower figures) directions. In Figure 114 the same information is reported for alignment 2.

Along alignment 1 (Figure 113) the profiles are very flat, with almost no amplification towards the soil surface for both 000149xa and 006326xa; regarding the difference between constitutive models there is higher amplification of HSss at $d = 2.5$ *m* from excavation, which is more pronounced for 006332xa applied along x, whereas along y direction no significant differences are observed. At d = 25 m acceleration profiles become very similar. Along alignment 2 (Figure 114) instead, the effect of the constitutive model is more visible: HSss analyses produce higher amplifications than UBC3D does, in the immediate vicinity of excavation ($d = 2.5$ *m*) in analyses carried out with 000149xa and 006326xa; some differences are observed in 006332xa input as well, especially at $d = 25$ *m* for analyses with input applied in x direction.

The state parameters of the two constitutive models are different, and the comparison is not straightforward. However, a possible interpretation of what is described regarding maximum acceleration profiles is linked to the static part of calculation. In fact, because of the higher flexibility of retaining structure along the main direction of excavation (*i.e.*, x direction, parallel to *alignment 1*), behind the wall more deformations occur with respect to what happens on the short side of excavation (parallel to y direction). As confirmed by sweep analysis results, the two models, as calibrated, are very similar when it comes to describing elastic conditions at very low levels of strain, but HSss incorporates decay curve of shear modulus at small strain levels, which produces, even in elastic regime, a reduction of stiffness that is not computed by UBC3D. It is therefore possible to hypothesize that the differences encountered in comparing the constitutive models are attributable to deformations induced by excavation activities, which, soliciting a range of strains where the behavior described by the two constitutive models starts to differ, lead to more considerable differences along *alignment 2* than along *alignment 1*, because of the different geometric stiffness of the walls.

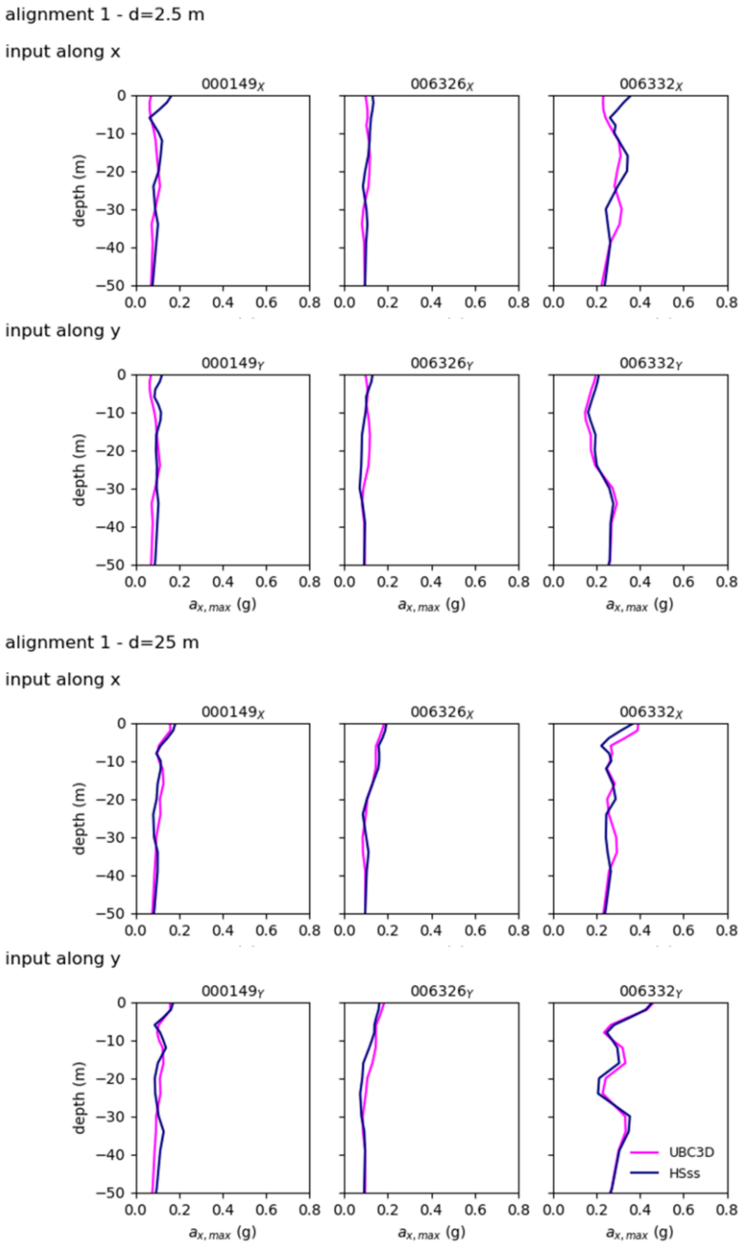

Figure 113. Maximum accelerations at d = 2.5 and d = 25 m of alignment 1 (see Figure 105), for analyses performed with input in x (upper figures) and y (lower figures).

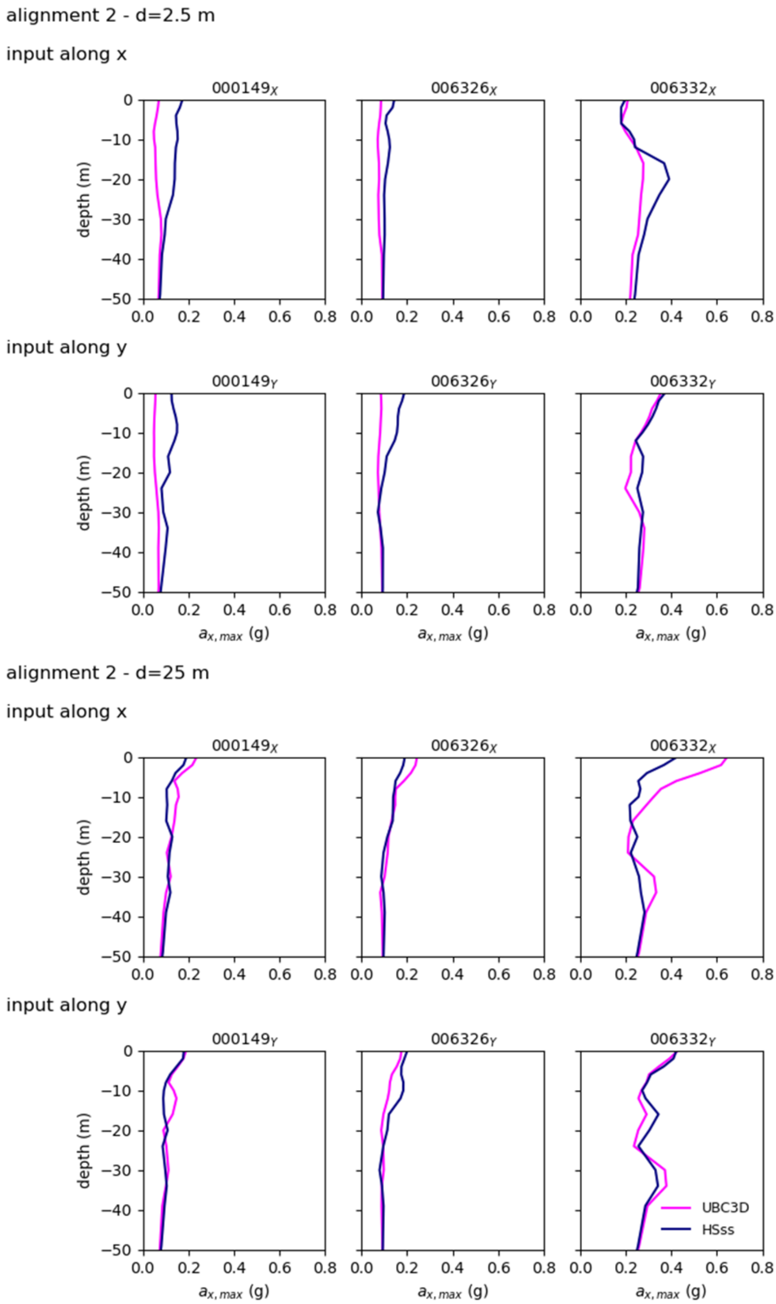

Figure 114. Maximum accelerations at d = 2.5 and d = 25 m of alignment 2 (see Figure 105), for analyses performed with input in x (upper figures) and y (lower figures) directions.

Effect of alignment and input direction

In this section only results obtained with UBC3D used in the first two layers of soil will be reported, since this second analysis is considered more accurate in seismic conditions, due to the specific characteristics of the constitutive model, previously discussed. Among the three alignments represented in Figure 109 and Figure 110, *alignment 3*, which develops obliquely with respect to excavation main dimensions (with a slope of 45°, starting from the corner), is the least affected by excavation, confirming that the problem here discussed is tridimensional and influenced by geometrical dimensions of the station. PGA increments of *alignment 3* are the lowest and in most cases the effect of excavation, visible at very small distances (< 5 m) disappears within 15 m away. Along *alignment 1* and *2*, although the considerations made above are still valid overall, the effect of input characteristics and direction of application seems to have a greater impact than along *alignment 3*. It can be noticed, however, that the greatest amplifications are usually attained along *alignment 2*, which is orthogonal to the main direction of the excavation and along the same alignment, *d = 15-20* m corresponds to the distance of RC building façade. In Figure 115 a comparison of results retrieved by analyses with UBC3D carried out applying the input in two orthogonal directions, is reported for *alignment 2*. The latter is the most sensitive in terms of PGA to the direction of input application and all the inputs produce the highest accelerations near the excavation structures, when they are applied along y direction. This finding is confirmed by Arias intensity increments, reported in Figure 116 for the same alignment.

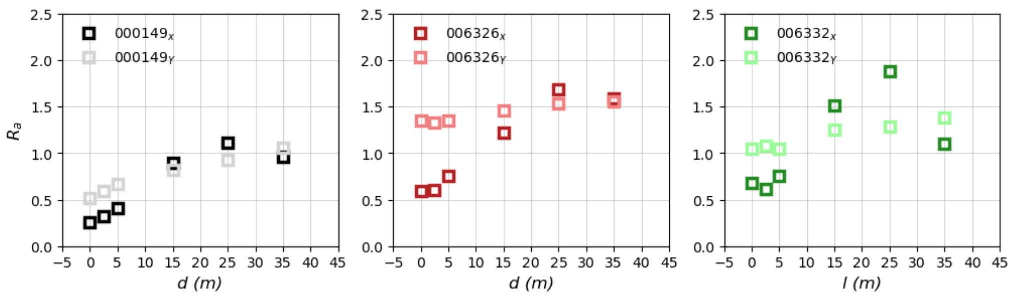

Figure 115. R_a vs distance from excavation walls for inputs applied along two orthogonal directions.

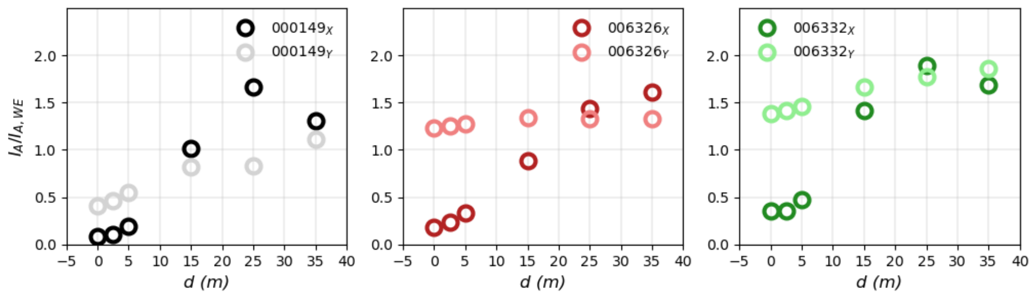

Figure 116. Arias intensity increments vs distance from excavation walls for inputs applied along two orthogonal directions.

Effect of input

In this section both amplifications of PGA with respect to input peak acceleration, A, and R_a are reported in Figure 117 and Figure 118 to clarify the role played by the input on the accelerations produced at the ground level. Both the information is required since the comparison among R_a and A, respectively, of different inputs not necessarily leads to the same observations: particularly, input 000149xa in any represented case produces the lowest R_a (*i.e.*, maximum effect of excavation in the first 5 m, and minimum dependency on excavation presence on PGA distribution) and the highest amplification A, while 006326xa and 006332xa assume very similar values in both the representations.

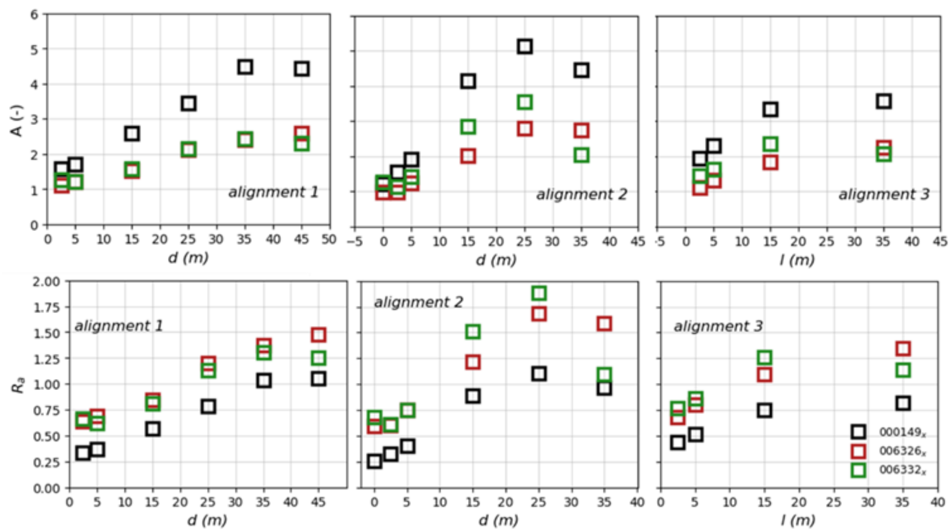

Figure 117. For each alignment and each input applied along x: upper figure, amplification of peak acceleration at the ground level; lower figure, R_a at the ground level.

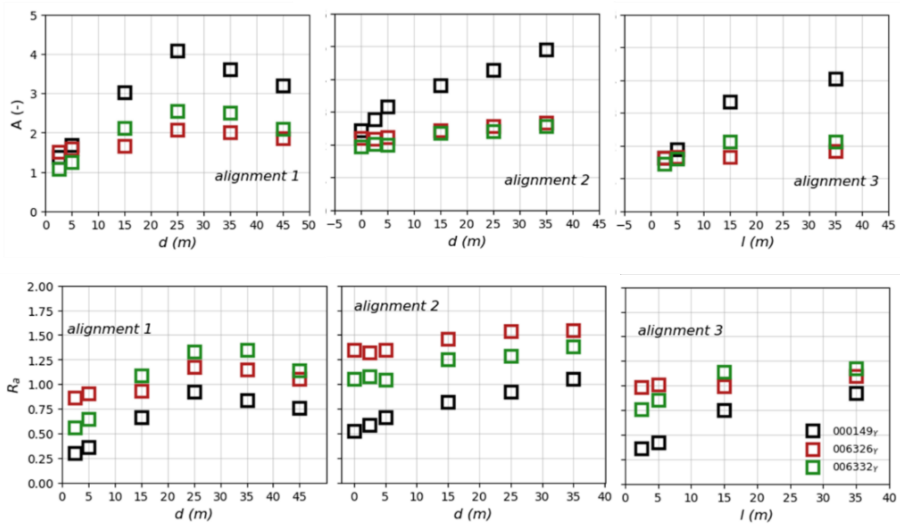

Figure 118. For each alignment and each input applied along y: upper figure, amplification of peak acceleration at the ground level; lower figure Ra at the ground level.

Fourier amplitudes

It is possible to try an explanation of some of the above observations, and some more information can be inferred from the Fourier spectra. According to Parseval theorem:

$$\int_{-\infty}^{+\infty} [a(t)]^2 dt = \frac{1}{2\pi} \int_{-\infty}^{+\infty} [A(\omega)]^2 d\omega \qquad (40)$$

where $a(t)$ represents the acceleration time history and $A(\omega)$ its Fourier amplitude spectrum. This means that Fourier spectrum gives the same information as Arias intensity does, if regarded in terms of energetic content. Therefore, Fourier spectra for both *with* and *without* excavation situations, are here reported in their units (g) instead of dimensionless form, to have an idea of the signal intensity in addition to the amplification produced by excavation. In Figure 119 and Figure 120 Fourier spectra of acceleration time histories obtained in different plan locations at the ground level are represented, for UBC3D and HSss analyses respectively.

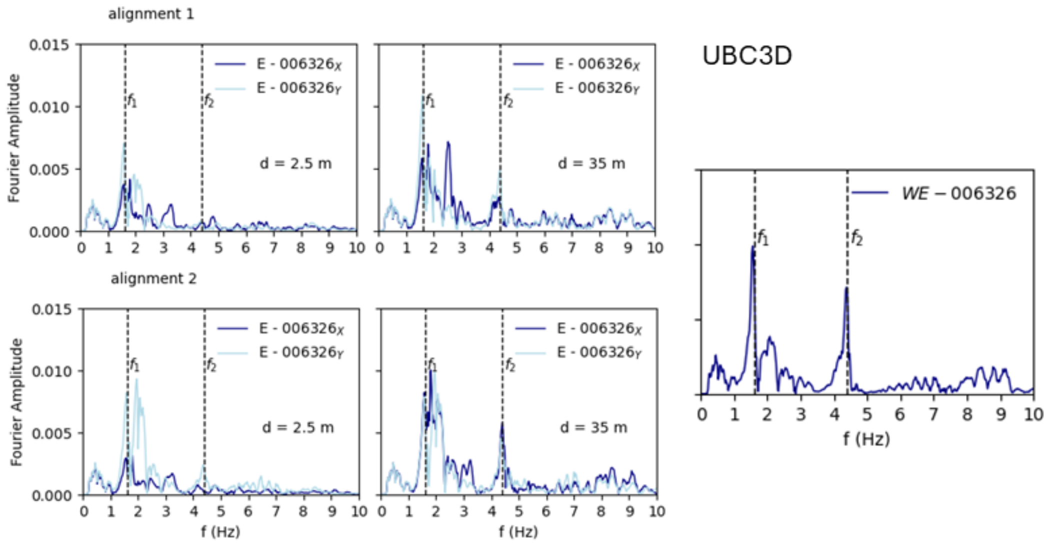

Figure 119. Fourier amplitudes of acceleration time histories retrieved at the ground level by UBC3D analyses, input 006326 in both directions.

The spectra represented are retrieved by analyses performed with 006326xa input, whose mean frequency is close to the first eigen-frequency of the system. Fourier spectrum of WE case with UBC3D (see Figure 119) shows two well defined peaks corresponding to the first two eigen-frequencies of the system. Excavation, as expected by looking at the results in terms of PGA and I_A, produces significant de-amplification of these peaks at small distance (d = 2.5 m), especially when the input is applied along x direction. At higher distances (*i.e.*, 35 m) de-amplification is no longer observed, and the spectra are similar to WE case, even if contributions of frequency around 2 Hz, not present in WE case, appear. At d = 35 m, differences between input application in two directions are less evident.
It is worth noticing that Fourier amplitude of *a(t)*, for frequencies ranging between 1.5 Hz and 2 Hz at d = 2.5 m of *alignment 2*, when the input is applied along y direction is much higher than that of input applied in orthogonal direction, which is consistent with the increased values of PGA and I_A already discussed in previous paragraphs. For what concerns HSss results (Figure 120) similar observations can be made about qualitatively trend of Fourier amplitude with distance and with input direction. The most evident difference with UBC3D model is in the absence of a well-defined peak at 4.4 Hz in WE graph.

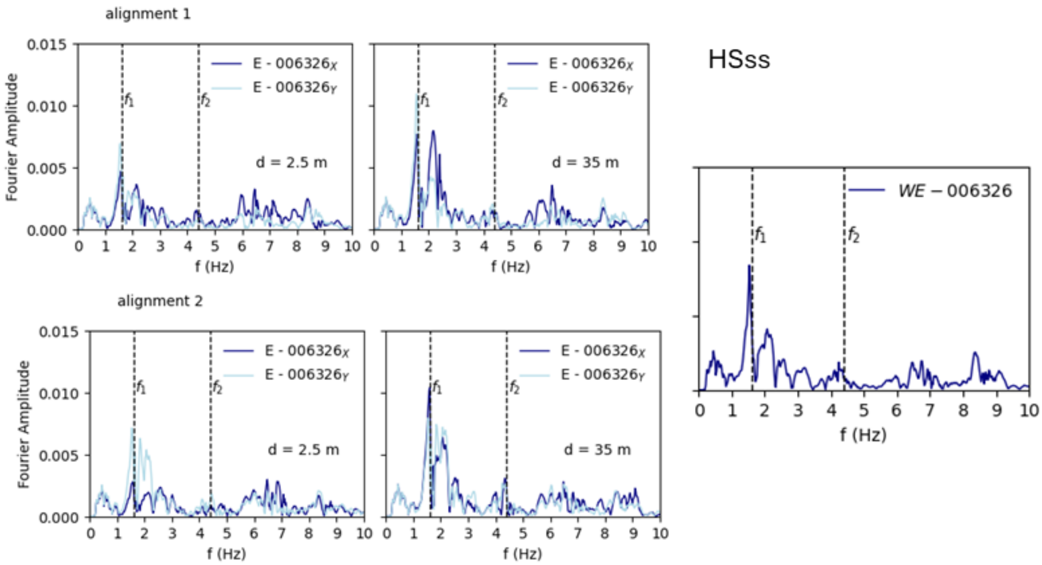

Figure 120. Fourier amplitudes of acceleration time histories retrieved at the ground level by HSss analyses, input 006326 in both directions.

Dynamic calculation with non-horizontal stratigraphy

Lastly, other two analyses were carried out to investigate the influence of non-horizontal tuff top surface (see Figure 121) and of the loads exerted by buildings on the peak accelerations. It was carried out only with the 006332xa input, the one with highest peak acceleration (0.182 g). The stratigraphy was reproduced by boreholes, and the shallower elevation of tuff roof surface was assumed at the borders of the model (*i.e.*, 29 m bgl). The buildings (Ludolf palace and the RC building) have been reproduced only as an equivalent surcharge, with a surface load.

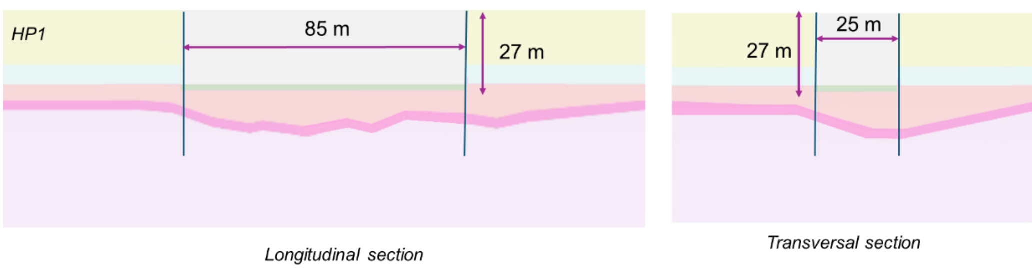

Figure 121. Longitudinal and transversal sections of the numerical model with the non-horizontal roof surface of the NYT reproduced with boreholes.

In Figure 122 the comparison among peak acceleration of the different models is reported

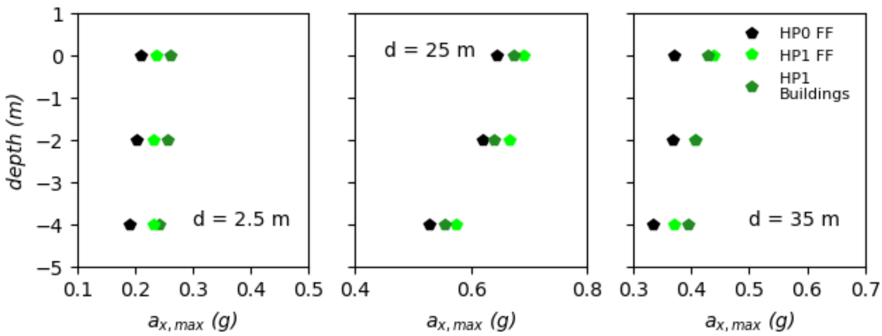

Figure 122. Peak accelerations along alignment 2, comparison among analyses HP0 (horizontal stratigraphy), HP1 (tuff top surface reproduced based on boreholes) and HP1 with buildings.

The difference among the calculated accelerations is small with a slight increase in case of HP1, probably due to the topographic effect of the valley produced by the roof surface of the tuff in the excavation area. For what concerns surcharge effect, it is negligible, which is also confirmed by Fourier spectra of acceleration time histories at the ground level that don't appear to be modified by the load, except for some minor differences around 5 Hz (see Figure 123).

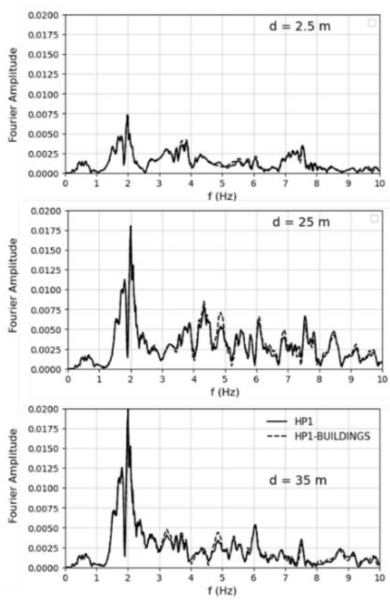

Figure 123. Fourier spectra along alignment 2, comparison among analyses HP1 (tuff top surface reproduced based on boreholes) and HP1 with buildings.

4.4. Conclusions

In this chapter San Pasquale case study has been described in terms of geotechnical characteristics of the site, structure of the station and sequence of works. Monitoring data related to water level drawdown, settlements of buildings and sidewalks and horizontal displacements of retaining structure collected during the works are exposed. The settlements are small and in line with numerical and empirical forecasts and with measurements of other experiences in the same city. A numerical model was calibrated satisfactorily replicating the observed behavior of the system in subsequent excavation phases; the buildings were accurately modelled, and damage parameters were calculated at the buildings' facades: they are not completely negligible if compared with damage assessment methods for masonry structures. However, the experimental observation of absence of damage on the buildings of interest suggests the need for a less conservative estimation of induced damage (*e.g*., numerical analyses). The back analysis carried out with the numerical model allowed for accounting for aspects like the effect of the water drawdown and the concrete creep, which is found to play a significant role in accumulation of horizontal displacement of retaining structures.
The calibrated numerical model served as a starting point for the dynamic analyses where effect of distance from the excavation structures and direction of the input motion were mainly explored.
The organization chosen for the results allows us to draw some conclusions valid for the case study under consideration and more in general, of some utility in understanding *how* and *why* the excavation affects the distribution of acceleration.

- The presence of the open pit deep excavation modifies peak ground accelerations, intensity and frequency content of the motion around it, leading to differences with respect to its absence that can even be significant.
- Arias intensity in many cases agrees with PGA values and, for every accelerometric input used in the analyses, produces a de-amplification of PGA and of the energy content of motion in the immediate vicinity of excavation (<5 m) retaining structures (between -25% and -50%), the de-amplification corresponds to a decrease in Fourier amplitude associated to the peak frequency; an amplification is then expected at variable distance, usually starting from 15 m away from retaining structures. The amplification does not exceed +100% of PGA and I_A in WE case.

- The problem here discussed is found to be tridimensional, and as such must be studied; as for static conditions, even in this case a sort of "corner effect" is observed, because of the increased stiffness of soil-structure system.
- The stiffness of the retaining structure significantly affects acceleration distribution in the nearby: alignment 2, when the model is solicited along y direction, shows R_a>1 also for $d = 0$, probably due to the higher flexibility exhibited by the retaining structure in the soliciting direction.
- The differences between the results of the two analyses, both in terms of Fourier amplitudes and maximum accelerations, reflect the differences between the two models when working in the plastic range. Based on the observation of the maximum acceleration profiles in particular, it is reasonable to assume that the results also depend on the stress state induced in the soil by excavation activities and, therefore, on the static calculation phases.

Chapter 5

Centrifuge experiments simulation

5.1. Experimental setup

This chapter is dedicated to the finite element simulation of centrifuge experiments, carried out with the aim of characterizing the seismic performance of a box tunnel, with a nearly squared section. In the context of this thesis, the simulation is intended to assess reliability as well as limitations of the tools adopted in C*hapters 3* and *4* in capturing the real behavior of a dynamic soil-structure interaction problem. The experiments have been carried out in Nantes, within project DRESBUS II, and they dealt with the investigation of the seismic response of shallow rectangular tunnels by dynamic centrifuge testing. The experimental study was carried out at the geotechnical centrifuge facility (Figure 124) of IFSTTAR at a centrifuge acceleration of 40 g (Tsinidis, 2015; Tsinidis *et al*., 2016). The relevant parameters are scaled down to the model level following standard scaling laws for centrifuge testing. For dynamic testing, the input motion is applied at the base of the model through the specially designed actuator Actidyn QS 80 (Chazelas *et al*., 2008), which is able to impose both sinusoidal and real earthquake excitations up to 400 kg of payload mass. Some functional limits of Actidyn QS 80 are: functional under centrifugal acceleration up to 80 g, peak acceleration of the input motion up to 0.5 g and frequency range at 30–300 Hz for real earthquake excitations. A large Equivalent Shear Beam (ESB) container was used to mount the models, having inner dimensions of 800 mm in length, 340 mm in width and 409 mm in depth. The ESB container is designed to match the shear stiffness of contained soils (Figure 124) for the desirable range of shear strains, thus minimizing spurious boundary effects due to soil-container interactions. The experiments were carried out on different configurations to compare flexible vs rigid box behavior, effect of interface (rough or smooth) and water content. The tests carried out are summarized in Table 33. Each configuration was subjected to the application of 4 accelerograms in sequence with increasing peak acceleration. The first 3 inputs derive from a scaling procedure of Northridge earthquake signal and have peak accelerations of 0.1, 0.2 and 0.3 g respectively, the last one is a sinusoidal signal with peak acceleration equal to 0.35g (Figure 125).

Table 33. Experiments carried out in centrifuge.

Analysis	Box tunnel	Interface	Water content
Case 1	Rigid	Rough	Dry
Case 2	Rigid	Rough	Saturated
Case 3	Rigid	Smooth	Dry
Case 4	Rigid	Smooth	Saturated
Case 5	Flexible	Rough	Dry
Case 6	Flexible	Smooth	Dry

Figure 124. Left: IFSTTAR centrifuge; right: shear box (ACTIDYN actuator).

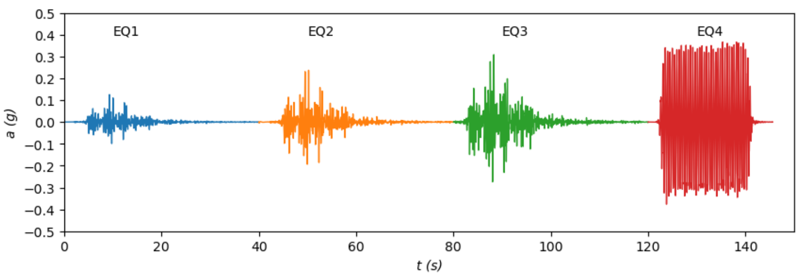

Figure 125. Input applied in sequence at the base of the centrifuge and in the FE model.

Dimensions of tunnel boxes (thickness S and length L of horizontal, H, and vertical, V, sides of the box), for flexible and rigid structures, in model and prototype scale are reported in Table 34, while the properties of aluminum of the box are in Table 35. The soil used during the experimental campaign is Fontainbleau sand, fraction N34, with a relative density equal to 70%. Details about the sand pouring and saturation procedure can be found in Tsinidis *et al*., (2015).

Table 34. Geometrical properties of the tunnel boxes at model and prototype scale.

		Rigid tunnel		Flexible tunnel	
Scale factor = 40		Model scale	Prototype scale	Model scale	Prototype scale
S_H	*m*	0.006	0.24	0.006	0.24
L_H	*m*	0.054	2.16	0.047	1.88
S_V	*m*	0.005	0.20	0.0015	0.06
L_V	*m*	0.050	2.00	0.050	2.00

Table 35. Mechanical properties of the aluminum

Unit weight γ	Elastic modulus E	Poisson ratio ν	Yield stress
kN/m^3	GPa	-	MPa
2.7	71	0.33	400

For the scope of the campaign a wide number of instruments were installed into the ESB to monitor distribution of accelerations and displacements of the tunnel box: the experimental setup is depicted in Figure 126. The vertical alignment of accelerometers individualizes 5 arrays (Ar. in figure) consisting of 3, 4 or 5 measuring points. The instrument represented in Figure 126b is an extensometer aimed at recording displacements of the side wall of the box at different depths. In saturated analyses also pore pressure sensors were added; however, their incorrect calibration made the recorded data useless.

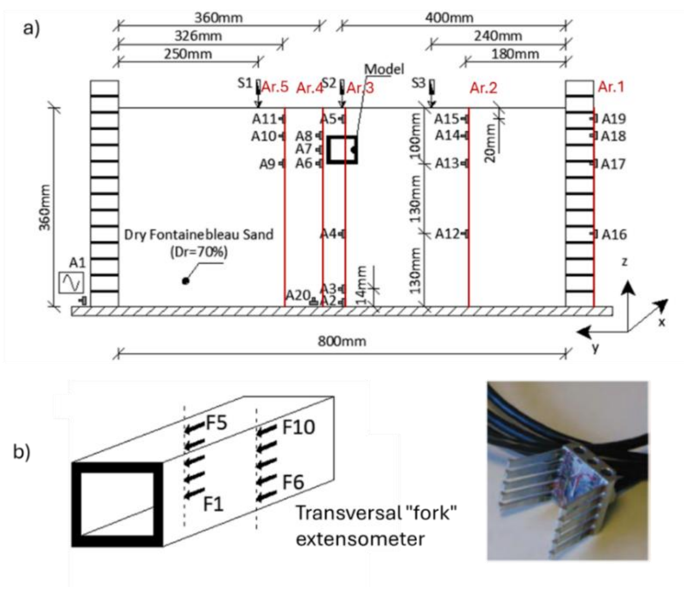

Figure 126. Experimental setup installed into the ESB consisting of: a) accelerometers (A), displacement sensors (S) and b) extensometers (F) placed around the box.

5.2. Numerical model

Plaxis 2D Ultimate version (Bentley, 2024) was used to model the soil-structure system in prototype scale, depicted in Figure 127. The domain is composed of a single soil layer representing Fontainebleau sand N54 characterized with the constitutive soil model *Hardening Soil with Small Strain stiffness* (HSss), developed by Benz (2007) and implemented in Plaxis both in 2D and 3D. The structure is modelled with 2D plate elements with external interfaces, which can be characterized to be full stick (perfect bonding) or full slip (Wang *et al.*, 1993) acting on $R_{interface}$ parameter that controls strength properties of soil at the interface. The interface is a 2 node (soil-structure) element, with a virtual thickness used to compute tangential and normal stiffnesses.

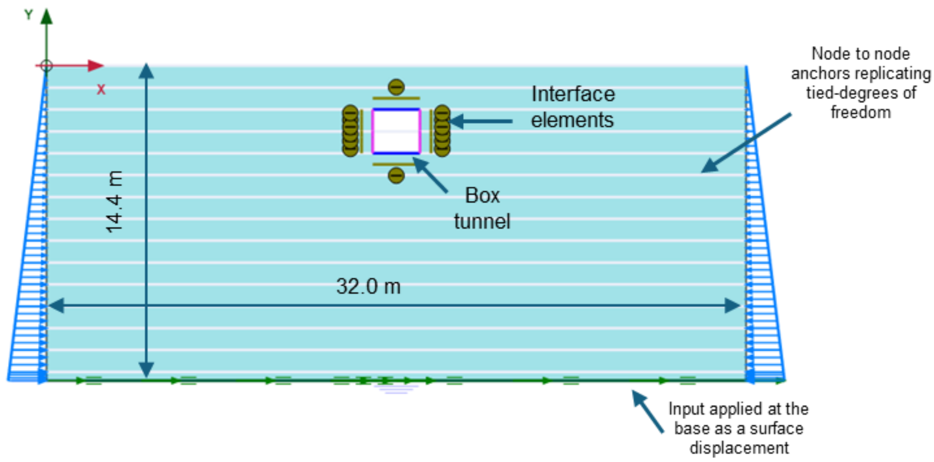

Figure 127. Numerical model in Plaxis 2D.

Unit weight, friction angle and cohesion of Fontainebleau sand were known from tests performed before starting the experimental campaign. Model's parameters (*i.e.*, E_{oed}, E_{50}, E_{ur}, G_0, m, γ_{07}) have been obtained from literature data referred to the same sand fraction, with equal or similar relative density. In Li *et al.*, (2013) decay curves (Figure 128a and b) and initial shear modulus profile (Figure 128c) with depth are reported. The decay curve was obtained at a confining pressure equal to 96 kPa. A campaign of triaxial tests on dry samples of Fontainebleau sand at different confining pressures and relative densities was carried out by Latini and Zania (2016). The report has been used to retrieve data about elastic moduli of the sand. In particular, TEST 5 (confining pressure equal to 100 kPa and Dr = 65%) has been chosen to extract E_{oed}, E_{50}, E_{ur}. The resulting set of parameters is reported in Table 36; in Figure 128 the comparison between experimental and numerical decay curves and damping ratio is reported. The agreement is satisfying, even for damping, especially considering that the range of strain expected falls within 0.1%. In Li *et al*., 2013, the damping curve starts, at low level of shear strain, from a value equal to 3.7%, therefore, in addition to the hysteretic damping provided by the constitutive model, a Rayleigh damping has been assigned to the soil in Plaxis. The calibration of the control frequencies for Rayleigh damping has been conducted first by evaluating the amplification function of the soil with STRATA code, with the soil subjected an input with peak acceleration equal to 0.1g, and assuming a shear wave velocity Vs = 200 m/s. The first two frequencies are 2.7 and 8.8 Hz respectively. Thus, in this case, the procedure proposed by Amorosi *et al*. (2010) was chosen: it consists in calibrating the frequencies for Rayleigh damping taking the first frequency amplified by the soil (2.7 Hz) and the frequency corresponding to the first de-amplification which happens at 4.6 Hz.

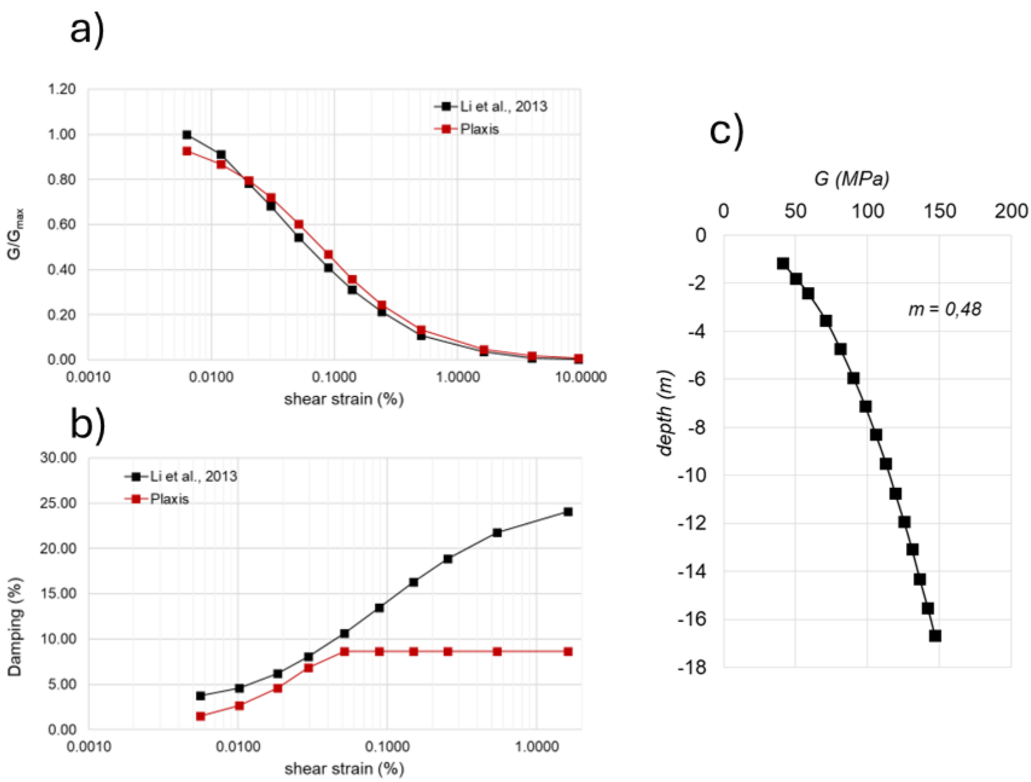

Figure 128. a) decay curve of initial shear modulus experimental vs numerical. b) damping experimental vs numerical. c) Initial shear modulus profile of Fontainebleau sand according to Li et al., (2013).

Table 36. Soil properties in Plaxis 2D.

$\gamma_{sat\text{-}unsat}$	E^{ref}_{50}, E^{ref}_{oed}	E_{ur}	G_0	G_0/G_{ur}	γ_{07}	m	p_{ref}
kN/m^3	MPa	MPa	MPa	-	%	-	kPa
16-18	27.7	151.0	133.7	2.3	0.3	0.48	100

According to Dano *et al.* (2024), the properties of Fontainebleau sand are significantly affected by its density. In their review the results of many monotonic triaxial tests are reported, where samples of different density are tested, at diverse strain levels (Figure 129). The unit weight of the dry sand after pouring is 15.82 kN/m^3, so that the most representative curves among those reported in Figure 129 are the red ones (ρ_d= 1551 kg/m^3 corresponding to $\gamma_d \approx 15.51$ kg/m^3). Based on this consideration the red curves at a confining pressure of *p'* = 100 kPa was used as a benchmark for comparison with the stiffness properties set in Plaxis. The triaxial results obtained with the soil test tool of Plaxis completely overlap with the mentioned red curve of Figure 129, in the q/ε_a plane. Regarding boundary conditions, they were set equal to those applied in 3D models discussed in C*hapters 3* and *4*, to make it possible the comparison. Moreover, since no dissipative boundaries were applied in the ESB, the reflective boundaries adopted in the numerical model are supposed to work well in replicating the experimental conditions.

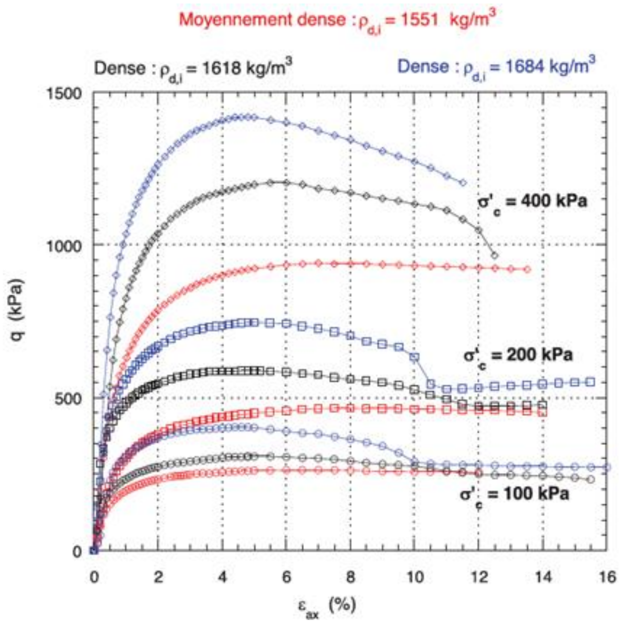

Figure 129. Effect of density on triaxial tests carried out on Fontainebleau sand specimens at different confining pressures (after Dano et al., 2024).

5.2.1. Analyses results

The first case reproduced with FE software is Case 1 of Table 33. As illustrated in Figure 127, the model is symmetrical along its vertical axis with the box placed at its center. The box is modeled with isotropic elastic plates with equivalent thickness. The geometrical properties of the box, reproduced at prototype scale, are reported in Table 34, and the mechanical properties are those of the aluminum used for the box (Table 35). The roughness of interface, experimentally obtained with sandblasting, was modeled using $R_{interface} = 0.67$, *i.e.* reducing 1/3 the strength properties of Fontainebleau sand at soil/structure interface. The 4 inputs were applied in sequence, as in experimental setup. Maximum horizontal displacements of lateral sides of the box were extracted in correspondence with the location of the extensometer's flaps and the comparisons with recorded data are reported in Figure 130. Maximum accelerations and acceleration time histories along the four out of five arrays of Figure 126 have been extracted and compared with recorded data, for each of the applied inputs the results in terms of maximum values are reported in Figure 131. Both the quantities underwent a bandpass filtering procedure with a Butterworth filter of 8th degree.

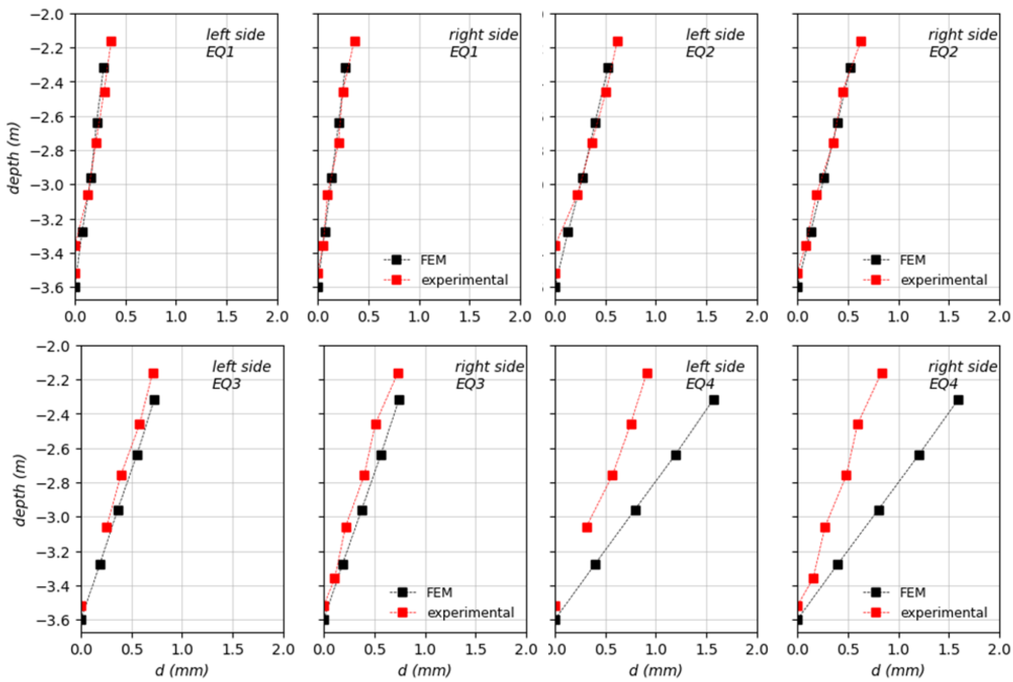

Figure 130. Maximum displacements at the sides of the tunnel box, experimental vs FEM.

The limit frequencies are 0.5 Hz and 10 Hz for accelerations, and 0.5 and 15 Hz for displacements, according to how recorded data were processed. Empty markers in array 3 plots (Figure 131) are, instead, experimental points used for comparison, but not perfectly aligned with other points of array 3, since at that depth there is the tunnel. Each point of Figure 130 is obtained as the maximum of the displacement time history recorded at that position in the soil domain, therefore, they are obtained as non-contemporary data. However, it was verified that the profile of maximum racking (*i.e.*, maximum displacement at the top of the box) is almost identical to that obtained with the described procedure. The calculated maximum displacements of the box perfectly overlap to those recorded for EQ1 and EQ2 and even for EQ3 the agreement is very good. Only for EQ4, FE data overestimate the recorded data of about 100%.
Recorded accelerations (Figure 131) amplify very little, or don't amplify at all, without significant differences among the position of the array in the shear box and with respect to the tunnel axis. In fact, for all the arrays considered, acceleration at the top of the box is nearly equal to the peak acceleration of the input. Numerically obtained peak accelerations, instead, show amplification with values up to +150% of the input peak acceleration. The amplification is maximum for input EQ1 and decreases as the input peak acceleration increases. However, values of computed accelerations range between +15% and +35% of recorded ones; moreover, similarly to the recorded data, no significant difference is found among the arrays that, for each input, produce very similar amplifications. Regarding array 3, along tunnel axis, the recorded de-amplification registered at the depth of the top slab of the tunnel (empty markers) is a finding confirmed by some researchers (*e.g.*, Abate and Massimino, 2017), as well as the amplification along the same array registered at the ground level and confirmed (even if with higher values) by FEM results.
From Husid plot in Figure 132 significant duration can be deducted, being nearly equal to 10 s. Therefore, to make comparison easier, acceleration time histories are reported in Figure 133 in the range of time 6-16 s for array 2 (*i.e.*, free field array), EQ3. In Figure 133 the plot for A13 shows some spikes (out of scale) in experimentally recorded signal, that's why it was considered non-reliable data, thus not represented in acceleration profiles.

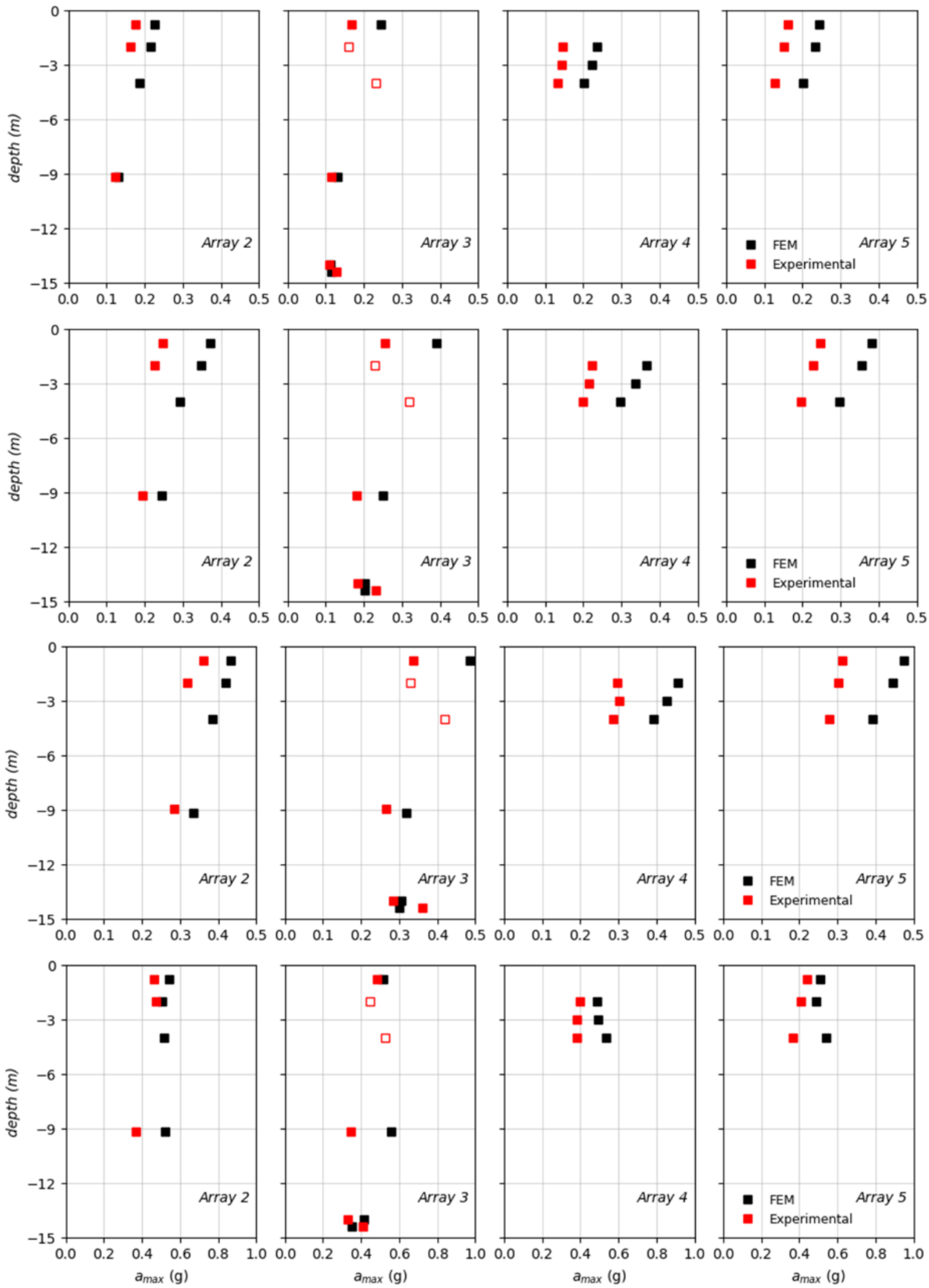

Figure 131. Maximum acceleration profiles along arrays 2, 3, 4, 5, recorded vs calculated (FEM).

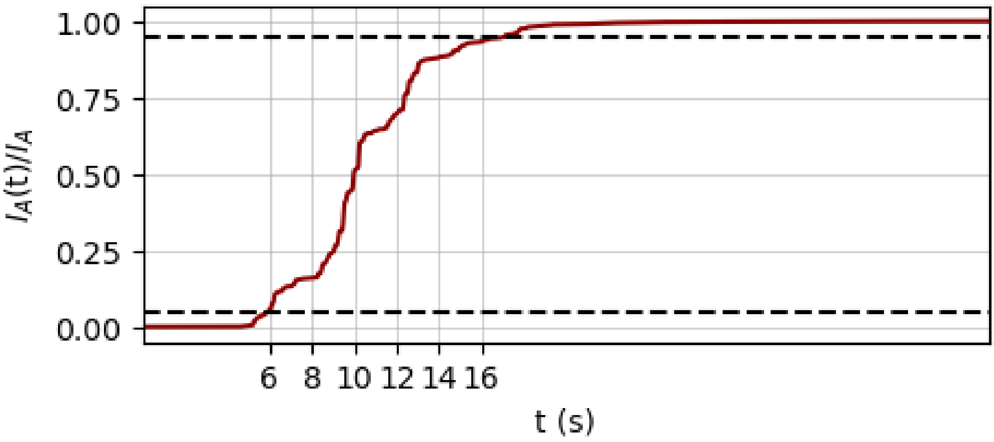

Figure 132. Husid plot for EQ1, EQ2, EQ3 inputs.

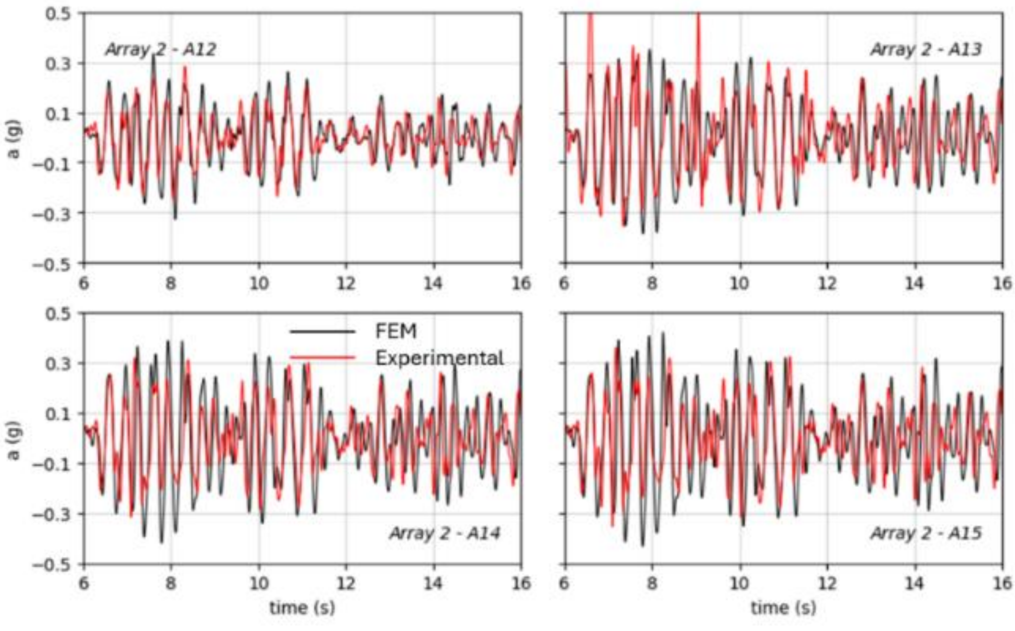

Figure 133. Acceleration time histories for the time interval 6-16 s for array 2 with EQ3 input: numerical (FEM) vs experimental.

Looking at the acceleration time histories, it is possible to notice that between recorded and numerical signals there is no phase difference, whereas numerical model tends to amplify acceleration while propagating upward more than the soil does in experiments; the difference, already noted in maximum acceleration profiles, is not attributable to some spikes of the signal, but constantly present over time. This is probably due to the way damping is implemented into the constitutive model. In fact, once G_0 attains a value equal to G_{ur} the damping in the model doesn't increase anymore and, according to Brinkgreve *et al*., (2007) it keeps a constant value as shown Figure 128, where, even for very low levels of strain the damping curve stays below the experimental one. However, Amorosi *et al*., (2016) pointed out that this is not correct, in fact according to the model formulation in Plaxis, for shear strain higher than $\gamma_{cut\text{-}off}$ the tangential shear modulus G_t presents a cut-off, but this is not the case for the secant shear modulus G_s, represented in Figure 128, that keeps decreasing as $\gamma_{cut\text{-}off}$ increases, thus producing a geometrical reduction of damping that tends asymptotically to zero.

Effect of tunnel stiffness

A second set of analyses, always in dry conditions, was performed simulating the flexible box (Case 5 of Table 33). The soil and the experimental setup are the same as that described for Case 1, while the dimensions assigned to plates are in Table 34. Recorded and computed displacements along the lateral sides of the box, referred to input EQ4, are shown in Figure 134. The displacements are much greater than in the rigid case (reported in figure for comparison), with values at the top that increase of about 280%. In flexible case, the agreement between recorded and calculated data significantly increases, in fact, the lateral side of the tunnel reaches the same slope and almost the same absolute value of displacement at a given depth. Again, for input EQ4 the same comparison is reported in Figure 135 in terms of maximum accelerations. Although the difference in amplification already observed for the rigid case is confirmed between computed and recorded data, it remains constant between the two cases and the slight difference between flexible and rigid box goes towards an increase in peak acceleration in flexible case for both numerical and experimental results.

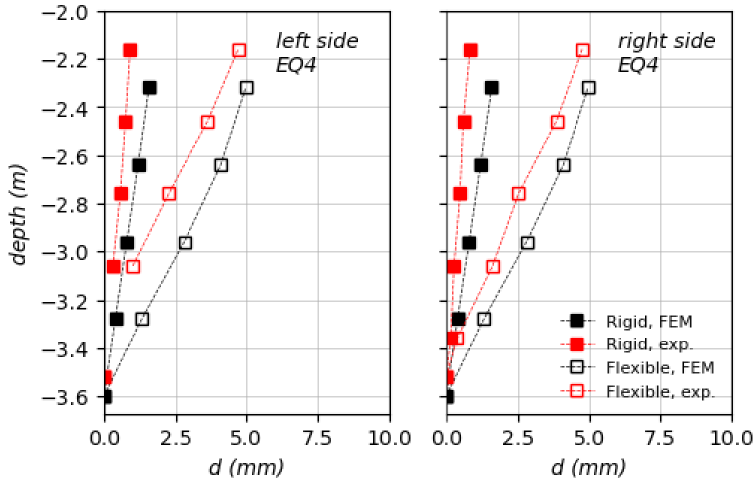

Figure 134. Maximum displacements of the lateral side of the box: numerical vs. experimental.

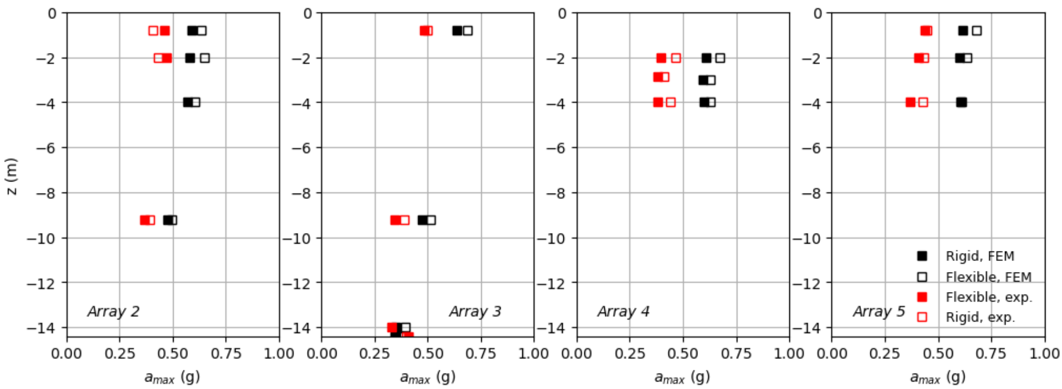

Figure 135. Maximum acceleration along the 4 arrays indicted in Figure 126, flexible tunnel, input EQ4: FEM vs. experimental.

5.3. Conclusions

This chapter has been dedicated to the description of the experimental apparatus and simulation of centrifuge experiments conducted with the aim of studying the seismic behavior of a box tunnel in dry sand (Fontainebleau N34), with focus on the deformation mode of the box and the peak accelerations around it. The analyses were conducted on Plaxis 2D using Hardening soil with small strain model for the sand calibrated with literature data. Among the various experiments carried out in centrifuge, here the dry case with flexible and rigid tunnel walls are compared with numerical results. The displacements of the box are very well predicted with the software; peak accelerations, instead, are overestimated since the simulation produces an amplification not registered in experiments. However, the considered location doesn't seem to affect the result, and no significative differences are found comparing flexible and rigid case if peak accelerations are considered, both the aspects are confirmed by calculation.

Chapter 6

Conclusions and future developments

This thesis investigated the static and seismic effects induced by deep supported excavations on the surrounding environment, treating the excavation as a coupled soil–structure system rather than as an isolated underground structure. The literature review referred to underground structures such as deep excavations, exposed in *Chapter 2*, highlighted significant gaps in current design approaches. Design of retaining structures such as bulkheads and anchors involves the sizing of structural elements in limit conditions and a strict control of induced displacements, in service conditions. Because of the complex structural systems and soil-structure interaction developing during realization, the design is often addressed with simplified methods, usually considered conservative, but disregarding many aspects of the real systems which are important for an adequate modelling the problem. The shortcoming is even more noticeable when it comes to designing seismic conditions, where few simplified methods for estimating the additional seismic load exist, but even less information is available about the effect that underground structures may have on above-ground buildings and existing facilities nearby. Such effects are expected to arise from two distinct mechanisms. First, the presence of the excavation immediately induces three-dimensional wave propagation conditions, overcoming the one-dimensional assumptions typically adopted in local seismic response analyses describing wave propagation from seismic bedrock to the ground surface. Second, excavation activities significantly modify the in-situ stress state of the soil prior to earthquake occurrence.
With the aim of overcoming some of the issues highlighted in literature review, this thesis has been dedicated to the analysis of the effect that in static and seismic conditions a deep excavation, intended as the whole soil-structure system, has on the surroundings. To this aim, two deep pits excavated in the center of the city of Napoli for the construction of metro stations, namely *Chiaia* and *San Pasquale* stations, part of the most recently opened metro line (Line 6) were used for reference, treated in *Chapter 3* and *Chapter 4* respectively. Due to the proximity of many residential and historical buildings, in both cases monitoring activities were carried out during all the

duration of excavation and subsequent construction of internal structures. The collection of many data retrieved by monitoring instruments installed on site mainly to control the displacements, together with the data of site and laboratory investigations were used to conduct static tridimensional back analyses of the excavation process with finite element methods. Particular attention has been paid to buildings, modelled with diverse degrees of approximation (*i.e.*, as surface loads, as plates with equivalent stiffness, or with a fully model of the structural system), to better replicate recorded displacements. The accurate modeling of the static part of the problem makes the results obtained in the subsequent seismic simulation more reliable. In fact the results confirm that the stress state induced by excavation plays a fundamental role in the seismic response of the system and cannot be neglected or oversimplified.
As mentioned above, in seismic conditions the prevailing scope of the work has been to explore the modification of motion at the ground due to excavation. To isolate the phenomenon from the reciprocal, namely the effect of above-ground buildings on the embedded structure, buildings were accounted for only in simplified ways, thus disregarding inertial interaction.
The exploration of *Chiaia* case study, carried out in dry sands and in Neapolitan yellow tuff led to observations about the role played by the excavation which was found to affect the peak acceleration at the ground level and in depth in different directions depending on input motion and distance from the excavation, and suggesting an involvement of the direction of the input motion application in the obtained results. The Chiaia station represents a particularly complex case study, as the excavation is embedded within a historically stratified urban environment characterized by pronounced topographic variations and the presence of buried pre-existing retaining structures. These features introduce strong geometric and mechanical asymmetries, which discouraged a systematic investigation of seismic response as a function of input motion direction, as such analyses would not have led to unambiguous or generalizable interpretations. However a parametric analysis was conducted on the role played by stiffness of the interface which is found to be a key parameter in assessing the effect of the excavation on both peak accelerations and displacements, at small distance from it. For the above peculiarities the observations related to this case study are strictly linked to the site conditions but have been useful to rationally design the analyses of *San Pasquale* station, which is better suited for parametric analysis thanks to its simpler geometrical characteristics.
The excavation for the construction of *San Pasquale* station was completely carried out in saturated sands, which produced significant differences in adopted retaining systems

with respect to *Chiaia*, moreover this allowed in this thesis for the exploration of different constitutive models in numerical simulations, accounting or not for the excess pore pressure cyclic accumulation. The study was conducted disregarding the presence of aboveground structures focusing on retaining structures and on the spatial distribution of accelerations around the excavation, even at significant distance from it, and derived parameters.

The problem, as already suggested by the analyses of *Chapter 3*, confirms to be affected by the direction of input motion application with respect to flexibility of the retaining structure along the loading direction. This is particularly visible in bending moments acting on bulkheads, where the direction of application of input motion and the constitutive model adopted for the soil are found to have considerable impact in determining the seismic increment of bending moment. Thus, the choice of the constitutive law, which in turn affects the soil-structure relative flexibility, can have a relevance in the seismic design of retaining structures.

For what concerns the results related to accelerations and derived parameters, some general and practical indications deriving from the *San Pasquale* case study, and applicable to *Chiaia* case as well, are listed here:

The presence of the open pit deep excavation modifies peak ground accelerations, intensity and frequency content of the motion around it, leading to differences with respect to its absence that can even be significant.

Referring to geometrical properties, in contrast with existing literature regarding tunnels, it is not found a clear effect of excavation plan dimensions, while the depth and the stiffness of retaining structure (thus its length) seems to influence the result. The latter is confirmed either by the parametric analysis on the interface stiffness carried out in *Chapter 3*, and by the different results retrieved in changing input direction in *Chapter 4*.

In the immediate vicinity of retaining structures (<5 m) a reduction of peak acceleration can usually be considered with respect to a free field analysis. Although higher values are found, most frequently the registered reduction is comprised within -25%.

For higher distances (nearly corresponding, in the case of San Pasquale, to half of the excavation depth) an amplification of peak acceleration and of the energetic content is registered, with values not exceeding +100%.

The need for a tridimensional modeling of the system is highlighted, in fact as for static conditions, even in this case a sort of "corner effect" is observed, because of the increased stiffness of soil-structure system that leads to a diminishment of excavation

effect, in both the analyzed case studies. In the middle part of the excavation wall, instead, the effect is maximized.
Often, in dynamic calculation soil behavior is simplified and considered linear visco-elastic; however, the need for accounting for the non-linear and plastic components of the soil behavior emerges from the comparison between the adopted constitutive models.
In addition to results related to accelerations and their distribution, excess pore water pressures Δu calculated by the software during dynamic loading were obtained and analyzed. It is interesting to note that the accumulation of Δu is negligible in free field analyses. In the case where the excavation is simulated, instead, an accumulation is visible and it is concentrated near the bottom part of the retaining structures. The pore pressure ratio reaches values in the range 0.2-0.6, depending on the frequency content of the input more than on the value of the peak acceleration.
Lastly, the reliability of the tools adopted for the dynamic analyses, involving constitutive model, calibration procedures and boundary conditions, that clearly have no experimental validation in the analyzed case studies, has been tested in C*hapter 5* successfully simulating centrifuge experiments carried out for characterizing the seismic behavior of a rectangularly shaped tunnel embedded in pluviated Fontainebleau sand. Despite the agreement between the results of the two cases and the obtained validation, although consistent trends emerged from the two case studies, the conclusions of this thesis remain inherently site-specific, reflecting the complexity and variability of deep excavation problems. Nevertheless, the work provides original contributions by combining detailed static back-analysis, three-dimensional numerical modeling, and fully coupled seismic analyses for deep open excavations—an area still scarcely explored in current literature.
Further research is required to develop design-oriented guidelines of broader applicability. Future studies should systematically investigate the influence of excavation geometry, soil properties, retaining structure stiffness, and seismic input direction. The interaction between excavations and above-ground buildings should be explicitly modeled to assess not only acceleration amplification but also damage-related parameters such as interstory drift and dissipated plastic energy. Additional experimental data from centrifuge testing or field monitoring would be invaluable for validation purposes.
As outlined in the literature section presented in this thesis, seismic wave propagation is typically investigated under visco-elastic assumptions while the stresses acting on retaining structures are evaluated by means of non-linear, elasto-plastic soil models.

Although this methodological distinction reflects common practice and allows a rational interpretation of results, the possibility of overcoming such separation appears both feasible and potentially advantageous in order to better capture the complex interaction between deep excavations and surrounding buildings. In the present work, buildings were modelled as elements influenced by the excavation-induced seismic response; however, the dual problem, namely the influence of buildings on the seismic behavior of the excavation through inertial interaction effects, also deserves attention. A thorough investigation of these mechanisms is required before design-oriented guidelines and recommendations can be proposed, particularly with respect to simplified design approaches aimed at accounting for the mutual interaction among closely spaced structures in urban environments.

Appendix 1

I. Calculation of stiffness of orthotropic plates

Herein a brief explanation of the procedure adopted to derive the stiffness properties of orthotropic elastic plates described in *Chapter 3* is reported.

The first attempt of estimating the stiffnesses of plates representing pile walls, was made following the formula suggested in Plaxis Material Models Manual (Bentley, 2023) specifically referred to structural elements whose main deformation mode is the flexural one. In Figure 136 the representation of the local direction of a plate element and the bending moments M11 and M22, as defined in Plaxis, is given.

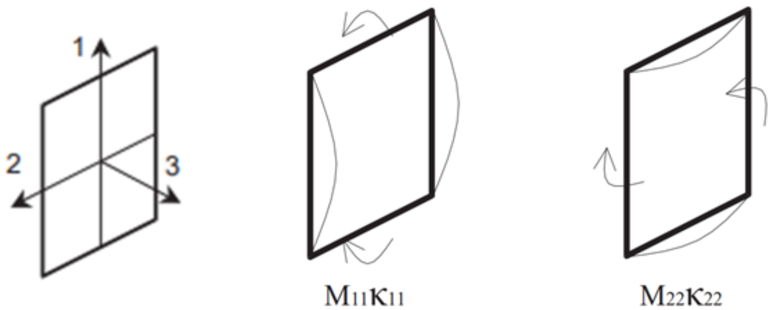

Figure 136. Local direction of a plate element and bending moments M11 and M22 (Plaxis Materials Models Manual, Bentley, 2024).

However, the formula suggested by the manual led to a significant overestimation of displacements of the retaining structure with respect to monitoring data. Therefore, it was preferred to proceed in another way, solving the system, composed of 2 equations, reported below:

$$\begin{cases} \dfrac{d_{eq}}{D} = \dfrac{\pi}{4} \cdot \dfrac{D}{i} \\ E_{eq} \dfrac{i \cdot d^3{}_{eq}}{12} = E_{cls} \dfrac{\pi \cdot D^4}{64} \end{cases}$$

Where D is the diameter of the pile, i the spacing between adjacent piles, E_{cls} is the Young's modulus of concrete (in this case the concrete class is C20/25) and E_{eq} the equivalent Young's modulus of the equivalent rectangular section. The first equation states the equivalence of the areas, determining the thickness of the equivalent rectangular cross section per unit length d_{eq}. The second one poses the bending stiffness of the pile wall along direction 1 (Figure 136) equal to that of the plate of equivalent thickness d_{eq} and from it the equivalent Young's modulus is derived. Lastly, E_2 (*i.e.*, the modulus governing the bending along direction 2) is assumed to be one order of magnitude lower than E_1.

It is worth noticing that, given the very short spacing between piles, it was assumed to be a pile wall of adjacent piles even if they were contiguous.

The same approach based on equivalence of stiffnesses was adopted to characterize the material for the T-shaped diaphragm wall of the San Pasquale case study (*Chapter 4*), that were modelled as rectangularly shaped panels, with the necessary differences given the different geometry of the section with respect to the case of pile walls.

II. Calculation of properties of orthotropic plates representing Military Court and Basilica of *Santa Maria degli Angeli*.

For what concerns the Military Court and Basilica of *Santa Maria degli Angeli*, mentioned in *Chapter 3*, they were modelled in the calculation domain for static analyses with linear elastic orthotropic plates, whose stiffnesses in the orthogonal directions playing in the plane of the plate, E_1 and E_2, were stated based on the distribution of bearing walls of the building.

In fact, the Young's modulus of masonry, regarded as a homogeneous material, is fixed for every direction of bearing walls. What is changing between the two directions, instead, is the inertia which depends on the number of bearing walls disposed on each side of the building. However, in Plaxis the definition of an orthotropic plate material requires the definition of an equivalent thickness d_{eq} (which in this case was calculated subtracting the space occupied by openings to the total height of the building) and the two mentioned moduli E_1 and E_2. Since the thickness of the plate schematizing the building is necessarily uniform over its area, the difference between the two inertias has been incorporated into the moduli, by simply applying an equivalence between bending stiffnesses per unit length.

$$EI_i = E_i I \qquad with\; i = 1, 2$$

More specifically, for the Military Court the entire plane distribution of bearing walls was accounted for in defining the plate properties. For the Basilica, instead, only the masonry wall of the façade was considered since it is noticeably more massive and stiffer than the rest of the structural elements of church, according to Ferraro (2012).

Regarding the height of the façade, which is variable along its length, it was chosen an equivalent mean value, constant over the length.

In the dynamic model, where the plates were replaced by solid elements modeled with JMM, the material properties were calibrated to replicate the properties already established for orthotropic plates.

Bibliography

Abate, G., & Massimino, M. R. (2017a). Numerical modelling of the seismic response of a tunnel–soil–aboveground building system in Catania (Italy). *Bulletin of Earthquake Engineering*, *15*(1), 469-491.

Abate, G., & Massimino, M. R. (2017b). Parametric analysis of the seismic response of coupled tunnel–soil–aboveground building systems by numerical modelling. *Bulletin of Earthquake Engineering*, *15*(1), 443-467.

Abbas, Q., Yoon, J., Jung, K., and Lee, J. (2025). Characterization of lateral earth pressure distribution on walls for deep excavation. *International Journal of Geotechnical Engineering*, 1-17.

Abuhajar, O., El Naggar, H., & Newson, T. (2015). Experimental and numerical investigations of the effect of buried box culverts on earthquake excitation. *Soil Dynamics and Earthquake Engineering*, *79*, 130-148.

Al Atik, L., & Sitar, N. (2010). Seismic earth pressures on cantilever retaining structures. *Journal of geotechnical and geoenvironmental engineering*, *136*(10), 1324-1333.

Al-Atik, L., & Sitar, N. (2009). Seismically induced lateral earth pressures: a new approach. In *Proceedings of the 17th International Conference on Soil Mechanics and Geotechnical Engineering (Volumes 1, 2, 3 and 4)* (pp. 1417-1420). IOS Press.

Alielahi, H., & Adampira, M. (2016). Seismic effects of two-dimensional subsurface cavity on the ground motion by BEM: Amplification patterns and engineering applications. *International Journal of Civil Engineering*, *14*(4), 233-251.

Alielahi, H., Kamalian, M., & Adampira, M. (2015). Seismic ground amplification by unlined tunnels subjected to vertically propagating SV and P waves using BEM. *Soil Dynamics and Earthquake Engineering*, *71*, 63-79.

Amorosi, A., & Sangirardi, M. (2021). Coupled three-dimensional analysis of the progressive tunnelling-induced damage to masonry buildings: is it always worth it?. *Tunnelling and Underground Space Technology*, *118*, 104173.

Amorosi, A., Boldini, D., & Di Lernia, A. (2016). Seismic ground response at Lotung: Hysteretic elasto-plastic-based 3D analyses. *Soil Dynamics and Earthquake Engineering*, *85*, 44-61.

Amorosi, A., Boldini, D., & Elia, G. (2010). Parametric study on seismic ground response by finite element modelling. *Computers and Geotechnics*, *37*(4), 515-528.

Anand, V., & Kumar, S. S. (2018, November). Seismic soil-structure interaction: a state-of-the-art review. In *Structures* (Vol. 16, pp. 317-326). Elsevier.

Arias, A. (1970). A measure of earthquake intensity, in Seismic Design for Nuclear Power Plants, R. J. Hansen (Editor), MIT Press, Cambridge, Massachusetts, 438–483.

Autuori, S., (2016) La stazione San Pasquale della metropolitana di Napoli. Costruzione, monitoraggio ed analisi dei comportamenti osservati., PhD Thesis (in italian)

Bang, S. (1985). Active Earth Pressure Behind Retaining Wall. *Journal of the Geotechnical Engineering Division*, ASCE, Vol. Ill, No. 3, Mar., pp. 407- 412

Bathe, K. J. (2006). *Finite element procedures*. Klaus-Jurgen Bathe.

Baziar, M. H., Moghadam, M. R., Kim, D. S., & Choo, Y. W. (2014). Effect of underground tunnel on the ground surface acceleration. *Tunnelling and Underground Space Technology*, *44*, 10-22.

Beaty, M.H., Byrne, P.M. (1998). An effective stress model for predicting liquefaction behaviour of sand. Geotechnical Earthquake Engineering and Soild Dynamics, ASCE Geotechnical Special Publication 75, 766–777.

Bentley (2024). “PLAXIS 3D 2024.2 – Reference Manual”.

Benz, T., Schwab, R., & Vermeer, P. (2009). Small-strain stiffness in geotechnical analyses. *Bautechnik*, *86*(S1), 16-27.

Benz, T.: Small-strain stiffness of soils and its numerical consequences. Dissertationsschrift. Mitteilung 55 des Instituts für Geotechnik, Universität Stuttgart, 2007.

Bilotta, E., A. Paolillo, G. Russo, and S. Aversa. 2017. “Displacements induced by tunnelling under a historical building.” *Tunnelling Underground Space Technology* 61 (Jan): 221–232.

Boone, S. J., Westland, J., & Nusink, R. (1999). Comparative evaluation of building responses to an adjacent braced excavation. *Canadian Geotechnical Journal*, *36*(2), 210-223.

Boscardin, M. D., & Cording, E. J. (1989). Building response to excavation-induced settlement. *Journal of Geotechnical engineering*, *115*(1), 1-21.

Boscardin, M. D., Cording, E. J. (1989). Building response to excavation-induced settlement. *Journal of Geotechnical Engineering*, vol. 115, no. 1, pp. 1–21,

Brandenberg, S. J., Mylonakis, G., & Stewart, J. P. (2015). Kinematic framework for evaluating seismic earth pressures on retaining walls. *Journal of Geotechnical and Geoenvironmental Engineering*, *141*(7), 04015031.

Brinkgreve, R. B. J., Kappert, M. H., & Bonnier, P. G. (2007). Hysteretic damping in a small-strain stiffness model. *Proc. of Num. Mod. in Geomech., NUMOG X, Rhodes*, 737-742.

Burland, J. B., & Wroth, C. P. (1975). *Settlement of buildings and associated damage* (No. CP 33/75).

Burland, J. B., Standing, J. R., & Jardine, F. M. (Eds.). (2001). *Building Response to Tunnelling: Case Studies from Construction of the Jubilee Line Extension, London. Case studies* (Vol. 2). Thomas Telford.

Burland, J.B.; Broms, B.B. & De Mello, V.F.B. (1977) Behaviour of foundations and structures. Proc. 9th Int. Conf. Soil Mechs & Fdn Engng, Tokyo, v. 2, pp. 495-546.

Cabanas, L., Benito, B., & Herráiz, M. I. G. U. E. L. (1997). An approach to the measurement of the potential structural damage of earthquake ground motions. *Earthquake engineering & structural dynamics*, *26*(1), 79-92.

Callisto, L. (2015). *MARTA v. 1.1: a computer program for the site response analysis of a layered soil deposit*.

Callisto, L. (2024). A method for the seismic design of multi-propped retaining walls. *Rivista italiana di geotecnica: LVIII, 1, 2024*, 44-51.

Cantone, A. (2010). Comportamento di scavi profondi in ambiente urbano. PhD Thesis (in Italian).

Caquot, A., & Kerisel, J. (1948). *Tables de butée, de poussée et de force portante des fondations*. Gauthier-Villars, Paris.

Castaldo, P., & De Iuliis, M. (2014). Effects of deep excavation on seismic vulnerability of existing reinforced concrete framed structures. *Soil Dynamics and Earthquake Engineering*, *64*, 102-112.

Castaldo, P., Calvello, M., & Palazzo, B. (2013). Probabilistic analysis of excavation-induced damages to existing structures. *Computers and Geotechnics*, *53*, 17-30.

CEN (2004) Eurocode 7: Geotechnical design - Part 1: General rules, EN 1997-1: 2004 (E), (F) and (G), November 2004, European Committee for Standardization: Brussels.

Chazelas, J. L., Escoffier, S., Garnier, J., Thorel, L., & Rault, G. (2008). Original technologies for proven performances for the new LCPC earthquake simulator. *Bulletin of earthquake engineering*, *6*(4), 723-728.

Chowdhury, S. S. (2019). A study on lateral earth pressure against strutted retaining wall in cohesionless soil deposit. *International Journal of Geotechnical Engineering*, *13*(2), 122-138.

Clayton, C. R., Woods, R. I., Bond, A. J., and Milititsky, J. (2014). *Earth Pressure and Earth-Retaining Structures*. CRC Press.

Clough G., Smith E., Sweeney B. (1989). Movement control of excavation systems by iterative design. *Proc. ASCE Geotech. Eng,* 2, 869-884.

Clough, G. W., & Duncan, J. M. (1971). Finite element analyses of retaining wall behavior. *Journal of the Soil Mechanics and Foundations Division*, *97*(12), 1657-1673.

Clough, G.W. and Fragaszy, R.F. (1977). “A Study of Earth Loadings on Floodway Retaining Structures in the 1971 San Fernando Valley Earthquake,” Proceedings of the Sixth World Conference on Earthquake Engineering, Vol. 3.

Clough, G.W., and O'Rourke, T.D. 1990. Construction-induced movements of in situ walls. In Proceedings, Design and Performance of Earth Retaining Structures, ASCE Special Conference, Ithaca, New York, pp. 439–470.

Coulomb, C. A. (1776). "Essai sur une application des regles des maximis et minimis a quelques problemes de statique relatifs a l'architecture." Memoires de l'Academie Royale pres Divers Savants 7.

Dano, C., Thorel, L., Dupla, J. C., Benahmed, N., & Li, Z. (2024). Compilation des propriétés physiques et mécaniques du sable de Fontainebleau NE34. *Revue Française de Géotechnique*, (179), 6.

De Felice, G., & Malena, M. (2019). Failure pattern prediction in masonry. *Journal of Mechanics of Materials and Structures*, *14*(5), 663-682.

Duncan, J. M., and Chang, C. Y. (1970). Nonlinear analysis of stress and strain in soils. *Journal of the soil mechanics and foundations division*, *96*(5), 1629-1653.

Elenas, A. (2000). Correlation between seismic acceleration parameters and overall structural damage indices of buildings. *Soil Dynamics and Earthquake Engineering*, *20*(1-4), 93-100.

Evangelista L. (2006). Suscettibilità alla liquefazione dinamica dei depositi sabbiosi in falda della città di Napoli. Tesi di laurea, Università degli Studi di Napoli Federico II. (in Italian)

Fabozzi, S. (2017) Behavior of segmental tunnel lining under static and dynamic loads. PhD Thesis

Fabozzi, S., V. Licata, S. Autuori, E. Bilotta, G. Russo, and F. Silvestri. (2017.) "Prediction of the seismic behavior of an underground railway station and a tunnel in Napoli (Italy)." *Underground Space* 2 (2): 88–105.

Fang, Y. S., Chen, T. J., and Wu, B. F. (1994). Passive earth pressures with various wall movements. *Journal of geotechnical engineering*, *120*(8), 1307-1323.

Fenelli, G. B., & Ramondini, M. (1997). Monitoring the behaviour of a multi-anchored diaphragm in pyroclastic soil. In *Proceedings of the international conference on soil mechanics and foundation engineering-international society for soil mechanics and foundation engineering* (vol. 2, pp. 1315-1318). AA Balkema.

Ferraro, I. (2010). Napoli. Atlante della Città storica “Chiaia”. Oikos Edizioni. (In Italian)

Ferraro, I. (2012). Napoli. Atlante della Città storica “Pizzofalcone e le Mortelle”. Oikos Edizioni. (In Italian)

Finno R.J., Bryson L.S. and Calvello M. (2002). Performance of a stiff support system in soft clay. *Journal of Geotechnical and Geoenvironmental Engineering*, ASCE, Vol. 128, No. 8, p. 660-671.

Finno, R. J. (2010). Recent trends in supported excavation practice. In *Earth Retention Conference 3*. pp. 1-18.

Frank, R. (2007). Basic principles of Eurocode 7 on ‘geotechnical design’. *Soils and Rocks*, *30*(1), 39-50.

Franzius, J. N., Potts, D. M., & Burland, J. B. (2006). The response of surface structures to tunnel construction. *Proceedings of the Institution of Civil Engineers-Geotechnical Engineering*, *159*(1), 3-17.

Gaba, A.R., Hardy, S., Doughty, L., Selemetas, D., and Powrie, W. (2017). Embedded Retaining Walls – Guidance for Design. Ciria, London, UK, Report C760

Gaudio, D., & Rampello, S. (2019). The influence of soil plasticity on the seismic performance of bridge piers on caisson foundations. *Soil Dynamics and Earthquake Engineering*, *118*, 120-133.

Gazetas G. (1991). Formulas and charts for impedances of surface and embedded foundations. *J Geotech Eng*; 117(9):1363–81.

Ghergu, M. & Ionescu, I.R., 2009. Structure-soil-structure coupling in seismic excitation and “city effect”, Int. J. Eng. Sci., 47, 342–354

Goh, K., Response of ground and buildings to deep excavations and tunnelling. (2011) Ph.D. dissertation, University of Cambridge.

Goldberg, D. T., Jaworski, W. E., & Gordon, M. D. (1976). Lateral support systems and underpinning. Volume I: design and construction.

Gonzalez, J. J., & Roesset, J. M. (1977). Dynamic interaction between adjacent structures. *R77-30. Department of Civil Engineering, Massachusetts Institute of Technology, Cambridge, Mass*.

Grant, R., Christian, J. T. and Vanmarcke, E. H. (1974). Differential settlement of buildings. Journal of the Geotechnical Engineering Division, ASCE 100, No.GT9, 973-991.

Guo, J., Chen, J., & Bobet, A. (2013). Influence of a subway station on the inter-story drift ratio of adjacent surface structures. *Tunnelling and underground space technology*, *35*, 8-19.

Hardin, B. O. (1978). “The nature of stress-strain behavior for soils.” *Proc. of the Geotechnical Division Specialty Conference on Earthquake Engineering and Soil Dynamics*, ASCE, Pasadena, 1, 3–90.

Hashash, Y. M. A., Karina, K., Koutsoftas, D., and O'Riordan, N. (2010, August). Seismic design considerations for underground box structures. In *Earth Retention Conference 3*. pp. 620-637.

Hashash, Y. M., Dashti, S., Musgrove, M., Gillis, K., Walker, M., Ellison, K., & Basarah, Y. I. (2018). Influence of tall buildings on seismic response of shallow underground structures. *Journal of Geotechnical and Geoenvironmental Engineering*, *144*(12), 04018097.

Hashash, Y. M., Hook, J. J., Schmidt, B., and Yao, J. I. C. (2001). Seismic design and analysis of underground structures. *Tunnelling and underground space technology*, *16*(4), 247-293.

Hong, N., Ling, Y., Yang, Z., Ha, X., & Xu, B. (2025). Shaking Table Test of a Subway Station–Soil–Aboveground Structures Interaction System: Structural Impact on the Field. *Buildings*, *15*(13), 2223.

Hsieh, P. G., & Ou, C. Y. (1998). Shape of ground surface settlement profiles caused by excavation. *Canadian geotechnical journal*, *35*(6), 1004-1017.

Hua, Z. K., and Shen, C. K. (1987). Lateral earth pressure on retaining structure with anchor plates. *Journal of geotechnical engineering*, *113*(3), 189-201.

Idriss IM. An update to the Seed-Idriss simplified procedure for evaluating liquefaction potential, Proc., TRB Workshop on New Approaches to Liquefaction, January, Publication No. FHWA-RD-99- 165, Federal Highway Administration, 1999.

Idriss, I. M., & Boulanger, R. W. (2006). Semi-empirical procedures for evaluating liquefaction potential during earthquakes. *Soil dynamics and earthquake engineering*, *26*(2-4), 115-130.

Idriss, I. M., & Seed, H. B. (1968). Seismic response of horizontal soil layers. *Journal of the Soil Mechanics and Foundations Division*, *94*(4), 1003-1031.

Idriss, I. M., & Seed, H. B. (1970). Seismic response of soil deposits. *Journal of the Soil Mechanics and Foundations Division*, *96*(2), 631-638.

Idriss, I.M., Boulanger, R. W. (2004). Semi-Empirical Procedures for Evaluating Liquefaction Potential During Earthquake. Proceedings of the 11th ICSDEE & 3rd ICEGE, (Doolin et al. Eds.), Berkeley, CA, USA, 1, 32-56.

Iervolino, I., Galasso, C. & Cosenza, E. (2010). REXEL: computer aided record selection for code-based seismic structural analysis. Bulletin of Earthquake Engineering, 8, 339–362.

Iida, H., Hiroto, T., Yoshida, N., Iwafuji, M. (1996). Damage to Daikai subway station. Soils and Foundations, *Special Issue on Geotechnical Aspects of the January 17 1995 Hyogoken-Nambu Earthquake*. Japanese Geotechnical Society, pp. 283-300.

Isari, M., Razavi, S. K., Tarinejad, R., & Sobhkhiz Foumani, R. (2022). Investigating the effects of underground structures on the scattering of seismic waves reaching the ground surface. *Transportation Infrastructure Geotechnology*, *9*(3), 321-337.

Iwasaki, T., Tokida, K., Tatsuoka, F., Watanabe, S., Yasuda, S., Sato, H., 1982. Microzonation for soil liquefaction potential using simplified methods. Proceedings of the 3rd International Conference on microzonation, Seattle, vol. 3, pp. 1319–1330.

Jappelli, R. (1996). Eurocodice 7: progettazione geotecnica. *Scopi, principi e compatibilità con le norme italiane. Rivista Italiana di Geotecnica, 2*, *3*, 26-35.

Jiang, Y., Gao, Y., & Wu, X. (2016). The nature frequency identification of tunnel lining based on the microtremor method. *Underground Space*, *1*(2), 108-113.

Jibson, R. W. (1993). Predicting earthquake-induced landslide displacements using Newmark's sliding block analysis, Transport. Res. Rec. 9–17

Jibson, R. W., E. L. Harp, and J. A. Michael (2000). A method for producing digital probabilistic seismic landslide hazard maps, Eng. Geol. 58, 271–289.

Kausel, E. and Roesset, J. M. (1974). Soil Structure Interaction Problems for Nuclear Containment Structures. *Electric Power and the Civil Engineer*, Proc. of the ASCE Power Div. Conf., Boulder, Colorado.

Kayen, R. E., & Mitchell, J. K. (1997). Assessment of liquefaction potential during earthquakes by Arias intensity. *Journal of Geotechnical and Geoenvironmental Engineering*, *123*(12), 1162-1174.

Kramer, S. L., & Stewart, J. P. (2025). Geotechnical Earthquake Engineering – II Edition. CRC Press – Taylor and Francis Group.

Kuhlemeyer, R.L., Lysmer, J., (1973). Finite element method accuracy for wave propagation problems. J. Soil Mech. Foundat. Div. 99 (5), 421–427. https://doi.org/10.1061/JSFEAQ.0001885.

L'Amante, D., Flora, A., Russo, G., & Viggiani, C. (2012). Displacements induced by the installation of diaphragm panels. *Acta Geotechnica*, *7*(3), 203-218.

Lambe, T. W. (1967). Stress path method. *Journal of Soil Mechanics and Foundations Division* 95(6): 309-331.

Lancellotta R. (2002). Analytical solution of passive earth pressure. *Géotechnique*, 52, n. 8, pp. 617-619

Lancellotta, R., Ciancimino, A., Costanzo, A., & Foti, S. (2020). *Progettazione geotecnica: Secondo l'Eurocodice 7 e le Norme Tecniche per le Costruzioni 2018*. HOEPLI EDITORE (in Italian).

Lasciarrea, W. G., Amorosi, A., Boldini, D., de Felice, G., & Malena, M. (2019). Jointed Masonry Model: A constitutive law for 3D soil-structure interaction analysis. *Engineering Structures*, *201*, 109803.

Latini, C., & Zania, V. (2016). Triaxial tests in Fontainebleau sand.

Lee, V. W. (1984). Three-dimensional diffraction of plane P, SV & SH waves by a hemispherical alluvial valley. *International Journal of Soil Dynamics and Earthquake Engineering*, *3*(3), 133-144.

Lee, V. W., & Karl, J. (1992). Diffraction of SV waves by underground, circular, cylindrical cavities. *Soil Dynamics and Earthquake Engineering*, *11*(8), 445-456.

Lee, V. W., and Trifunac, M. O. (1979). "Response of tunnels to incident Sh-waves." Engrg. Mech. Div., ASCE, 105,643-659.

Lee, V. W., Chen, S., & Hsu, I. R. (1999). Antiplane diffraction from canyon above subsurface unlined tunnel. *Journal of Engineering Mechanics*, *125*(6), 668-675.

Lew, M., Sitar, N., and Al Atik, L. (2010). Seismic Earth Pressures: Fact or Fiction. Invited Keynote Paper, Earth Retention Conference, ER 2010, ASCE, Seattle.

Li, Z., Escoffier, S., & Kotronis, P. (2013). Using centrifuge tests data to identify the dynamic soil properties: Application to Fontainebleau sand. *Soil Dynamics and Earthquake Engineering*, *52*, 77-87.

Liang, J., Zhang, J., & Ba, Z. (2012). Amplification of in-plane seismic ground motion by group cavities in layered half-space (I). Earthquake Science, 25(4), 275-285.

Liang, L., Xu, C., Fan, X., and Chen, Q. (2023). Hyperbolic stress-strain behaviour of sandy soil under plane strain unloading condition and its application on predicting displacement-dependent active earth pressure. *Computers and Geotechnics*, *155*, 105219.

Licata, V. (2015) A laboratory and field study on cyclic liquefaction of a pyroclastic soil. PhD Thesis

Lin, H. T., Roesset, J. M., & Tassoulas, J. L. (1987). Dynamic interaction between adjacent foundations. *Earthquake engineering & structural dynamics*, *15*(3), 323-343.

Liu, J. M., M. T. Gao, and J. J. Xie (2015). Spatial variability and attenuation of Arias intensity during the 1999 Chi-Chi Mw 7.6 earthquake, Taiwan, Bull. Seismol. Soc. Am. 105, 1768–1778.

Liu, J. M., Wang, T., Wu, S. R., & Gao, M. T. (2016). New empirical relationships between Arias intensity and peak ground acceleration. *Bulletin of the Seismological Society of America*, *106*(5), 2168-2176.

Long, H., Chen, G. X., & Zhuang, H. Y. (2012). Influence of ground structure on the seismic response of underground subway station in soft site. *Advanced materials research*, *368*, 2769-2775.

Lou, M., Wang, H., Chen, X., & Zhai, Y. (2011). Structure–soil–structure interaction: Literature review. *Soil dynamics and earthquake engineering*, *31*(12), 1724-1731.

Luco, J. E., & De Barros, F. C. P. (1994). Dynamic displacements and stresses in the vicinity of a cylindrical cavity embedded in a half-space. *Earthquake engineering & structural dynamics*, *23*(3), 321-340.

Luco, J.E., Contesse, L., 1973. Dynamic structure-soil-structure interaction. Bull. Seismol. Soc. Am. 63 (4), 1289–1303. https://doi.org/10.1785/BSSA0630041289.

Luzi, L., Lanzano, G., Felicetta, C., D'Amico, M. C., Russo, E., Sgobba, S., Pacor, F., & ORFEUS Working 594 Group 5 (2020). Engineering Strong Motion Database (ESM) (Version 2.0). Istituto Nazionale di Geofisica 595 e Vulcanologia (INGV)

Lysmer, J., Seed, H. B., Udaka, T., Hwang, R. N., & Tsai, C. F. (1975). Efficient finite element analysis of seismic soil structure interaction. *Report No. EERC*, 75-34.

MacCalden, P. B. (1969). *Transmission of steady-state vibrations between rigid circular foundations*. University of California, Los Angeles.

Makra, A. (2013) Evaluation of the UBC3D-PLM constitutive model for prediction of earthquake induced liquefaction on embankment dams. MD Thesis. University of Delft

Mana A. I., Clough G.W. (1981). Prediction of movements for braced cuts in clay. ASCE *J. Geotech. Engng*, 107, jun., 759-777.

Mangir, A., Cosgun, T., Sayin, B., Okumus, V., & Gunes, B. (2023, March). Determination of the change in the structural performance of an RC building due to a nearby deep excavation. In *Structures* (Vol. 49, pp. 792-806). Elsevier.

Manoogian, M. E., & Lee, V. W. (1996). Diffraction of SH-waves by subsurface inclusions of arbitrary shape. *Journal of Engineering Mechanics*, *122*(2), 123-129.

Manual for the geotechnical design of structures to Eurocode 7. (2013). The institution of structural engineers.

Medeiros, L. V., and Eisenstein, Z. (1983). A deep retaining structure in till and sand. Part I: Stress path effects. *Canadian Geotechnical Journal*, *20*(1), 120-130.

Mei, G., Chen, Q., and Song, L. (2009). Model for predicting displacement-dependent lateral earth pressure. *Canadian geotechnical journal*, *46*(8), 969-975.

Meyerhof, G. G. (1947). The settlement analysis of building frames. The Structural Engineer 25, 369-409.

Miao, Y., Zhong, Y., Ruan, B., Cheng, K., & Wang, G. (2020). Seismic response of a subway station in soft soil considering the structure-soil-structure interaction. *Tunnelling and Underground Space Technology*, *106*, 103629.

Ministero delle Infrastrutture (2018). "Norme tecniche per le costruzioni. Gazzetta Ufficiale della Repubblica Italiana 42, Decreto Ministero Infrastrutture", 17/01/2018 (in Italian).

Mo, Y. L., & Hwang, J. M. (1997). Seismic response of reinforced concrete buildings close to deep excavation. *Computer methods in applied mechanics and engineering*, *145*(1-2), 117-134.

Moghadam, M. R., & Baziar, M. H. (2016). Seismic ground motion amplification pattern induced by a subway tunnel: shaking table testing and numerical simulation. *Soil Dynamics and Earthquake Engineering*, *83*, 81-97.

Mononobe, N. and Matsuo M. (1929). On the Determination of Earth Pressures during Earthquakes. Proceedings, World Engineering Congress, Vol. 9, 179- 187.

Mormone, L., Falconio, G., & Mandolini, A. (2012). Groundwater management during excav.s of S. Pasquale station in Naples. In *2nd International Symposium on Geotechnical Engineering for the Preservation of Monuments and Historic Sites* (pp. 579-587). CRC PRESS-TAYLOR & FRANCIS GROUP.

Mylonakis, G., & Gazetas, G. (2000). Seismic soil-structure interaction: beneficial or detrimental?. *Journal of earthquake engineering*, *4*(3), 277-301.

Mylonakis, G., Kloukinas, P., & Papantonopoulos, C. (2007). An alternative to the Mononobe–Okabe equations for seismic earth pressures. *Soil Dynamics and Earthquake Engineering*, *27*(10), 957-969.

Navarro, C. (1992). Seismic analysis of underground structures.

Nawir, H., Prasetyo, B. E., and Apoji, D. (2017). Excavation Analysis using Stress Path Dependent Soil Parameters. *IPTEK Journal of Proceedings Series*, *3*(6).

Negussey, D. (1984). *An experimental study of the small strain response of sand* (Doctoral dissertation, University of British Columbia).

Netzel, H. D. (2009). “Building response due to ground movements.” Ph.D. thesis, Faculty of Architecture and Dept. of Structural Mechanics, Delft Univ. of Technology

Newmark, N. M. (1959). A method of computation for structural dynamics. *Journal of the engineering mechanics division*, *85*(3), 67-94.

Ng, C. W. (1999). Stress paths in relation to deep excavations. *Journal of geotechnical and geoenvironmental engineering*, *125*(5), 357-363.

Ni, P., Mangalathu, S., Song, L., Mei, G., and Zhao, Y. (2018). Displacement-dependent lateral earth pressure models. *Journal of Engineering Mechanics*, *144*(6), 04018032.

Okabe S. (1926). General Theory of Earth Pressure. *Journal of the Japanese Society of Civil Engineers*, Tokyo, Japan, (12) 1.

Ostadan, F. (2005). Seismic soil pressure for building walls: An updated approach. *Soil Dynamics and Earthquake Engineering*, *25*(7-10), 785-793.

Ou, C. Y. (2006). Deep excavation: Theory and practice. Crc Press.

Ou, C. Y., & Hsieh, P. G. (2011). A simplified method for predicting ground settlement profiles induced by excavation in soft clay. *Computers and Geotechnics*, *38*(8), 987-997.

Ou, C. Y., Chiou, D. C., & Wu, T. S. (1996). Three-dimensional finite element analysis of deep excavations. *Journal of Geotechnical Engineering*, *122*(5), 337-345.

Owen, G.N., Scholl, R.E. (1981). Earthquake engineering of large underground structures. Report no. FHWA_RD-80_195. Federal Highway Administration and National Science Foundation.

Panji, M., & Ansari, B. (2017). Transient SH-wave scattering by the lined tunnels embedded in an elastic half-plane. Engineering Analysis with Boundary Elements, 84, 220-230.

Parra-Montesinos, Gustavo J., Antonio Bobet, and Julio A. Ramirez (2006) Evaluation of soil-structure interaction and structural collapse in Daikai subway station during Kobe earthquake. *ACI Structural Journal*, Vol. 103, No. 1, pp 113-122.

Peck, R.B. (1969). Deep excavationsand tunneling in soft ground. *VII Proc. Int. Conf. S.M.F.E., Mexico City, 1969, State of the art volume*, 225-290. Sociedad de Mexicanica de Mecanica de Suelos, Mexico City.

Peck, R.B. (1969b). Advantages and limitations of the observational method in applied soil mechanics. Geotechnique, 19(2), pp.171-187.

Pellegrino, A. (1967). "Proprietà fisico-meccaniche dei terreni vulcanici del Napoletano." In Vol. 3 of Proc., 8th Italian Soil Mechanics Conf., 113–145. Napoli, Italy: Edizioni Scientifiche Italiane (in Italian).

Penzien, J. (2000). Seismically induced racking of tunnel linings. *Earthquake Engineering & Structural Dynamics*, *29*(5), 683-691.

Pepe, M., Sangirardi, M., Reccia, E., Pingaro, M., Trovalusci, P., & De Felice, G. (2020). Discrete and continuous approaches for the failure analysis of masonry structures subjected to settlements. *Frontiers in Built Environment*, *6*, 43.

Petalas, A., & Galavi, V. (2013). Plaxis liquefaction model UBC3D-PLM. *Plaxis report*.

Picarelli, L., A. Evangelista, G. Rolandi, M. V. Nicotera, A. Paone, L. Olivares, A. Scotto di Santolo, S. Lampitiello, and M. Rolandi. (2007). Mechanical properties of pyroclastic soils in Campania region. In Vol. 4. of *Proc. Int. Workshop on Characterisation & Engineering Properties of Natural Soils*, edited by P. Tan and L. Hight, 2331–2383. London: Taylor & Francis.

Pickhaver, J. A. (2006). “Numerical modelling of building response to tunnelling.” Ph.D. thesis, Dept. of Engineering Science, Univ. of Oxford

Pitilakis, K., & Tsinidis, G. (2013). Performance and seismic design of underground structures. In *Earthquake geotechnical engineering design* (pp. 279-340). Cham: Springer International Publishing.

Pitilakis, K., Tsinidis, G., Leanza, A., & Maugeri, M. (2014). Seismic behaviour of circular tunnels accounting for above ground structures interaction effects. *Soil Dynamics and Earthquake Engineering*, *67*, 1-15.

Polshin, D. E., & Tokar, R. A. (1957, August). Maximum allowable non-uniform settlement of structures. In *Proc., 4th Int. Conf. on Soil Mechanics and Foundation Engineering* (Vol. 1, pp. 402-405). London: Butterworth’s.

Power, M., Rosidi, D., Kaneshiro, J., (1998). Seismic vulnerability of tunnels-revisited. In: Ozedimir, L., Ed. Proceedings of the North American Tunneling Conference. Elsevier, Long Beach, CA, USA.

Prosperi, A. Modelling of subsidence induced damage to masonry buildings. (2025). PhD Thesis. TU Delft.

Puebla, H., Byrne, M., Phillips, P. (1997). Analysis of canlex liquefaction embankments prototype and centrifuce models. Canadian Geotechnical Journal, 34, 641–657.

Qian, J., & Beskos, D. E. (1996). Harmonic wave response of two 3-D rigid surface foundations. *Soil Dynamics and Earthquake Engineering*, *15*(2), 95-110.

Qiu, Y. J., Zhang, H. R., Yu, Z. Y., & Zhang, J. K. (2021). A modified simplified analysis method to evaluate seismic responses of subway stations considering the inertial interaction effect of adjacent buildings. *Soil Dynamics and Earthquake Engineering*, *150*, 106896.

Rankine, W. (1857). "On the stability of loose earth." Philosophical Transactions of the Royal Society of London 147: 9 - 27.

Rathje, E. M., Abrahamson, N. A., & Bray, J. D. (1998). Simplified frequency content estimates of earthquake ground motions. *Journal of geotechnical and geoenvironmental engineering*, *124*(2), 150-159.

Roboski, J., & Finno, R. J. (2006). Distributions of ground movements parallel to deep excavations in clay. *Canadian geotechnical journal*, *43*(1), 43-58.

Romeo, R. (2000). Seismically induced landslide displacements: A predictive model, Eng. Geol. 58, 337–351.

Russo, G., & Nicotera, M. V. (2022). A closed form shape function describing 3D settlement field around a deep excavation in sand. *Scientific Reports*, *12*(1), 18528.

Russo, G., and Viggiani, C. (1998). "Osservazione del comportamento di opere a sostegno di uno scavo nel centro storico di Napoli". In *National Italian Conference of the Geotechnical University Researchers* 423–442 (1997).

Russo, G., Autuori, S., & Nicotera, M. V. (2014). San Pasquale station of the Linea 6 in Napoli: dewatering field tests, measurements and back-analyses. In *Soil-Structure Interaction, Underground Structures and Retaining Walls* (pp. 337-344). IOS Press.

Russo, G., Nicotera, M. V., & Autuori, S. (2016). San Pasquale station of line 6 in Naples: Measurements and numerical analyses. *Procedia Engineering*, *143*, 1503-1510.

Russo, G., Nicotera, M. V., & Autuori, S. (2019). Three-dimensional performance of a deep excav. in sand. *Journal of Geotechnical and Geoenvironmental Engineering*, *145*(4), 05019001.

Russo, G., Nicotera, M. V., and Esposito, I. (2024). 3D FEM back analysis of the observed performance of a very deep excavation in the historical center of Naples, Italy. *Journal of Geotechnical and Geoenvironmental Engineering*, *150*(4), 04024010.

Russo, G., Viggiani, C., & Viggiani, G. M. B. (2012). Geotechnical design and construction issues for Lines 1 and 6 of the Naples Underground/Geotechnische Planung und Ausführung der U-Bahnlinien 1 und 6 in Neapel. *Geomechanics and Tunnelling*, *5*(3), 300-311.

Sabatini, P.J., Pass, D.G. and Bachus, R.C. (1999). Geotechnical Engineering Circular NO. 4, Ground Anchors and Anchored Systems. Federal Highway Administration, report FHWA-SA-99-015, 281 p.

Schanz, T. (1998). Zur modellierung des mechanischen verhaltens von reinbungsmaterialien. Mitt Inst fur Geotechnik, Universitat Stuttgart, 1998, 45. 11 (in German)

Schanz, T., Vermeer, P. A., & Bonnier, P. G. (2019). The hardening soil model: Formulation and verification. In *Beyond 2000 in computational geotechnics* (pp. 281-296). Routledge.

Schnaid, F. (2005). Geo-characterisation and properties of natural soils by in situ tests. In *Proceedings of the 16th international conference on soil Mechanics and Geotechnical engineering* (pp. 3-45). IOS Press.

Schofield, A.N. (1980). Cambridge Geotechnical Centrifuge Operations. *Geotechnique 30* (3): 227–268.

Schwan L, Boutin C, Padr´on LA, Dietz MS, Bard P-Y, Taylor C. Site-city interaction: Theoretical, numerical and experimental crossed-analysis. *Geophys J Int* 2016;205(2):1006–31.

Seed, H. B., Hwang, R. N., & Lysmer, J. (1975). Soil-structure interaction analyses for seismic response. *Journal of the Geotechnical Engineering Division*, *101*(5), 439-457.

Seed, H.B. and Whitman, R.V. (1970). Design of Earth Retaining Structures for Dynamic Load. ASCE Specialty Conference, Lateral Stresses in the Ground and Design of Earth Retaining Structures, Cornell Univ., Ithaca, New York, 103–147.

Sharma, S., Judd, W.R., (1991). Underground opening damage from earthquakes. Eng. Geol. 30, 263_276.

Sica, S., Dello Russo, A., Rotili, F., & Simonelli, A. L. (2014). Ground motion amplification due to shallow cavities in nonlinear soils. *Natural Hazards*, *71*(3), 1913-1935.

Sitar, N., Mikola, R. G., and Candia, G. (2012). Seismically induced lateral earth pressures on retaining structures and basement walls. In *Geotechnical engineering state of the art and practice: Keynote lectures from geocongress 2012* (pp. 335-358).

Skempton, A. W. and MacDonald, D. H. (1956). Allowable settlement of buildings. Proc. Inst. Civ. Engrs. 5, Pt.III, 727-768.

Smerzini, C., Aviles, J., Paolucci, R., & Sánchez-Sesma, F. J. (2009). Effect of underground cavities on surface earthquake ground motion under SH wave propagation. *Earthquake Engineering & Structural Dynamics*, *38*(12), 1441-1460.

Smith, G. The behavior of modern flexible framed structures undergoing differential settlements. PhD Thesis.

Son, M. (2003). *The response of buildings to excavation-induced ground movements*. University of Illinois at Urbana-Champaign.

Son, M., & Cording, E. J. (2005). Estimation of building damage due to excavation-induced ground movements. *Journal of geotechnical and geoenvironmental engineering*, *131*(2), 162-177.

Stamos, A. A., & Beskos, D. E. (1995). Dynamic analysis of large 3-D underground structures by the bem. *Earthquake engineering & structural dynamics*, *24*(6), 917-934.

Sun, Q., Dias, D., Guo, X., & Li, P. (2019). Numerical study on the effect of a subway station on the surface ground motion. *Computers and Geotechnics*, *111*, 243-254.

Terzaghi, K. (1934). Large retaining-wall tests. (1). Pressure of dry sand. Eng. News REC., 112 : 136.

Terzaghi, K. (1943). *Theoretical soil mechanics*.

Terzaghi, K. and Peck, R. (1967). Soil Mechanics in Engineering Practice. John Wiley and Sons, New York.

Triantafyllidis, T., & Prange, B. (1987). Dynamic subsoil-coupling between rigid rectangular foundations. *Soil Dynamics and Earthquake Engineering*, *6*(3), 164-179

Trifunac, M. D., & Brady, A. G. (1975). On the correlation of seismic intensity scales with the peaks of recorded strong ground motion. *Bulletin of the Seismological Society of America*, *65*(1), 139-162.

Tsinidis, G. (2018). Response of urban single and twin circular tunnels subjected to transversal ground seismic shaking. *Tunnelling and underground space technology*, *76*, 177-193.

Tsinidis, G., Rovithis, E., Pitilakis, K., & Chazelas, J. L. (2015, April). Dynamic response of shallow rectangular tunnels in sand by centrifuge testing. In *Experimental Research in Earthquake Engineering: EU-SERIES Concluding Workshop* (pp. 493-507). Cham: Springer International Publishing.

Tsinidis, G., Rovithis, E., Pitilakis, K., & Chazelas, J. L. (2016). Seismic response of box-type tunnels in soft soil: experimental and numerical investigation. *Tunnelling and Underground Space Technology*, *59*, 199-214.

Tsuchida, H. (1970). Prediction and Countermeasure against Liquefaction in Sand Deposits. Abstract of the Seminar of the Port and Harbour Research Institute, Ministry of Transport, Yokosuka, Japan, pp. 3.1-3.33 (In Japanese).

Van Nguyen, D., Kim, D., & Choo, Y. (2024). Nonlinear seismic performance of buildings considering deep excavation-soil-structure interaction. Bulletin of Earthquake Engineering, 22(10), 5119-5145.

Veletsos, A. S., & Younan, A. (1994). Dynamic soil pressures on rigid vertical walls. *Earthquake engineering & structural dynamics*, *23*(3), 275-301.

Vicencio, F., Alexander, N. A., & Flores, E. I. S. (2023, October). A State-of-the-Art review on Structure-Soil-Structure interaction (SSSI) and Site-City interactions (SCI). In *Structures* (Vol. 56, p. 105002). Elsevier.

Visone, C., & Santucci de Magistris, F. (2007). Some aspects of seismic design methods for flexible earth retaining structures. In *Workshop of ERTC12-Evaluation Committee for the Application of EC8*.

Vozza, A. (2017) Analisi numeriche della suscettibilità alla liquefazione di sabbie sciolte con un modello costitutivo avanzato. MD Thesis. Università degli Studi di Napoli Federico II. (in Italian)

Wang, G., Yuan, M., Miao, Y., Wu, J., & Wang, Y. (2018). Experimental study on seismic response of underground tunnel-soil-surface structure interaction system. *Tunnelling and Underground Space Technology*, *76*, 145-159.

Wang, H. F., Lou, M. L., & Zhang, R. L. (2017). Influence of presence of adjacent surface structure on seismic response of underground structure. *Soil Dynamics and Earthquake Engineering*, *100*, 131-143.

Wang, H. F., Lou, M. L., Chen, X., & Zhai, Y. M. (2013). Structure–soil–structure interaction between underground structure and ground structure. *Soil Dynamics and Earthquake Engineering*, *54*, 31-38.

Wang, J.N. (1993). Seismic design of tunnels: a simple state of the art design approach. New York: Parsons Brinckerhoff Inc.

Warburton GB, Richardson JD, Webster JJ. Forced vibrations of two masses on an elastic half space. J Appl Mech 1971;38:148–56.

Whitman, R. V. (1991). Seismic design of earth retaining structures.

Wolf, J. P. (1985). Dynamic soil-structure interaction. Prentice Hall International series in Civil Engineering and Engineering Mechanics.

Wood, J. H. (1973). *Earthquake-induced soil pressures on structures* (Doctoral dissertation, California Institute of Technology).

Yahyai, M., Mirtaheri, M., Mahoutian, M., Daryan, A.S., Assareh, M.A. (2008) Soil Structure Interaction between two Adjacent Buildings under Earthquake Load. *American Journal of Engineering and Applied Sciences*;1:121–5. https://doi.org/10.3844/ajeassp.2008.121.125.

Yeganeh, N., Bazaz, J. B., & Akhtarpour, A. (2015). Seismic analysis of the soil–structure interaction for a high rise building adjacent to deep excavation. *Soil dynamics and earthquake engineering*, *79*, 149-170.

Yiouta-Mitra, P., Kouretzis, G., Bouckovalas, G., & Sofianos, A. (2007). Effect of underground structures in earthquake resistant design of surface structures. In *Dynamic response and soil properties* (pp. 1-10).

Zhu, S., Chen, C., Zhang, G., and Du, C. (2022). Theoretical and experimental investigations of anchoring force loss behavior for prestressed ground anchors. *Can. Geotech. Journ.* 59(9), 1587–1601.

Zienkiewicz, O. C., Bicanic, N., & Shen, F. Q. (1989). Earthquake input definition and the trasmitting boundary conditions. In *Advances in computational nonlinear mechanics* (pp. 109-138). Vienna: Springer Vienna.